

**Clean catalytic technologies for
converting renewable feedstocks to
chemicals and fuels**

Amin Osatiashtiani

A thesis for the degree of
Doctor of Philosophy in Chemistry

Cardiff University
School of Chemistry
2014

Abstract

Concerns over dwindling fossil fuel reserves, and the impact of CO₂ emissions on climate change, is driving the quest for alternative feedstocks to reduce dependence on non-renewable sources of fuels and chemicals. Biomass offers the only renewable source of organic molecules for the manufacture of bulk, fine and speciality chemicals necessary to secure the future needs of society. In this regard, conversion of biomass derived C₆ sugars to 5-hydroxymethylfurfural (HMF), the latter a potential, bio-derived platform chemical, is of significant current interest. However, commercial implementation of HMF as a chemical intermediate is impeded by high production costs. A heterogeneously catalysed route to directly convert glucose into HMF in aqueous media thus remains highly sought after.

In this thesis, the telescopic conversion of glucose to fructose and then HMF has been explored over a family of bifunctional sulfated zirconia catalysts possessing tuneable acid–base properties. Characterisation by acid–base titration, XPS, XRD and Raman reveal that sub-monolayer SO₄ coverages offer the ideal balance of basic and Lewis–Brønsted acid sites required to respectively isomerise glucose to fructose, and subsequently dehydrate fructose to HMF. Here we demonstrate that systematic control over the Lewis–Brønsted acid and base properties of SZ enables one-pot conversion of glucose to HMF in aqueous media, employing a single bi-functional heterogeneous catalyst.

Further improvements in catalytic performance have been achieved through the synthesis of monolayer grafted ZrO₂/SBA-15 catalysts in which conformal layers of ZrO₂ are grown from Zr propoxide. Analysis reveals 1-3ML can be achieved; subsequent sulfation yields a catalyst with 1.25 to 2 times the activity of bulk SZ. These catalysts also exhibit remarkable water tolerance with retention of pore structure upon hydrothermal treatment at 170 °C for 6 h. All catalysts find application in esterification, with optimum activity for samples treated with 0.1 M H₂SO₄.

Acknowledgement

This thesis would not have been possible without the help and support of many people, to whom I am extremely grateful.

I would like to express my deepest gratitude to my supervisor, Prof Karen Wilson, for her excellent guidance, patience and support throughout the duration of my PhD. I would like to thank Prof Adam F. Lee for providing additional supervision, support and advice. I lack the words to thank Prof Juan A. Melero of King Juan Carlos University in Madrid who gave me the opportunity to carry out some part of my research in his research group and for the funding.

Several of the results in this thesis were obtained with the assistance of some very helpful individuals. I thank Dr Gabriel Morales, Dr Marta Paniagua and Dr Rebeca Sánchez Vázquez of King Juan Carlos University in Madrid, for helping me with the synthesis of SBA-15 and SEM/EDX analysis and also their assistance during my stay in Madrid. Additional thanks go to Prof Rob Brown and Dr Marta Granollers of University of Huddersfield for their contribution to adsorption calorimetry and TPD.

To past and present members of the Surface, Material and Applied Chemistry group formerly based in Cardiff University, thank you so much for your continuous support, help and friendship. Individually, I would like to thank Dr Chris Parlett, Dr Mark Isaacs and Mr Lee Durndell for their assistance. I am also thankful to all members of staff at the School of Chemistry at Cardiff University and also European Bioenergy Research Institute, Aston University.

Last but not least, I would like to thank my parents for all their love, support and encouragement. Without your unconditional support throughout my life and studies, I am sure I would not be where I am today. I love you so much.

Table of contents

Abstract	i
Acknowledgements	ii
Declaration	iii
Table of contents	iv
List of Abbreviations	ix

Chapter 1 – Introduction

1.1 Introduction	2
1.1.1 History of biofuel production	6
1.1.2 Environmental concerns	7
1.1.2.1 USA	8
1.1.2.2 Europe	8
1.1.2.3 UK	8
1.1.3 Renewable transport fuels	8
1.1.4 Classification of biofuels	9
1.1.4.1 First generation biofuels	9
1.1.4.2 Second generation biofuels	10
1.1.4.3 Third generation biofuels	11
1.1.5 The bioenergy concept	11
1.1.6 Biomass conversion technologies	12
1.1.6.1 Thermo-chemical conversion	13
1.1.6.2 Biochemical conversion	15
1.1.7 Green chemistry and the role of catalysis	16
1.1.8 Production of fine chemicals and fuels from lignocellulosic biomass	18
1.1.8.1 HMF	20
1.1.9 Glucose transformation to HMF	21
1.1.9.1 Mechanism of glucose to HMF conversion	21
1.1.9.2 Glucose dehydration in single-phase systems	23
1.1.9.3 Glucose dehydration in biphasic systems	35
1.1.9.4 Glucose dehydration in ionic liquids	40
1.2 Thesis aims	45
1.3 References	46

Chapter 2 – Experimental

2.1 Catalyst preparation	58
2.1.1 Sulphated zirconia	58
2.1.2 Supported sulphated zirconia	58
2.1.2.1 Preparation of SBA-15 support	58
2.1.2.2 Incorporation of zirconia on SBA-15	58
2.2 Catalyst characterization	59
2.2.1 Scanning Electron Microscopy / Energy-dispersive X-ray spectroscopy	59
2.2.2 Transmission electron microscopy	60
2.2.3 Inductively coupled plasma – optical emission spectrometry	61
2.2.4 N ₂ porosimetry	61
2.2.5 Thermal gravimetric analysis (TGA)	64
2.2.6 X-ray Photoelectron Spectroscopy (XPS)	64
2.2.7 Powder X-Ray Diffraction (XRD)	67
2.2.8 Vibrational spectroscopy	69
2.2.8.1 Diffuse reflection infrared Fourier transform spectroscopy (DRIFTS) and <i>in situ</i> pyridine chemisorption	69
2.2.8.2 Raman spectroscopy	70
2.2.9 Measurement of Acidity and basicity by microcalorimetry and TPD	70
2.3 Catalyst testing	72
2.3.1 Dehydration of saccharides	72
2.3.1.1 Leaching test	75
2.3.1.2 Recyclability test	75
2.3.1.3 Hydrothermal stability test	75
2.3.2 Esterification of free fatty acids	76
2.3.2.1 Studying the effect of FFA alkyl chain length and alcohol type	76
2.3.2.2 Leaching test	77
2.4 List of chemicals	78
2.5 References	79

Chapter 3 – Bifunctional SO₄²⁻/ZrO₂ catalysts for production of platform chemicals from biomass derived sugars

3.1 Introduction	82
3.1.1 Sulphated zirconia	82
3.1.1.1 Crystallinity	82
3.1.1.2 Acidity	83

3.1.1.3 Active site	84
3.1.2 Application of SZ catalyst in HMF production	87
3.2 Results and discussion	87
3.2.1 Catalyst characterization	87
3.2.1.1 Surface and bulk elemental analysis	87
3.2.1.2 N ₂ porosimetry	89
3.2.1.3 X-Ray Photoelectron Spectroscopy	91
3.2.1.4 <i>In situ</i> Diffuse reflectance infrared Fourier transform	93
3.2.1.5 Powder X-ray Diffraction	94
3.2.1.6 Raman spectroscopy	94
3.2.1.7 Acid and base sites measurements	96
3.2.1.8 Pyridine titration	97
3.2.2 Glucose conversion to HMF	98
3.2.3 Fructose conversion to HMF	103
3.2.4 Effect of reactant concentration	107
3.2.5 Effect of catalyst loading	108
3.2.6 Leaching test and recyclability	110
3.2.7 Xylose conversion to furfural	111
3.3 Conclusion	117
3.4 References	119

Chapter 4 – Glucose transformation to HMF over SBA-15 supported sulphated zirconia catalysts: the role of zirconia film and sulphur content

4.1 Introduction	126
4.2 Results and discussion	127
4.2.1 Characterization of parent Zr/SBA-15	129
4.2.1.1 Powder X-ray diffraction	129
4.2.1.2 N ₂ porosimetry	130
4.2.1.3 Calculation of ZrO ₂ film thickness and elemental analysis by XPS and SEM/EDX	131
4.2.1.4 Acid site measurements	133
4.2.2 Characterization of xML-SZ/SBA-15 catalysts	133
4.2.2.1 Powder X-ray diffraction	134
4.2.2.2 N ₂ porosimetry	135
4.2.2.3 Surface and bulk elemental analysis	136

4.2.2.4 Acid and base site measurements	138
4.2.2.5 Transmission electron microscopy	143
4.2.3 Effect of [H ₂ SO ₄] molarity on 2ML Zr/SBA-15	144
4.2.3.1 Powder X-ray diffraction	144
4.2.3.2 N ₂ porosimetry	146
4.2.3.3 Surface and bulk elemental analysis	149
4.2.3.4 Diffuse reflectance infrared Fourier transform spectroscopy	152
4.2.3.5 Acid and base sites measurements	155
4.2.4 Glucose and fructose conversion to HMF over SZ/SBA-15 catalysts	162
4.2.4.1 Effect of zirconia monolayers on glucose conversion	162
4.2.4.2 Effect of sulphur loading on glucose conversion	167
4.2.4.3 Effect of sulphur loading on fructose conversion	172
4.2.5 Comparison between bulk SZ and SBA-15 supported SZ	176
4.2.6 Catalyst stability and recyclability	177
4.2.6.1 Stability assessment via leaching test	177
4.2.6.2 Recyclability	178
4.2.6.3 Hydrothermal stability test	179
4.2.7 Catalyst deactivation	181
4.3 Conclusion	182
4.4 References	183

Chapter 5 – Biodiesel production via esterification of free fatty acids over sulphated zirconia based catalysts

5.1 Introduction	187
5.1.1 Esterification	189
5.2 Results and discussion	192
5.2.1 Bulk sulphated zirconia for esterification of FFAs	192
5.2.1.1 Effect of carbon chain length on esterification of fatty acids with methanol	192
5.2.1.2 Effect of alcohol type on propionic acid esterification	196
5.2.2 SBA-15 supported sulphated zirconia catalysts for esterification of FFAs	200
5.2.2.1 Esterification of propionic acid with methanol over the series of SZ/SBA-15 catalysts with different S content	201
5.2.2.2 Esterification of palmitic acid with methanol over the series of SZ/SBA-15 catalysts with different S content	202
5.2.3 Comparison between bulk SZ and SBA-15 supported SZ materials in esterification of FFAs with methanol	203
5.2.4 Leaching test	204

5.3 Conclusion	205
5.3 References	206
 Chapter 6 – Summary	
6.1 Conclusion	210
6.2 Future work	213
6.3 References	213

List of abbreviations

[BMIm]Cl	1-Butyl-3-methylimidazolium chloride
[C ₄ mim]Cl	1-n-butyl-3-methylimidazolium chloride
[EMIm]Cl	1-Ethyl-3-methylimidazolium chloride
AD	Anaerobic digestion
AHG	Anhydroglucose
APD/H	Aqueous-phase dehydration/hydrogenation
BET	Brunauer–Emmet–Teller
BJH	Barrett–Joyner–Halenda
BSE	Backscattered electrons
BTL	Biomass to liquid
CMF	5-chloromethylfurfural
DA	Diode array
DMA	Dimethylacetamide
DMF	Dimethylformamide
DMSO	Dimethyl sulfoxide
DOE	Department of energy
DRIFTS	Diffuse reflectance infra-red Fourier transform spectroscopy
DSC	Differential scanning calorimetry
EDX	Energy-dispersive X-ray
EMF	5-ethoxymethylfurfural
EPA	Environmental protection agency
EU	European union
FAME	Fatty acid methyl ester
FFA	Free fatty acid
FWHM	Full width at half maximum
GC	Gas chromatography
GHG	Greenhouse gases
GHL	γ -hexalactone
GOL	γ -octalactones
GVL	γ -valerolactone
HAF	2-(2-hydroxyacetyl)furan
HMF	5-hydroxymethyl-furfural
HPA	Heteropolyacids
HPLC	High performance liquid chromatography
HRTEM	High resolution transmission electron microscopy
ICP-OES	Inductively coupled plasma-optical emission spectroscopy
IL	Ionic liquid
IMFP	Inelastic mean free path
IR	Infra-red

MF	5-methylfurfural
MIBK	Methyl isobutyl ketone
ML	Monolayer
MS	Mass spectroscopy
MTBE	Methyl tert-butyl ether
MTHF	Methyltetrahydrofuran
NHC	N-heterocyclic carbene
NMR	Nuclear magnetic resonance
OPEC	Organization of the petroleum exporting countries
PE	Primary electrons
R&D	Research and development
RED	Renewable energy directive
RFS	Renewable fuel standard
RI	Refractive index
SBA-15	Santa Barbara Amorphous-15
SE	Secondary electrons
SEM	Scanning electron microscopy
SRC	Short rotation coppice
SSF	Solid state fermentation
STEM	Scanning transmission electron microscopy
SZ	Sulphated zirconia
TAG	Triacylglycerol
TEM	Transmission electron microscopy
TEOS	Tetraethyl orthosilicate
TGA	Thermal gravimetric analysis
THF	Tetrahydrofuran
TOF	Turnover frequency
TPD	Temperature programmed desorption
UAE	United Arab Emirates
UK	United Kingdom
UV	Ultra violet
VIH	Vapor induced hydrolysis
XPS	X-ray photoelectron spectroscopy
XRD	X-Ray diffraction
ZSM-5	Zeolite Socony Mobil-5

Chapter 1

Introduction

1.1 Introduction

Bioresources are one of the major parts of renewable resources. Transition from fossil fuel based energy carriers to renewable alternatives in order to meet the increasing demand for energy, fuel and chemicals is a significant challenge facing sustainable industrial development. **Figure 1.1** illustrates the world energy consumption since 90's and the forecasts for energy demand in future decades. Today, the development of sustainable biomass feedstocks for energy/biofuel and biochemical production is at the centre of attention around the world; with extensive effort being made to convert academic and scientific advances into commercial reality.¹

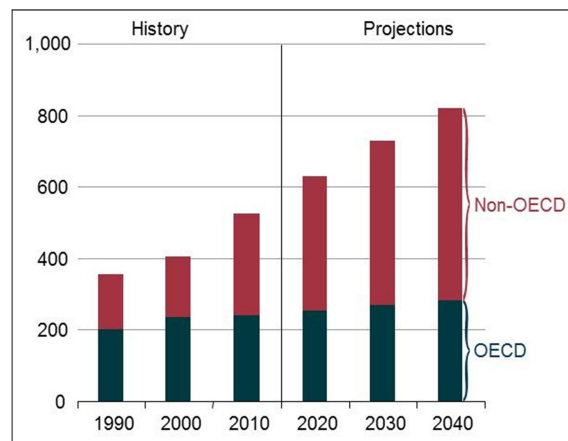


Figure 1.1: World energy consumption, 1990-2040 (quadrillion Btu)²

The term biofuel here refers to any liquid fuel that is made from plant material, residues and wastes that can replace the petroleum based fuels. Biofuels are increasingly being considered as an alternative for petroleum base fuels for transport to help with the problems associated with fossil fuels.¹ The growing trend in energy consumption over the past decades and predictions for increase in energy demand in future along with limited sources of fossil fuels has caused a great deriving force for researchers and industries to move towards sustainable sources of energy.

Climate change and environmental concerns are another motivation for researchers within academia and industry to search for a green and renewable source of energy. The so called greenhouse gas effect is known as the main reason for the global warming phenomenon. The expression of “greenhouse gas” is attributed to those gaseous constituents of the atmosphere both natural and anthropogenic that absorb and emit

radiation at specific wavelengths within the spectrum of thermal infrared radiation emitted by the earth's surface, the atmosphere itself, and by clouds. The major greenhouse gasses in the Earth's atmosphere include water vapor (H_2O), carbon dioxide (CO_2), nitrous oxide (N_2O), methane (CH_4) and ozone (O_3).³ Atmospheric radiation is emitted to all directions, including downward to the Earth's surface. Thus greenhouse gases trap heat within the surface-troposphere system. This is called the greenhouse effect.^{4, 5}

Undeniable evidence from *in situ* measurements and ice core data shows that the atmospheric concentrations of important greenhouse gases such as carbon dioxide (CO_2), methane (CH_4), and nitrous oxide (N_2O) have increased over the last few centuries, resulting in a global temperature increase.⁶

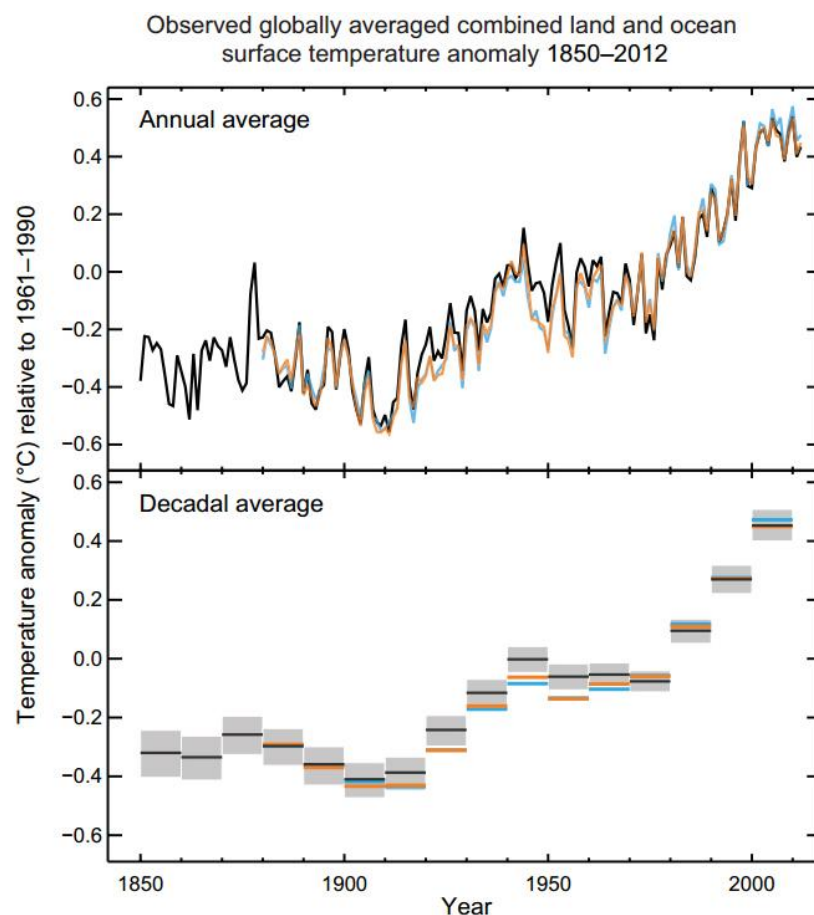


Figure 1.2: Observed global mean combined land and ocean surface temperature anomalies, from 1850 to 2012 from three data sets. Top panel: annual mean values. Bottom panel: decadal mean values including the estimate of uncertainty for one dataset (black). Anomalies are relative to the mean of 1961–1990.⁶

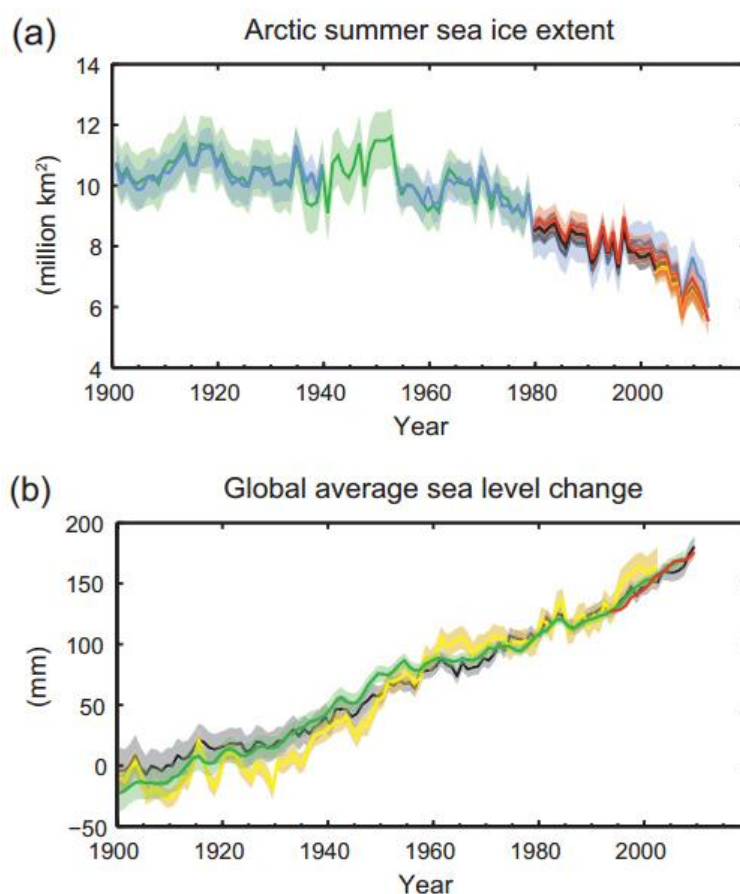


Figure 1.3: Multiple observed indicators of a changing global climate: (a) extent of Arctic July-August-September (summer) average sea ice; (b) global mean sea level relative to the 1900–1905 mean of the longest running dataset, and with all datasets aligned to have the same value in 1993, the first year of satellite altimetry data. All time-series (coloured lines indicating different data sets) show annual values, and where assessed, uncertainties are indicated by coloured shading. See Technical Summary Supplementary Material for a listing of the datasets.⁶

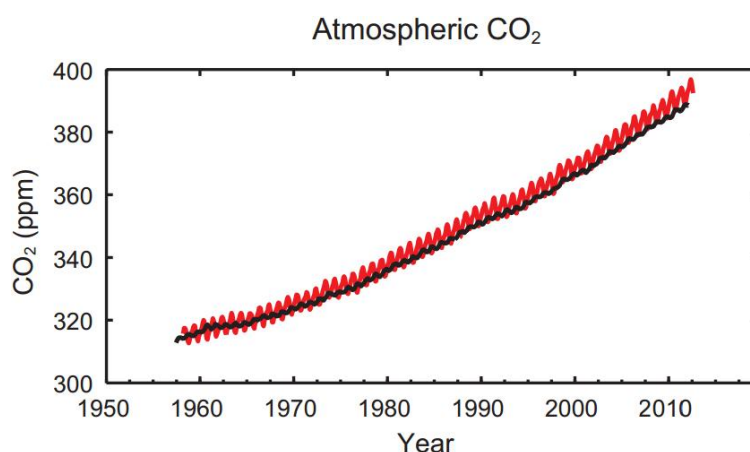


Figure 1.4: Multiple observed indicators of a changing global carbon cycle: atmospheric concentrations of carbon dioxide (CO₂) from Mauna Loa (19°32'N, 155°34'W – red) and South Pole (89°59'S, 24°48'W – black) since 1958.⁶

Although, scientists are not clear about the true extent of the human effect on climate change and global warming, there is no doubt about the evidence that shows our planet has warmed over the last century and human activities have intensified the global warming.⁷ Reduction in greenhouse gas emissions and temperature increases require a radical change in the energy sources utilised by industry shifting from an over-reliance on fossil fuels to renewable and green motifs. Current reports by the International Energy Agency highlight that 69% of all CO₂ emissions, and 60% of all greenhouse gas emissions, are energy-related.⁸

Extensive combustion of these fossil fuels, to produce sufficient energy for a growing world population, has also led to rising atmospheric levels of the greenhouse gas carbon dioxide (the main source of greenhouse gas pollution). Aside from the obvious environmental benefits associated with their use, the development of renewable transport fuels may also promote energy security for some crude oil consumers. Currently, the Middle East, with 48.4% % of the world's proved oil reserves, is the major exporter of crude oil.⁹ In 2012 Saudi Arabia alone sold around one fifth of the total world exports and Saudi Arabia, Iran, Iraq, UAE and Kuwait together supplied almost 30% of total crude oil exports.¹⁰ 66.5% of the total oil consumption was centred on light distillates (consists of aviation and motor gasolines and light distillate feedstock) and middle distillates (consists of jet and heating kerosenes, and gas and diesel oils). However this number for the European Union members is 74%.⁹ The top 5 importers in 2012 were the USA, China, Japan, India and South Korea while Germany, France, Spain, Italy and the Netherlands are the biggest European oil importers.¹¹ In the current global political climate however, importing oil from the politically unstable countries in Middle East and also Russia which had many political conflicts with its neighbour countries and west, could become problematic¹² and producing alternative and sustainable fuels from locally owned resources could be a viable solution to this.

Table 1.1: Top 10 world oil producers¹⁰ (2012 data)

Producers	Mtoe	% of world total
Saudi Arabia	544	13.1
Russia	520	12.6
US	387	9.3
China	206	5
Iran	186	4.5
Canada	182	4.4
UAE	163	3.9
Venezuela	162	3.9
Kuwait	152	3.7
Iraq	148	3.6
Rest of the world	1492	36
World	4142	100

The second generation of biofuels include biofuels that are products of biological processes and also fuels made by thermochemical processes, which represent two completely different approaches. The successful commercial development of second generation biofuels requires major progress in feedstock selection, its optimization through genetic, crop breeding as well as crop husbandry and production practices. Technology improvements are essential for biofuel production either that is via a biochemical pathway or by converting biomass. One of the greatest privileges of thermochemical processing over biological processing is greater feedstock flexibility but it requires a larger scale relative to biological processing to be an economically viable process. Worldwide efforts are ongoing to commercialise second generation biofuels derived from both routes.¹

1.1.1 History of biofuel production

Biofuels in the solid form has been in use ever since man discovered fire. Wood was the first form of biofuel that was used even by the ancient people for cooking and heating. Discovery of electricity resulted in exploring a new way for utilizing the biofuel. Use of biofuel as a fuel for transport has a history as old as the history of internal engines. In 19th century, Nicholas Otto ran his first spark-ignition engines on ethanol, and Rudolph Diesel, who invented the engine that bears his name, used peanut oil in his prototype compression-ignition engines. However, just as automobiles were becoming popular at the beginning of the 1900s and subsequent development of cheap and readily available

petroleum-derived fuels, there became little incentive for research into new biofuel-derived technologies to produce more sustainable transport fuels.¹³

During the World War I and II bioethanol received a lot of attention in Europe, the US and Brazil due to shortage in petroleum supplies. However, biofuel had virtually disappeared from fuel market soon after the Second World War, when liquid fuels became easily available.¹³ The oil crisis in the 1970s and political instability in oil-rich Middle East countries prompted oil importer countries again to seek alternatives to Middle East oil. For instance, in October 1973 Arab members of OPEC announced an embargo on oil exports to selected countries viewed as supporting Israel, which was followed by significant cutbacks in OPEC's total oil production. Production from Arab members of OPEC in November was down 4.4 mb/d from production values quoted September previous, a shortfall corresponding to 7.5% of global output. There are many other examples where the oil market has been massively influenced by a political move or military action in that region.¹⁴ The 2009 Russia-Ukraine gas dispute is one of the newest examples of this type, causing widespread disruption to many European nations.¹⁵

1.1.2 Environmental concerns

More recently, environmental standards have become important drivers for biofuel markets. In the US, the Environmental Protection Agency (EPA) began requiring cities with high ozone levels to blend gasoline with fuel oxygenates, including ethanol. When state governments learned in the late 1990s and early 2000s that the most common oxygenate, methyl tertiary-butyl ether (MTBE), was a possible carcinogen that was seeping into groundwater, 20 states passed laws to phase it out, creating a surge in demand for US ethanol in the early 2000s.

In the European Union, the world's largest biodiesel producer, biofuel consumption is mostly driven by blending mandates. External incentives are required to achieve the biofuel targets set by national administrations. Production is unprofitable (Brazil being the only exception) and it needs to be promoted via tax exemptions, subsidies or other forms of financial incentives.

1.1.2.1 USA

In July 2010 the updated Renewable Fuel Standard (RFS2) went into effect, finalizing proposals made with the Energy Independence and Security Act of 2007. According to RFS2, the volume of renewable fuel required to be blended into transportation fuel must be increased from 9 billion gallons in 2008 to 36 billion gallons by 2022; Also from 2015 onwards, the volume of conventional biofuels (e.g. corn ethanol) should be 15 million gallons. Lignocellulose-derived biofuels are expected to amount to 16 billion gallons in 2022, while the total contribution of advanced biofuels should not fall below 21 billion gallons line by 2022.¹⁶

1.1.2.2 Europe

In April 2009 the parliament of the European Union endorsed a minimum binding target of 10% for biofuels in transport by 2020 as part of the EU Directive 2009/28/EC on renewable energy. The directive also specified a minimum 35% reduction in GHG emissions to be achieved by biofuels during their life cycle and No bio-feedstock shall originate from primary forests, highly bio-diverse grassland, protected territories and carbon-rich areas. In several countries tax reductions or exemptions have been implemented in order to support production or consumption.¹⁶

1.1.2.3 UK

UK has the same goal as the European Union to achieve the target of Renewable Energy Directive (RED) by providing 10% of energy demand in transport sector from renewable energy.¹⁷

1.1.3 Renewable transport fuels

Road transport is a significant source of greenhouse gas emissions as the department of energy and climate change in UK reported that in 2013, carbon dioxide emissions from the transport sector were about a quarter of all carbon dioxide emissions.¹⁸ On the other hand, in addition to renewability and sustainability of biofuels compared to their conventional petroleum-based competitors, biofuels are also biodegradable, non-toxic and can considerably prevent carbon emission compared to fossil fuel. Biofuel biodegradability prevents soil and underground water pollution if spilt, making them less of an environmental risk than non-renewable fuels.¹⁹ Biofuels can be used in all

vehicles from buses to boats and aeroplanes, requiring minor or no modification in engine or fuel distribution infrastructure. Moreover, their use can lead to a significant cut in carbon dioxide emissions of 50-80% compared with fossil fuels.²⁰ Biofuels come in the form of liquid and gas. Liquid biofuels can be substituted for the existing fossil petrol or diesel.

1.1.4 Classification of biofuels

Biofuels are categorized into two major classes. The “primary biofuels” are mostly the traditional and unprocessed form of using biomass for heating, cooking and electricity power generation by means of direct combustion of the natural material. This class of biofuels includes fuel-wood, wood chips and pellets, etc. Low efficiency, environmental risks and toxic emissions associated with this type of biofuels make them an undesired source of energy for large scale processes.²¹ The other class of biofuels known as “secondary biofuels” are obtained by biomass processing and come in solid (charcoal), liquid (ethanol, biodiesel, etc.) or gas (biogas) forms and can be used as fuels for transport or various other industrial processes. The secondary biofuels themselves are further categorized into three main groups based on their feedstock and processing technology that are known as first, second and third generation biofuels.²²

1.1.4.1 First generation biofuels

The term “first generation biofuels” generally refers to those biofuels that are produced from sugars, starch or oil rich food crops.^{13, 21-25} This type of renewable fuels mainly includes alcohols (bioethanol) and oils (biodiesel).

The technology required for the production of these biofuels is well understood and has been subject to substantial process development. Therefore, first generation biofuels are relatively easy to produce on a commercial scale. Although first generation biofuels are very well developed and highly commercialised, the main challenge in their research is the optimization of processes intended to reduce cost so that the products can compete with their traditional non-renewable rivals.²⁴

The most important drawback associated with the first generation biofuels is the competition between food and fuel production from edible crops.^{26, 27} This so called “food-versus-fuel dilemma” has caused considerable rises in food prices in many

biofuel-producing countries and has been the major criticism for first generation biofuels.^{28, 29} Apart from land use competition between fuel and food, deforestation is another major concern regarding the 1G biofuels. For instance, in Indonesia vast tracts of rainforest and peat land are being cleared in favour of palm oil plantation.³⁰ Moreover, disagreement about the final GHG-emissions and energy balance and the suspicious social sustainability, make the first generation biofuels less interesting source of energy.^{22, 23, 25, 31, 32}

1.1.4.2 Second generation biofuels

Various concerns about first generation biofuels have aroused great interest for developing the next generation of biofuels produced from non-food feedstocks.^{33, 34} Second generation biofuels, also known as Biofuels 2.0 or Biofuels 2G, usually refers to biofuels produced from non-edible cellulosic materials like purpose-grown vegetative grasses, short rotation forests and other energy crops such as miscanthus and SRC willow, agricultural forestry residues or co-products such as wheat straw and woody biomass.^{33, 35, 36} Since the feedstock for second generation biofuels does not require usage of agricultural land, the food versus fuel issue becomes moot.^{34, 37} Because the main component of biomass feedstock for this type of biofuels is cellulose, they are also known as cellulosic fuels.³⁷

One of the main advantages of the 2nd generation biofuels over the first generation is the potential to process readily available, lower cost and more abundant feedstocks. More importantly, 2nd generation biofuels can process a wider range of feedstocks than the 1st generation biofuels. It is also claimed that these 2nd generation biofuels may offer even greater benefits in terms of environmental performance, efficiency, and getting integrated into the existing fuel supply and distribution system, compared with 1st generation biofuels.³⁸ Additionally, to obtain the same amount of biomass Biofuels 2G requires less farmland, because in contrast with 1st generation biofuels, the whole plant can be used instead of just the grain or oil. Also a mixture of crops can be grown, which generally requires less fertiliser and has less impact on biodiversity.

1.1.4.3 Third generation biofuels

Third-generation biofuels are directly produced from CO₂ and sunlight via photosynthesis process and usually refers to renewable fuels derived from algae, which are either unicellular or multicellular autotrophic organisms.^{37, 39, 40} However, it shouldn't be understood that algae is the only feedstock for third generation biofuels production. Other third generation biofuels include biodiesel produced from yeast and fungus²² and bioethanol produced via direct cellulose fermentation (consolidated bioprocessing).⁴¹

Unlike Biofuels 2G that increase land use change and requires pretreatment and complicated process and production equipment, more investment per unit of production and larger-scale facilities to confine and curtail capital cost, which has resulted in preventing it from being fully commercialized^{42, 43}, Biofuels 3G production do not need to occupy farmland or use sophisticated production processes, and also requires less energy than other feedstock during conversion process. Obviously it doesn't compete with food crops and additionally, it produces considerably greater amounts of biomass and lipids than Biofuels 1G and 2G.³⁴ They capture CO₂ which can be utilized from power plants emissions and moreover, algae remove N and P from wastewater thus reducing the potential for pollution.^{42, 44, 45} Algal biomass offer the opportunity to choose from various processes such as liquefaction, pyrolysis, gasification, extraction and transesterification, fermentation, and anaerobic digestion to convert biomass to different fuels.⁴⁶⁻⁵¹

1.1.5 The biorefinery concept

The production of 2nd generation biofuels from biomass residues are yet to be fully commercialized. But if necessary investments on R&D and infrastructure are achieved, it could enter the energy market within 10-15 years. In this respect, coproduction of valuable biofuels and chemicals as well as electricity and heat is crucial for economic viability of 2nd generation biofuels. Here is where the concept of biorefinery comes in.⁵²

By definition, "Biorefining is the sustainable processing of biomass into a spectrum of marketable products and energy".⁵³ So in biorefinery concept a wide range of technologies and processes come together to break biomass feedstocks (wood, grasses, corn...) into their building blocks (carbohydrates, proteins, triglycerides...) and convert

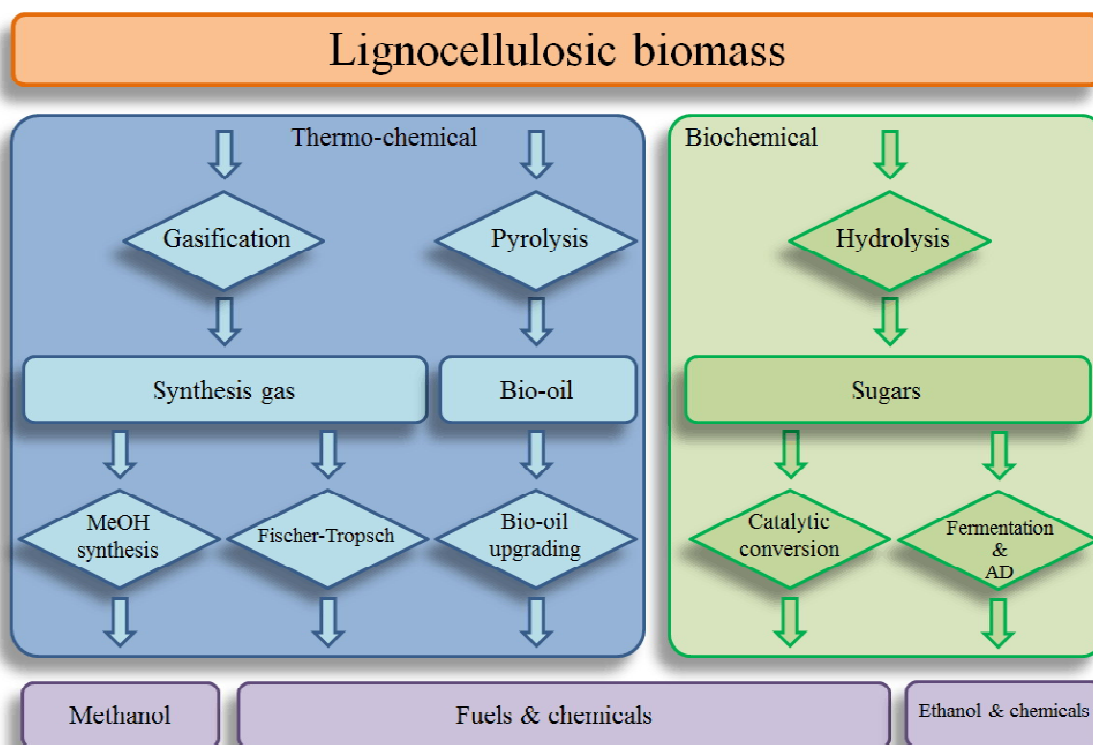
those to value added products, biofuels and chemicals. This is very similar to the concept of today's petroleum refinery which produces variety of fuels and co-products from crude oil. However the main challenge in biorefinery development appears to be efficient and cost effective production of transportation fuels and this could be achieved by co-production of bio-chemicals. This is beneficial economically and environmentally to production of both biofuels and biochemical,⁵³ since currently most existing biofuels and biochemicals are produced in separate production units where feedstock is in competition with the food industry and therefore their exploitation is limited, thus ensuring relatively high production costs.^{52, 54} However, it is important to minimize the consumption of non-renewable fuels and resources in the biorefinery processing while complete and efficient biomass use should be maximized, otherwise it would be self-defeating.

Unlike oil refineries which are large, dedicated plants, centred strategically in special locations, biorefineries are expected to be dispersed complexes with a different range of sizes making them able to revitalize rural areas. In this context, several bio-industries can combine their material flows in order to reach a complete utilization of all biomass components: the residue from one bio-industry (e.g. lignin from a lignocellulosic ethanol production plant) becomes an input for other industries, giving rise to integrated bio-industrial systems. In addition, biomass resources are locally available in many countries and their use, may contribute to reduce dependency on fossil fuels.⁵³

1.1.6 Biomass conversion technologies

There are a variety of ways to convert biomass to energy carriers and useful chemicals.

Scheme 1.1 illustrates the main conversion routes that are used or under development for production of transport fuels and chemicals.



Scheme 1.1: Main thermo-chemical and biochemical routes for conversion of lignocellulosic biomass to fuels and chemicals

1.1.6.1 Thermo-chemical conversion

1.1.6.1.1 Combustion

Apart from the classic application of biomass for heat production in domestic applications, it is also used on an industrial scale for electricity, heat and process steam utilization worldwide. Co-combustion of biomass, in particular in coal-fired power plants, is the single largest growing conversion route for biomass in many EU countries (e.g. Spain, Germany, and the Netherlands to name a few).²⁰

1.1.6.1.2 Gasification

The partial combustion of biomass at high temperatures which results in production of combustible gases consisting of carbon monoxide (CO), hydrogen (H₂) and traces of methane (CH₄), is known as “Gasification”.⁵² The mixture of these gases is called a “producer gas”. Producer gas has a variety of applications predominantly in the operation of internal combustion engines, substitution for furnace oil in direct heat applications and the production of methanol in an economically viable way.⁵³ It also

could be subjected to Fischer-Tropsch processes (after purification) to produce liquid hydrocarbons.⁵⁴

1.1.6.1.3 Pyrolysis

Pyrolysis is the decomposition of biomass by heating in an oxygen-free or oxygen-limited environment to liquid (known as bio-oil or bio-crude), solid and gaseous fractions at temperatures ranging from 350 to 700 °C.⁵⁵ Residence time is a key factor for determining the reaction products of pyrolysis. As a general rule, for the production of liquid bio-oils short residence times (seconds) are required. Longer reaction times mainly lead to production of solid coke (slow pyrolysis) that can be used to generate energy by combustion.^{24, 56} Catalytic fast pyrolysis has recently been developed as a means for producing aromatic compounds, rather than bio-oil, from direct pyrolysis of lignocellulosic biomass, and yields of 20–30% aromatics have been reported when pyrolysis takes place in the presence of HZSM-5.²⁴

However crude bio-oils are a promising source for renewable energy, it has multiple shortcomings, such as low heating value (16–19 MJ kg⁻¹; less than half that of petroleum-derived fuels), strong corrosiveness (pH of 2–3), high viscosity (35–1000 cP at 40 °C), and poor chemical stability (viscosity and phase change with time). Despite these deficiencies, bio-oils can be transformed into transportation fuels, chemicals or even hydrogen by downstream upgrading. There are several routes available for bio-oils upgrading, including hydrotreating, zeolite upgrading, bio-oil mixtures, and steam reforming.^{56, 57}

1.1.5.1.4 Liquefaction

Liquefaction is a process that is carried out in a solvent (mostly water)^{58, 59} and liquid is obtained by thermo-chemical conversion at low temperature (300–400 °C) and high pressure (120–200 atm) using a catalyst^{60, 61} in presence of hydrogen. One of the biggest advantages of liquefaction is that wet biomass can directly be introduced to the process without any pre-drying.⁶² Moreover, the oxygen content of bio-oils produced through liquefaction is lower than that of produced by fast pyrolysis. This yields more favorable C/H ratio, water-insoluble bio-oils than those generated via fast pyrolysis. On the other hand, liquefaction requires higher capital investment than pyrolysis because of high pressure of reaction condition.⁶³

1.1.6.2 Biochemical conversion

1.1.6.2.1 Hydrolysis

Hydrolysis is alternative route to convert lignocellulosic biomass when selective production of chemical intermediates or targeted hydrocarbons for transportation fuels is required.²⁴ Isolation of sugar monomers is a prerequisite for such selective transformations which is a complex and costly step. But once sugar monomers are liberated, they can be used to produce second generation ethanol fuel through fermentation routes. Alternatively, it is possible to convert them into numerous platform chemicals and liquid fuels at relatively mild conditions by a wide range of catalytic technologies. The key advantage of this route, in comparison with BTL and pyrolysis-upgrading approaches, is derived from the mild reaction conditions used, allowing for better control of conversion selectivity. However, costly pretreatment and hydrolysis steps are required to hydrolyze solid lignocellulose to soluble sugar feeds, and the lignin fraction, once isolated, is typically combusted to provide heat and power.⁵⁷

1.1.6.2.2 Anaerobic digestion

Anaerobic digestion (AD) is a natural process where biomass is broken down by micro-organisms in the absence of air.⁶⁴ Various forms of biomass can be fed into an AD plant ranging from aquatic biomass to food waste, slurry and manure, to crops and crop residues. AD of lignocellulosic materials lately received more attention because of their abundant availability and the increased needs for bioenergy. Biodegradability of lignocellulosic biomass during AD is, however, impeded by the recalcitrant nature attributed to the lignin shield around carbohydrates (cellulose and hemicelluloses) and the highly crystalline cellulose.⁶⁵⁻⁶⁸ Some of the benefits of AD process include ability to process biomass with high water content, overall efficiency and the environmental friendly valorization of the produced biogas (consisting of ca. 65% CH₄, 35% CO₂ and trace gases such as H₂S, H₂ and N₂). Also, the application of nitrogen-rich digestates as fertilizer and/or organic amendments can be noted.⁶⁹ Moreover, it is not only economically viable in large scale, but also can be applied in small scale.⁷⁰

1.1.6.2.3 Fermentation

Fermentation of sugar and starch crops is a well-known process and has been used commercially on a large scale in many countries to produce ethanol. In this process, the

biomass is ground down and the starch converted by enzymes to sugars, with yeast then converting the sugars to ethanol. In contrast, the conversion of lignocellulosic biomass is more complex, due to the presence of longer-chain polysaccharide molecules and requires acid or enzymatic hydrolysis before the resulting sugars can be fermented to ethanol. Recently Solid State Fermentation (SSF) has gained significant attention for the development of industrial bioprocesses due to its low energy requirement along with high product yields.⁷¹

1.1.7 Green chemistry and the role of catalysis

Employment of clean processes in industrial production of fine and commodity chemicals is becoming increasingly essential. In addition to that, poor resource management could escalate the energy and raw materials demand and consequently increase the cost of produced chemical.^{72, 73} Thus the concept of “green chemistry” is becoming more important.

In 1998 Anastas and Warner developed the 12 principles of green chemistry.^{74, 75} These principles address specific criteria that must be developed in order to attain a clean, sustainable industry whilst continuing to meet with the chemical demands of a growing population.⁷⁴ In this respect, catalysis is playing a key role to make chemical industries sustainable.⁷⁶

In 1894 Ostwald defined a catalyst as a substance that accelerates the rate of chemical reaction without itself being consumed.^{77, 78} But increasing the rate of reaction is not the only influence of catalysts. A catalyst can also change the distribution of the products.⁷⁹ Traditionally catalysts are classified as homogeneous, heterogeneous and biocatalysts (enzymatic catalysts). In homogeneous catalysis the reactants, products and the catalyst are in the same phase (either liquid or gas) whilst in heterogeneous catalysis reactants and catalyst are in different phases. In most cases, heterogeneous catalysis refers to systems where reactants are in liquid or gas phase and the catalyst is solid.⁸⁰ The main advantage of heterogeneous catalysts is that because they are solid, they can be easily separated and recycled from the reactants and products that are in gas or liquid form.⁸¹ Moreover, heterogeneous catalysts are stable even in severe reaction environments (e.g. high temperature and pressure).⁸² Furthermore, unlike homogeneous catalysts (such as

sulphuric acid) that are corrosive and need to be stored in corrosion-proof facilities, heterogeneous catalysts are non-corrosive.

Typically a heterogeneous catalyst is a porous material that possesses high surface area (e.g., 10–1000 m² g⁻¹). The reaction takes place at the surface of catalysts. Therefore, it is desirable to maximise the accessibility of active sites to reactants by increasing the surface area.

In a heterogeneous catalytic reaction, reactants and products undergo 7 steps as below:

- 1- Diffusion of reactants from bulk of fluid to the catalyst.
- 2- Diffusion of reactants through the catalyst intraparticle pores.
- 3- Adsorption of reactants on the active sites.
- 4- Reaction between the reactions at the surface of catalyst.
- 5- Desorption of products from surface of the catalyst.
- 6- Diffusion of products through intraparticle pores.
- 7- Diffusion of products from catalyst to the bulk of fluid.

Any of these steps can limit the rate of catalytic reaction depending on the catalysts design, reaction setup and the reaction conditions.^{83, 84}

There are four factors that distinguish a successful catalyst from a poor performing catalyst. Firstly, a good catalyst should exhibit high selectivity for the desired products and low selectivity for potential by-products. A good catalyst also demonstrates adequate reaction rate under reaction conditions and moreover, the successful catalyst must be stable at those conditions which means catalytic activity should not decline quickly. Furthermore, the catalyst should have good accessibility of reactants and products to the active sites so that high rates can be achieved per reactor volume. This factor is greatly affected by porosity or pore shape of the catalyst.^{83, 85} An ideal catalyst functions catalytically under its inherent reaction conditions, but deactivation phenomena, where activity and selectivity decline with time, are common. This phenomenon is caused by different reasons including poisoning, fouling, degrading, sintering, active phase leaching, attrition, and crushing.⁸³ However a good catalyst can be easily regenerated, for example in case of coke deposition on catalyst in cracking of hydrocarbons, the catalyst can be regenerated by oxidation of the coke.⁸⁶

1.1.8 Production of fine chemicals and fuels from lignocellulosic biomass

Production of biomass-derived chemicals is not a new process nor is it an historic artefact. Currently the total amount of bio-based chemicals and polymers excluding biofuels, is estimated to be 50 million tonnes per annum.⁸⁷ Among the bio-chemicals, there is one class of intermediate products which has attracted great attention. They are known as the furan compounds and they are potentially suitable for production of chemicals and fuels.

In 2004, the US DoE identified a range of sugar-derived platform chemicals obtainable via chemical or biochemical transformation of lignocellulosic biomass⁸⁸, subsequently revisited by Bozell and Petersen in 2010⁸⁹, where furan molecules such as 5-hydroxymethyl-furfural (HMF), furfural, and 2,5-furandicarboxylic acid are mentioned in the “Top 10 +4” as additions to the original DOE list. Furan compounds such as furfural (2-furaldehyde) and HMF (5-hydroxymethylfurfural) can be obtained by dehydration of C₅ and C₆ sugars in presence of a mineral acid such as HCl or H₂SO₄ at mild temperatures (e.g. 150 °C). The production of these intermediate furan compounds is of great interest as they have applications in production of industrials solvents, bio-polymers, fuel additives and bio-fuels.

Production of furfural from C₅ sugars, such as xylose, is a well-developed industrial process.⁹⁰ In contrast, HMF production from C₆ sugars is faced with many challenges such as utilization of glucose as a sugar feedstock, and therefore yet to be commercialized. Thus, production of HMF from glucose suffers from low yield and with current technologies an additional isomerization step to fructose is necessary for better selectivity towards HMF and higher rates.^{91, 92} Another challenge that must be overcome is control over the undesired side reactions involving the reactants, intermediates and the final HMF product. It is particularly important to prevent HMF degradation in the aqueous phase, as employing a biphasic system where HMF is continuously extracted into an organic solvent has shown promise.⁹³ Furans, such as HMF and furfural, can be used as precursors to liquid hydrocarbon fuels for the production of linear alkanes in the molecular weight range appropriate for diesel or jet fuel^{94, 95} as shown in **Figure 1.5**. The first step of this process is the acid-catalysed

depolymerisation of polysaccharides (e.g., starch, cellulose or hemicellulose) to produce C_5 and C_6 sugar monomers. Subsequently, the sugars are dehydrated (in presence of acid catalyst) to form furfural and HMF. Furthermore, furfural and HMF can go through aldol condensation reactions in polar solvents like water and in presence of base catalysts such as NaOH and Mg/Al oxides.^{96, 97} The products of aldol condensation reactions are large molecules with unsaturated $C=C$ and $C=O$ bonds (i.e aldol-adduct) which precipitate in aqueous solutions. By allowing adducts to undergo another aldol condensation reaction with the initial furan compound, it is possible to increase the molecular weight of the final alkane product. Moreover, the unsaturated $C=C$ and $C=O$ bonds in the aldol adducts can be hydrogenated over metal catalysts such as Pd in order to obtain greatly water-soluble polyol compounds. This process can be simplified by using a bifunctional (metal/basic) water-stable catalyst such as Pd/MgO-ZrO₂, so that both reactions can take place in one single step.⁹⁸ As a final step, the oxygen atoms must be removed completely to produce liquid alkanes through aqueous-phase dehydration/hydrogenation (APD/H) reactions.⁹⁹ The oxygen removal process takes place in the presence of a bifunctional metal-acid catalyst where oxygen is removed by cycles of dehydration and hydrogenation reactions.^{94, 100}

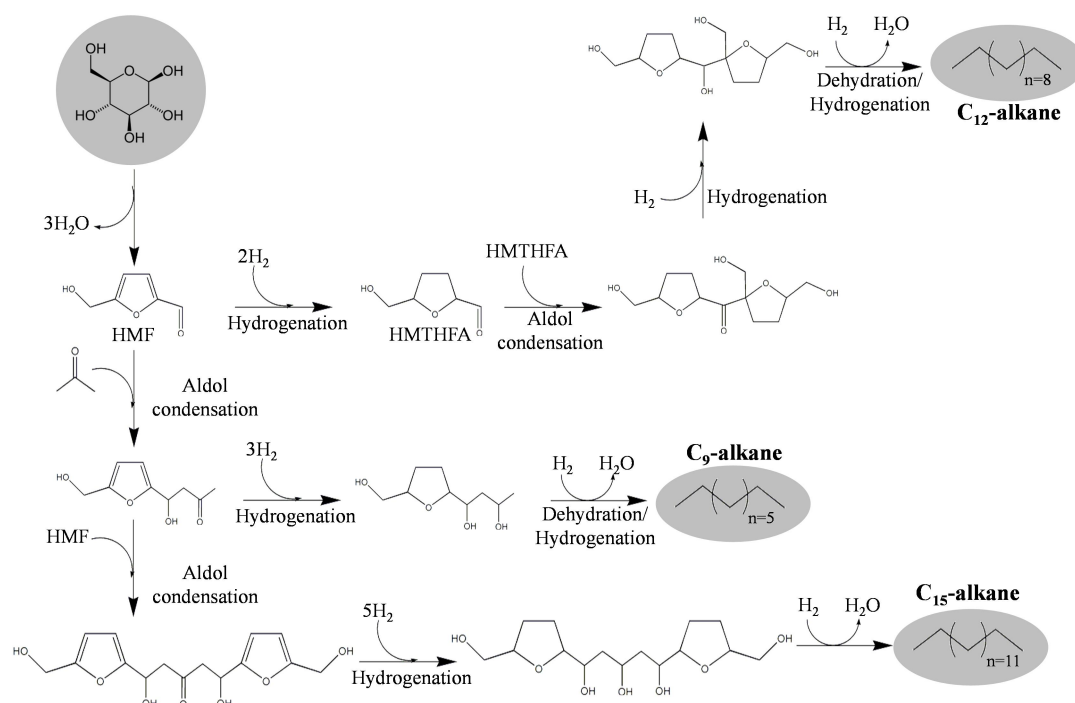
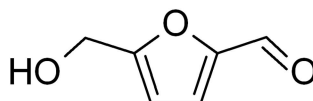


Figure 1.5: Reaction pathways for the conversion of biomass-derived glucose into liquid alkanes via HMF. Adapted from ref. 94

1.1.8.1 HMF

In this project the focus is the production of HMF, particularly from the dehydration of hexoses. HMF stands out among the platform chemicals for a number of reasons; it has the same number of carbon atoms to those of hexose feedstocks. Moreover, the selectivity towards HMF is reportedly higher than other platform chemicals such as levulinic acid or bioethanol, especially when fructose is used as the starting material.



Scheme 1.2: 5-Hydroxymethylfurfural (HMF)

Düll ¹⁰¹ and Kiermayer ¹⁰² were the pioneer researchers who reported the synthesis of HMF for the first time in 1895. Since then, the interests in furanic derivatives which are important compounds in food and chemical industries have progressively grown. Especially the past few years have seen an enormous increase in the number of publications on HMF chemistry, as described in **Figure 1.6**. **Table 1.2** provides an overview of the physical and chemical properties of HMF.

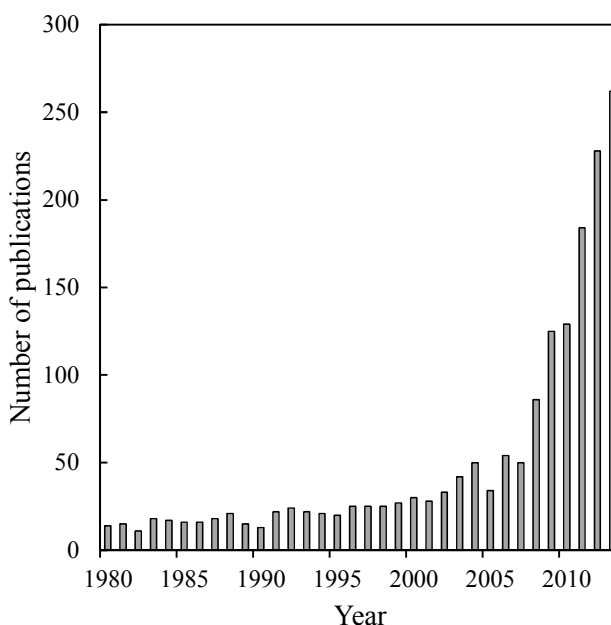


Figure 1.6: Number of publications on HMF per year, as registered by Web of Science

Table 1.2: Chemical and physical properties of HMF

CAS registry number	67-47-0
IUPAC name	5-(hydroxymethyl)-2-furaldehyde
Synonyms	5-HMF, HMF, 5-(hydroxymethyl)-2-furancarbal, 5-(hydroxymethyl)-2-furfural, 5-hydroxymethyl-2-formylfuran, 5-oxymethylfurfurole, hydroxymethyl furfuraldehyde
Molecular formula	C ₆ H ₆ O ₃
Molecular weight	126.11
Description	Faint yellow to yellow-tan powder or liquid; ¹⁰³ odour of chamomile flowers ¹⁰⁴
Boiling point	110 °C at 0.02 mmHg, ¹⁰⁴ 114–116 °C at 1 hPa ¹⁰³
Melting point	31.5 °C, ¹⁰⁴ 28–34 °C ¹⁰³
Solubility	freely soluble in water, methanol, ethanol, acetone, ethyl acetate, dimethylformamide; soluble in ether, benzene, chloroform; less soluble in carbon tetrachloride; sparingly soluble in petroleum ether ¹⁰⁴
Density	1.243 at 25 °C ¹⁰³
Refractive index	1.5627 at 18 °C ¹⁰⁴
Flash point	79 °C, closed cup ¹⁰³
UV absorption maximum	283 nm

1.1.9 Glucose transformation to HMF

1.1.9.1 Mechanism of glucose to HMF conversion

Several mechanisms for direct formation of HMF from by dehydration of hexoses in acid catalysed reactions have been proposed in the literature.

In 1944, Haworth and Jones published the first mechanism for fructose dehydration to HMF.¹⁰⁵ Later Dam *et al.*¹⁰⁶, Kuster¹⁰⁷, and Antal *et al.*¹⁰⁸ assumed that the dehydration of hexoses either goes through the transformation of ring structure (known as cyclic pathway), or through the acyclic intermediates. (**Figure 1.7**)

In general, the mechanism of hexoses dehydration to HMF is composed of isomerization, dehydration, fragmentation, reversion and condensation steps. A group of researchers suggest that hexoses go through open-chain 1, 2-enediol mechanism or through fructofuranosyl intermediate.¹⁰⁹⁻¹¹²

On the other hand, Antal *et al.* and Newth suggest that d-fructose is transformed to HMF via cyclic intermediates.^{113, 114} The evidences for this proposal was facile conversion of 2,5-anhydro-D-mannose (an intermediate enol in cyclic mechanism) to HMF as well as facile formation of HMF from d-fructose but difficult from glucose which can be concluded from the dehydration of sucrose. The other evidence is lack of carbon-deuterium bond formation in HMF due to ketoenol tautomerism in the open-chain mechanism when the reaction was carried out in D₂O solvent.¹¹⁵ Furthermore, Amarasekara *et al.*¹¹⁵ identified two key intermediates as (4R, 5R)-4-hydroxy-5-hydroxymethyl-4,5-dihydrofuran-2-carbaldehyde in the reaction based on the data of ¹H and ¹³C NMR spectra.

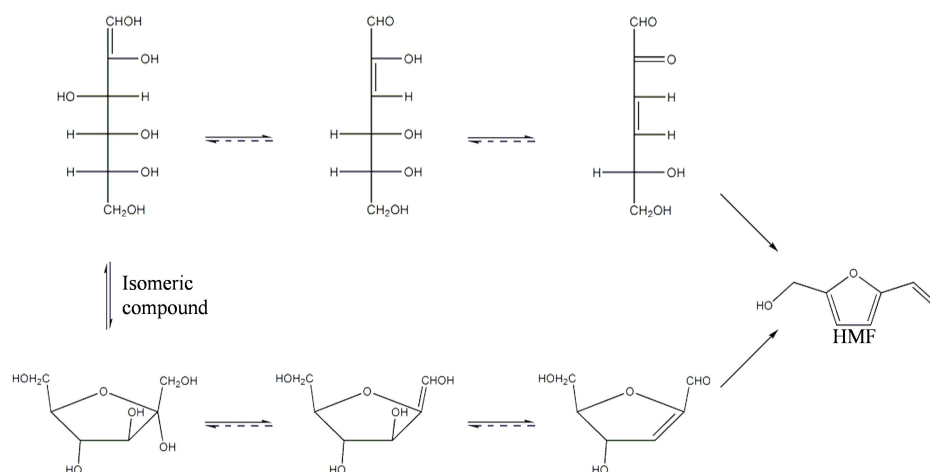


Figure 1.7: Acyclic (top) and cyclic (bottom) mechanism for the dehydration of hexoses.

Glucose is the other hexose which has been reported as substrate for formation of HMF and it has been studied to a vast extent due to greater interest on it because of its cheaper price and abundance in the nature in the form of lignocellulosic biomass.

Typically, HMF yield from fructose is much greater than reactions starting from glucose. Kuster explains that glucose shows much lower selectivity for HMF formation because of its more stable ring structure, which hinders its ability to form the acyclic enediol intermediate.¹⁰⁷ The cyclic mechanism requires glucose to isomerize to fructose prior to dehydration to HMF.

Reaction temperature and the solvent can also affect the reaction pathway by changing distribution of the tautomers of different sugars. Glucose only exists in the form of

pyranose (6-ring) at room temperature in water, while two pyranose forms are prevalent when fructose is dissolved in water at room temperature. However, furanose forms are also present in considerable amounts.¹¹⁶ In connection with solvent effects on tautomers distribution, there has been many more research carried out on solvents other than water. However, NMR studies show that under reaction conditions the tautomerisation of fructose is very rapid.^{117, 118} When tautomerisation proceeds at a significantly higher rate than dehydration this is not expected to be an important factor in improving the selectivity of HMF formation. Moreover, several studies on glucose decomposition in high temperature liquid water (in the absence of catalyst) report the formation of fructose.¹¹⁹⁻¹²¹

In conclusion, conversion of fructose to HMF is much more facile compared to glucose to HMF transformation. This is confirmed by experimental works which show an efficient isomerization catalyst is essential for reaching high HMF yields from glucose. This information favours the cyclic dehydration mechanism rather than acyclic dehydration mechanism from an intermediate enediol, as the latter does not explain the significant difference in reactivity and selectivity between glucose and fructose to HMF, since enediol would be a common intermediate.

1.1.9.2 Glucose dehydration in single-phase systems

In this section, the glucose dehydration in traditional single phase systems will be reviewed, along with more recent progress in this area using sub- and supercritical conditions. Publications on HMF synthesis in aqueous systems will be discussed first, followed by a review of the research on reactions in organic solvents and aqueous/organic single-phase mixtures.

1.1.9.2.1 Glucose dehydration in aqueous solutions

Early research on glucose transformation to HMF focussed on single phase systems using either water or an organic liquid as solvent. However, glucose dehydration in pure water is non-selective and HMF yields are typically very low. For example, glucose dehydration in hot water at high temperatures (above 200 °C) results in the formation of HMF as well as formic acid and acetic acid side-products. These acids act as catalysts for further transformation of glucose to HMF. Based around this, Lopes de Souza *et al.*

reported HMF production in an autocatalytic system using a 1 wt% glucose solution at a temperature range of 150-250 °C. A maximum HMF yield of 25% was achieved, where 69% of glucose was converted at 220 °C.¹²² In another study, Chareonlimkun reported a 10% HMF yield following conversion of a 9 wt% glucose solution at 250 °C, after only 5 minutes.¹²³ Non-catalytic degradation of glucose was also reported by Jing and Lu in an aqueous system at 180-220 °C and 100 bar, with a 30% HMF yield obtained when 70% of glucose (1 wt% solution) was converted after 30 min heating at 220 °C.¹²⁴ Aida and co-workers studied the effect of increased pressure on glucose dehydration in water at 350-400 °C at pressures of 40, 70 and 80 MPa, using short reaction times ($t < 2s$). These resulted in less than 10% HMF yield, however furfural yields as high as 12% were obtained.¹²⁵ Overall it can be summarised that non-catalytic/autocatalytic conversion of glucose is inefficient for HMF production. The formation of by-products such as formic acid and levulinic acid, which take place through decomposition of HMF, as well as the utilisation of high pressures, prevent the process from industrial implementation.¹²⁶

Table 1.2: Glucose dehydration to HMF in aqueous systems in the absence of catalyst

Glucose conc. wt%	Temperature °C	Reaction time	Conversion %	Yield %	Selectivity %	Ref
1	180	120 min	47	17	37	127
9	200	10 min	31	7	23	128
2	200 ^a	3 min	15	3	23	129
9	200	5 min	21	3	15	130
1	220	2 h	69	25	36	122
1	220	30 min	71	32	45	124
9	250	5 min	21	10 ^c	51	123
0.9	350 ^d	0.7 s ^b	72	2 ^{c,f}	3	125
0.9	350 ^e	0.8 s ^b	83	4 ^{c,g}	5	125
0.9	350 ^e	1.6 s ^b	84	7 ^{c,g}	8	125

^a Heating by microwave irradiation, ^b Continuous flow process, ^c Furfural formation was observed, ^d At 400 bar, ^e At 800 bar, ^f 14% fructose yield, ^g 7–8.5% fructose yield

a) Homogeneously catalysed processes

In 1962, Mednick examined various acids, ammonium salts and combinations of liquid acids and a base (pyridine) for conversion of 20 wt% aqueous solution of glucose at 160–190 °C or a 1 : 1 water–dioxane mixture of glucose at 200–250 °C.¹³¹ In pure

water, HMF yields varied between 3 and 23%. The highest yield of HMF was obtained when a combination of phosphoric acid and diammonium phosphate was used at an initial pH of approximately 4. In another study, Smith and co-workers patented ammonium sulfate-catalysed aldose dehydration using a 10% glucose mixture at pH 1.65 and 150–155 °C, which yielded an HMF yield of 31.5% after 50 min.¹³² HMF production from glucose dehydration in a 10 wt% sulphuric acid solution was reported by Li *et al.* under microwave heating, at 400 W for 1 min, where 49% HMF was yielded.¹³³

The use of metal halide salts was investigated by Seri *et al.* who employed lanthanide(III) chlorides for the dehydration of glucose in water at 140 °C. After 1 h reaction, the yield of HMF was between 3 and 8%, with a small amount of levulinic acid generated, along with a significant amount of insoluble humins.^{134 135} ZnCl₂ and ZnBr₂ have also been explored as catalysts for glucose conversion at 120 °C, however a high loading of 63 wt% ZnCl₂ aqueous solution was required to achieve total conversion of glucose, with only a 16% HMF yield obtained after 35 min. Similarly a 76 wt% ZnBr₂ solution converted 82% glucose and resulting in 29% HMF yield.¹³⁶ A variety of metal salts were also tested by Tyrlik and co-workers for glucose dehydration in aqueous systems under reflux who reported the highest HMF yield of 9% was achieved with 15 wt% glucose in a 5 M MgCl₂ system.¹³⁷⁻¹³⁹

b) Heterogeneously catalysed processes

The use of solid acids has been explored by Lourvanij using Y-zeolite as catalyst for glucose decomposition in water. In this work, while a 33% fructose yield was found after 2 min at 160 °C,¹⁴⁰ HMF was only formed at relatively low yields (<10%). This may be a reflection of the poor hydrothermal stability of zeolites under such conditions.

Metal oxides such as TiO₂ and ZrO₂ exhibit greater hydrothermal stability and are more suitable for such applications; hence Watanabe *et al.* explored the use of TiO₂ in glucose dehydration in aqueous solution at 200 °C. A HMF yield of 20% at 81% conversion was obtained after 5 min in presence of anatase, TiO₂. It was discovered that rutile TiO₂ is catalytically inactive for this reaction, as it presented identical results to a non-catalysed reaction (6.6% HMF yield at 20% conversion after 10 min). In the same report and under similar conditions, ZrO₂ was tested yielding 13% fructose and only

5.2% HMF at 47% glucose conversion. The same group later reported microwave heating could produce a 64% conversion and 19% HMF yield after 5 min, for the dehydration of a 2 wt% aqueous solution glucose by anatase TiO_2 . Using ZrO_2 as catalyst likewise resulted in increased yields with 10 % HMF formed under the same reaction conditions.¹²⁸⁻¹³⁰

Dutta and co-workers showed that the use of mesoporous TiO_2 nanoparticles could further enhance HMF yields under microwave heating of a 5wt% glucose solution at 120 °C with a 26% HMF yield observed.¹⁴¹ The performance of high surface area titanate nanotubes for glucose dehydration in water was investigated by Hara and co-workers. In this study, protonated titanate nanotubes with high surface area ($\sim 400 \text{ m}^2 \text{ g}^{-1}$) were used in a system of 1 wt% glucose in aqueous media with an equal weight of catalyst, and a reaction temperature of 120 °C with reaction time of 3 h. An HMF yield of 14% was achieved with titanate nanotubes, whereas only 2% was observed with conventional TiO_2 .¹⁴²

Chareonlimkun and co-workers compared performance of TiO_2 and ZrO_2 catalysts in glucose dehydration,¹²³ and studied the effect of catalyst calcination temperature (500 – 700 °C) as well as metal precursor such as nitrates and chlorides. TiO_2 formed from its chloride precursor that had subsequently been calcined at 500 °C was found to exhibit the highest HMF yield (27%) following reaction in hot compressed water at 250 °C. Calcination of the catalyst at 600 and 700 °C resulted in decreased HMF yield of 25 and 20% respectively, with the trend attributed to a transition from the anatase phase at 500°C, to the rutile phase at higher temperature. This is in agreement with Watanabe's findings, with regard to anatase and rutile phase TiO_2 catalysts, in which rutile TiO_2 was not very active. Regardless of calcination temperature, HMF yields obtained with titania from its nitrate precursor were around 5% lower than those from titania prepared from its chloride precursor, which may be due to higher acid site density of TiO_2 from TiCl_4 than TiO_2 from $\text{TiO}(\text{NO}_3)_2$ as a result of higher acid site content. Similar studies of ZrO_2 showed the same trends with regard to precursor and calcination temperature as for TiO_2 , with the highest HMF yield, around 17% reported when 500 °C calcined ZrO_2 was used as catalyst. TPD results showed a lower acid site density for ZrO_2 than for TiO_2 . A TiO_2 – ZrO_2 mixed oxide catalyst was found to give a superior HMF yield of 30% under similar conditions, suggesting there is a synergy between the two

components potentially attributed to higher surface area and increased acid and base site density.¹⁴³

Other mixed oxides were explored by Zeng *et al.* who studied aluminium and zirconium mixed oxides for glucose dehydration in aqueous solution (4g glucose in 400 ml water).¹²⁷ Here, the variation in Al/Zr ratio significantly affected the acid-base properties demonstrating decay of acid and base sites quantity as well as their strength by going from pure Al₂O₃ to pure ZrO₂ sample. The highest glucose conversion (97%) was achieved over the sample which contained equal moles of Al and Zr, while the maximum yield of HMF (17%) obtained in absence of catalyst where 47% of glucose was converted.

Another report from the same group shows niobic acid, Nb₂O₅·nH₂O, as a heterogeneous water-tolerant Lewis acid.¹⁴⁴ A HMF yield of 12% was obtained using this catalyst with reaction temperature of 120 °C and reaction time of 3 h. When Nb₂O₅·nH₂O was used together with H₃PO₄, an improved HMF yield of 52% was found. Asghari and Yoshida explored glucose dehydration catalysed by a heterogeneous crystalline zirconium phosphate catalyst.¹⁴⁵ They used 1 wt% glucose in water solution and a 1:1 (w/w) catalyst/substrate ratio at 240 °C and 33.5 bar. The result was 23.5% HMF yield (72% conversion) at a residence time of 240 s.

Table 1.3 and **Table 1.4** show an overview of results published on glucose dehydration to HMF under aqueous conditions. HMF yields in processes catalyzed by heterogeneous metal oxides are generally somewhat higher than those obtained in homogeneous systems. A bifunctional type of catalyst with basic sites for isomerization and acid sites for dehydration showed the most promise. Results from Chareonlimkun and Watanabe indicated that ZrO₂ functioned mainly as an isomerization catalyst to form fructose, whereas anatase TiO₂ functioned as an acidic catalyst for dehydration to HMF. A ZrO₂–TiO₂ mixed oxide catalyst appeared to combine these functions to achieve a relatively high HMF yield of 30% under aqueous conditions.

Table 1.3: Glucose dehydration to HMF in aqueous systems catalysed by homogeneous catalysts

Glucose concentration wt%	Catalyst	Catalyst loading	Temperature °C	Reaction time	Conversion %	Yield %	Selectivity %	Ref
10	HCl	pH 1	170	45 min	20	2.2	11	91
20	(NH ₄) ₂ HPO ₄	0.07 M	172-182 ^b	20 min		11		131
20	(NH ₄) ₂ HPO ₄ /H ₃ PO ₄	0.07M/0.05M	174-180 ^b	20 min		23		131
20	H ₃ PO ₄	0.15M	173-187	20 min		5		131
5	AlCl ₃	50 mol %	120 ^a	20 min		40		146
8	DyCl ₃	0.7 mol %	140	1h	17	7	41	134
8	DyCl ₃	0.7 mol %	140	2h	30	12	40	134
2	H ₂ SO ₄	50 wt %	200 ^a	3 min	11	2	23	129
9	H ₂ SO ₄	1 mM	200	5 min	32	2 ^d	8	128
2	NaOH	50 wt%	200 ^a	3 min	47	5	11	129
10	H ₂ SO ₄ ·(NH ₄) ₂ SO ₄	pH 1.65	150-155	50 min		32		132
13	MgCl ₂	593 mol %	Reflux	3 h		9 ^c		138
1	H ₃ PO ₄ /Nb ₂ O ₅	1000 wt%	120	3 h	92	52	57	144
2	ZnCl ₂	3150 wt%	120	35 min	100	16	16	136
2	ZnBr ₂	3800 wt%	120		82	29	35	136

^a Heating by microwave irradiation, ^b Warm up time of 0.5 h or more, ^c 26% yield of humins reported, ^d 3% fructose yield reported,

Table 1.4: Glucose dehydration to HMF in aqueous systems catalysed by heterogeneous catalysts

Glucose concentration	Catalyst	Catalyst loading	Temperature	Reaction time	Conversion	Yield	Selectivity	Ref
wt%		wt%	°C	min	%	%	%	
12	HY-zeolite	50	160	3	83	8	10	140
5	meso-TiO ₂	100	120	5		25		141
1	Titanate nanotubes	100	120	180		14		142
9	TiO ₂	100	250	5	39	27 ^c	71	123
9	TiO ₂ (A)	100	200	5	81	20 ^c	25	128
2	TiO ₂ (A)	50	200 ^a	5	64	19	29	129
9	TiO ₂ - ZrO ₂	100	250	5	44	29 ^c	67	143
9	ZrO ₂	100	250	5	38	17 ^c	46	123
9	ZrO ₂	100	200	5	48	5 ^b	11	128
2	ZrO ₂	50	200 ^a	3	57	10	18	129
1	ZrO ₂	75	180	120	89	13	14	127
1	Al ₂ O ₃ /ZrO ₂	75	180	120	97	12	12	127
1	Al ₂ O ₃	75	180	120	94	12	13	127
1	Nb ₂ O ₅	10	120	180	100	12	12	144
1	Nb ₂ O ₅ (pretreated with H ₃ PO ₄)	10	120	180	92	48	52	144
1	ZrP	100	240	4	72	24	33	145

^a Heating by microwave irradiation, ^b 13% fructose yield reported, ^c 2-2.5% fructose yield reported

1.1.8.2.2 Glucose dehydration in organic solvents

The experiments of Mednick¹³¹ on glucose dehydration suggest that lowering the amount of water in the reaction media, improves the yield of HMF, whilst suppressing some undesirable parallel reactions and the rehydration of HMF.^{93, 147} For this reason, glucose dehydration in organic solvents drew the attention of many research groups since then. Yan *et al.* looked at the dehydration of glucose in DMSO in absence of catalyst and in presence of low surface area (7 to 66 m² g⁻¹) SO₄²⁻/ZrO₂ and SO₄²⁻/ZrO₂/Al₂O₃ catalysts.¹⁴⁸ In a typical reaction they used 7.6 wt % glucose in DMSO solution and heated to 130 °C. In the absence of catalyst, 94% of glucose converted but only 4.3% HMF yield was obtained after 4 h. Using 20 wt% SO₄²⁻/ZrO₂ catalyst (relative to glucose) resulted in a considerable improvement in HMF production, as the yield increased to 19.2% and 95.2% glucose conversion. Among the SO₄²⁻/ZrO₂/Al₂O₃ catalysts, the highest HMF yield of 48% was obtained after 4 h, when 20 wt% catalyst having an Al–Zr molar ratio of 1:1 was used. Interestingly, extending the reaction time to 6 h and 15 h did not influence HMF yield, showing the stability of HMF under these reaction conditions.

The performance of LaCl₃ in glucose dehydration in DMSO at 120 °C was found to produce a HMF yield of 9.8%,¹⁴⁹ while the use of 10 mol% SnCl₄ as catalyst and 9 wt% glucose as substrate at 100 °C yields 44% HMF at 96% conversion.¹⁵⁰ Similar studies on rare earth metals in DMA as the solvent, report much higher HMF yields of up to 30% from glucose.¹⁵¹

Ebitani's group investigated the potential for a combined isomerization and dehydration catalytic system for glucose conversion in DMF.¹⁵² For this purpose they used 3 wt% glucose in DMF solution and carried out the reaction at 80 °C. Adding 200 wt% (relative to glucose) hydrotalcite as catalyst for isomerization of glucose to fructose led to a 40% yield of fructose at 47% glucose conversion after 3 h. When a physical mixture of hydrotalcite and Amberlyst 15 was used HMF formation was observed, with the highest HMF yield of 42% at 73% glucose conversion obtained. No HMF formation was reported when either catalyst was tested separately under similar conditions. A number of other solvents such as DMA, DMSO, acetonitrile, and water were also tested with the same Hydrotalcite/Amberlyst system at 100 °C. With DMSO at 80 °C an HMF yield of 25% at 41% conversion was obtained.¹⁵² The results of the other solvents are

described in **Table 1.5**. The highest yields of HMF were obtained when DMF was used as the reaction media while in water only glucose isomerization took place and giving 23% fructose yield and no HMF. This was explained by the loss of activity of Amberlyst-15 in water. Addition of a small amount of water (3 vol%) to DMF however resulted in almost 30% decrease in glucose conversion but it was beneficial to HMF selectivity. Later the same group reported comparable work¹⁵³ in which Amberlyst-15 catalyzed dehydration of glucose in DMF resulting only in 1,6-anhydroglucose formation, with yields of up to 70% were obtained. Higher temperatures favoured the formation of 1,6-anhydroglucose relative to the formation of HMF.^{152, 154}

Binder and Raines reported high HMF yields from glucose dehydration in homogeneous DMA/LiBr/CrX_n systems (X = Br or Cl).^{155, 156} Using 10 % LiBr in DMA and 6 % CrX_n at 100 °C an HMF yield of 80% at 100% glucose conversion was obtained within 4–6 h. Using either CrCl₂, CrCl₃, or CrBr₃ did not massively change the yield and conversion. These HMF yields are by far the highest reported from glucose in systems without ionic liquids.

In another report, Chen and Lin applied a mixture of LiCl in caprolactam as solvent in combination with a number of catalysts that are known to facilitate the isomerization/dehydration of glucose to HMF.¹⁵⁷ Using 10 wt% glucose in 3:1 (mole:mole) caprolactam/LiCl solution, HMF yield of around 60% at >90% conversion were obtained in presence of CrCl₂, SnCl₄ and SnCl₂ with 6 mol % catalyst at 100°C for 3 h. Yasuda *et al.* used acetonitrile as solvent and a composite of MgCl₂ with silica gel as acid catalyst for HMF production from glucose, obtaining a 70% HMF yield at 140 °C under dry conditions. 10% and 32% yields of HMF were obtained from mannose and galactose, respectively.¹⁵⁸

In a mixture of water and ethanol Yang *et al.* obtained a combined yield of HMF and EMF of 57% with AlCl₃ as the catalyst.¹⁵⁹ Tyrlik *et al.* also carried out glucose dehydration in water/ethanol mixture in addition to what they had done in pure water,^{138, 139} The highest combined yield of HMF and HMF alkyl ether of 22% was obtained in a system in which saturated Al₂(SO₄)₃ in water was combined with ethanol (>30 M).

Dumesic explored HMF production using heterogeneous catalysts in biomass derived solvents such as γ -octalactones (GOL), γ -hexalactone (GHL), tetrahydrofuran (THF), methyltetrahydrofuran (MTHF) and γ -valerolactone (GVL).¹⁶⁰ A combination of Sn- β as Lewis acid catalyst for isomerization step and Amberlyst 70 as Brønsted acid catalyst for dehydration step were used to convert the glucose in 2 wt% solution at 130 °C. In GVL, 40% HMF yield was obtained at 92% conversion after 20 min when 1.5g of glucose solution and 0.05g of each catalyst was used. At the same reaction condition, using GHL as solvent resulted in 55% HMF yield at 93% conversion. Using THF as solvent yielded 63% HMF at 90% conversion in 30 min. They also tested a monophasic system made of 10 wt% and 90wt% mixture of MTHF : THF (1:1 weight ratio). At this condition, 90% HMF yield was obtained at 91% conversion after 40 min. The authors claim that water in low concentrations can be beneficial to HMF selectivity which is in agreement with Ebitani's findings.^{152, 160}

Table 1.5 and **Table 1.6** give an overview of the highest reported HMF yields from glucose in organic solvents. When comparing these results with those in water, it is clear that the yields are generally significantly higher in organic solvents. Especially when dehydration catalysts are combined with isomerization catalysts in aprotic polar solvents good yields of almost 50% are reported. Use of chromium halides as isomerization catalyst in HCl/DMA even resulted in yields of around 80% HMF.

Table 1.5: Glucose dehydration to HMF in organic systems catalysed by homogeneous catalysts

Glucose concentration	Solvent	Catalyst	Catalyst loading	Temperature	Reaction time	Conversion	Yield	Selectivity	Ref
wt%			mol%	°C	h	%	%	%	
5	DMSO	AlCl ₃	50	140	0.08		52		146
9	DMSO	CrCl ₃	7	100	3	79	28	35	161
5	DMSO	GeCl ₄	10	100	1.25	85	37	43	162
9	DMSO	H ₃ BO ₃	80	120	3	35	13	37	163
3.6	DMSO	LaCl ₃	5	120	2		10		149
9	DMSO	SnCl ₄	10	100	3	96	44	45	150
9	DMF	H ₃ BO ₃	80	120	3	64	7	11	163
5	DMF	GeCl ₄	10	100	1.25	85	34	40	162
10	DMA	LnCl ₃	10	145	2	100	34	34	151
10	DMA (10 wt % LiBr)	CrBr ₃	6	100	6		80		155
10	DMA (10 wt % LiBr)	CrCl ₂	6	100	4		76		155
10	DMA (10 wt % LiBr)	CrCl ₃	6	100	6		79		155
10	caprolactam/LiCl 3:1 (mole/mole)	CrCl ₂	6	100	3	94	59	62	157
10	caprolactam/LiCl 3:1 (mole/mole)	SnCl ₂	6	100	3	94	55	59	157
10	caprolactam/LiCl 3:1 (mole/mole)	SnCl ₄	6	100	3	98	65	66	157
6	water/ethanol	Al ₂ (SO ₄) ₃	100	reflux	144		22 ^a		139
0.05	water/ethanol	AlCl ₃	40	160	0.25		24 ^b		159

^a Combined yield of HMF and EMF, ^b 33% EMF yield was observed

Table 1.6: Glucose dehydration to HMF in organic systems catalysed by heterogeneous catalysts

Glucose concentration wt%	Solvent	Catalyst	Catalyst loading wt%	Temperature °C	Reaction time h	Conversion %	Yield %	Selectivity %	Ref
3	DMA	Hydrotalcite/Amberlyst 15 (2:1 w/w)	300	100	3	97	14	14	152
3	DMF	Hydrotalcite/Amberlyst 15 (2:1 w/w)	300	80	9	73	42	58	152
3	DMF	Hydrotalcite/Amberlyst 15 (2:1 w/w)	300	100	3	72	41 ^a	57	152
3	DMF	Hydrotalcite/Amberlyst 15 (2:1 w/w)	300	100	4.5 ^b	61	45	73	152
3	DMF + 3 vol% water	Hydrotalcite/Amberlyst 15 (2:1 w/w)	300	100	3	45	29	64	152
3	DMSO	Hydrotalcite/Amberlyst 15 (2:1 w/w)	300	80	3	41	25	61	152
3	DMSO	Hydrotalcite/Amberlyst 15 (2:1 w/w)	300	100	3	94	12 ^c	13	152
7.6	DMSO	SO ₄ ²⁻ /ZrO ₂ /Al ₂ O ₃ (Zr/Al = 1:1 n/n)	20	130	4	97	48	49	148
7.6	DMSO	SO ₄ ²⁻ /ZrO ₂ /Al ₂ O ₃ (Zr/Al = 1:1 n/n)	20	130	6	100	48	48	148
7.6	DMSO	SO ₄ ²⁻ /ZrO ₂ /Al ₂ O ₃ (Zr/Al = 1:1 n/n)	20	130	15	100	48	48	148
3.5	DMSO/water (4:1 v/v)	SO ₄ ²⁻ /ZrO ₂ /Al ₂ O ₃ (Zr/Al = 3:7 n/n)	19	150	4		56		164
3	MeCN	Hydrotalcite/Amberlyst 15 (2:1 w/w)	300	100	3	88	10 ^d	12	152
3	MeCN + 3 vol% water	Hydrotalcite/Amberlyst 15 (2:1 w/w)	300	100	3	91	28	31	152
2	GVL	Sn-β/Amberlyst 70 (1:1 w/w)	333	130	0.33	92	59	64	160
2	GHL	Sn-β/Amberlyst 70 (1:1 w/w)	333	130	0.33	93	55	59	160
2	THF	Sn-β/Amberlyst 70 (1:1 w/w)	333	130	0.5	90	63	70	160
2	MTHF : THF (1:1 w/w)	Sn-β/Amberlyst 70 (1:1 w/w)	333	130	0.67	91	60	66	160

^a 4% fructose yield and 10% AHG yield, ^b Amberlyst 15 was added 2.5 h after the started, ^c 6% fructose yield, ^d 12% AHG yield.

1.1.9.3 Glucose dehydration in biphasic systems

Rehydration of HMF to levulinic acid is one of the known factors that can have a negative effect on HMF yield. Moreover, reaction of HMF with sugars and other intermediate compounds to form so-called humins is another possibility for decreased HMF yield. A solution to this problem is *in situ* extraction of HMF from the aqueous reaction media by an organic solvent. Therefore HMF is produced in an aqueous phase, but will spontaneously be transferred to an organic phase (i.e. HMF is extracted). By doing this, the undesired side reactions can be suppressed to a large extent and thus HMF yield and selectivity will be enhanced.^{165, 166}

Peniston is known to be the inventor of such extraction system for HMF synthesis from carbohydrates who patented his idea in 1956.¹⁶⁷ A biphasic system for HMF production from glucose was first patented by Cope in 1957, in which a 50 wt% aqueous glucose solution was reacted at 160 °C for 9 h in presence of 20 volumetric equivalents of MIBK to produce a 21-25% isolated yield of HMF.¹⁶⁸ Rigal and Gaset further explored catalytic aldose dehydration in water/MIBK system using an acidic ion exchange resin to obtain HMF yield ~10% at 78 °C.¹⁶⁹ Without using any catalyst Dumesic's group claimed to produce a 30% HMF yield at 62% conversion from 10 wt% glucose in water/DMSO (3:7 w/w) in presence of dichloromethane at 140 °C after 4.5 h. They also reported a 24% HMF yield at 50% glucose conversion in water/DMSO (1:1 w/w) using HCl as catalyst (pH 1) in presence of 2 weight eq MIBK/2-butanol (7:3 w/w) at 170 °C after 17 min.⁹¹ Dumesic *et al.* also applied a number of solvents derived from lignin as extracting phase. The highest HMF yield (~61%) was obtained with 2-sec-butylphenol (SBP) from 5 wt% glucose at 170 °C.¹⁷⁰

In a more recent work, combinations of AlCl₃ and HCl have been used as a bifunctional catalyst system to obtain 62% HMF yield.¹⁷¹ Yang *et al.* achieved almost the same results in a biphasic water-NaCl/THF system with AlCl₃ as catalyst.¹⁷² The claim to have a Lewis acid in this work is quite confusing however as AlCl₃ will react violently with water to form Al(OH)₃ and HCl hence the mechanism is at odds with text book inorganic chemistry.

A biphasic system composed of aqueous substrate and organic extraction solvent were used by McNeff and co-workers to dehydrate a number of carbohydrate feedstocks at 160-200 °C.^{173, 174} The reaction carried out in presence of TiO₂ catalyst and n-butanol and MIBK as extraction solvent. The effect of variations in organic/aqueous were investigated and the maximum HMF yield (25-30%) were obtained at 180 °C with MIBK as extraction solvent (organic/aqueous 10:1) and with aqueous feed containing 23 or 50 wt % glucose. Using n-butanol as extraction solvent typically resulted in yields between 6 and 13% from glucose.¹⁷³ The authors explain the lower HMF yield in presence of *n*-butanol as organic phase can be attributed to high solubility of water in *n*-butanol under the reaction conditions. Moreover, the effect of addition of homogeneous acid catalysts such as HCl (0.005-0.15 M) and H₃PO₄ (0.1 M) to the system at 180 °C was studied.¹⁷³ Applying 0.15 M HCl as the only catalyst in the system yielded 13% HMF from glucose. Combination of TiO₂ with 0.15 M HCl gave the highest HMF yield around 37%.

Hansen *et al.* reported very low HMF yield from glucose dehydration using boric acid as catalyst.¹⁷⁵ They obtained an HMF yield of 14% from 30 wt% glucose at conversion level of 41% at 150 °C after 5 h in presence of boric acid and NaCl as catalyst and MIBK as extraction solvent (organic/aqueous: 4/1 v/v). Yang and co-workers reported high HMF yield and selectivity in a biphasic system.¹⁷⁶ From a 6 wt% aqueous glucose solution, in presence of 8 wt% phosphated niobia and 1.5 eq (v/v) 2-butanol, a 49% HMF yield was obtained at 72% conversion at 160 °C for 110 min. Additionally, using phosphated tantalum hydroxide as catalyst resulted in 58% HMF yield at 70% conversion after 140 min.¹⁷⁷

The application of Ag₃PW₁₂O₄₀ as catalyst for glucose dehydration in a biphasic system was studied by Fan *et al.*¹⁷⁸ A 23 wt % aqueous mixture with a 2.25 volume ratio of MIBK as extracting solvent was reacted at 130 °C in presence of 13 wt% catalyst to obtain 76% HMF yield at 90% conversion after 4 h.

A bifunctional catalytic system was used by Nikolla *et al.* for glucose dehydration. After 70 min reaction at 180 °C, they managed to obtain 57% HMF yield at 79% conversion from a 10 wt% glucose solution in 26 wt% NaCl in presence of HCl (pH

1) and 0.5 wt% Sn- β and 3 eq. (v/v) of THF as extraction solvent. Using Ti- β as catalyst in the same reaction condition led to 53% yield at 76% conversion after 105 min.¹⁷⁹

The application of H₂O-DMSO/2-BuOH-MIBK solvent systems were studied by a number of research groups and HMF yields as high as 35% and selectivities up to 70% were reported. More recently, some research have been carried out on glucose dehydration in aqueous/organic biphasic solvents systems with acid catalysts.¹⁸⁰⁻¹⁸²

Mascal and Nikitin looked at water–1,2-dichloroethane system for HCl catalyzed carbohydrate conversion to 5-chloromethylfurfural (CMF).¹⁸³ When LiCl was used as homogeneous catalyst, after 30 h reaction at 65 °C, three types of furanic compounds were isolated with combined yield of 85%: 71% CMF yield, 7% 2-(2-hydroxyacetyl)furan (HAF) yield and 8% HMF yield. Reportedly, CMF can be easily converted to HMF, 5-methylfurfural (MF), 5-ethoxymethylfurfural (EMF), and 2,5-dimethylfuran.^{183, 184} Modifying this system by application of a closed system in which 1,2-dichloroethane could be refreshed every hour led to improved results. For reaction at 100 °C for 3 h, 81% CMF was yielded from a 1 wt% glucose solution.¹⁸⁵ Similar research was carried out by Brasholz *et al.* in which a 2 wt% glucose solution reacted in 32 wt% HCl_(aq) at 120 °C with a residence time of 5 min.¹⁸⁶ 58% CMF was yielded when equal flow of reaction mixture and 1,2-dichloroethane as extraction solvent were used.

Table 1.7 summarises the production of HMF from glucose dehydration reactions using biphasic solvent systems. Making a fair comparison between the data on glucose dehydration in aqueous solutions and biphasic systems is very difficult because of the small number of experiments that were carried out at comparable reaction conditions. However, it is clear that the use of an extracting solvent can improve HMF yield and the application of a bifunctional catalyst is necessary to obtain high yields of HMF from glucose.

Table 1.7: Glucose dehydration to HMF in biphasic systems (continued on next page)

Glucose conc.	Reaction solvent	Extraction solvent	Organic/Aqueous ratio	Catalyst	Catalyst loading	Temperature	Reaction time	Conversion	Yield	Selectivity	Ref
wt%			(v/v)			°C		%	%	%	
10	Water/DMSO (3:7 w/w)	DCM	1 (w/w)	None		140	4.5 h	62	30	48	91
23	Water	MIBK	2.25	Ag ₃ PW ₁₂ O ₄₀	13 wt%	130	4 h	90	76	85	178
9	Water	Toluene	2.3	Al-TUD-1	67 wt%	170	6 h	76	18	23	187
5	Water	MIBK	2	AlCl ₃	50 mol%	130 ^a	5 min		43 ^b		146
30	Water (0.87 M NaCl)	MIBK	4	H ₃ BO ₃	85 mol%	150	5 h	41	14	34	175
10	Water/DMSO (1:1 w/w)	MIBK/2 BuOH (7:3 w/w)	2 (w/w)	HCl (pH 1)		170	17 min	50	24	47	91
6	Water	2-BuOH	1.5	Nb ₂ O ₅ (pretreated with H ₃ PO ₄)	8 wt%	160	110 min	72	49	68	176
6	Water	2-BuOH	1.5	Ta ₂ O ₅ (pretreated with H ₃ PO ₄)	8 wt%	160	140	58	70	83	177
10	Water/DMSO (2:8 w/w)	MIBK/2 BuOH (7:3 w/w)	1	SBA-15-[PMIm]Cl/CrCl ₂	8 wt%	150	3 h	50	35	70	188
10	Water	n-BuOH	3	Sn-β/HCl (pH 1)	0.5 mol% Sn	160	90 min	77	20	26	179
10	Water (26 wt% NaCl)	n-BuOH	3	Sn-β/HCl (pH 1)	0.5 mol% Sn	160	90 min	75	41	55	179
10	Water (26 wt% NaCl)	THF	3	Sn-β/HCl (pH 1)	0.5 mol% Sn	180	70 min	79	57	72	179
10	Water (26 wt% NaCl)	THF	3	Ti-β/HCl (pH 1)	0.5 mol% Ti	180	105 min	76	53	70	179
23	Water	MIBK	10	TiO ₂	Fixed bed	180	2 min ^c		29		173
50	Water	MIBK	10	TiO ₂	Fixed bed	180	2 min ^c		26		173

Table 1.7: Glucose dehydration to HMF in biphasic systems (Continued from previous page)

50	Water (1.5 M HCl)	MIBK	10	TiO ₂ /HCl	Fixed bed	180	2 min ^c		37		173
23	Water	n-BuOH	1	TiO ₂	Fixed bed	200	3 min ^c		13		173
23	Water	MIBK	10	ZrO ₂	Fixed bed	180	2 min ^c		21		173
5	Water	MIBK	2	Meso-TiO ₂	50 wt%	130	5 min		26		141
5	Water (saturated with NaCl)	SBP	2	AlCl ₃ /HCl (pH 2.5)	1.5 mol% Al	170	40 min	91	62	68	171
4.5	Water (NaCl 35 wt%)	THF	3	AlCl ₃	40 mol%	160	10 min	99	61	60	172
6.5	Water	MIBK	3	ZrPO	20 wt%	165	360 min	60	24	40	189
6.5	Water	MIBK	3	ZrPO/Si	20 wt%	165	400 min	40	21	52	189

^a Microwave irradiation, ^b Isolated yield, ^c Continuous flow.

1.1.9.4 Glucose dehydration in ionic liquids

Ionic liquids (IL)s are salts that consist of organic cations and either inorganic or organic anions and they exhibit exceptional behaviour compared to conventional molecular solvents.¹⁹⁰ ILs usually have low melting point (below 100 °C), and relatively low viscosity and extremely low vapour pressure.¹⁹¹ They possess a high thermal and chemical stability as well as high ionic conductivity and recyclability.^{190, 192}

As the comprising parts of the IL (the anion and cation) can be varied, the IL can be designed and adjusted to suit a particular process and exhibit a particular set of properties. Therefore sometimes are referred to as “designer solvents”.¹⁹³ These outstanding properties make ILs suitable candidates as reaction media, and are promising in addressing the difficulties associated with the solubility of cellulosic materials.¹⁹⁰

Most of early ionic liquids suffer from sensitivity to air and moisture which significantly limit their applications. But in 1992, Wilkes’ group made a breakthrough by reporting the development of a series of air and moisture stable imidazolium type ILs.^{194, 195} The most common ionic liquids are N,N'-dialkylimidazolium, N-alkylpyridinium, alkylammonium and alkylphosphonium based.

The application of ILs as solvents and co-catalysts for HMF production from biomass derived sugars have been in the center of attentions since Zhao *et al.* made a breakthrough in 2007.¹⁹⁶ They reported 68% HMF yield at 94% conversion from 9 wt % glucose in [EMIm]Cl with 1 mol % CrCl₂ at 100 °C after 3 h. Later Sievers *et al.* studied the effect of Brønsted acid addition (H₂SO₄) into [BMIm]Cl for conversion of glucose to HMF.¹⁹⁷ A low HMF yield of 12% was achieved in this work, considerably lower than the result reported by Zhao. Thus suggesting that under these conditions a Lewis acid (e.g. CrCl₂) is more efficient for glucose transformation.

Li *et al.* found out that microwave irradiation can play a significant role in controlling HMF selectivity when using ILs.¹³³ They reported 91% HMF yield in [C₄mim]Cl and CrCl₃ as catalyst under microwave irradiation at 100 °C for 1 min. When a conventional oil-bath heating method was used for comparison, at similar conversion levels, only

17% HMF was yielded. Qi and co-workers observed similar effect from microwave irradiation heating method. They obtained 71% HMF yield in [BMIm]Cl in presence of 10 mol% CrCl₃ catalyst after 30 sec heating at 140 °C. For the similar reaction condition but using oil bath heating, the yield was 23% smaller.¹⁹⁸ In another study, Hu *et al.* investigated the application of commonly used Lewis acid in IL instead of effective CrCl_x (x = 2,3). They used SnCl₄ as catalyst in [BMIm]BF₄ for glucose conversion and after 3 h reaction at 100 °C they obtained 61% HMF yield.¹⁵⁰ The toxicity of chromium and tin persuaded Zhang and co-workers to examine the use of GeCl₄ as Lewis acid for glucose dehydration. In this study, 5 wt% glucose dissolved in [BMIm]Cl and then heated at 120 °C for 30 min. Under these conditions moderate HMF yield of 48% was achieved.¹⁶² Khokhlova *et al.* explored B₂O₃ as an environmentally friendly metal free promoter for conversion of carbohydrates in ILs.¹⁹⁹ Effective transformation of glucose to HMF in ILs was also reported by Liu *et al.* In this case, Al(OiPr)₃ and AlEt₃ were used as catalysts and after 6 h heating at 120 °C in [EMIm]Cl, HMF yield of 49 and 51% was obtained respectively.²⁰⁰ Chen *et al.* looked at the performance of Cr⁰ nanoparticles as catalyst for glucose dehydration to HMF in [BMIm]Cl. Carrying out the reaction for 6 h at 120 °C resulted in 49% HMF yield from a 23 wt% glucose solution.²⁰¹

Zhang *et al.* reported an HMF yield of 40% at 78% conversion from 5 wt% glucose in [BMIm]Cl by employing 60 wt% hydroxyapatite supported chromium chloride (Cr-HAP) as catalyst at 150 °C for 2.5 min by means of microwave irradiation.²⁰² These studies proved that in order to obtain a high yield of HMF, an optimised combination of ILs having appropriate hydrophilic/hydrophobic properties as well as effective Brønsted or Lewis acids catalysts are essential.

Table 1.8 summarises some of the outstanding studies on glucose dehydration in ionic liquids. It is possible to conclude from multiple publications that chromium plays an important role in obtaining high HMF yields from glucose. However, differences in activity between CrCl₂ and CrCl₃ are not significant. Moreover, using ILs as reaction media for glucose transformation to HMF, the cost of ILs should be considered and its stability against the presence of air and moisture should be examined under the reaction conditions.

Table 1.8: Glucose dehydration to HMF in ionic liquid systems (Continued on next page)

Glucose concentration wt%	Solvent	Catalyst	Catalyst loading	Temperature °C	Reaction time	Conversion %	Yield %	Selectivity %	Ref
8	[BMIm]Cl	CF ₃ COOH	1 mol%	120	3 h	58	44	75	203
8	[BMIm]Cl	CF ₃ SO ₃ H	1 mol%	120	3 h	87	40	46	203
8	[BMIm]Cl	CH ₃ SO ₃ H	1 mol%	120	3 h	73	42	58	203
9	[BMIm]Cl	Cr(NO ₃) ₃	7 mol%	100	3 h	82	37	45	161
9	[EMIm]Cl	CrCl ₂	6 mol%	100	3 h	93	62	67	204
9	[EMIm]Cl	CrCl ₂	6 mol%	100	3 h	94	68	72	196
40	ChoCl	CrCl ₂	10 mol%	110	1 h		45		205
2.2 M	NBu ₄ Cl	CrCl ₂	10 mol%	110	4 h		54		206
10	[BMIm]Cl	CrCl ₂ /NHC	9 mol%	100	6 h		81		207
5	[BMIm]Cl	CrCl ₃	20 mol%	90 ^a	1 h	51	40	80	198
9	[BMIm]Cl	CrCl ₃	3.6 wt%	100	1 h		17		133
5	[BMIm]Cl	CrCl ₃	20 mol%	100 ^a	30 min	77	56	73	198
5	[BMIm]Cl	CrCl ₃	20 mol%	100 ^a	1 h	85	67	78	198
9	[BMIm]Cl	CrCl ₃	7 mol%	100	3 h	79	35	45	198
9	[EMIm]Cl	CrCl ₃	6 mol%	100	3 h	72	44	62	196
40	ChoCl	CrCl ₃	10 mol%	110	1 h		31		205
5	[BMIm]Cl	CrCl ₃	20 mol%	120 ^a	10 min	94	69	73	198
23	[BMIm]Cl	CrCl ₃	20 mol%	120 ^a	10 min	97	55	56	198
5	[BMIm]Cl	CrCl ₃	10 mol%	120 ^a	10 min	88	66	75	198
9	[BMIm]Cl ^b	CrCl ₃	6 mol%	120	4 h	91	91	100	208

Table 1.8: Glucose dehydration to HMF in ionic liquid systems (Continued from previous page)

5	[BMIm]HSO ₄	CrCl ₃	20 mol%	120 ^a	10 min	86	5	6	198
5	[EMIm]Cl	CrCl ₃	20 mol%	120 ^a	10 min	97	72	74	198
5	[HexylMIm]Cl	CrCl ₃	20 mol%	120 ^a	10 min	94	63	67	198
5	[BMIm]Cl	CrCl ₃	20 mol%	140 ^a	0.5 min	96	71	74	198
9	[BMIm]Cl	CrCl ₃	3.6 wt%	unknown ^a	1 min		91		133
9	[EMIm]Cl	CrCl ₃ .6H ₂ O	6 mol%	100	3 h	97	72	74	157
9	[BenzylMIm]Cl	CrCl ₃ .6H ₂ O	25 mol%	120	1 h		65		209
9	[BMIm]Cl	CrCl ₃ .6H ₂ O	25 mol%	120	1 h		67		209
9	Net ₄ Cl	CrCl ₃ .6H ₂ O	10 mol%	130	10 min		71		210
5	[BMIm]Cl	GeCl ₄	10 mol%	100	75 min	93	38	42	162
5	[BMIm]Cl ^c	GeCl ₄	10 mol%	100	75 min	93	48	52	162
5	[BMIm]Cl	GeCl ₄	10 mol%	120	30 min	99	48	48	162
8	[BMIm]Cl	H ₂ SO ₄	1 mol%	120	3 h	93	61	66	203
9	[BMIm]Cl	H ₂ SO ₄	10 wt%	unknown ^a	1 min		49		133
9	[BMIm]Cl	H ₃ BO ₃	100 mol%	120	3 h	68	22	32	163
9	[BMIm]Cl	H ₃ BO ₃	80 mol%	120	3 h	47	14	30	163
9	[EMIm]Cl	H ₃ BO ₃	100 mol%	120	3 h	87	40	46	163
9	[EMIm]Cl	H ₃ BO ₃	80 mol%	120	3 h	95	41	43	163
9	[HexylMIm]Cl	H ₃ BO ₃	80 mol%	120	3 h	68	32	47	163
9	[HMIm]Cl	H ₃ BO ₃	80 mol%	120	3 h	95	19	20	163
9	[OctylMIm]Cl	H ₃ BO ₃	80 mol%	120	3 h	63	26	41	163
8	[BMIm]Cl	H ₃ PMo ₁₂ O ₄₀	1 mol%	120	3 h	71	63	89	203
8	[BMIm]Cl	H ₃ PW ₁₂ O ₄₀	1 mol%	120	3 h	82	66	81	203

Table 1.8: Glucose dehydration to HMF in ionic liquid systems (Continued from previous page)

8	[BMIm]Cl	HNO ₃	1 mol%	120	3 h	56	43	77	203
5	[BMIm]Cl	Hydroxyapatite with 4.6 wt% Cr(III)	60 wt%	unknown ^a	2.5 min	78	40	52	202
9	[BMIm]Cl	NHC/(CrCl ₂) ₂	9 mol%	100	6 h		81		207
9	[BMIm]Cl	NHC/CrCl ₂	9 mol%	100	6 h		81		207
9	[BMIm]Cl	NHC/CrCl ₂	9 mol%	100	6 h		80		207
9	[BMIm]Cl	NHC/CrCl ₃	9 mol%	100	6 h		78		207
9	[BMIm]Cl	NHC/CrCl ₃	9 mol%	100	6 h		78		207
0.28 M	[BMIm]Cl	H-ZSM-5	198 wt%	110	8 h		45		206
9	[EMIm]BF ₄	SnCl ₄	10 mol%	100	3 h	97	53	55	150
9	[BMIm]Cl	Yb(OTf) ₃	10 mol%	140	6 h	65	24	37	211
9	[EMIm]Cl	Yb(OTf) ₃	10 mol%	140	6 h	63	10	16	211
2	[HexylMIm]Cl/H ₂ O (1:1 w/w)	ZrO ₂	40 wt%	200	10 min	92	53	56	212
	[BMIm]Cl	B ₂ O ₃		120	5 h		60		199
10	DMSO/[BMIm]Cl	Lignin derived solid acid	50 wt%	160	50 min	99	68	69	213

^a Heating by microwave irradiation, ^b 2.3 volume equivalent of MIBK as extraction solvent, ^c Molecular sieves used for water adsorption

1.2 Thesis aims

As outlined earlier in this report, the need for clean, renewable and sustainable energy has driven research into the development of alternative heterogeneous catalysts. A heterogeneous catalytic approach offers many advantages. The primary advantage is that they are in the solid phase and the ease of separation from the liquid phase (and or gas) and products without involving quenching steps. So, fewer waste streams are generated and efficient recyclability can be achieved. As can be seen from the literature survey, there is a vast body of work under a range of conditions making it difficult to gain a fundamental understanding of the key requirements for designing improved catalysts for glucose conversion. The work of Ebitani, nicely demonstrates there is a need for a bifunctional base-acid catalyst to achieve one-pot conversion of glucose to HMF. However, it would be desirable to achieve this with a single catalyst.

To address this, this project aims to develop a systematic series of bifunctional catalysts with tuneable acid and basic character for the direct production of 5-HMF from glucose. For this purpose, sulphated zirconia catalysts were synthesised using a commercial ZrO_2 support. Acid and base properties were carefully tailored through the variation of surface sulphur loading. Furthermore, the efficiency of this process as well as the physical properties of the catalyst was improved through the use of nano-templated material as a support. Finally, the catalytic performance of each prepared solid acid catalyst was examined in the esterification reaction of free fatty acids - a key reaction for the production of biodiesel.

1.3 References

1. V. K. Gupta and M. G. Tuohy, *Biofuel Technologies: Recent Developments*, Springer, 2013.
2. *International Energy Outlook 2013*, U.S. Energy Information Administration, Washington DC, USA.
3. A. P. M. Baede, *IPCC AR4 SYR Appendix Glossary*, 2010.
4. E. Arrhenius and T. W. Waltz, *The greenhouse effect*, World Bank, 1990.
5. M. Pidwirny, *Fundamentals of Physical Geography, 2nd Edition*. <http://www.physicalgeography.net/fundamentals>, 2006.
6. T. F. Stocker, D. Qin, G.-K. Plattner, M. Tignor, S.K. Allen, J. Boschung, A. Nauels, Y. Xia, V. Bex and P.M. Midgley (eds.), *IPCC, 2013: Climate Change 2013: The Physical Science Basis. Contribution of Working Group I to the Fifth Assessment Report of the Intergovernmental Panel on Climate Change*, Cambridge, United Kingdom and New York, NY, USA.
7. B. D. Santer, *AIP Conference Proceedings*, 2011, **1401**, 183-197.
8. K. Bennaceur, D. Gielen, T. Kerr and C. Tam, *CO2 capture and storage: a key carbon abatement option*, OECD, 2008.
9. *BP Statistical Review of World Energy*, 2013.
10. *Key World Energy Statistics*, International Energy Agency (IEA), Paris, France, 2013.
11. C.-Y. Chen, S.-Q. Xiao and M. E. Davis, *Microporous Materials*, 1995, **4**, 1-20.
12. G. Bahgat, *International Affairs*, 2006, **82**, 961-975.
13. W. Institute, *Biofuels for transport: Global potential and implications for sustainable energy and agriculture*, Earthscan, 2007.
14. J. D. Hamilton, *Historical oil shocks*, National Bureau of Economic Research, 2011.
15. J. M. Torres, A. Alvarez, M. A. Laugé and J. M. Sarriegi, *Proceedings of the 27th International Conference of the System Dynamics Society*, 2009.
16. G. Sorda, M. Banse and C. Kemfert, *Energy Policy*, 2010, **38**, 6977-6988.
17. G. B. Alexander, W. M. Heston and R. K. Iler, *The Journal of Physical Chemistry*, 1954, **58**, 453-455.

18. Department of Energy & Climate Change, *2013 UK Greenhouse Gas Emissions, Provisional Figures and 2012 UK Greenhouse Gas Emissions, Final Figures by Fuel Type and End-User*, 2014.
19. A. Demirbas, *Biodiesel*, Springer, 2008.
20. D. McCollum and C. Yang, *Energy Policy*, 2009, **37**, 5580-5596.
21. S. Chakraborty, V. Aggarwal, D. Mukherjee and K. Andras, *Asia-Pacific Journal of Chemical Engineering*, 2012, **7**, S254-S262.
22. P. S. Nigam and A. Singh, *Progress in Energy and Combustion Science*, 2011, **37**, 52-68.
23. T. Jokiniemi and J. Ahokas, *Agronomy Research*, 2013, **11**, 239-248.
24. D. M. Alonso, J. Q. Bond and J. A. Dumesic, *Green Chemistry*, 2010, **12**, 1493-1513.
25. A. Singh, P. S. Nigam and J. D. Murphy, *Bioresource Technology*, 2011, **102**, 10-16.
26. J. Fargione, J. Hill, D. Tilman, S. Polasky and P. Hawthorne, *Science*, 2008, **319**, 1235-1238.
27. T. Searchinger, R. Heimlich, R. A. Houghton, F. Dong, A. Elobeid, J. Fabiosa, S. Tokgoz, D. Hayes and T.-H. Yu, *Science*, 2008, **319**, 1238-1240.
28. *HLPE, Biofuels and food security*, Rome, Italy, 2013.
29. V. Patil, K.-Q. Tran and H. R. Giselsrød, *International Journal of Molecular Sciences*, 2008, **9**, 1188-1195.
30. F. Danielsen, H. Beukema, N. D. Burgess, F. Parish, C. A. BrÜhl, P. F. Donald, D. Murdiyarso, B. E. N. Phalan, L. Reijnders, M. Struebig and E. B. Fitzherbert, *Conservation Biology*, 2009, **23**, 348-358.
31. A. Demirbas, *Applied Energy*, 2011, **88**, 17-28.
32. *National Biofuels Action Plan*, Biomass Research and Development Board, USA, 2008.
33. R. E. H. Sims, W. Mabey, J. N. Saddler and M. Taylor, *Bioresource Technology*, 2010, **101**, 1570-1580.
34. W. H. Liew, M. H. Hassim and D. K. S. Ng, *Journal of Cleaner Production*.
35. S. Raman and A. Mohr, *Journal of Cleaner Production*, 2014, **65**, 224-233.
36. R. A. Jansen, *Second Generation Biofuels and Biomass: Essential Guide for Investors, Scientists and Decision Makers*, John Wiley & Sons, 2012.
37. J. G. Speight, *The Biofuels Handbook*, Royal Society of Chemistry, 2011.

38. *Second Generation Biofuels A Review From A Market Barrier Prospective*, IEA Bioenergy Task 39 Liquid Biofuels from Biomass, Canada, 2006.
39. S. Freguia, B. Virdis and K. Rabaey, in *The Prokaryotes*, eds. E. Rosenberg, E. DeLong, S. Lory, E. Stackebrandt and F. Thompson, Springer Berlin Heidelberg, 2013, pp. 373-381.
40. C. Huang, M.-h. Zong, H. Wu and Q.-p. Liu, *Bioresource technology*, 2009, **100**, 4535-4538.
41. C. R. Carere, R. Sparling, N. Cicek and D. B. Levin, *International journal of molecular sciences*, 2008, **9**, 1342-1360.
42. A. Singh, S. I. Olsen and P. S. Nigam, *Journal of Chemical Technology & Biotechnology*, 2011, **86**, 1349-1353.
43. R. Picazo-Espinosa, J. González-López and M. Manzanera, *Biofuel's Engineering Process Technology. Wiedeń. MA dosSantos-Bernandes*, 2011, 16-133.
44. L. Zhu and T. Ketola, *International Journal of Sustainable Development & World Ecology*, 2012, **19**, 268-274.
45. L. D. Zhu, E. Hiltunen, E. Antila, J. J. Zhong, Z. H. Yuan and Z. M. Wang, *Renewable and Sustainable Energy Reviews*, 2014, **30**, 1035-1046.
46. A. Demirbaş, *Energy Sources, Part A: Recovery, Utilization, and Environmental Effects*, 2008, **31**, 163-168.
47. A. Singh and S. I. Olsen, *Applied Energy*, 2011, **88**, 3548-3555.
48. M. F. Demirbas, *Applied Energy*, 2011, **88**, 3473-3480.
49. K. Tsukahara and S. Sawayama, *J Jpn Pet Inst*, 2005, **48**, 251.
50. A. Singh, P. S. Nigam and J. D. Murphy, *Bioresource technology*, 2011, **102**, 26-34.
51. K. Kita, S. Okada, H. Sekino, K. Imou, S. Yokoyama and T. Amano, *Applied Energy*, 2010, **87**, 2420-2423.
52. B. Kamm, P. R. Gruber and M. Kamm, *Biorefineries–industrial processes and products*, Wiley-VCH Verlag, Weinheim (Germany), 2005.
53. F. Cherubini, *Energy Conversion and Management*, 2010, **51**, 1412-1421.
54. R. Katzen and D. J. Schell, *Biorefineries-Industrial Processes and Products: Status Quo and Future Directions*, 2006, 129-138.
55. P. McKendry, *Bioresource Technology*, 2002, **83**, 47-54.

56. L. Guzzi and A. Erdőhelyi, *Catalysis for Alternative Energy Generation*, Springer, 2012.
57. Y.-C. Lin and G. W. Huber, *Energy & Environmental Science*, 2009, **2**, 68-80.
58. J. M. Moffatt and R. P. Overend, *Biomass*, 1985, **7**, 99-123.
59. F. Goudriaan and D. G. R. Peferoen, *Chemical Engineering Science*, 1990, **45**, 2729-2734.
60. D. J. Stevens, *Review and analysis of the 1980-1989 biomass thermochemical conversion program*, National Renewable Energy Laboratory, 1994.
61. A. Demirbaş, *Energy conversion and Management*, 2001, **42**, 1357-1378.
62. B. t. Chemical, E. B. t. L. Biofuels and G. W. Huber, *Breaking the chemical and engineering barriers to lignocellulosic biofuels: next generation hydrocarbon biorefineries*, Citeseer, 2008.
63. D. Elliott, D. Beckman, A. Bridgwater, J. Diebold, S. Gevert and Y. Solantausta, *Energy & Fuels*, 1991, **5**, 399-410.
64. NNFCC, The Andersons Centre, *NNFCC Renewable Fuels and Energy Factsheet: Anaerobic Digestion*, 2011.
65. L. Appels, J. Lauwers, J. Degreë, L. Helsen, B. Lievens, K. Willems, J. Van Impe and R. Dewil, *Renewable and Sustainable Energy Reviews*, 2011, **15**, 4295-4301.
66. V. Nallathambi Gunaseelan, *Biomass and Bioenergy*, 1997, **13**, 83-114.
67. H. Wu, P. Zhang, J. Guo and Y. Wu, *Huan jing ke xue= Huanjing kexue/[bian ji, Zhongguo ke xue yuan huan jing ke xue wei yuan hui" Huan jing ke xue" bian ji wei yuan hui.]*, 2013, **34**, 810-816.
68. L. N. Liew, J. Shi and Y. Li, *Biomass and Bioenergy*, 2012, **46**, 125-132.
69. F. Tambone, P. Genevini, G. D'Imporzano and F. Adani, *Bioresource technology*, 2009, **100**, 3140-3142.
70. J. Singh and S. Gu, *Renewable and Sustainable Energy Reviews*, 2010, **14**, 1367-1378.
71. L. Thomas, C. Larroche and A. Pandey, *Biochemical Engineering Journal*, 2013, **81**, 146-161.
72. K. Sanderson, *Nature*, 2011, **469**, 18-20.
73. G. Rothenberg, *Catalysis: concepts and green applications*, Wiley-VCH, 2008.
74. P. T. Anastas and J. C. Warner, *Green chemistry: theory and practice*, Oxford University Press, 2000.

75. P. T. Anastas and M. M. Kirchhoff, *Accounts of chemical research*, 2002, **35**, 686-694.
76. R. A. Sheldon, *Pure and applied chemistry*, 2000, **72**, 1233-1246.
77. W. Z. Ostwald, *physikalische Chemie*, 1894, **15**, 705-706.
78. S. T. Oyama and G. A. Somorjai, *Journal of Chemical Education*, 1988, **65**, 765.
79. B. C. Gates, G. W. Huber, C. L. Marshall, P. N. Ross, J. Siirola and Y. Wang, *MRS Bulletin*, 2008, **33**, 429-435.
80. E. Farnetti, R. Di Monte and J. Kašpar.
81. J. A. Dumesic, G. W. Huber and M. Boudart, *Handbook of Heterogeneous Catalysis*, 2008.
82. G. Bond, Oxford, 1987.
83. C. H. Bartholomew and R. J. Farrauto, *Fundamentals of industrial catalytic processes*, John Wiley & Sons, 2011.
84. H. S. Fogler, 1999.
85. D. R. Rolison, *Science*, 2003, **299**, 1698-1701.
86. D. L. Trimm, *Applied Catalysis A: General*, 2001, **212**, 153-160.
87. E. de Jong, *IEA Bioenergy, Task42 Biorefinery*, 2012.
88. T. Werpy and G. Petersen, *U. S. D. o. Energy*, 2004.
89. J. J. Bozell and G. R. Petersen, *Green Chemistry*, 2010, **12**, 539-554.
90. K. J. Zeitsch, *The chemistry and technology of furfural and its many by-products*, Elsevier, 2000.
91. J. N. Chheda, Y. Roman-Leshkov and J. A. Dumesic, *Green Chemistry*, 2007, **9**, 342-350.
92. C. Moreau, M. N. Belgacem and A. Gandini, *Top Catal*, 2004, **27**, 11-30.
93. Y. Roman-Leshkov, J. N. Chheda and J. A. Dumesic, *Science*, 2006, **312**, 1933-1937.
94. G. W. Huber, J. N. Chheda, C. J. Barrett and J. A. Dumesic, *Science*, 2005, **308**, 1446-1450.
95. R. M. West, Z. Y. Liu, M. Peter and J. A. Dumesic, *ChemSusChem*, 2008, **1**, 417-424.
96. D. T. Jones and D. R. Woods, *Microbiological reviews*, 1986, **50**, 484.
97. M. Sasaki, K. Goto, K. Tajima, T. Adschiri and K. Arai, *Green Chemistry*, 2002, **4**, 285-287.

98. C. J. Barrett, J. N. Chheda, G. W. Huber and J. A. Dumesic, *Applied Catalysis B: Environmental*, 2006, **66**, 111-118.
99. G. W. Huber, R. D. Cortright and J. A. Dumesic, *Angewandte Chemie International Edition*, 2004, **43**, 1549-1551.
100. R. M. West, D. J. Braden and J. A. Dumesic, *Journal of Catalysis*, 2009, **262**, 134-143.
101. G. Düll, *Chemiker Zeitung*, 1895, **19**, 216.
102. J. Kiermayer, *Chemiker Zeitung*, 1895, **19**, 1003.
103. Sigma-Aldrich, St. Louis, MO, 2010.
104. S. Budavari, 1989, 767.
105. W. N. Haworth and W. G. M. Jones, *Journal of the Chemical Society (Resumed)*, 1944, 667-670.
106. H. E. van Dam, A. P. G. Kieboom and H. van Bekkum, *Starch - Stärke*, 1986, **38**, 95-101.
107. B. F. M. Kuster, *Starch - Stärke*, 1990, **42**, 314-321.
108. M. J. Antal Jr, W. S. L. Mok and G. N. Richards, *Carbohydrate Research*, 1990, **199**, 91-109.
109. C. Moreau, R. Durand, S. Razigade, J. Duhamet, P. Faugeras, P. Rivalier, P. Ros and G. Avignon, *Applied Catalysis a-General*, 1996, **145**, 211-224.
110. M. J. Antal Jr, T. Leesomboon, W. S. Mok and G. N. Richards, *Carbohydrate Research*, 1991, **217**, 71-85.
111. X. Qian, M. R. Nimlos, M. Davis, D. K. Johnson and M. E. Himmel, *Carbohydrate Research*, 2005, **340**, 2319-2327.
112. E. F. L. J. Anet, in *Advances in Carbohydrate Chemistry*, ed. L. W. Melville, Academic Press, 1964, vol. Volume 19, pp. 181-218.
113. M. J. Antal Jr, W. S. L. Mok and G. N. Richards, *Carbohydrate Research*, 1990, **199**, 111-115.
114. F. H. Newth, in *Advances in Carbohydrate Chemistry*, eds. S. H. Claude and M. C. Sidney, Academic Press, 1951, vol. Volume 6, pp. 83-106.
115. A. S. Amarasekara, L. D. Williams and C. C. Ebede, *Carbohydrate Research*, 2008, **343**, 3021-3024.
116. B. Schneider, F. W. Lichtenthaler, G. Steinle and H. Schiweck, *Liebigs Annalen der Chemie*, 1985, **1985**, 2443-2453.
117. G. R. Akien, L. Qi and I. T. Horvath, *Chem Commun*, 2012, **48**, 5850-5852.

118. H. Kimura, M. Nakahara and N. Matubayasi, *The Journal of Physical Chemistry A*, 2011, **115**, 14013-14021.
119. T. Yoshida, S. Yanachi and Y. Matsumura, *Journal of the Japan Institute of Energy*, 2007, **86**, 700-706.
120. B. M. Kabyemela, T. Adschiri, R. M. Malaluan and K. Arai, *Industrial & Engineering Chemistry Research*, 1999, **38**, 2888-2895.
121. B. M. Kabyemela, T. Adschiri, R. M. Malaluan and K. Arai, *Industrial & Engineering Chemistry Research*, 1997, **36**, 1552-1558.
122. R. L. de Souza, H. Yu, F. Rataboul and N. Essayem, *Challenges*, 2012, **3**, 212-232.
123. A. Chareonlimkun, V. Champreda, A. Shotipruk and N. Laosiripojana, *Fuel*, 2010, **89**, 2873-2880.
124. Q. Jing and X. LÜ, *Chinese Journal of Chemical Engineering*, 2008, **16**, 890-894.
125. T. M. Aida, Y. Sato, M. Watanabe, K. Tajima, T. Nonaka, H. Hattori and K. Arai, *The Journal of Supercritical Fluids*, 2007, **40**, 381-388.
126. M. Dashtban, A. Gilbert and P. Fatehi, *RSC Advances*, 2014, **4**, 2037-2050.
127. W. Zeng, D.-g. Cheng, F. Chen and X. Zhan, *Catal Lett*, 2009, **133**, 221-226.
128. M. Watanabe, Y. Aizawa, T. Iida, T. M. Aida, C. Levy, K. Sue and H. Inomata, *Carbohydrate Research*, 2005, **340**, 1925-1930.
129. X. Qi, M. Watanabe, T. M. Aida and R. L. Smith, Jr., *Catalysis Communications*, 2008, **9**, 2244-2249.
130. M. Watanabe, Y. Aizawa, T. Iida, R. Nishimura and H. Inomata, *Applied Catalysis A: General*, 2005, **295**, 150-156.
131. M. L. Mednick, *The Journal of Organic Chemistry*, 1962, **27**, 398-403.
132. N. H. Smith, Google Patents, 1964.
133. C. Li, Z. Zhang and Z. K. Zhao, *Tetrahedron Letters*, 2009, **50**, 5403-5405.
134. K.-i. Seri, Y. Inoue and H. Ishida, *B Chem Soc Jpn*, 2001, **74**, 1145-1150.
135. H. Ishida and K.-i. Seri, *Journal of Molecular Catalysis A: Chemical*, 1996, **112**, L163-L165.
136. T. Deng, X. Cui, Y. Qi, Y. Wang, X. Hou and Y. Zhu, *Chem Commun*, 2012, **48**, 5494-5496.
137. S. K. Tyrlik, D. Szerszen, B. Kurzak and K. Bal, *Starch - Stärke*, 1995, **47**, 171-174.

138. S. K. Tyrlik, D. Szerszen, M. Olejnik and W. Danikiewicz, *Journal of Molecular Catalysis A: Chemical*, 1996, **106**, 223-233.
139. S. K. Tyrlik, D. Szerszeń, M. Olejnik and W. Danikiewicz, *Carbohydrate Research*, 1999, **315**, 268-272.
140. K. Lourvanij and G. L. Rorrer, *Industrial & Engineering Chemistry Research*, 1993, **32**, 11-19.
141. S. Dutta, S. De, A. K. Patra, M. Sasidharan, A. Bhaumik and B. Saha, *Applied Catalysis A: General*, 2011, **409–410**, 133-139.
142. M. Kitano, K. Nakajima, J. N. Kondo, S. Hayashi and M. Hara, *Journal of the American Chemical Society*, 2010, **132**, 6622-6623.
143. A. Chareonlimkun, V. Champreda, A. Shotipruk and N. Laosiripojana, *Bioresource Technology*, 2010, **101**, 4179-4186.
144. K. Nakajima, Y. Baba, R. Noma, M. Kitano, J. N. Kondo, S. Hayashi and M. Hara, *Journal of the American Chemical Society*, 2011, **133**, 4224-4227.
145. F. S. Asghari and H. Yoshida, *Carbohydrate Research*, 2006, **341**, 2379-2387.
146. S. De, S. Dutta and B. Saha, *Green Chemistry*, 2011, **13**, 2859-2868.
147. Q. Bao, K. Qiao, D. Tomida and C. Yokoyama, *Catalysis Communications*, 2008, **9**, 1383-1388.
148. H. Yan, Y. Yang, D. Tong, X. Xiang and C. Hu, *Catalysis Communications*, 2009, **10**, 1558-1563.
149. K.-i. Seri, Y. Inoue and H. Ishida, *Chemistry Letters*, 2000, **29**, 22-23.
150. S. Hu, Z. Zhang, J. Song, Y. Zhou and B. Han, *Green Chemistry*, 2009, **11**, 1746-1749.
151. K. Beckerle and J. Okuda, *Journal of Molecular Catalysis A: Chemical*, 2012, **356**, 158-164.
152. M. Ohara, A. Takagaki, S. Nishimura and K. Ebitani, *Applied Catalysis A: General*, 2010, **383**, 149-155.
153. J. Tuteja, S. Nishimura and K. Ebitani, *B Chem Soc Jpn*, 2012, **85**, 275-281.
154. A. Takagaki, M. Ohara, S. Nishimura and K. Ebitani, *Chem Commun*, 2009, 6276-6278.
155. J. B. Binder and R. T. Raines, *Journal of the American Chemical Society*, 2009, **131**, 1979-1985.
156. J. B. Binder and R. T. Raines, Google Patents, 2009.
157. T. Chen and L. Lin, *Chinese Journal of Chemistry*, 2010, **28**, 1773-1776.

158. M. Yasuda, Y. Nakamura, J. Matsumoto, H. Yokoi and T. Shiragami, *B Chem Soc Jpn*, 2011, **84**, 416-418.
159. Y. Yang, C. Hu and M. M. Abu-Omar, *Bioresource Technology*, 2012, **116**, 190-194.
160. J. M. R. Gallo, D. M. Alonso, M. A. Mellmer and J. A. Dumesic, *Green Chemistry*, 2013, **15**, 85-90.
161. Z. Wei, Y. Li, D. Thushara, Y. Liu and Q. Ren, *Journal of the Taiwan Institute of Chemical Engineers*, 2011, **42**, 363-370.
162. Z. Zhang, Q. Wang, H. Xie, W. Liu and Z. Zhao, *ChemSusChem*, 2011, **4**, 131-138.
163. T. Ståhlberg, S. Rodriguez-Rodriguez, P. Fristrup and A. Riisager, *Chemistry – A European Journal*, 2011, **17**, 1456-1464.
164. Y. Yang, X. Xiang, D. Tong, C. Hu and M. M. Abu-Omar, *Bioresource Technology*, 2012, **116**, 302-306.
165. M. Dashtban, A. Gilbert and P. Fatehi, *J-FOR-JOURNAL OF SCIENCE & TECHNOLOGY FOR FOREST PRODUCTS AND PROCESSES*, 2012, **2**, 44-53.
166. Y. Román-Leshkov and J. Dumesic, *Top Catal*, 2009, **52**, 297-303.
167. Q. P. Peniston, Google Patents, 1956.
168. A. C. Cope, Google Patents, 1959.
169. L. Rigal and A. Gaset, *Biomass*, 1983, **3**, 151-163.
170. P. Azadi, R. Carrasquillo-Flores, Y. J. Pagan-Torres, E. I. Gurbuz, R. Farnood and J. A. Dumesic, *Green Chemistry*, 2012, **14**, 1573-1576.
171. Y. J. Pagan-Torres, T. Wang, J. M. R. Gallo, B. H. Shanks and J. A. Dumesic, *Acs Catalysis*, 2012, **2**, 930-934.
172. Y. Yang, C.-w. Hu and M. M. Abu-Omar, *Green Chemistry*, 2012, **14**, 509-513.
173. C. V. McNeff, D. T. Nowlan, L. C. McNeff, B. W. Yan and R. L. Fedie, *Applied Catalysis a-General*, 2010, **384**, 65-69.
174. C. V. McNeff and D. T. Nowlan, Google Patents, 2014.
175. T. S. Hansen, J. Mielby and A. Riisager, *Green Chemistry*, 2011, **13**, 109-114.
176. F. Yang, Q. Liu, X. Bai and Y. Du, *Bioresource Technology*, 2011, **102**, 3424-3429.
177. F. Yang, Q. Liu, M. Yue, X. Bai and Y. Du, *Chem Commun*, 2011, **47**, 4469-4471.

178. C. Fan, H. Guan, H. Zhang, J. Wang, S. Wang and X. Wang, *Biomass and Bioenergy*, 2011, **35**, 2659-2665.
179. E. Nikolla, Y. Roman-Leshkov, M. Moliner and M. E. Davis, *Acs Catalysis*, 2011, **1**, 408-410.
180. L. Yang, Y. H. Liu and R. S. Ruan, *Advanced Materials Research*, 2011, **335**, 1448-1453.
181. S. Pedersen, T. B. Christensen, A. Boisen, V. W. JÜRGENSEN, T. S. Hansen, S. Kegnaes, A. Riisager, J. M. Woodley, J. S. Jensen and W. Fu, Google Patents, 2011.
182. J. P. Zhuang, L. Lin, C. S. Pang and Y. Liu, *Advanced Materials Research*, 2011, **236**, 134-137.
183. M. Mascal and E. B. Nikitin, *Angewandte Chemie International Edition*, 2008, **47**, 7924-7926.
184. M. Mascal and E. B. Nikitin, *Green Chemistry*, 2010, **12**, 370-373.
185. M. Mascal and E. B. Nikitin, *ChemSusChem*, 2009, **2**, 859-861.
186. M. Brasholz, K. von Kanel, C. H. Hornung, S. Saubern and J. Tsanaktsidis, *Green Chemistry*, 2011, **13**, 1114-1117.
187. S. Lima, M. M. Antunes, A. Fernandes, M. Pillinger, M. F. Ribeiro and A. A. Valente, *Molecules*, 2010, **15**, 3863-3877.
188. V. Degirmenci, E. A. Pidko, P. C. M. M. Magusin and E. J. M. Hensen, *ChemCatChem*, 2011, **3**, 969-972.
189. V. V. Ordonsky, J. van der Schaaf, J. C. Schouten and T. A. Nijhuis, *ChemSusChem*, 2013, **6**, 1697-1707.
190. Y. Chen, Y. Zhang, F. Ke, J. Zhou, H. Wang and D. Liang, *Polymer*, 2011, **52**, 481-488.
191. K. R. Seddon, *Journal of Chemical Technology & Biotechnology*, 1997, **68**, 351-356.
192. P. Wang, H. Yu, S. Zhan and S. Wang, *Bioresource Technology*, 2011, **102**, 4179-4183.
193. M. J. Earle and K. R. Seddon, *Pure and applied chemistry*, 2000, **72**, 1391-1398.
194. J. P. Hallett and T. Welton, *Chemical Reviews*, 2011, **111**, 3508-3576.
195. J. S. Wilkes and M. J. Zaworotko, *Journal of the Chemical Society, Chemical Communications*, 1992, 965-967.

196. H. B. Zhao, J. E. Holladay, H. Brown and Z. C. Zhang, *Science*, 2007, **316**, 1597-1600.
197. C. Sievers, I. Musin, T. MarzIAletti, M. B. Valenzuela Olarte, P. K. Agrawal and C. W. Jones, *ChemSusChem*, 2009, **2**, 665-671.
198. X. Qi, M. Watanabe, T. M. Aida and R. L. Smith, *ChemSusChem*, 2010, **3**, 1071-1077.
199. E. A. Khokhlova, V. V. Kachala and V. P. Ananikov, *ChemSusChem*, 2012, **5**, 783-789.
200. D. D. Liu and E. Y.-X. Chen, *Applied Catalysis A: General*, 2012, **435**, 78-85.
201. J. He, Y. Zhang and E. Y. X. Chen, *ChemSusChem*, 2013, **6**, 61-64.
202. Z. Zhang and Z. Zhao, *Bioresource Technology*, 2011, **102**, 3970-3972.
203. M. Chidambaram and A. T. Bell, *Green Chemistry*, 2010, **12**, 1253-1262.
204. Y. Zhang, E. A. Pidko and E. J. M. Hensen, *Chemistry – A European Journal*, 2011, **17**, 5281-5288.
205. F. Ilgen, D. Ott, D. Kralisch, C. Reil, A. Palmberger and B. Konig, *Green Chemistry*, 2009, **11**, 1948-1954.
206. H. Jadhav, E. Taarning, C. M. Pedersen and M. Bols, *Tetrahedron Letters*, 2012, **53**, 983-985.
207. G. Yong, Y. Zhang and J. Y. Ying, *Angewandte Chemie International Edition*, 2008, **47**, 9345-9348.
208. S. Lima, P. Neves, M. M. Antunes, M. Pillinger, N. Ignatyev and A. A. Valente, *Applied Catalysis A: General*, 2009, **363**, 93-99.
209. Q. Cao, X. Guo, S. Yao, J. Guan, X. Wang, X. Mu and D. Zhang, *Carbohydrate Research*, 2011, **346**, 956-959.
210. L. Hu, Y. Sun and L. Lin, *Industrial & Engineering Chemistry Research*, 2011, **51**, 1099-1104.
211. T. Stahlberg, M. G. Sorensen and A. Riisager, *Green Chemistry*, 2010, **12**, 321-325.
212. X. Qi, M. Watanabe, T. M. Aida and R. L. Smith, *Bioresource Technology*, 2012, **109**, 224-228.
213. F. Guo, Z. Fang and T.-J. Zhou, *Bioresource Technology*, 2012, **112**, 313-318.

Chapter 2

Experimental

2.1 Catalyst preparation

2.1.1 Sulphated zirconia

A series of sulphated zirconia (SZ) catalysts with different SO_4^{2-} loadings were prepared by impregnation of 50 g $\text{Zr}(\text{OH})_4$ with 500 ml $\text{H}_2\text{SO}_{4(\text{aq})}$ of molarity 0.01-0.5 M. The slurry was stirred for 5 h at ambient temperature, filtered and dried at 80 °C overnight, and then calcined at 550 °C for 3 h. Catalysts were stored in air and used without pretreatment.

2.1.2 SBA-15 supported sulphated zirconia

2.1.2.1 Preparation of SBA-15 support

Pure silica mesoporous SBA-15 was synthesised by Dr Gabriel Morales following the procedure of Zhao *et al.*¹ The structure directing agent, Pluronic P123 (100 g) was dissolved in an aqueous solution of 1.9M HCl (3125 ml) with stirring at 40 °C. Then, 191.75 g tetraethyl orthosilicate (TEOS) was added and left for 20 h with agitation at 40 °C. The resulting gel was hydrothermally treated under sealed conditions for 24 h at 100 °C under static condition. The materials were finally recovered by filtration and air-dried overnight. Surfactant was removed by calcination at 550 °C (5 h in static air).

2.1.2.2 Incorporation of zirconia on SBA-15

The primary goal of this preparation method was synthesis of uniformly coated ZrO_2 /SBA-15 materials exhibiting high dispersion and accessibility of zirconium using a layerwise deposition method to minimize growth of large crystallites. Upon preparation of SBA-15 (Section 2.1.2.1), 10 g was dried at 300 °C for 4 h in order to remove physisorbed moisture on the surface of the material. Following this, the dried SBA-15 and 58.5 g of zirconium precursor (70% zirconium propoxide in propanol, Sigma-Aldrich) were added to 300 ml of anhydrous hexane in a 500 ml round bottom flask. The amount of zirconium precursor is based on the number of hydroxyl groups of SBA-15 calculated according to thermal gravimetric analysis. This was to allow individual hydroxyl groups to react with zirconium propoxide and a uniform layer to form on the surface of the parent SBA-15. The mixture was refluxed at 69 °C overnight and then filtered and washed 3 times with hexane in order to remove any unreacted precursor. The material was subsequently rehydrated by addition to 300 ml deionized

water with stirring for 4 h to fully hydrolyse any residual propoxide groups. Finally, the catalyst was filtered and dried at 80 °C overnight. To form additional monolayers, the identical procedure was repeated two more times. A subsequent step of sulfation with H₂SO₄ was made by adding the ZrO₂/SBA-15 catalysts to a 0.075 M aqueous sulphuric acid solution (10 ml acid H₂SO₄ solution per gram sample) for 5 h, after which the sample was filtered and dried at 80 °C overnight. As a final step of the preparation, synthesised materials were calcined at 550 °C for 3 h. These materials were named xML SZ/SBA-15 where xML represents the nominal number of zirconia monolayers (ML) grafted on the surface of SBA-15.

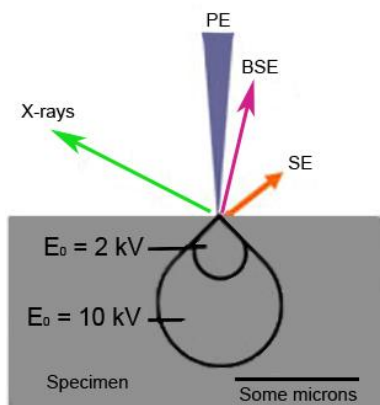
Subsequently, the zirconia grafted SBA-15 (2 grafting cycles) was chosen to study the effect of sulphur content on the characteristics and catalytic performance of ZrO₂/SBA-15. Similar to sulfation of bulk zirconia, each gram of ZrO₂/SBA-15 was added to 10 ml aqueous H₂SO₄ solution with concentrations ranging from 0.01 to 0.25 M and kept under vigorous stirring at ambient temperature for 5 h. Then, it was filtered and dried at 80 °C overnight and finally calcined at 550 °C for 3 h.

2.2 Catalyst characterization

2.2.1 Scanning Electron Microscopy / Energy-Dispersive X-ray spectroscopy

In Scanning Electron Microscopy a beam of electrons is discharged from an electron gun that is located at the top of the microscope. The electron beam gets focused when it passes through a series of condenser lenses and electromagnetic coils and directed to the sample surface. The interaction of Primary Electrons (PE) with the surface of specimen generates three main signals; Secondary Electrons (SE) through inelastic scattering, high energy Backscattered Electrons (BSE) and X-ray radiations. The difference between these signals originates from the difference in volume of the specimen that the primary electrons interacted with according to the energy of the primary electrons (typically between 200 eV and 30 keV). For instance, SE come from a small layer on the surface and yields the best resolution, which can be realized with a scanning electron microscope and can give information relating to the topography of samples; Although, the BSE come from deeper regions of the investigated material thus giving a

lower resolution. A schematic of different type electron and x-ray beams that are generated in a SEM is depicted in **Scheme 2.1**. In addition to imaging by SEM, information about the chemical composition of the material can be acquired by detection of characteristic X-ray radiations from the sample.²



Scheme 2.1: Schematic of primary, secondary and backscattered electron as well as x-ray beam generated in SEM³

In this thesis, chemical compositions of the bulk of sulphated zirconia series and 1, 2, 3 ML SZ/SBA-15 catalysts were investigated by analysis of the generated X-rays on an energy dispersive X-ray (EDX) system attached to a Carl Zeiss EVO-40 electronic microscope at Cardiff University. Samples were mounted on aluminium stubs using adhesive carbon tape. In addition to that, the SZ/SBA-15 samples with different sulphur loadings were analysed on a PHILIPS XL 30 ESEM by Dr Gabriel Morales in Rey Juan Carlos University in Madrid.

2.2.2 Transmission electron microscopy

In transmission electron microscopy (TEM), the wavelength of electrons ($\sim 12.3 \text{ pm}$ at 10 kV decreasing to 2.5 pm at 200 kV) is significantly shorter than both visible and x-ray radiation, enhancing microscope resolution to an atomic level under high resolution TEM/STEM conditions.⁴ An electron beam is focused, through a series of electromagnetic lens, onto the sample with interaction occurring in multiple ways.

Bright field images are formed when a beam of electrons, generated by an electron gun at the top of the instrument, is directed at the sample after passing through one or more condenser lenses. The transmitted, un-deviated beam is focussed and magnified by the objective lens and an image is formed on a phosphorescent screen and digital images are generated by a charge-coupled device.⁵

Standard sample preparation for microscopy was used for the materials. Samples were prepared by dispersion in methanol and drop casting onto a copper grid coated with a holey carbon support film prior to analysis by transmission electron microscopy (TEM) on a PHILIPS TECNAI-20T electronic microscope operating at 200kV at Rey Juan Carlos University.

2.2.3 Inductively Coupled Plasma – Optical Emission Spectrometry

One of the techniques that was employed to analyse the in-bulk composition of the SZ/SBA-15 catalyst was Inductively Coupled Plasma-Optical Emission Spectroscopy (ICP-OES) with a VARIAN VISTA AX apparatus at University of Rey Juan Carlos in Madrid, Spain. Moreover, in order to measure the amount of zirconium dissolved into the solution during the impregnation of Zr/SBA-15 materials by H₂SO₄, upon the completion of the impregnation of SZ/SBA-15 0.05M and SZ/SBA-15 0.25M, the catalysts were filtered off and the remaining solutions were sent off to MEDAC Ltd for liquid ICP analysis.

In this technique, plasma (typically argon) is created through electromagnetic induction into which the aqueous sample is injected. The atoms in the sample will emit radiation of characteristic wavelength upon ionisation in the plasma, which can be quantitatively assessed for elemental analysis. For further information on this technique refer to reference 6.

2.2.4 N₂ porosimetry

Surface area and pore size analysis was performed by N₂ physisorption on a Quantasorb Nova 4000 instrument at 77 K, after outgassing approximately 50 mg of catalyst which was accurately weighed into the sample tube, at 120 °C for at least 2 h. Subsequently, the data was processed using NOVWin software version 2.2. Surface areas were calculated using the Brunauer–Emmet–Teller (BET). BET is an extended version of the Langmuir model. Langmuir assumed that energy of absorption for the first monolayer is generally considerably larger than that of the second and higher layers, thus forming multilayer is only possible at much higher pressures than the pressure required for formation of the first monolayer.⁷ According to BET model, the molecules in the first

layer were assumed to act as sites for the second-layer molecules, and so on to infinite layers. It is also assumed that the adsorption behaviour of all layers above the first monolayer is the same.⁸ Moreover, assuming that the multilayer has an infinite thickness at $p/p^0 = 1$, Brunauer, Emmet and Teller were able to derive their famous BET equation, which is usually expressed in the following linear form⁹:

$$\frac{p}{n(p^0-p)} = \frac{1}{n_m C} + \frac{C-1}{n_m C} \times \frac{p}{p^0} \quad \text{Equation 2.1}$$

Where n is total adsorbed amount of molecules, n_m is the monolayer capacity and C is an empirical constant that is assumed to be exponentially related to the net heat of adsorption (energy of adsorption by the first monolayer minus the energy of adsorption by the subsequent layers) as the following simplified equation:

$$C \approx \text{EXP} \left(\frac{E_1 - E_L}{RT} \right) \quad \text{Equation 2.2}$$

Using the BET method over the range $P/P^0 = 0.03\text{--}0.18$, where a linear relationship was maintained, surface areas were calculated based on the following equation⁷:

$$a_{\text{BET}} = n_m L \sigma \quad \text{Equation 2.3}$$

Where BET surface area is related to n through the effective molecular cross-sectional area, σ , which is equal to 0.162 nm^2 for N_2 at 77 K and L is Avogadro's number.

Pore size distributions were calculated using the Barrett–Joyner–Halenda (BJH) model applied to the desorption branch of the isotherm.

Calculation of the meso-pore distribution of the material can be determined by analysis of the profile of the Type IV adsorption isotherm. As the relative pressure is increased beyond 0.2, a rapid rise in N_2 adsorption is observed as the mesopores saturate by capillary condensation. The pressure required for saturation is dependent on the pore diameter and the radius of curvature of the resulting meniscus formed by the condensed N_2 . The quantitative expression of this phenomenon is given by Kelvin's equation¹⁰ relating the radius of curvature of the meniscus to P/P^0 :

$$r_k = -\frac{2\gamma v_l}{RT} \cos \theta \ln\left(\frac{p}{p^0}\right) \quad \text{Equation 2.4}$$

Where r_k is Kelvis radius which represents the radius of curvature of a hemispherical meniscus, γ is surface tension of condensed phase at temperature T , v_l is the molar volume of the liquid and θ is contact angle of liquid with pore wall which is often considered zero assuming perfect wetting.

In particular case when the pore is cylindrical shape, it would be fair to assume that the condensate has a hemispherical meniscus with radius of r_k . But because there has been already some physisorption taken place, r_k will not be equal to pore radius, r_p . Therefore considering that the multilayer has a thickness of t and assuming the contact angle is zero ($\theta=0$), r_p can be calculated from the following equation:

$$r_p = r_k + t \quad \text{Equation 2.5}$$

Applying this modification to Kelvin equation based on a cylindrical pore model (Equation 2.4) has been a basis for many methods applied for mesopore analysis, including the Barrett–Joyner–Halenda (BJH) method, which is the simplest and by far the most frequently used.⁷

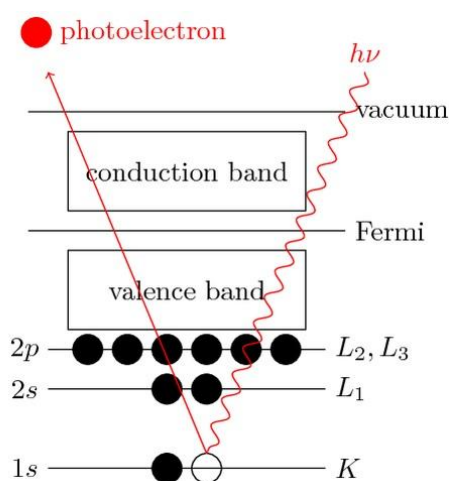
The volume of micropores has been calculated using method developed by Lippens and de Boer which is mostly known as t-plot. In this method, using the surface area calculated from the BET, the amount of adsorbed gas n is plotted versus multilayer thickness t , i.e. the standard multilayer thickness on the reference non-porous material. In other words, the experimental test isotherm is redrawn as a t-curve, i.e. a plot of the volume of gas adsorbed as a function of t , at corresponding p/p^0 . The slope of the linear part of the t-plot, before capillary condensation occurs, equates to the external surface area, and is compared with a standard reference which is a non-porous solid having the same surface structure. In this case p/p^0 over the range 0.2-0.5 was used for t-plot micropore analysis. Deviation from the reference is indicative of micropore filling. Multilayer adsorption will not occur in micropores, thus the micropore volume can be calculated from subtracting the external surface area from the total surface area obtained from the BET method.¹⁰

2.2.5 Thermal Gravimetric Analysis (TGA)

TGA involves the use of microbalance to monitor sample weight loss during thermal processing under an inert gas flow (N_2 or He). When performed in conjunction with differential scanning calorimetry (DSC) detailed information regarding the thermodynamics of sample decomposition and phase changes can be obtained. DSC measurements are typically performed by monitoring the heat flow to/from the sample with reference to an empty sample holder. In this thesis, a Stanton Redcroft STA-780 series of thermal gravimetric instrument was used to monitor the changes to the mass of SBA-15 when temperature rose to 1100 °C with heating rate of 10 °C/min under 20 ml/min flow of nitrogen.

2.2.6 X-ray Photoelectron Spectroscopy (XPS)

X-ray photoelectron spectroscopy is a technique that provides qualitative and quantitative information about various components in the external surface layers (2 to 10 nm) of catalyst and is able to provide information about the chemical environment of the studied sample. Furthermore, it can reveal the degree of oxidation or electronic state of the various elements. Using this method all elements can be detected with the exception of hydrogen and helium. In XPS analysis, the sample to be studied is exposed to an X-ray photon beam. Usually, the $K\alpha$ emission of Al ($h\nu = 1486.6$ eV) or Mg ($h\nu = 1253.6$ eV) are used.¹¹ As a result of this impact, a photoelectron is ejected leaving behind a core hole (see **Scheme 2.2**).



Scheme 2.2: Schematic diagram of the XPS process, showing photoionization of an atom by the ejection of a 1s electron

This creates an excited ionic state, which then relaxes into the final ground state as outer electrons fill the core holes.¹² The kinetic energy of ejected photoelectron is detected in XPS. The measured kinetic energy E_k , is directly related to the electron binding energy, E_B , of the various orbitals involved as shown in **Equation 2.6** and it can be used to identify the elements. The binding energy of a core electron is affected by chemical bonding and changes in oxidation state of the atom which results in a chemical shift in the detected photoelectron kinetic energy. In other words, if the positive charge on the atom is increased through electron withdrawing species bound to the surface or increased oxidation state, the binding energy of the core electron is also increased.¹³

$$E_k = h\nu - E_B \quad \text{Equation 2.6}$$

$h\nu$ is the energy of the incoming photon, E_B the initial binding energy. Once a photoelectron has been emitted, the ionized atom must relax in some way. Relaxation of the excited ionic state to fill the core hole can lead to two final states due to spin-orbit coupling shown in **Equation 2.7**.

$$j = l + s \quad \text{Equation 2.7}$$

For one unpaired electron, $s = \pm\frac{1}{2}$ and the orbital angular momentum $l = 0, 1, 2, 3...$ corresponding to s, p, d, f... orbitals. Hence for a state where $l > 0$ and there is one unpaired electron, a doublet peak will be observed. For example, analysis of the Zr 3d state will result in doublet peaks corresponding to $3d_{5/2}$ and $3d_{3/2}$ states.

XPS is also a powerful tool for probing information about the film thickness of a material. Here the relative angle between the emitted electrons and the analyser can play a major role. As demonstrated by **Figure 2.1**, two spectra of an oxidised silicon wafer are recorded at normal and grazing emission. Recording the spectra at normal emission, keeps the analysis at its least surface sensitivity and probes the furthest into the bulk of the sample. In this scenario, if the film is sufficiently thin, the signal will be aroused from both sub-surface and surface Si atoms. Surface sensitivity can be enhanced by recording spectra at greater grazing emission, therefore the emitted electrons from sub-

surface Si have to travel a longer distance in order to emerge and thus the signal from sub-surface Si atoms attenuated.¹⁴

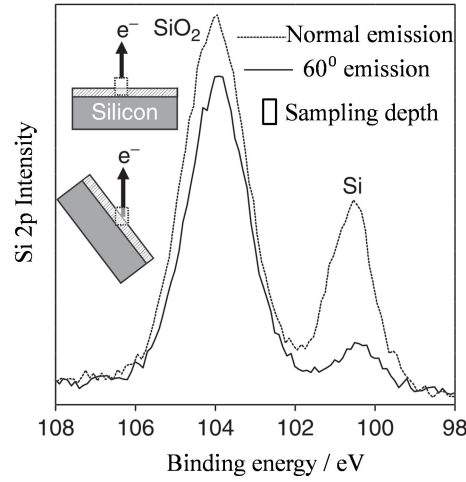


Figure 2.1: Angular resolved XP spectra of an oxidised silicon wafer¹⁴

Calculation of thickness requires knowledge of film density, a parameter that may not be constant across the film depth and may not be equal to known bulk values. Moreover, the situation is complicated by the fact that not all electrons emitted by the sample escape to be detected, but some can be inelastically scattered within the sample. Thus, the probability of detecting an electron originating from a specific depth in the sample falls off exponentially with depth.¹⁵

The attenuation of the underlying silicon components could give an estimation of the oxide film thickness (d) calculated from the following equation:

$$I_d = I_0 \exp\left(\frac{-d}{\lambda \cos\theta}\right) \quad \text{Equation 2.8}$$

where I_d is the intensity of the underlying substrate signal, I_0 is the intensity of the clean surface, λ is the inelastic mean free path (IMFP) of the photoelectron and θ is the angle between the analyser and the surface normal, where $\theta = 90^\circ$ is normal to the surface.^{14,}

¹⁵

Throughout this study XPS measurements were performed using a Kratos Axis HSi photoelectron spectrometer equipped with a charge neutralizer and a Mg K α X-ray source ($h\nu = 1253.6$ eV) and monochromated Al K α ($h\nu = 1486.6$ eV). Using Mg source, high resolution spectra were recorded with analyser pass energy of 20 eV and

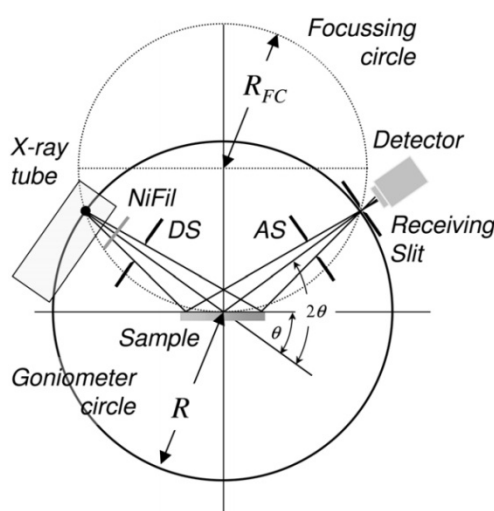
and 80 eV for survey scans while for the monochromated Al source analyser pass energy of 40 eV for high resolution and 160 eV for survey scans were employed. Also X-ray power of 225 W was used.

2.2.7 Powder X-Ray Diffraction (XRD)

Powder X-Ray diffraction (XRD) is a rapid analytical technique primarily used for phase identification of a crystalline material and can provide information on unit cell dimensions. This technique is based on the fact that when x-rays interact with a crystalline substance, a diffraction pattern can be obtained because of similarity in the distance between atoms and X-ray wavelengths. According to Bragg's law, the angle at which the x-ray is diffracted is dependent on the wavelength of the x-ray beam and the distance between lattice planes. This is mathematically explained by Bragg's equation (Equation 2.9)¹⁶:

$$\lambda = 2d\sin\theta \quad \text{Equation 2.9}$$

Where λ is the wavelength of the x-ray source, θ is the diffraction angle and d is the glancing angle between the incident X-ray and the lattice plane. A simple schematic of the experimental setup for powder XRD is shown in **Scheme 2.3**.



Scheme 2.3: Schematic setup of X-Ray Diffraction instrument¹⁷

Because of complexity of XRD patterns, having it obtained, it should be compared with a reference sample or database in order to identify the crystal phase. The volume-

averaged sizes of the crystalline particles in a solid material can also be determined for the most intense peaks in the patterns using the Scherrer formula (**Equation 2.10**).^{18, 19} In this equation the width of an individual X-ray reflection is inversely related to the size of the crystallites.

$$L = \frac{K\lambda}{B(2\theta) \cos \theta} \quad \text{Equation 2.10}$$

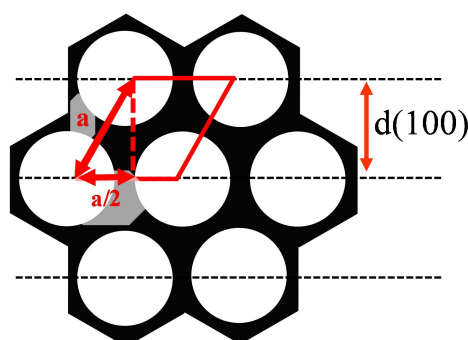
Where L = crystallite size in Å, K is a dimensionless shape factor, λ = incident wavelength in Å, θ = position of peak maximum in degrees and $B(2\theta)$ = peak full width at half maximum (FWHM) in radians. Moreover, the Bragg's law can be used to obtain the lattice spacing of a particular cubic system through the following relation:

$$d = \frac{\lambda \sqrt{(h^2 + k^2 + l^2)}}{2 \sin \theta} \quad \text{Equation 2.11}$$

Where d is layer spacing, λ is Wavelength of Cu K_α radiation (0.1541nm), h , k and l are Miller indices and θ is diffraction angle. Upon calculation of layer spacing, the unit cell size (or pore spacing) could be calculated using the following equation

$$a = \frac{2d_{(100)}}{\sqrt{3}} \quad \text{Equation 2.12}$$

Furthermore, as it is illustrated in **Scheme 2.4**, if the pore diameter is measured (for example, by means of N_2 porosimetry) the wall thickness could be calculated by subtracting pore diameter from unit cell size.



Scheme 2.4: Schematic representation of cross sectional SBA-15 pore channels, layer spacing and unit cell²⁰

In this thesis, XRD patterns were recorded on a Panalytical X'pert-Pro diffractometer fitted with an X'celerator detector or Bruker d8 advance fitted with LYNXEYE multi-channel detector; using Cu K α (1.54 Å) sources with a nickel filter, calibrated against Si standards. The patterns were obtained by measuring the diffracted X-ray beam intensity as a function of angle. Low angle patterns were recorded over a range of $2\theta = 0.45\text{--}8^\circ$ (step size 0.01° , time per step 0.6 s) and wide angle patterns over a range of $2\theta = 10\text{--}80^\circ$ (step size 0.02° , time per step 1 s).

2.2.8 Vibrational spectroscopy

2.2.8.1 Diffuse Reflection Infrared Fourier Transform Spectroscopy (DRIFTS) and *in situ* pyridine chemisorption

Diffuse reflectance infra-red Fourier transform spectroscopy (DRIFTS) is a surface sensitive infra-red spectroscopic technique. In DRIFTS, the infrared beam is focussed onto the sample where it can interact with the material in several different ways. The beam can be scattered or reflected from neighbouring particles in the sample, or transmitted through particles, after which the beam can be scattered or reflected once more. The absorption of infra-red radiation excites the vibrational modes of bonding moieties in molecular species. IR radiation that is not absorbed by the sample reaches a detector, and the functionalities in the sample can be identified.²¹

Titration of the surface of catalyst with probe molecules is a powerful technique for quantitative analysis of surface acidity (and basicity) of solid catalysts. NH₃, pyridine, CH₃CN, NO or CO are the most well-known probe molecules for characterization of nature of acid sites by DRIFTS. Among these probe molecules, pyridine has been preferred as an IR probe molecule of finely divided metal oxide surfaces since it is (i) more selective and stable than NH₃; (ii) much more strongly adsorbed than CO and CH₃CN; and (iii) relatively more sensitive to the strength of Lewis acid sites than NO.^{22,}

23

DRIFT spectra were obtained using a Nicolet Avatar 370 MCT with Smart Collector accessory, mid/near infrared source and mercury cadmium telluride (MCT-A) photon detector at -196°C (liquid N₂). Samples were diluted with KBr powder (10 wt% in KBr) for analysis then loaded into an environmental cell and subjected to additional

drying under vacuum at 110 °C for 10 min prior to measurements to remove moisture physisorbed during air exposure. Samples were scanned between 4000 and 650 cm^{-1} *in vacuo* at a resolution of 4 cm^{-1} . *In situ* pyridine adsorption was performed by exposure of samples to pyridine vapour in a desiccator overnight. Excess physisorbed pyridine was removed in a vacuum oven prior to sample loading in the environmental cell, with spectra recorded at 25 °C *in vacuo*.

2.2.8.2 Raman spectroscopy

On a similar basis to DRIFTS, Raman spectroscopy provides a means of crystallography. In Raman spectroscopy, an electron is excited to a virtual state by the incident photon, and relaxes to a vibrationally excited state, resulting in an overall process equivalent to direct excitation to the final state via IR.⁸ In the present work, Raman spectra were obtained on a Renishaw Ramascope fitted with a 785 and 514 nm lasers. The spectra were recorded in the range of 0–1350 cm^{-1} using 514 nm source, 5x lens, 2 second exposure time, 100 accumulation and 100 % laser power.

2.2.9 Measurement of acidity and basicity by microcalorimetry and TPD

Many techniques have been reported for the measurement of acid-base properties; adsorption microcalorimetry is particularly valued for giving an explicit description of the strength, number and distribution of sites and by selection of the adsorbing gas, acidic or basic properties can be measured.^{24, 25}

In this work, measurements of enthalpy of adsorption and acid and base sites content of SZ/SBA-15 materials and also enthalpy of adsorption and acid site loading of bulk SZ catalysts were carried out by Dr Marta Granollers at the University of Huddersfield via flow adsorption calorimetry of NH_3 followed by Temperature Programmed Desorption (TPD) on a Setaram DSC111 system connected to gas flow and switching systems. However, for studying the basicity of SBA-15 supported sulphated zirconia catalysts, SO_2 was used as probe molecule. Samples were outgassed at 450 °C under flowing N_2 (10 ml min^{-1}) for 2 h prior to pulse titration at 150 °C. Gas flow rates were controlled by automated mass flow controllers. The sample (15-25 mg) was held on a glass frit in a vertical silica glass sample tube in the calorimeter. A steady 10 ml min^{-1} flow of N_2 was

maintained across the sample for 3 h at 150 °C to effect activation. A sequence of 10 probe gas pulses (1% of probe gas in N₂) were delivered to the carrier gas stream from a 2 ml sample loop for NH₃ using a two position Valco valve with an automated micro-electric actuator. Heat output associated with interaction between the probe gas and the sample was detected by DSC, and the concentration of the probe molecules in the gas flow downstream of the DSC was measured with a HPR 20 Hiden MS gas analyzer via a heated capillary at 175 °C. A pulse delay of 90 min for NH₃ was employed to allow reversibly adsorbed probe gas to desorb back into the pure N₂ stream and/or redistribute on the sample, and for baselines to stabilize. To complement the calorimetry data, after adsorption of ammonia/SO₂, temperature programmed desorption (TPD) was carried out. TPD consisted in increasing the temperature from 150 °C to 400 °C at 5 °C min⁻¹ followed by a hold of 1 h at 400 °C. The amount of ammonia/SO₂ desorbed from the samples was then determined by comparing MS signal of the TPD experiment with a signal recorded during a control experiment by passing a calibrated pulse through a blank sample tube.

Base site titration of bulk sulphated zirconia samples (SZ) was performed on a Quantachrome Chembet 3000 and analysis using TPRWin software by outgassing approximately 50 mg of the sample at 100 °C for 2 h followed by pulsing 50 µL doses of carbon dioxide onto the sample at 40 °C until achieving total saturation of the available basic sites. Complete base-site titration was determined by monitoring the carbon dioxide level in the gas stream after passing through the sample until the size of three consecutive pulses were the same, indicating the surface of sample is saturated with CO₂ and no more carbon dioxide was being chemisorbed. TPD of the carbon dioxide saturated samples was subsequently performed on the same instrument by heating the titrated samples under flowing helium gas at 5 °C/min to the required temperature. On heating the sample, carbon dioxide adsorbed on the surface desorbs and flows to the detector. The temperature at which desorption occurs is related to the strength of carbon dioxide adsorption and, therefore, surface base site strength.

2.3 Catalytic testing

2.3.1 Dehydration of saccharides

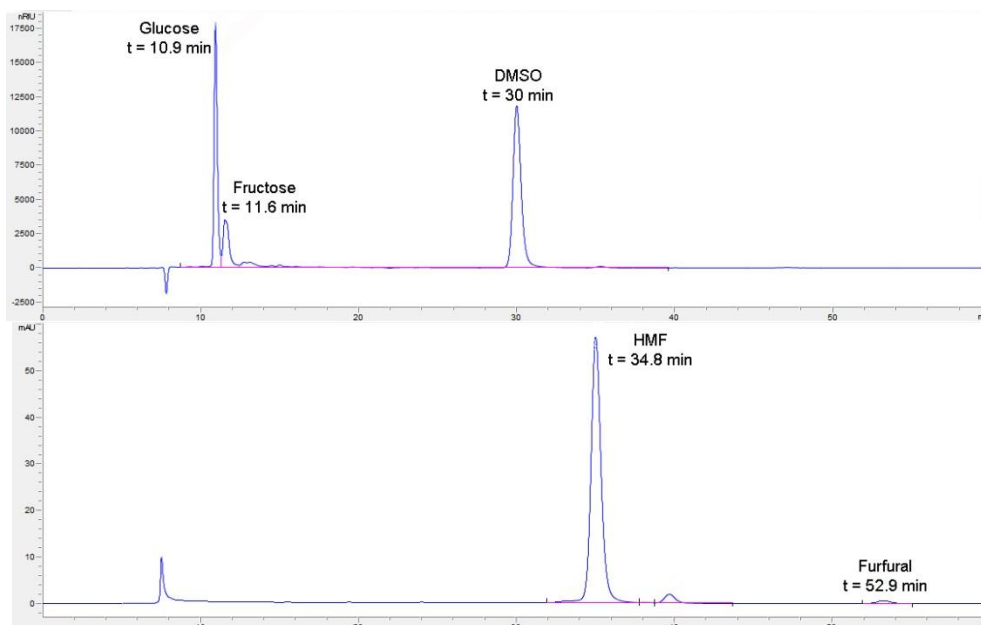
Initial kinetic studies of glucose, fructose and xylose conversion were conducted on a Radleys Starfish carousel under stirred batch conditions at 100 °C to facilitate detailed reaction profiling and minimise side reactions. Reactions were performed using 0.1 g reactant, 0.1 g catalyst, and 20 ml deionised water. Samples were withdrawn periodically and filtered prior to analysis on an Agilent 1200 series HPLC equipped with RI and diode array detectors and a Hi-Plex H column for analysis. A 5 mM aqueous solution of sulphuric acid was used as the eluent phase, with a flow rate of 0.6 ml min⁻¹ and 65 °C column temperature. Product yields were calculated from response factors determined from multi-point calibration curves. List of compounds that the HPLC was calibrated for and their response factors are given in **Table 2.1** and **2.2**. Also a representation of typical HPLC chromatograms from glucose and fructose dehydration are demonstrated in **Figure 2.2** and the calibration curves are shown on **Figure 2.3**.

Table 2.1: List of compounds detected by refractive index detector on HPLC

Compound	Detector	Retention time min	Response factor M (nRIU.s) ⁻¹
Cellobiose	RI	9.1	3.537E-08
Glucose (Low concentration)	RI	10.9	6.765E-08
Glucose (High concentration)	RI	10.9	6.739E-08
Xylose	RI	11.5	8.323E-08
Fructose	RI	11.6	7.006E-08
Xylulose	RI	12.0	7.011E-08
Lyxose	RI	12.0	8.675E-08
AHG	RI	14.1	8.503E-08
Formic acid	RI	15.9	7.157E-07
Acetic acid	RI	17.4	4.485E-07
Dimethyl sulfoxide	RI	30.0	-

Table 2.2: List of compounds detected by diode array detector on HPLC

Compound	Detector	Retention time min	Response factor M (mAU.s) ⁻¹
Xylulose	DA	11.8	1.598E-04
Levulinic acid	DA	18.3	1.821E-04
HMF	DA	34.8	1.333E-07
Furfural	DA	52.9	1.705E-07

**Figure 2.2:** A sample of typical HPLC chromatograms dehydration of glucose in water from (top) RI detector and (bottom) DA detector

Furthermore, yields and selectivity were calculated on a carbon basis as below:

$$Yield [\%] = \frac{\text{moles of carbon in product}}{\text{moles of carbon in reactant at } t=0} \times 100 \quad \text{Equation 2.13}$$

$$Selectivity [\%] = \frac{\text{yield}}{\text{reactant conversion}} \times 100 \quad \text{Equation 2.14}$$

Carbon balance is calculated based on moles of carbon in the identified products, relative to moles of carbon atoms in the glucose converted.

$$\frac{C_{out}}{C_{in}} [\%] = \frac{\Sigma(\text{Moles of C in products and remaining reactant})}{\text{Moles of C in reactant at } t=0} \times 100 \quad \text{Equation 2.15}$$

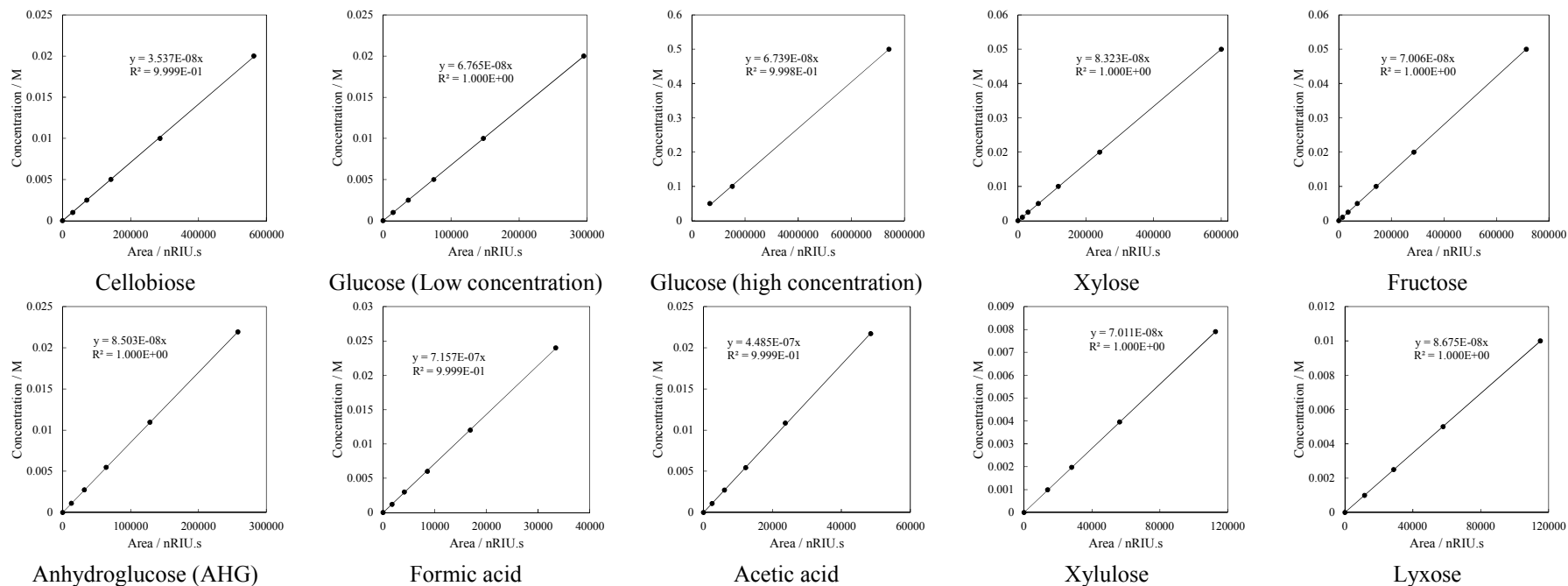


Figure 2.3: Calibration of reactants and potential products detected by Refractive Index detector on HPLC

Rate of reactions were determined from the initial linear portion of the profile of conversion ($t < 3$ h). Turnover frequency (TOF) was obtained by normalizing the rate of reaction with the mass of catalyst as well as the acid site concentration determined from NH_3 TPD. Similarly rate of formation of HMF was measured. However, usually TOF is defined as reactant molecules converted per active site per unit time, HMF TOF is a representation of HMF formation rate normalized with mass of catalyst and acid site concentration.

2.3.1.1 Leaching test

Leaching tests on the samples were performed in a stirred Radley's batch reactor in order to determine the extent of homogeneous reaction occurring during the dehydration of fructose. The reactors (glass round bottom flasks) were charged with 0.1 g fructose and 20 ml deionized water and then heated to 100 °C. Subsequently, 0.1 g of catalyst was added to the mixture and stirring was started. After 1 h the solutions were filtered hot and the leachate was returned to a clean reactor and non-catalytic reaction was continued for 5 h under stirring at 100 °C. Samples of the reaction mixture were taken at time zero (at room temperature and before adding the catalyst), before and after filtration and also at the end of the test and then analysed on HPLC.

2.3.1.2 Recyclability test

Catalyst recyclability was assessed for 2 consecutive reactions. After 6 h (and 24 h in case of bulk SZ catalyst) glucose dehydration reaction, the catalyst was recovered by filtration and then reactivated by calcination at 550 °C for 3 h in static air. The first reaction was conducted using the standard protocol (0.1 g glucose, 0.1 catalyst and 20 ml water). Due to loss of material during catalyst recovery, the 2nd reaction was carried out on half normal scale using 0.05 g glucose, 0.05 g recovered catalyst and 10 ml deionized water.

2.3.1.3 Hydrothermal stability test

To examine the hydrothermal stability of SBA-15 and Zr grafted SBA-15 a Parr compact reactor 5513 model was used. The reactor was charged with 30 ml deionized water and 0.1 g catalyst. Then, it was sealed and heated to 170 °C and kept under vigorous stirring for 6 h. Following reaching the set point temperature, ~7 bar self-

generated pressure was observed on the pressure gauge. Upon the completion of the test, the reactor was cooled down to the room temperature and the catalyst was recovered by filtration and then dried at 80 °C overnight and subsequently its textural properties was analysed by N₂ porosimetry and XRD.

2.3.2 Esterification of free fatty acids

2.3.2.1 Studying the effect of FFA alkyl chain length and alcohol type

Esterification reactions were performed using a Radleys Carousel Reactor Station at atmospheric pressure. 6.25 cm³ alcohol (methanol, ethanol, 1-propanol or 1-butanol), 5 mmol of propionic (C₃), hexanoic (C₆), lauric (C₁₂) or palmitic (C₁₆) acid, and 1.25 mmol of dihexylether (as an internal standard) were added to a sealed glass reactor tube under stirring at 60 °C. 0.025 g of catalyst was subsequently introduced, and aliquots of the reaction mixture periodically withdrawn and filtered and diluted with dichloromethane for analysis on a GC. C₃ and C₆ acid esterification was monitored using a Varian 450-GC equipped with a Phenomenex ZB-5HT Inferno 15 m × 0.32 mm × 0.10 µm while analysis of reaction products from lauric and palmitic acid esterification employed a 1079 programmable, direct on-column injector and Phenomenex ZB-1HT Inferno 15 m × 0.53 mm × 0.15 µm capillary column. All catalytic profiles are an average of 3 injections per sample. Throughout this thesis, when talking about esterification reaction, conversion refers to conversion of the free fatty acid and not the alcohol. Initial rates were calculated over the first three hours of reaction, wherein conversion profile was linear (**Figure 2.4**). Turnover frequencies (TOF) were determined from the initial reaction rate which was normalized to the acid site concentration determined from NH₃ titrations.

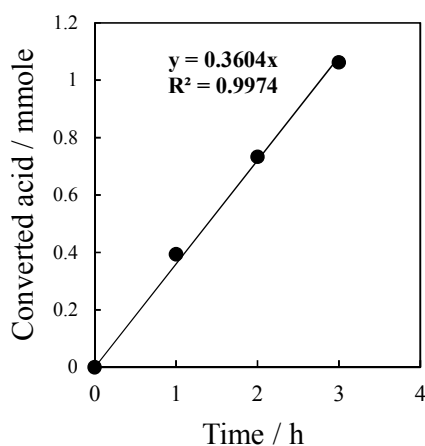


Figure 2.4: Linear portion of a reaction profile for esterification of propionic acid with methanol over SZ/SBA-15 0.25M for the calculation of initial activity

2.3.2.2 Leaching test

To assess the level of homogeneous catalysis contribution due to potential leaching of sulphur species from bulk SZ and SBA-15 supported materials into reaction mixture, two separate experiments were conducted. The experiments were started following the normal esterification reaction protocol (5 mmol propionic acid, 6.25 ml methanol, 25 mg catalyst, 60 °C). After an hour the reaction mixture hot filtered and the reaction was continued in absence of catalyst for 23 h.

2.4 List of chemicals

All chemical compounds that were used throughout this project are listed in **Table 2.3** along with the purity of them and the name of suppliers.

Table 2.3: List of chemicals, their purity and the suppliers

Compound	Purity	Supplier
1,6-Anhydro- β -D-glucose	99%	Sigma-Aldrich
1-Butanol	$\geq 99.4\%$	Sigma-Aldrich
1-Propanol	$\geq 99\%$	Fisher
Acetic acid	$\geq 99.7\%$	Sigma-Aldrich
D-Cellobiose	$\geq 98\%$	Sigma-Aldrich
D-Fructose	$\geq 99\%$	Sigma-Aldrich
D-Glucose	$\geq 99.5\%$	Sigma-Aldrich
Dichloromethane	$\geq 99.8\%$	Fisher
Diethyl ether	97%	Sigma-Aldrich
Dimethyl sulfoxide	99.7%	Sigma-Aldrich
D-Lyxose	$> 99\%$	Carbosynth
D-Xylose	$\geq 99\%$	Sigma-Aldrich
D-Xylulose	$> 98\%$	Carbosynth
Ethanol	$\geq 99.8\%$	Fisher
Formic acid	$\geq 95\%$	Sigma-Aldrich
Furfural	99%	Sigma-Aldrich
HCl	35% in water	Scharlau
Hexane (anhydrous)	95%	Sigma-Aldrich
Hexane fraction from petroleum		Fisher
Hexanoic acid	$\geq 99.5\%$	Sigma-Aldrich
Hydroxymethylfurfural	$\geq 99\%$	Sigma-Aldrich
Lauric acid	$\geq 98\%$	Sigma-Aldrich
Levulinic acid	$\geq 97\%$	Sigma-Aldrich
Methanol	$\geq 99.8\%$	Fisher
Palmitic acid	$\geq 99\%$	Sigma-Aldrich
Poly(ethylene glycol)-block-poly(propylene glycol)-block-poly(ethylene glycol)		Sigma-Aldrich
Propionic acid	$\geq 99.5\%$	Sigma-Aldrich
Sulfuric acid		Sigma-Aldrich
Tetraethyl orthosilicate (TEOS)	98%	Sigma-Aldrich
Zirconium(IV) propoxide solution	70 wt % in 1-propanol	Sigma-Aldrich
Zr(OH) ₄		MEL chemicals

2.5 References

1. D. Zhao, J. Feng, Q. Huo, N. Melosh, G. H. Fredrickson, B. F. Chmelka and G. D. Stucky, *Science*, 1998, **279**, 548-552.
2. L. Reimer, *Measurement Science and Technology*, 2000, **11**, 1826.
3. Austrian Centre for Electron Microscopy and Nanocatalysis, *The principles of SEM and Microanalysis*, <http://portal.tugraz.at/portal/page/portal/felmi/research/Scanning%20Electron%20Microscopy/Principles%20of%20SEM>, Accessed September, 2014.
4. T. G. Rochow and P. A. Tucker, *Introduction to microscopy by means of light, electrons, X-rays, or acoustics*, Springer, 1994.
5. S. L. Flegler, J. W. Heckman, K. L. Klomparens, K. L. Klomparens and K. L. Klomparens, *Scanning and transmission electron microscopy: an introduction*, WH Freeman New York, 1993.
6. X. Hou and B. T. Jones, in *Encyclopedia of Analytical Chemistry*, John Wiley & Sons, Ltd, 2006.
7. F. Rouquerol, J. Rouquerol and K. Sing, Academic Press, London.
8. G. Ertl, H. Knozinger, F. Schuth and J. Weitkamp, Wiley Online Library.
9. S. Brunauer, P. H. Emmett and E. Teller, *Journal of the American Chemical Society*, 1938, **60**, 309-319.
10. P. A. Webb and C. Orr, *Analytical methods in fine particle technology*, Micromeritics Instrument Corp, 1997.
11. J. Lynch, *Physico-chemical analysis of industrial catalysts: a practical guide to characterisation*, Editions Technip, 2003.
12. J. F. Watts, *Surface science techniques*, Elsevier Science, UK, 1994.
13. K. K. Kolasinski, *Surface science: foundations of catalysis and nanoscience*, John Wiley & Sons, 2012.
14. D. W. Bruce, D. O'Hare and R. I. Walton, *Local Structural Characterisation: Inorganic Materials Series*, John Wiley & Sons, 2013.
15. D. F. Mitchell, K. B. Clark, J. A. Bardwell, W. N. Lennard, G. R. Massoumi and I. V. Mitchell, *Surface and Interface Analysis*, 1994, **21**, 44-50.
16. P. Atkins and J. De Paula, *Atkins' physical chemistry*, Eighth edn., Oxford University Press, Oxford, 2006.
17. M. Birkholz, *Thin film analysis by X-ray scattering*, John Wiley & Sons, 2006.

18. H. Itoh, S. Utamapanya, J. V. Stark, K. J. Klabunde and J. R. Schlup, *Chemistry of Materials*, 1993, **5**, 71-77.
19. R. J. Matyi, L. H. Schwartz and J. B. Butt, *Catalysis Reviews*, 1987, **29**, 41-99.
20. M. Keppeler, J. Holzbock, J. Akbarzadeh, H. Peterlik and N. Hüsing, *Beilstein journal of nanotechnology*, 2011, **2**, 486-498.
21. H. Günzler and H.-U. Gremlich, *IR spectroscopy. An introduction*, Wiley-VCH, Weinheim, Germany, 2002.
22. T. Barzetti, E. Selli, D. Moscotti and L. Forni, *Journal of the Chemical Society, Faraday Transactions*, 1996, **92**, 1401-1407.
23. M. I. Zaki, M. A. Hasan, F. A. Al-Sagheer and L. Pasupulety, *Colloids and Surfaces A: Physicochemical and Engineering Aspects*, 2001, **190**, 261-274.
24. P. F. Siril and D. R. Brown, *Journal of Molecular Catalysis A: Chemical*, 2006, **252**, 125-131.
25. S. P. Felix, C. Savill-Jowitt and D. R. Brown, *Thermochimica Acta*, 2005, **433**, 59-65.

Chapter 3

**Bifunctional $\text{SO}_4^{2-}/\text{ZrO}_2$ catalysts for production
of platform chemicals from biomass-derived
sugars**

3.1 Introduction

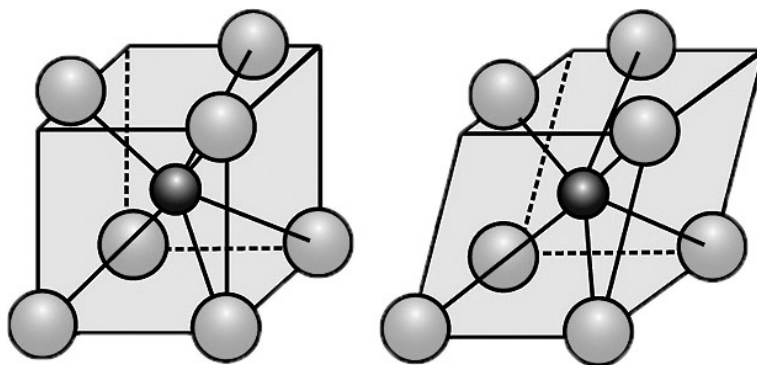
3.1.1 Sulphated zirconia

Zirconium oxide, ZrO_2 , is a very interesting material for catalytic applications because of its thermal and hydrothermal stability and excellent mechanical properties. Moreover, zirconium oxide is claimed to be the only catalyst whose surface possesses four chemical properties: acidic, basic, oxidizing and reducing properties.¹ In the early eighties, it was discovered that when ZrO_2 was sulphated with either sulphuric acid or ammonium sulphate and subsequently calcined, a remarkable increase in the surface acidity and catalytic activity for carbenium ion reactions occurred.² Since then, sulphated zirconia (SZ) has been employed in a wide range of industrial processes such as Friedel–Crafts alkylation, acylation, condensation, esterification, etherification, isomerization, nitration, cracking, dehydration, oligomerization, etc. The application of SZ as a catalyst for these reactions is not only industrially important, but is also of academic interest because the exact functioning of this catalyst is yet to be fully understood.³

3.1.1.1 Crystallinity

The zirconia crystal structure itself may play an important role in determining the final reactivity of SZs. Crystalline SZs are highly active, whereas amorphous forms are essentially inactive, hence controlling the crystallisation process via calcination is an important step in regulating the catalytic activity. A number of parameters have been identified as central to the generation of strong acid sites⁴, specifically that zirconia should be in tetragonal phase, the sulphate loading should be sufficient to complete a monolayer, and the calcination temperature should lie between 550 and 700 °C.

It appears that one of the key points related to SZ is the amount of tetragonal-phase zirconia in the sulphated zirconia^{5, 6}, (**Scheme 3.1**) as the catalytic activity is higher when the amount of tetragonal phase is larger.^{5, 6} This tetragonal phase appears to be stabilized by the sulphate groups on the surface which prevent sintering of the zirconia framework.^{7, 8} This also results in an increase in surface area of the sulphated material. The reason for this could be that the tetragonal phase has a higher content of nonbridging surface hydroxyl groups than the monoclinic phase and this seems to be a crucial factor for producing active materials.⁹



Scheme 3.1: Structure of tetragonal (left) and monoclinic (right) zirconia crystal¹⁰

Pure zirconia exhibits a number of polymorphs, crystallising in tetragonal form at 500 °C and transforming to the monoclinic form at higher temperatures, with 100% transformation at ~900 °C. The strong acid properties of SZ are formed following sulphate adsorption onto amorphous zirconia, and subsequent calcination in air to convert them into crystalline forms¹¹, i.e. via the interaction between the oxide surface and the sulphate ions.¹² Sulphate addition retards the tetragonal crystallisation of amorphous zirconia, and the subsequent tetragonal to monoclinic phase transformation^{13, 14}: SZ remains purely tetragonal after calcination at 700 °C following thermal degradation of the sulphate groups whereas zirconia presents a mixture of tetragonal and monoclinic phases at this temperature.

3.1.1.2 Acidity

There is much debate over the acid strength of SZ, with some studies using Hammett indicators revealing materials with H_0 values of -16 (c.f. $H_0 = -12$ for 100% H_2SO_4) leading to claims they are ‘super-acidic’. However, this finding has been queried by some researchers who suggest that the Hammett titration method is not suitable for solid acids^{8, 15} and that theoretical calculations, UV, *in situ* NMR and H/D exchange experiments indicate SZ in fact only possesses acidity comparable to sulphuric acid. A better means of evaluating the strength of solid acids is to study their efficiency in the isomerization of linear small alkanes (usually n-butane). SZ is remarkable in effecting the isomerization of n-butane at room temperature, revealing its true superacidic nature. In general, superacidity of SZ is attributed to the Lewis acid sites which predominate at high temperatures or under anhydrous/apolar reaction conditions.

3.1.1.3 Active phase

The actual nature of the catalytic centres, as well as the mechanism through which the catalytic centers are produced, is still the subject of debate.¹⁶ It is a general consensus that properly activated sulphated metal oxides contain both Brønsted and Lewis acid sites. Discrepancies can be found regarding the predominant role played by a particular site or even by the coupled Brønsted plus Lewis sites with respect to the final activity showed by these materials.^{9, 17-22} As an example, for models showing the possibilities of sulphated zirconia acting as a Brønsted acid, Lewis acid and Brønsted plus Lewis acid²³ see **Figure 3.1**.

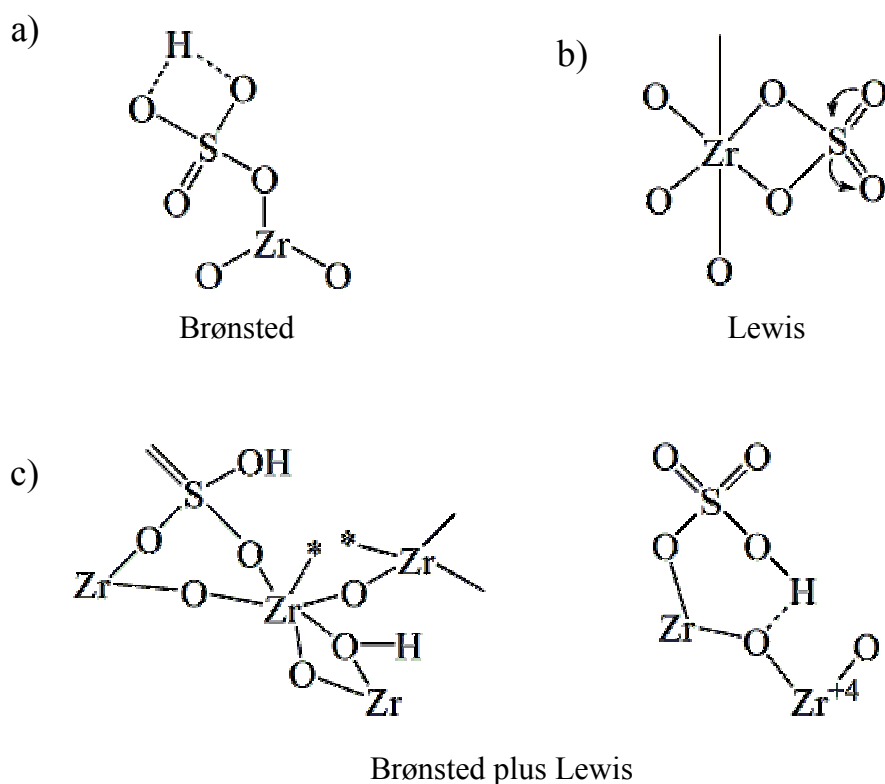


Figure 3.1: Acid sites on sulphated zirconia. (a) Brønsted, (b) Lewis and (c) Brønsted plus Lewis sites.

The S=O double bond nature in the sulphate complex is much stronger than that of a simple metal sulphate; thus, the Lewis acid strength of Zr^{4+} becomes remarkably greater by the inductive effect of S=O in the complex, as illustrated by arrows. (**Figure 3.2**) In the presence of water, the Lewis acid sites are converted to Brønsted acid sites via proton transfer. By means of CO adsorption, the analogous model was proposed by Bolis *et al.*, but in their case H_2O dissociates on sites involving strongly acidic Zr^{4+} cations, next to a sulphate group; an interaction gives rise to a bridged OH group and to a protonated sulphate.⁴

A number of other studies attempted to determine the nature of acid sites in the catalyst. Tanabe and co-workers^{24, 25} proposed one of the most widely accepted models of the surface, wherein the sulphate bridges across two zirconium atoms (**Figure 3.2**). This model accounts for the formation of Brønsted sites as a result of adsorbed water molecules, acting as weak Lewis base on the Lewis acid site, which is verified by IR studies and finds widespread support.²⁶⁻²⁸ However, in the Arata and Hino model the formation of Lewis-type sites is solely attributed to the highly covalent character of the adsorbed sulphate, with the Brønsted sites arising due to residual amounts of water.²⁷

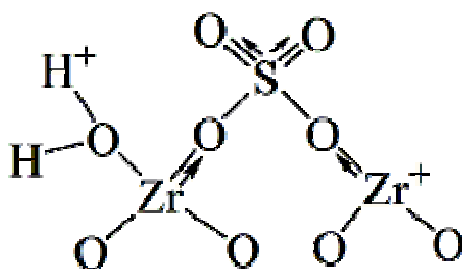


Figure 3.2: Model of SZ surface proposed by Tanabe and co-workers²⁴

This model (**Figure 3.2**), a chelating bidentate, was also proposed by Ward and Ko, but in this case a hydroxyl group is bonded to a Zr atom adjacent to the Zr chelated with a sulphate species; thus, the proton is strengthened by the electron inductive effect of two S=O bonds in the sulphate group.¹³ Morrow and co-workers showed a structure, in the experiment of ¹⁸O exchange using H₂¹⁸O in addition to IR analysis, in which three oxygens of the sulphate are bonded to Zr elements in a tridentate form, whereas in the presence of H₂O the sulphate species is converted to a bridged bidentate sulphate, accounting for the Brønsted acidity.²⁹ They also proposed the formation of a polysulphate structure with a high sulphate loading.³⁰ This polysulphate structure was supported by Morterra *et al.* using IR data of adsorbed pyridine.³¹ A monodentate structural model, which contains a bisulphate group, has been proposed by several workers.^{22, 23} The bisulphate OH group is hydrogen-bonded to an oxygen atom on the surface of zirconia. A similar model was, recently, pointed out for the surface of sulphated alumina on the basis of NMR studies.³² Another bisulphate structure was proposed by Riemer *et al.* using NMR and Raman spectroscopies in which two oxygens are bonded to Zr atoms in a bridged bidentate state.³³ The strong Brønsted acidity based on the OH group originates from the electron withdrawing effect of neighboring Zr

ions. The same model was also proposed by Lunsford and Clearfield, who suggested that electrons are withdrawn through S–OH to adjacent Zr.^{20, 34}

A similar scheme to describe Brønsted acid site generation was proposed by Kustov *et al.*²², wherein bisulphate anions substitute for terminal ZrOH species thereby enhancing the acid strength of the remaining bridging ZrOH groups. In both ionic and covalent models it is evident that Lewis and Brønsted acid sites are readily interchangeable following the adsorption/desorption of water molecules.^{11, 34} This is important since the catalytic activity of SZ depends not only on the total acid strength but also on the ratio of Brønsted:Lewis sites.³⁵

Models in which SO₃ species are coordinated with zirconia are also proposed. The model of Vedrine and co-workers³⁶ suggests coordination of the SO₃ sulfur with lone pairs of the zirconia oxygen in addition to one of the SO₃ oxygens with a Zr while White *et al.*¹⁸ showed that two of the SO₃ oxygens coordinate with surface zirconium atoms, leaving a single S=O moiety. A species of thionyl tetraoxide with four oxygens bonded to zirconia together with a single S=O is represented when loaded with a low sulphate.³⁷

The addition of water causes the coordination bonds to break and brings about formation of Brønsted acid sites which strengthen Lewis acid sites, as shown in **Figure 3.3** as an example.³⁸ Many research groups report the simultaneous existence of Brønsted and Lewis acid sites or the reversible transformation between Brønsted and Lewis acidity upon hydration or dehydration.^{13, 33, 34} Fraenkel suggested that sulphated zirconia with an effective superacid should contain a critical amount of moisture.³⁹ Several workers suggest that the strong acidity originates from the presence of both Lewis and Brønsted sites.

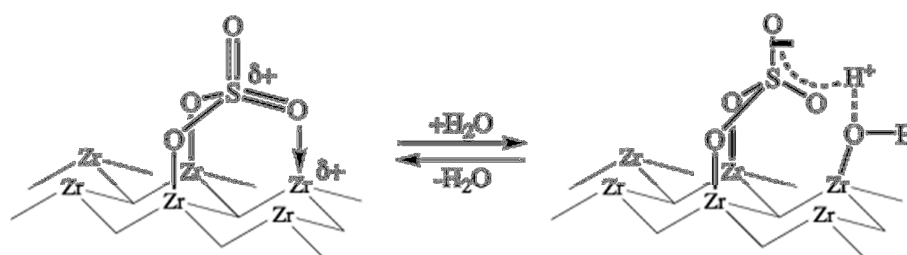


Figure 3.3: A mono-sulphate structure proposed by Arata *et al.*³⁸

3.1.2 Application of SZ catalyst in HMF production

The amphoteric properties of zirconia make it an attractive catalytic material to employ in glucose dehydration to HMF since the presence of a bi-functional catalyst is essential.^{40, 41} Indeed zirconia has been reported as a catalyst for the isomerisation of glucose to fructose at 200 °C,⁴² while sulphated zirconia (SZ) is also an attractive strong solid acid catalyst. Initial reports relating to the performance of SZ in aqueous phase catalysis were somewhat disappointing, because of the instability of SZ under high temperature hydrothermal conditions. This instability was most likely associated with dissolution of multilayer sulphate species present at the high S contents employed.^{43, 44} The potential for tuning the acid strength in SO_4/ZrO_2 and thereby imparting bi-functionality at low sulphate contents for glucose conversion has been neglected to date. Previous works showed that the acid strength of SZ can be readily tuned to direct selectivity in liquid phase terpene isomerisation.⁴⁵ Thus it is hypothesised that judicious control over sulfur loading content may enable predictable tuning of the one-pot conversion of glucose to HMF, by optimising the relative surface coverage of sulphate acid and ZrO_2 base sites arising from the parent support. This chapter demonstrates that systematic control over the Lewis/Brønsted acid and base properties of SZ enables the telescopic isomerisation of glucose to fructose, and subsequent fructose dehydration to HMF in aqueous media by employing a single bi-functional heterogeneous catalyst.

3.2 Results and discussion

3.2.1 Catalyst characterisation

Bifunctional SZ catalysts require surface sulfation of the $\text{Zr}(\text{OH})_4$ precursor within the monolayer (ML) regime, and concomitant retention of a high accessible surface area. The impact of surface functionalization with sulphate groups upon the physico-chemical properties of calcined $\text{Zr}(\text{OH})_4$ has been systematically investigated by means of different characterization techniques as well as chemical probes.

3.2.1.1 Surface and bulk elemental analysis

The impact of zirconium hydroxide impregnation by 0.01–0.5 M H_2SO_4 was probed by XPS and EDX to determine the SO_4 saturation monolayer coverage. **Figure 3.4** shows that increasing the concentration of the impregnating acid solution results in a steep

initial rise in both surface and bulk S content, which subsequently plateau at ~5 and 3 wt% sulphur respectively.

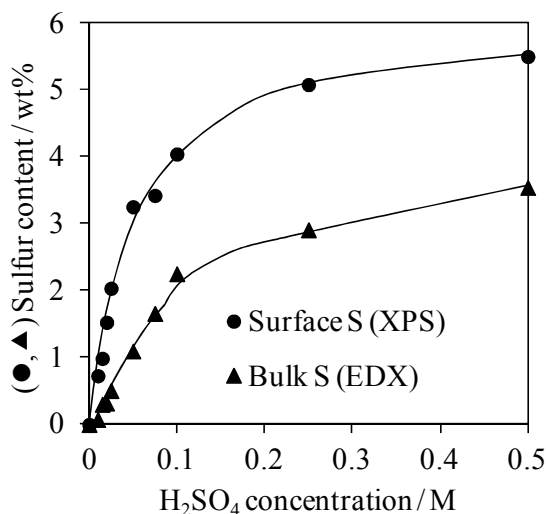


Figure 3.4: Dependence of SZ surface and bulk sulfur content upon [H₂SO₄]

The transition between these regimes occurs at [H₂SO₄] > 0.25 M, indicative of a saturated sulphate monolayer. The surface S content is consistently higher than that of the bulk, confirming localisation of SO₄ species at the Zr(OH)₄ surface. Defining the sulphate saturated monolayer point as 5 wt% S enables a sulphate calibration scale to be constructed for all SZ materials as implemented in **Table 3.1**.

Table 3.1: Calibration of surface sulphate coverage for SZ catalysts

H ₂ SO ₄ concentration M	Bulk content ^a wt%			Surface content ^b wt%			SO ₄ coverage ^c ML
	Zr	O	S	Zr	O	S	
Zr(OH) ₄	58.8	41.2	0.0	72.7	27.3	0.0	0.0
0.010	62.3	37.6	0.1	67.6	31.7	0.73	0.1
0.015	60.2	39.5	0.3	63.2	35.8	0.99	0.2
0.020	59.7	39.8	0.4	68.5	29.9	1.53	0.3
0.025	63.1	36.6	0.5	66.3	31.7	2.04	0.4
0.050	61.4	37.5	1.1	65.1	31.6	3.26	0.6
0.075	59.0	39.4	1.7	58.6	38.0	3.43	0.7
0.1	58.5	39.2	2.3	57.7	38.3	4.05	0.8
0.25	56.5	40.6	2.9	58.0	36.9	5.09	1.0
0.5	55.2	41.2	3.6	58.6	35.9	5.51	1.1

From ^aEDX; ^bXPS; ^cAssuming 1 ML corresponds to 5 wt% surface S content

3.2.1.2 N₂ porosimetry

Porosimetry data (**Figure 3.5**) reveal all samples in the series exhibit a type IV isotherm with hysteresis loops indicative of bottle-necked mesopores. Corresponding BET surface areas increase with SO₄ coverage up to the monolayer point (**Table 3.2**), with a subsequent decrease suggesting some structural collapse for the highest loading, e.g. formation of amorphous zirconium sulphate. Such surface area enhancements have been previously reported for SZ materials, wherein sulfation is reported to inhibit bulk crystallisation of the parent Zr(OH)₄ during calcination.³ A shift in the hysteresis loop from P/P₀ = 0.6–0.8 to 0.4–0.6 with increasing S content reflects a decrease in the mean mesopore diameter in the BJH pore size distribution shown in **Figure 3.6** which falls from 5 nm for the unsulphated calcined Zr(OH)₄ to 3.5 nm for samples impregnated with 0.01–0.025 M H₂SO₄. This mesoporosity probably arises from interparticle voids between sulphate-functionalised ZrO₂ crystallites. Higher acid loadings induce additional microporosity, which is attributed to contraction of these interparticle voids as a result of more uniform crystallite packing as supported by XRD (see **section 3.2.1.5**), with [H₂SO₄] > 0.5M eliminating this microporosity and suppressing mesoporosity, consistent with bulk sulfation.

SO₄ surface densities were calculated for comparison with literature, and are in good agreement with those of Morterra⁴⁶, who determined a monolayer coverage of ~4 SO₄ per nm². (**Table 3.2**)

Table 3.2: Physical properties of SZ as a function of SO₄ coverage

SO ₄ coverage ^a	Surface area ^b	SO ₄ density ^c
ML	m ² g ⁻¹	nm ⁻²
0.0	93	0
0.1	143	0.10
0.2	142	0.35
0.3	169	0.40
0.4	175	0.55
0.6	189	1.10
0.7	175	1.79
0.8	203	2.09
1.0	194	2.83
1.1	118	5.66

^aAssuming 1 ML corresponds to 5 wt% surface S content; From ^bBET; ^cusing S content from EDX

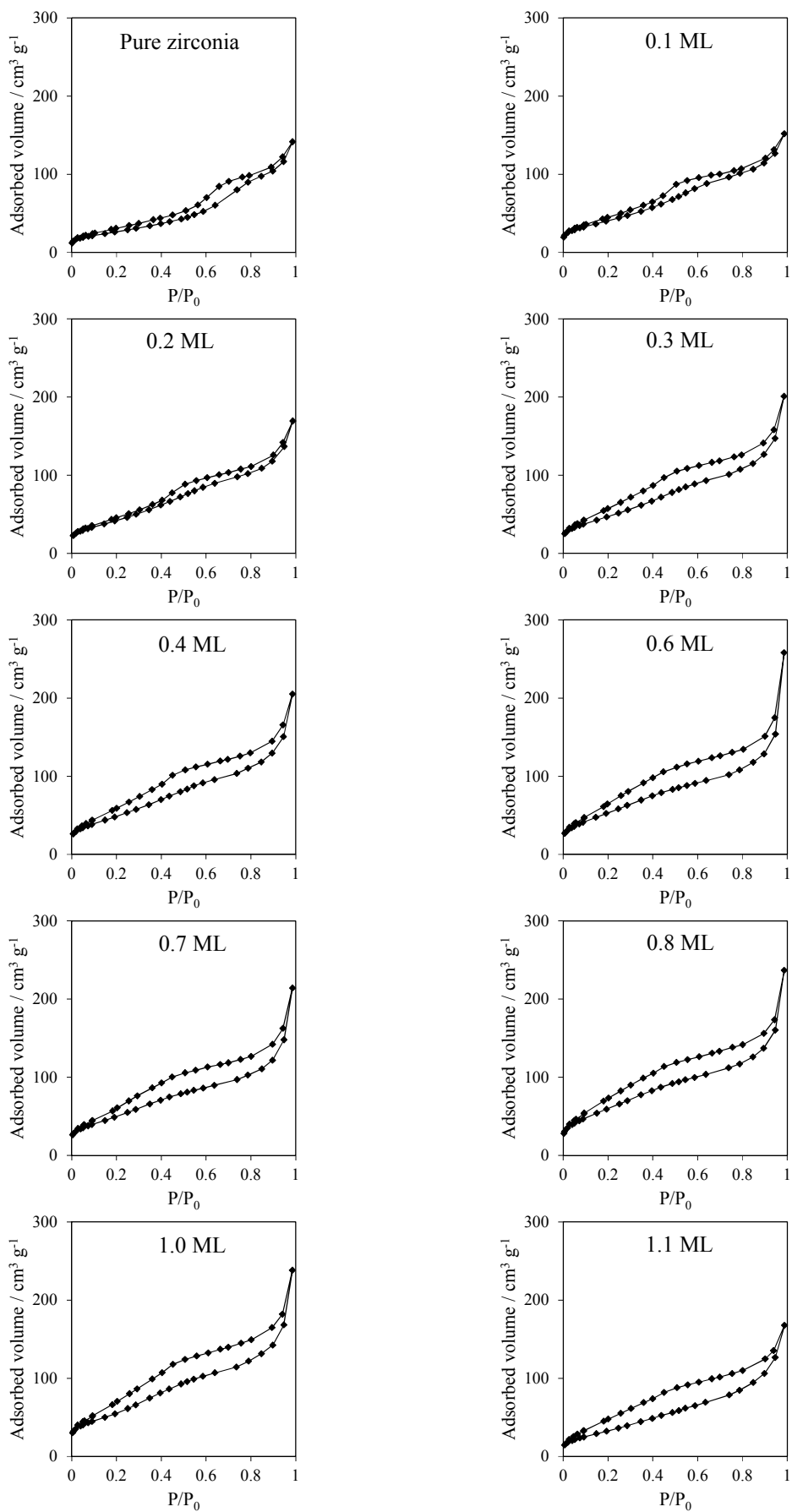


Figure 3.5: N_2 porosimetry on the series of calcined SZ catalysts prepared from impregnation of $Zr(OH)_4$ with 0.01-0.5M H_2SO_4

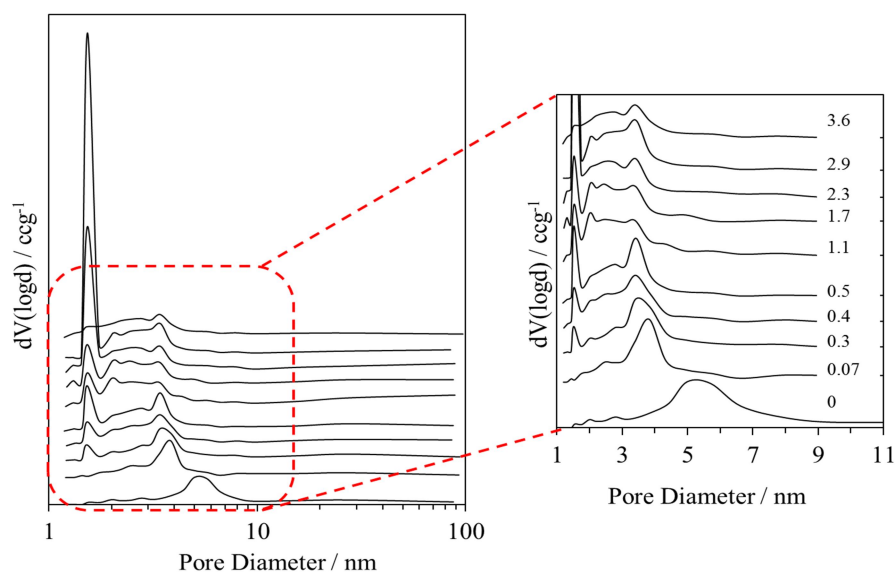


Figure 3.6: BJH pore size distributions for the calcined SZ catalyst series prepared from impregnation of $\text{Zr}(\text{OH})_4$ with 0.01-0.5M H_2SO_4 as a function of surface sulphur content

3.2.1.3 X-Ray Photoelectron Spectroscopy

The nature of the surface environment within the sulphated zirconia series of catalysts were explored by XPS. **Figure 3.7** shows a regular Zr 3d poorly resolved doublet with binding energies (181.9, 184.3 eV) in agreement with literature data for Zr IV in ZrO_2 .^{47, 48} Sulphation resulted in a slight Zr peak shift up to 0.7 eV to higher binding energy, suggesting the direct coordination of zirconium atoms to strongly electron-withdrawing SO_x centres.⁴⁵

Figure 3.8 shows that the oxygen 1s spectrum for calcined, unsulphated zirconia comprises a single dominant peak at ~ 529.6 eV consistent with literature.^{38, 49} Sulphation resulted in the gradual attenuation of this principal zirconia state and concomitant growth of a new high-binding-energy feature at ~ 532.2 eV. The separation of these oxygen states (~ 1.7 eV) is independent of sulphur loading, indicating the formation of a common (higher sulphony⁵⁰) surface species for all materials. These observations are supported by the sulphur 2p spectra (**Figure 3.9**), which exhibit a single broad state between 168-172 eV for all SZ samples, consistent with a unique SO_4 environment^{50, 51} In the low coverage regime ($\theta_{\text{SO}_4} < 0.5$ ML), this sulphate species shifts from 168.5 to 169 eV and broadens with increasing surface sulfation. These concomitant changes indicate the genesis of multiple, co-existing SO_4 species as surface sulfation progresses, probably associated with a change in coordination geometry from

bidentate to monodentate⁴⁵ and diminishing charge withdrawal from the zirconia due to lateral interactions.

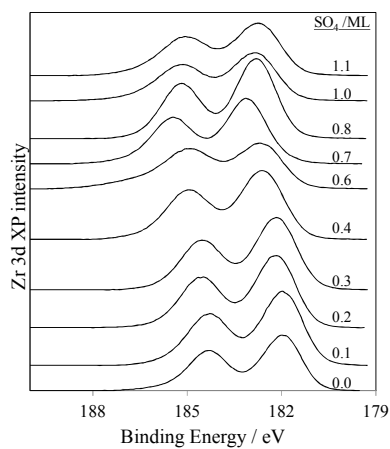


Figure 3.7: Zr 3d XP spectra of sulphated Zr(OH)_4 as a function of SO_4 coverage

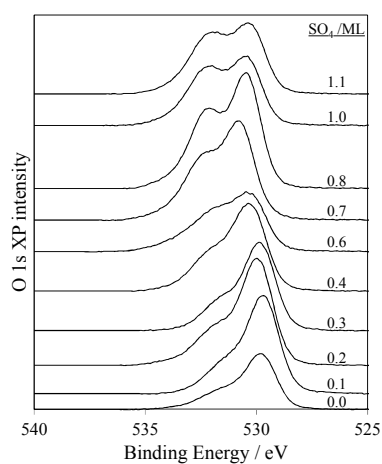


Figure 3.8: O 1s XP spectra of sulphated Zr(OH)_4 as a function of SO_4 coverage

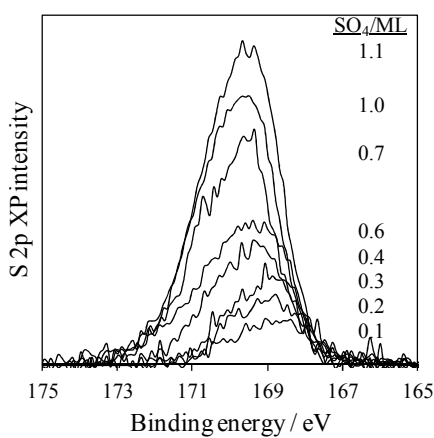


Figure 3.9: S 2p XP spectra of sulphated Zr(OH)_4 as a function of SO_4 coverage

3.2.1.4 *In situ* Diffuse Reflectance Infrared Fourier Transform

The presence of multiple SO_4^{2-} species is supported by DRIFTS measurements shown in **Figure 3.10**, which show the progressive evolution of surface sulphony modes with increasing acid site loading. Vibrational bands are observed attributable to $\nu_s(\text{S-O})$ at 1010, $\nu_{as}(\text{S-O})$ at 1130, $\nu_s(\text{S=O})$ at 1260 and $\nu_{as}(\text{S=O})$ at 1362 cm^{-1} , consistent with bidentate or tridentate SO_4^{2-} ,⁵²⁻⁵⁴ which grow monotonically with sulphate coverage up to 0.5 ML. The high $\nu_{as}(\text{S=O})$ frequency indicates a highly covalent sulphate species, as reported by Morterra *et al.* for dehydrated samples measured in vacuo.^{46, 55} Peak broadening and poorer spectral resolution at higher coverage is attributable to the presence of multiple sulphate species as the monolayer is saturated.^{24, 56, 57} The transition between isolated and polynuclear sulphate species is in good agreement with that reported by Bensitel³⁰ and Morterra⁴⁶ at SO_4 loadings $>1.5 \text{ nm}^{-2}$.

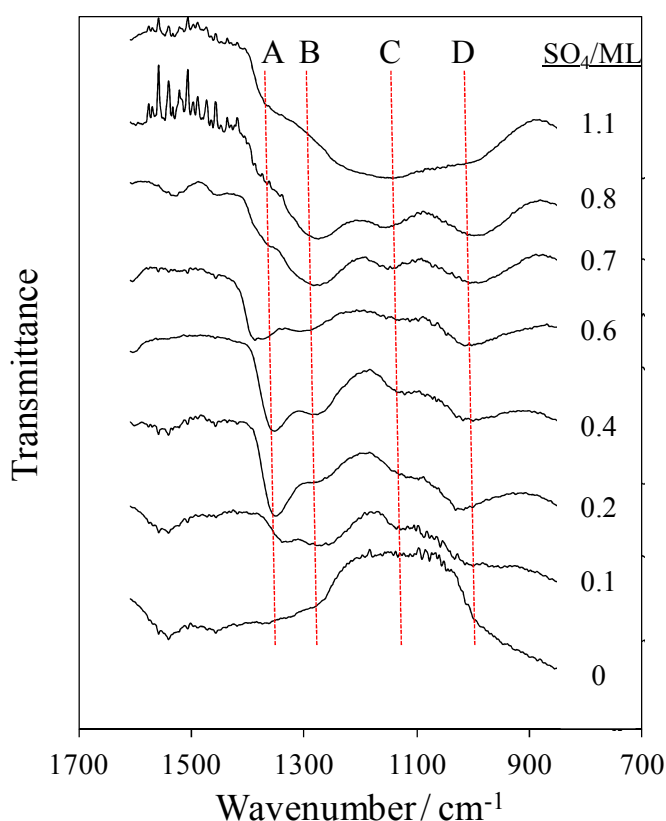


Figure 3.10: DRIFTS spectra of impregnated sulphated zirconia as a function of bulk S content (spectra recorded *in situ* at 200°C in vacuo).

3.2.1.5 Powder X-ray Diffraction

The formation of crystalline species in calcined SZ samples was explored using powder XRD, **Figure 3.11**. The calcined and sulphur-free sample exhibited reflections arising from both monoclinic⁵⁸ ($2\theta = 24.7^\circ, 28.4^\circ, 31.6^\circ$) and tetragonal⁵⁹ ($2\theta = 30.3^\circ, 35.3^\circ, 50.7^\circ, 59.9^\circ, 60.6^\circ$ and 63.5°) ZrO_2 phases. The tetragonal phase progressively increases with surface coverage, becoming the dominant phase for 0.6 ML SO_4^{2-} . A loss of crystallinity observed at higher S contents, is most likely due to the formation of an amorphous bulk $\text{Zr}(\text{SO}_4)_2$ species.⁶⁰ Based on Scherrer equation (See **Chapter 2**), the monoclinic crystallite size in the pure zirconia sample is calculated to be 9.2 nm. However, due to complexity of the diffraction pattern it is not possible to obtain a reliable value for tetragonal crystallite size in this sample. The largest tetragonal crystal size of 6.7 nm was calculated for the SZ sample with 0.6 ML surface sulphate coverage.

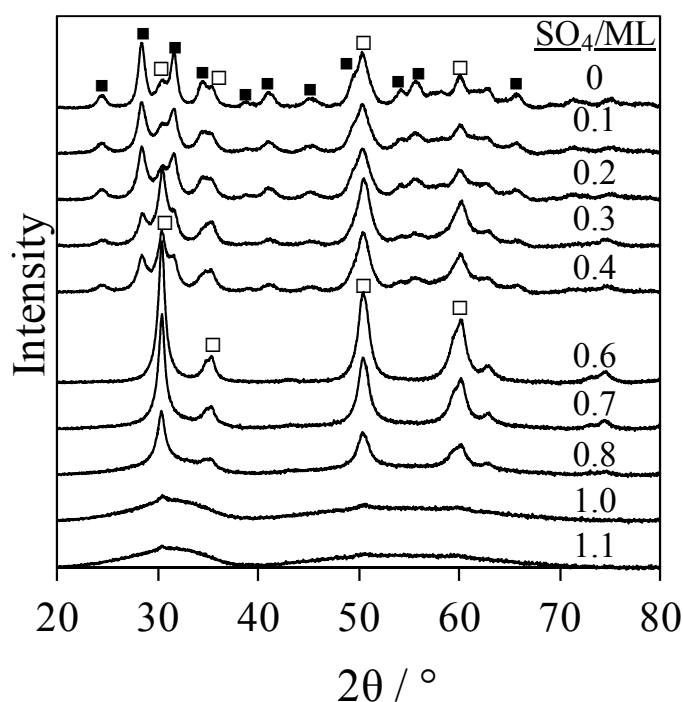


Figure 3.11: Powder XRD analysis of impregnated sulphated zirconia catalysts showing the evolution of monoclinic (■) and tetragonal (□) phases as the bulk S content increases

3.2.1.6 Raman spectroscopy

Raman spectroscopy allows the clear discrimination of the monoclinic and tetragonal phases of ZrO_2 (**Figure 3.12**), and is in accordance with the powder XRD. Decreases in band intensity at 180, 307, 337, 381, 476 and 618 cm^{-1} for ZrO_2 are assigned to the monoclinic phase, while bands evolving at 148, 271, 320, 456 and 645 cm^{-1} with

increasing θSO_4 are attributable to the tetragonal phase.⁶¹ High sulphate loadings degrade spectral resolution, resulting in poorer discrimination between the monoclinic and tetragonal modes as the monolayer point is reached, reflecting the surface sensitivity of Raman⁶², while new features emerge $\sim 1000\text{ cm}^{-1}$ characteristic of surface sulphate species (**Figure 3.13**). At low SO_4 loadings a single peak at 997 cm^{-1} is observed, with a second feature emerging at 1029 cm^{-1} which grows continuously above 0.2 ML to form a broad feature upon completion of the monolayer. This intense feature is attributed to the symmetric sulphate stretching mode, with peak-splitting suggesting a change in sulphate geometry. This transition in the Raman spectra occurs at θSO_4 between 0.2 to 0.4 ML, precisely the point at which the tetragonal phase of ZrO_2 becomes stabilised. Hence, tentatively the 997 cm^{-1} and 1029 cm^{-1} Raman features are assigned to SO_4 coordinated to monoclinic and tetragonal surface sites respectively.

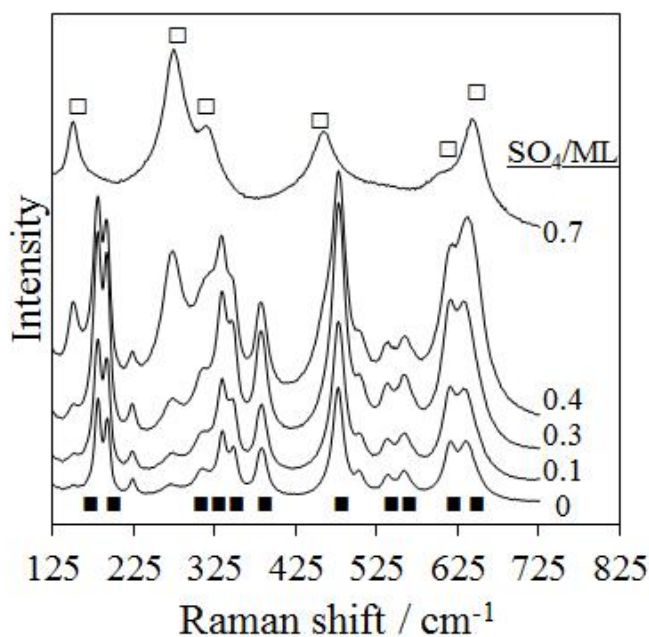


Figure 3.12: Raman spectra of impregnated SZ catalysts showing the evolution of monoclinic (■) and tetragonal (□) phases with bulk S content.

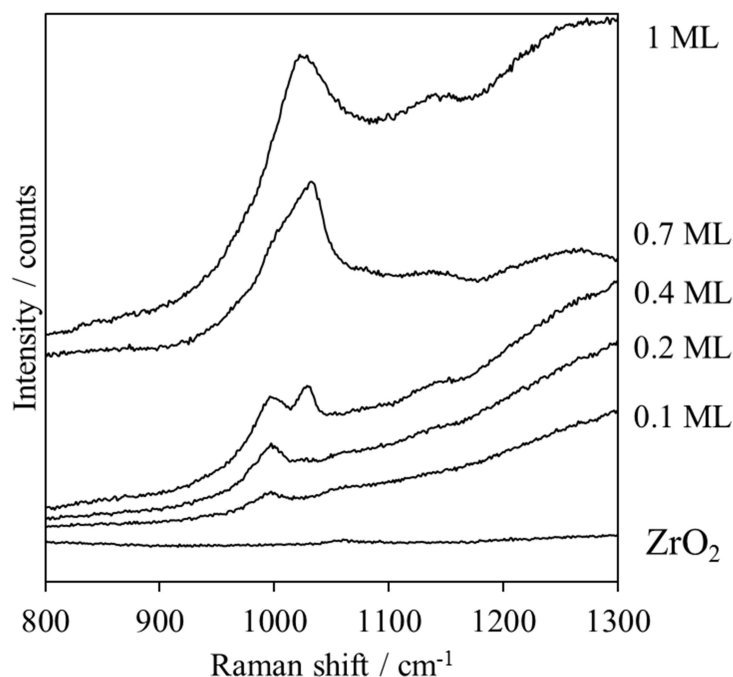


Figure 3.13: Raman of SZ catalyst series prepared showing evolution of symmetric stretching mode of sulphate with coverage. Splitting of peaks is attributed to a transition from SO_4 coordinated on monoclinic and tetragonal phases of ZrO_2

3.2.1.7 Acid and base sites measurements

Calculations show that ZrO_2 exhibits basic properties⁵⁴; hence CO_2 titrations were employed to map the base site density as a function of sulphate loading. **Figure 3.14** shows that the calcined parent $\text{Zr}(\text{OH})_4$, and submonolayer sulphated zirconia materials, possess appreciable base site densities, albeit significantly lower than the corresponding acid site loadings (determined via NH_3 titration). CO_2 and NH_3 titration revealed that calcined unsulphated zirconia has the same number of acid and base sites however with the growth of SO_4 coverage, the number of base sites declines down to a point where remaining base sites are inaccessible and the surface is fully covered with sulphur species. The base site density decreases monotonically with increasing sulphate coverage, confirming that the balance of SZ acid–base character can be precisely tuned within the submonolayer regime ($\theta_{\text{SO}_4} < 1$). NH_3 titration and calorimetry also indicated that increasing SO_4 coverage enhanced both the acid site loading and strength up to one monolayer. (**Table 3.3**)

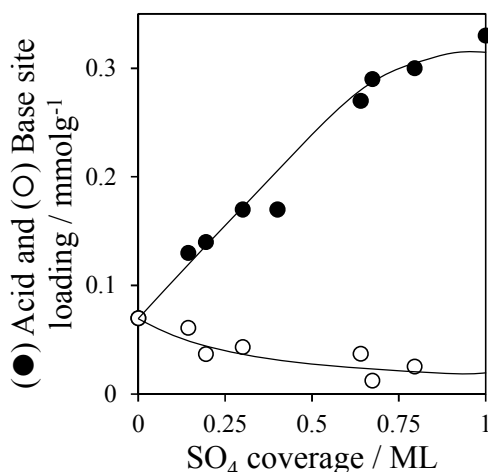


Figure 3.14: Titration of acid and base site loadings of SZ catalysts as a function of S content

Table 3.3: Acid and base properties of sulphated zirconia series

SO ₄ coverage	Base Loading ^a	Acid loading ^b	-ΔH _{ads} (NH ₃) ^c
ML	mmol g ⁻¹	mmol g ⁻¹	kJ mol ⁻¹
0.0	0.07	0.07	-
0.1	0.06	0.13	87
0.2	0.04	0.14	-
0.3	0.04	0.17	95
0.4	-	0.17	-
0.6	0.04	0.27	102
0.7	0.01	0.29	115
0.8	0.03	0.30	115
1.0	0.00	0.37	115
1.1	-	0.29	115

^aCO₂ titration, ^bNH₃ titration; ^cNH₃ adsorption calorimetry

3.2.1.8 Pyridine titration

Zirconia is amphoteric, with the potential to exhibit Lewis basicity but also varying degrees of Lewis or Brønsted acidity depending on the crystalline phase, with monoclinic ZrO₂ generated via calcination reported to exhibit predominantly Lewis acidity.⁶³⁻⁶⁵ The evolution of basic and Lewis–Brønsted acidic properties for the SZ materials was also probed by pyridine titration. The inset to **Figure 3.15** shows representative DRIFT spectra for pyridine adsorbed on submonolayer and monolayer SZ samples which exhibit bands at 1450, 1470, 1610 cm⁻¹ attributed to pyridine bound to Lewis acid sites, while those at 1490, 1540, 1610 and 1635 cm⁻¹ are characteristic of pyridiniums coordinated to Brønsted sites. The unique Brønsted–Lewis features at

1540/1450 cm^{-1} were integrated to quantify the variation in Brønsted : Lewis ratio, which increases with both acid strength and SO_4 coverage (**Figure 3.15**) and correlates directly with the variation in tetragonal:monoclinic zirconia ratio (determined by integrating the latter's fingerprint Raman bands at 270 and 380 cm^{-1} respectively from **Figure 3.12**).

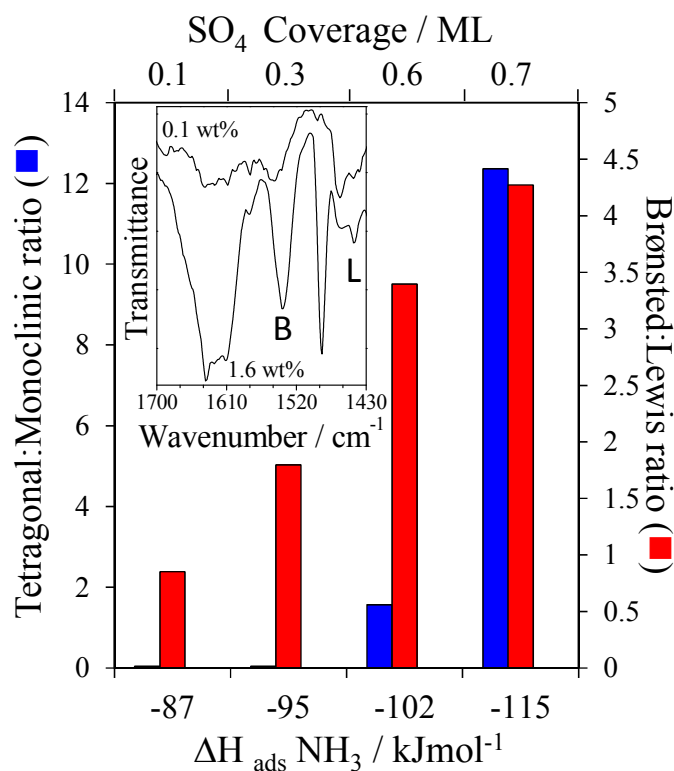


Figure 3.15: Correlation between acid strength of SZ catalysts determined from calorimetry and evolution of Brønsted : Lewis ratio determined from pyridine titration (inset) and Tetragonal : Monoclinic ratios determined from Raman

These observations confirm that ZrO_2 morphology and acidity can be readily tuned by sub-monolayers of surface sulphate, consistent with previous reports that ZrO_2 crystallisation is dependent on surface sulphate density.⁴⁶

3.2.2 Glucose conversion to HMF

3.2.2.1 Glucose conversion versus fructose conversion

Glucose conversion to HMF is proposed to initiate via a Lewis acid- or base-catalysed isomerisation to fructose, followed by a Brønsted acid catalysed dehydration as shown in **Figure 3.16**. To establish the validity of this hypothesis, the kinetics of glucose versus fructose conversion to HMF were compared at 100 °C using 0.1 g substrate, 0.1 g catalyst in 20 ml of deionized water as it was explained in more detail in **Chapter 2**.

The relatively low reaction temperature was employed in order to minimise competing degradation of HMF to levulinic acid or formation of humins, and thus permit accurate rate data to be obtained across the series of SZ materials.

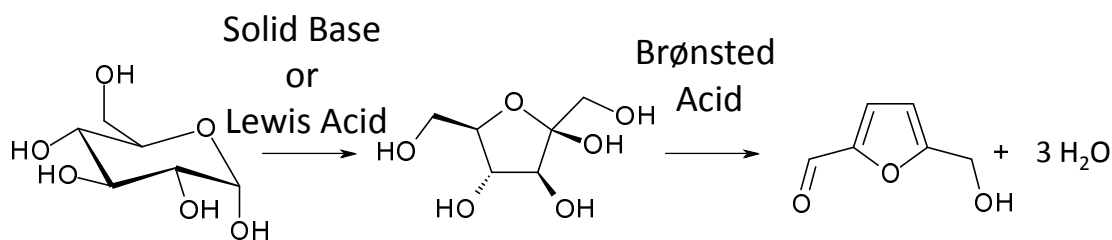


Figure 3.16: Conversion of glucose to fructose and HMF

Figure 3.17 shows the resulting variations in glucose conversions after 6 h as a function of surface sulphate coverage. The first striking observation is glucose conversion shows a large decrease for coverages above 0.25 ML and then for $\theta_{\text{SO}_4^{2-}} > 0.6$ ML the conversion remains unchanged at around 7%.

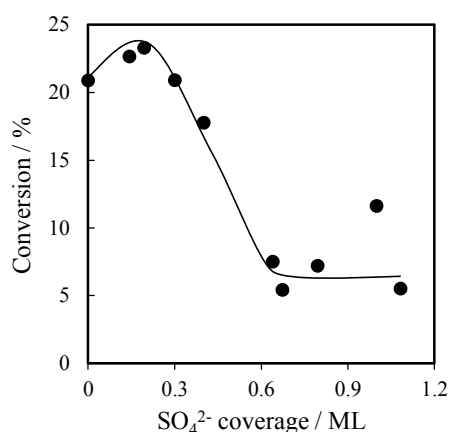


Figure 3.17: Glucose conversion in water after 6 h reaction at 100°C over bulk SZ catalyst as a function of surface sulphate coverage

Figure 3.18 shows the yield of main products of glucose dehydration reaction, fructose and HMF. As seen in this figure, similar to glucose conversion, fructose yield reaches a maximum where almost 25% of zirconia's surface is covered with sulphate groups, while HMF yield increases with surface sulphur coverage and reaches its highest value around $\theta_{\text{SO}_4} = 0.6$ ML and then levels off. While it is noticeable that HMF yields are lower than those obtained in biphasic systems and ionic liquids, where HMF yields as high as 60–70% are observed from glucose, it must be noted that these typically operate under higher temperature conditions of 120–200 °C and use homogeneous catalysts.⁶⁶

The trends in conversion and product yields can be rationalised in terms of the change in acid–base character with sulfur loading by comparing the associated product yields. Moreover, from **Figure 3.18** it can be observed that the fructose selectivity of ~80% remains unchanged regardless of the surface sulphur coverage, while HMF selectivity considerably increases from 1.7% over pure zirconia to about 17% over 0.6 ML sample and then plateaus. The initial rise in HMF selectivity is attributable to the increased number of acid sites. However, when there are fewer base sites available to isomerize glucose to fructose, less fructose is generated and thus less HMF is produced. As a result, the selectivity of HMF levels off.

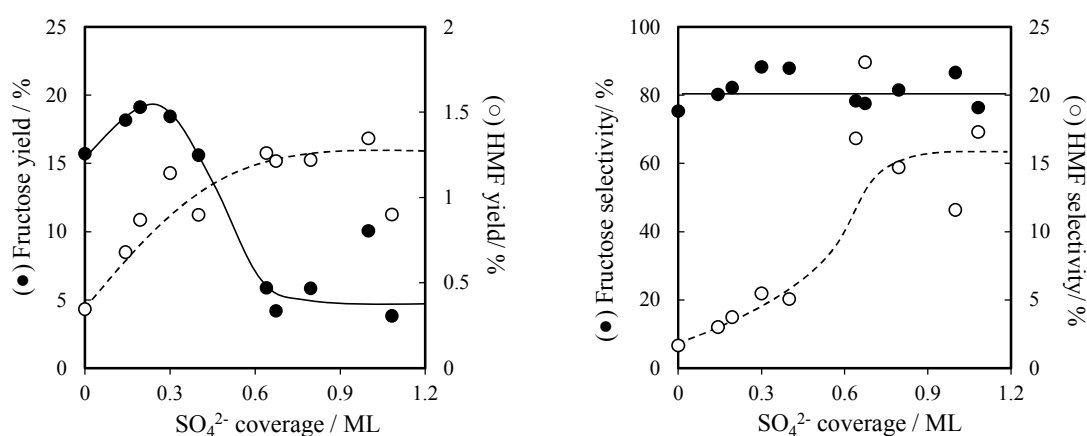


Figure 3.18: Left) Yields and Right) selectivities of fructose and HMF during SZ catalysed glucose dehydration after 6 h reaction at 100 °C

Figures 3.19 shows glucose dehydration reactions profiles over the series of SZ catalysts. The main products of glucose dehydration in water were fructose and HMF however negligible amounts of 1,6-anhydroglucose, formic acid and acetic acid were also detected. There were also some humins formed during each reaction as well as other un-identified soluble compounds.

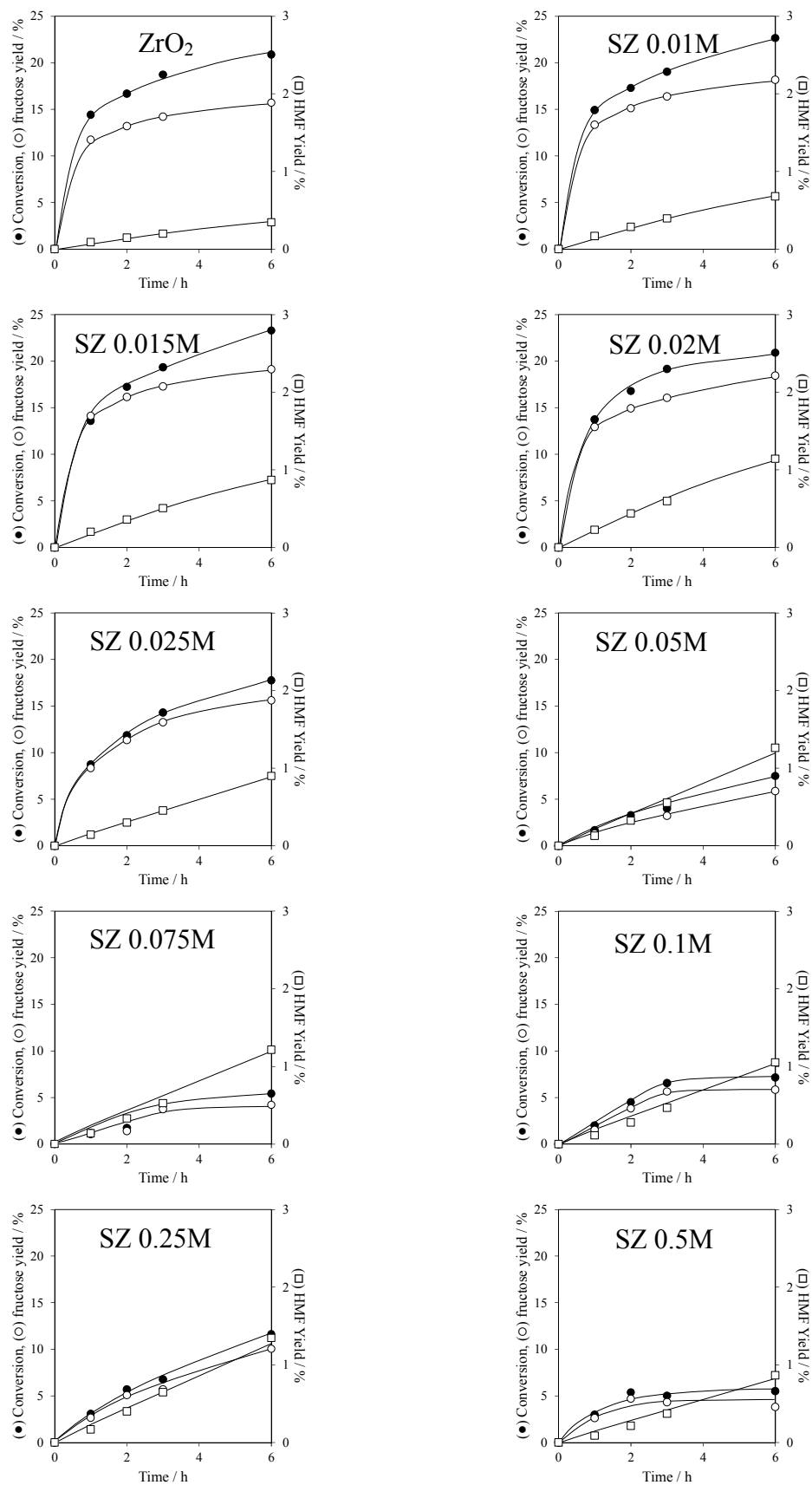


Figure 3.19: Glucose conversion, fructose and HMF yield profiles for glucose to HMF reactions over bulk SZs at 100 °C

From the reaction profiles, the rates of glucose conversion and HMF formation and consequently glucose and HMF turnover frequencies were calculated. **Figure 3.20** shows turnover frequency for glucose conversion and HMF formation normalized to the number of acid sites. As seen in this figure, glucose TOF drops significantly from 5.9 h⁻¹ over ZrO₂ to 0.4 h⁻¹ where $\theta_{\text{SO}_4^{2-}} = 0.6$ ML. Further increases to sulphate coverage have no impact on glucose TOF. In addition to that, HMF TOF reaches a maximum of 0.07 h⁻¹ which corresponds to a SO₄²⁻ coverage of about 0.3. Beyond this coverage value, the HMF TOF gradually decreases to about 0.02 h⁻¹ for $\theta_{\text{SO}_4} = 1.1$ ML. The decreased glucose and HMF TOF is likely due to loss of base sites as a result of growing surface sulphate coverage and the corresponding decreased rate of fructose formation. In other words, as the number of acid sites increases across the series, base sites gradually disappear and consequently glucose isomerization to fructose reduces and in turn less HMF can be formed due to lack of fructose in the reaction medium.

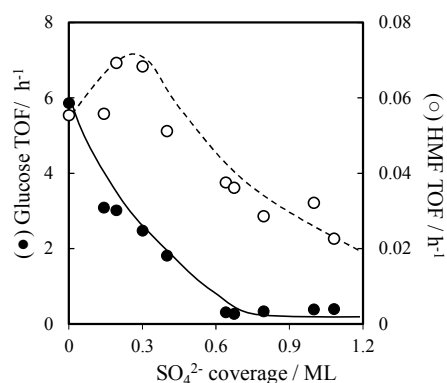


Figure 3.20: (●) glucose and (○) HMF turnover frequency for glucose conversion at 100 °C over SZ catalysts

3.2.3 Fructose conversion to HMF

In order to validate the idea of telescopic conversion of glucose to HMF via isomerization to fructose, it is essential to conduct some experiment in which fructose is the starting material. Therefore, the catalytic transformation of fructose to HMF over sulphated zirconia series was studied.

Figure 3.21 demonstrates that fructose conversion with a 10% increase reaches to 25.4% when the sulphate group coverage expands from 0 to 0.8 ML. However, further increase in sulphate coverage resulted in a drop in fructose conversion. This is consistent with the sulphated zirconia structure collapse at high sulphuric acid concentrations.

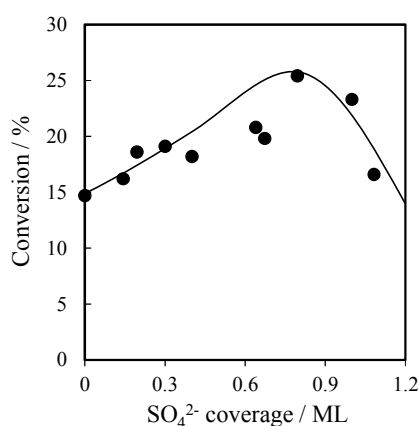


Figure 3.21: Fructose conversion over SZ catalysts as a function of surface coverage by sulphate groups

Furthermore, it was found out that the main products of fructose conversion over sulphated zirconia catalysts at 100 °C are glucose and HMF. **Figure 3.22** shows that glucose yield drops from ~2.5% to 1% for $\text{SO}_4^{2-} > 0.6$ ML. Moreover, HMF yield progressively increases from 1% over pure zirconia and achieves its maximum of 5% at $\theta\text{SO}_4^{2-} = 0.8$ ML. SZs with greater sulphate coverages exhibited a slightly lower HMF yield compared to 0.8 ML catalysts. Furthermore, as illustrated in **Figure 3.22**, glucose selectivity after almost a 10% drop reaches 5% selectivity and remains unchanged. However, HMF selectivity monotonically increases with surface sulphate coverage.

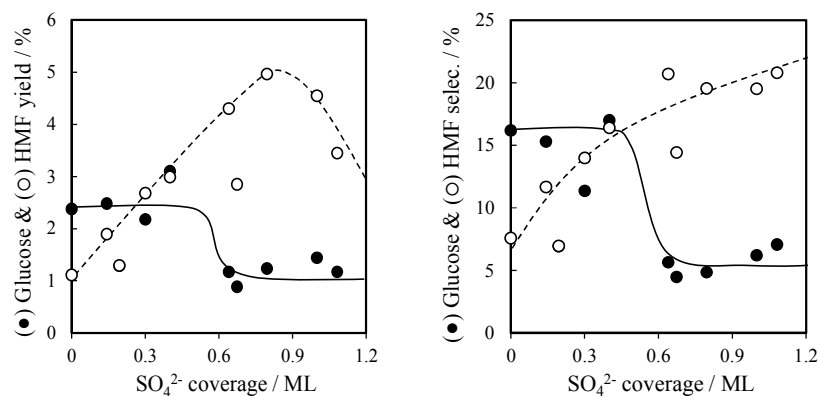


Figure 3.22: Left) Yields and Right) selectivities of glucose and HMF during SZ catalysed fructose dehydration after 6 h reaction at 100 °C

The profile of fructose conversion and yields of glucose and HMF over the entire series of SZ catalysts at 100 °C are shown in **Figure 3.23**. Similar to reactions of glucose, the rate of fructose conversion and HMF formation was measured based on the values obtained from the first 3 h of reaction. And consequently, the fructose and HMF TOFs were calculated by normalizing the rate to both the mass of catalyst and the number of acid sites.

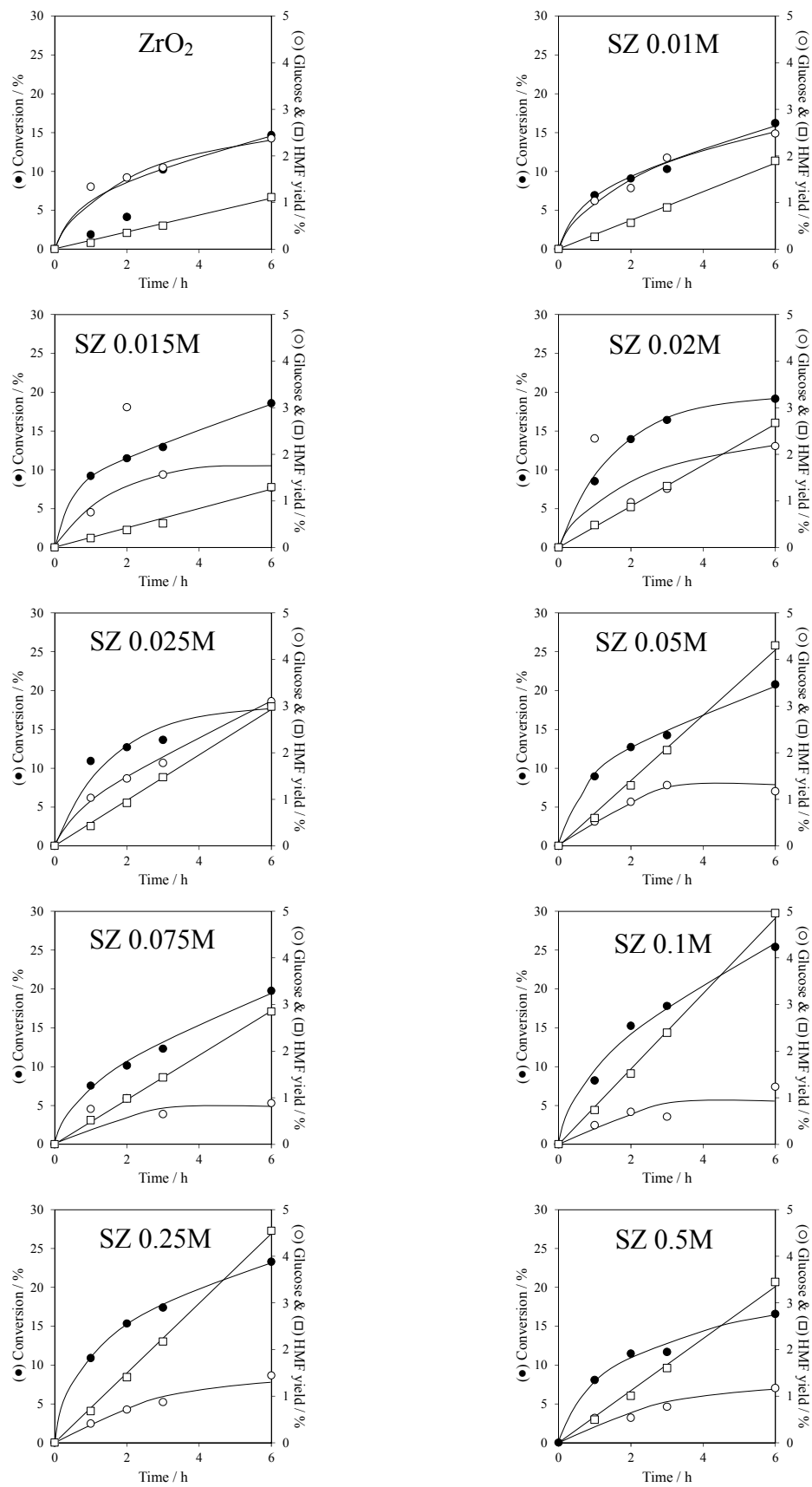


Figure 3.23: Fructose conversion, glucose and HMF yield profiles for fructose to HMF reactions over bulk SZs

As depicted in **Figure 3.24**, fructose TOF continuously decreases with a modest gradient from 2.2 over ZrO_2 to 0.9 where $\theta_{\text{SO}_4^{2-}} = 1.1$. Additionally, constant HMF TOFs of $\sim 1.2 \text{ h}^{-1}$ was obtained at all surface sulphate coverages. Therefore, it can be concluded that because the glucose yield and selectivity drops with increase in sulphate groups coverage (**Figure 3.22**), thus the fall in fructose TOF can be ascribed to decreased isomerization of fructose to glucose due to disappearance of base sites as the sulphur content increases.

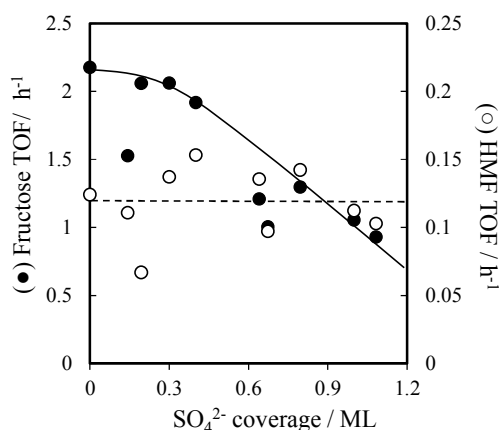


Figure 3.24: (●) Fructose and (○) HMF turnover frequency for fructose conversion at 100 °C over SZ catalysts

In summary, the high glucose conversion and rate of reaction observed for pure ZrO_2 and SZ catalysts possessing low SO_4 coverages correlates with high fructose yields and rate of formation, and is thus a reflection of the correspondingly significant Lewis acid–base properties of these materials comprising predominantly monoclinic zirconia. In contrast, high SO_4 coverages (i.e. Brønsted acid site densities) suppress glucose isomerisation to fructose in favour of HMF production associated with enhanced dehydration of the fructose intermediate. Hence loss of basicity and Lewis acidity upon zirconia sulfation switches off glucose \leftrightarrow fructose isomerisation but promotes the Brønsted acid catalysed fructose \rightarrow HMF pathway, in perfect agreement with the proposal in **Figure 3.16**. The requirement for Brønsted acid character to produce HMF is confirmed by inspecting the yield of products obtained from fructose as a substrate.

3.2.4 Effect of reactant concentration

In order to study the impact of the initial glucose concentration on its reactivity and also to measure the order of the glucose dehydration reaction in respect to glucose concentration, SZ 0.015M was chosen to carry out the reactivity and kinetic studies at 100 °C. In all cases, the amount of catalyst and water were kept constant at 0.1 g and 20 ml respectively.

Figure 3.25 demonstrates the amount of substrate that is converted to other compounds as a function of initial glucose concentration. And it shows that for concentrations below 0.3 M, the amount of converted glucose linearly increases with C_0 .

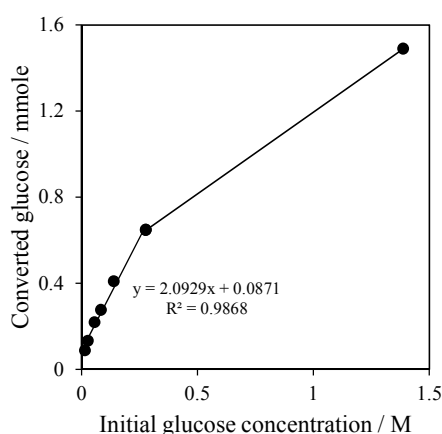


Figure 3.25: Amount of converted glucose over 0.1 g SZ 0.015M as a function of initial glucose concentration

The rates of glucose conversion calculated for the first 3 hours of reaction are plotted against the concentration of glucose. Referring to **Figure 3.26**, below 0.3 M, the rates of conversion increase linearly with initial concentration of glucose and subsequently plateau, consistent with saturation of active sites.

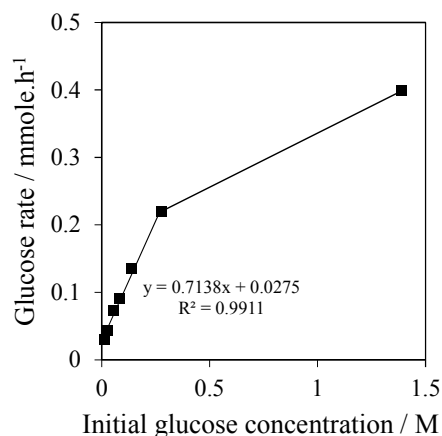


Figure 3.26: Rate of glucose conversion and fructose and HMF formation as a function of initial glucose concentration over SZ 0.015M

According to the definition, rate of glucose conversion is explained by the following equation:

$$r = k [\text{glucose}]^a [\text{catalyst}]^b \quad \text{Equation 3.1}$$

where r is the rate of glucose conversion, k is the rate constant, $[\text{glucose}]$ is the concentration of glucose, a is the order of reaction with regard to glucose, $[\text{catalyst}]$ is the concentration of catalyst and b is the order of reaction in respect to catalyst. Since the same amount of catalyst was used in all reactions, thus **Equation 3.1** can be simplified as:

$$r = k' [\text{glucose}]^a \quad \text{Equation 3.2}$$

Where $k' = k[\text{catalyst}]^b$. If a linear relationship between the rate of reaction and concentration of glucose is established (as it is shown in **Figure 3.26**), then a , the order of reaction with respect to glucose will be equal to 1. This finding is in complete agreement with previous reports by many authors including Saeman⁶⁷, Heimlich *et al.*⁶⁸, McKibbins *et al.*⁶⁹ and Bienkowski *et al.*⁷⁰

3.2.5 Effect of catalyst loading

In order to measure the order of reaction with respect to catalysts loading, the experiments of glucose conversion in water were conducted at 100 °C using the same

concentration of glucose (0.05 wt%), whilst varying the different catalyst : reactant ratios from 0.05 to 0.3. **Figure 3.27** demonstrates that glucose conversion increases linearly with catalyst loading.

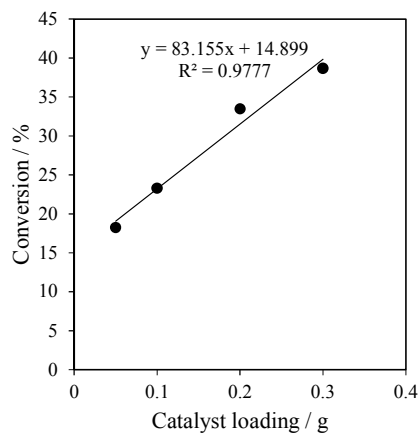


Figure 3.27: Glucose conversion over SZ 0.015M as a function of catalyst to substrate weight ratio

Furthermore, the rate of glucose conversion was calculated and plotted against the catalyst loading as presented in **Figure 3.28**. As the catalyst loading is increased, glucose was converted faster with a linear fashion. This linear increase in the rate of glucose transformation with catalyst loading suggests that the rate of glucose consumption is first order, with respect to catalyst loading.

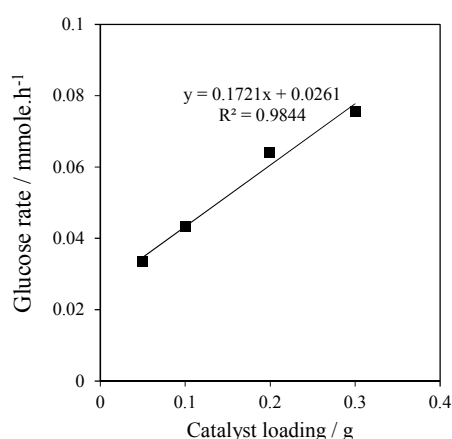


Figure 3.28: Rate of glucose conversion and fructose and HMF formation as a function of catalyst to substrate weight ratio

3.2.6 Leaching test and recyclability

To verify the stability of the catalyst possessing optimal behaviour (SZ 0.1M), a recycle test was performed following re-calcination of the spent catalyst at 550 °C. This revealed only a minor decrease in the absolute fructose conversion being observed after 6 and 24 h reaction (**Figure 3.29**).

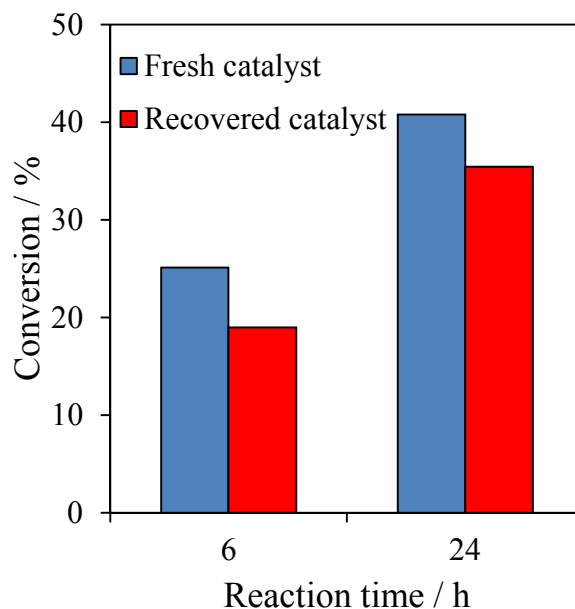
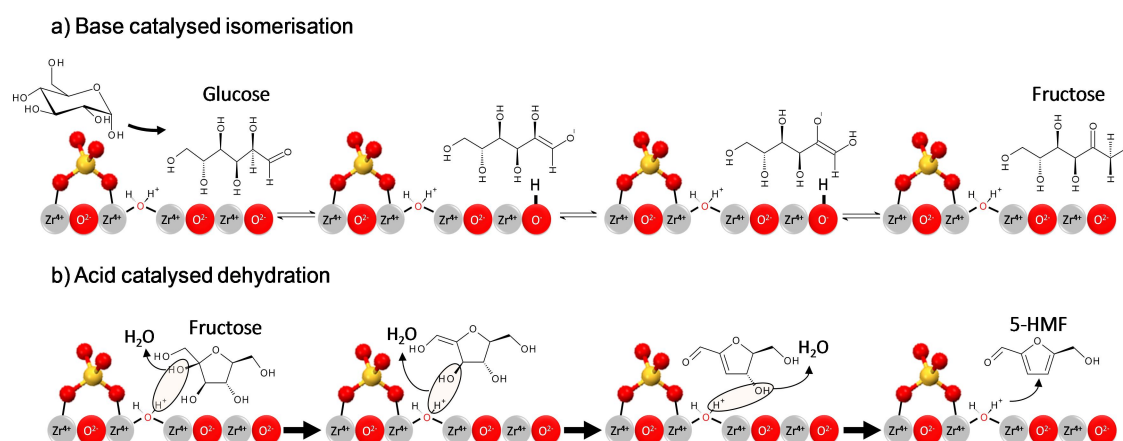


Figure 3.29: Comparison of fructose conversions in water at 100°C for fresh and recycled SZ 0.1M catalyst (re-calcined at 550°C before reaction)

As such, we can propose a bifunctional catalytic surface mechanism for glucose conversion to HMF. The first step of this is most likely the Lewis base catalysed transformation of glucose into an enol intermediate (**Scheme 3.2**),^{71, 72} with subsequent protonation of the resulting C=C bonds yielding either fructose or mannose. We propose that O²⁻ sites on the surface of basic ZrO₂ (monoclinic phase) initiate this transformation via proton abstraction to form the enol (akin to that proposed over sodium aluminate⁷³) which undergoes subsequent hydrogen transfer forming fructose. Spillover onto neighbouring Brønsted acid sulphate moieties then catalyses the stepwise dehydration of fructose to HMF⁷⁴ as illustrated in **Scheme 3.2**. Lewis acid sites also have the potential to initiate glucose isomerisation via an intramolecular hydride shift.⁷⁵ However, the extent to which Lewis acid routes are able to participate in aqueous phase reactions remains contentious due to their likelihood of hydration to their Brønsted counterparts. Although it has been suggested that Lewis acidity may be retained at defect sites⁴⁶ or when hydrophobic supports such as Sn-β are employed⁷⁶, wherein a

Meerwein–Ponndorf–Verley mechanism has been postulated.^{77, 78} As **Figure 3.16** highlights, careful tuning of the degree of zirconia surface sulfation enables the successful genesis of bi-functional catalysts possessing dual solid acid–base character which facilitate the telescopic conversion of glucose to HMF under mild reaction conditions.



Scheme 3.2: Bi-functional surface catalysed mechanism for a) isomerisation of glucose to fructose over basic O^{2-} sites of monoclinic ZrO_2 (Lewis acidic Zr^{4+} may help stabilise the enolate intermediate) and b) dehydration of fructose to 5-HMF over Brønsted acid sites present in submonolayer SO_4/ZrO_2 catalysts

3.2.7 Xylose conversion to furfural

Analogous to the glucose transformation to HMF, dehydration of xylose which is the main precursor to hemicellulose, is of great interest as it will result in the production of furfural, another platform chemical. Furfural is envisaged as a potential platform chemical for the biofuel, biochemical and biopolymer industries. In addition, 2-methylfuran, 2,5-dimethylfuran, 2-methyltetrahydrofuran, 5-methylfurfural (MF), and 5-(ethoxymethyl)furfural (EMF) have been reported as promising biofuel components and octane boosters.^{79, 80}

Industrial furfural production is based on biomass hydrolysis and subsequent dehydration of the obtained pentoses using a homogeneous Brønsted acid catalyst in aqueous media.⁸¹ The first industrial furfural production process was established by Quaker Oats in 1921.⁸² In this process, oat hulls were converted into furfural using concentrated sulphuric acid and high pressure steam to supply heat and strip out furfural. Presently, most furfural is produced in China using small-scale fixed bed

reactors.⁸¹ The current furfural process is not only environmentally harsh but also quite inefficient, achieving only ~50% of the theoretical furfural yield. This suggests a need for more efficient processes given the importance of furfural in green chemistry processes.

Furfural production systems in the absence of heterogeneous catalysts are predominately based on homogeneous catalysts processes utilising H₂SO₄, HCl, maleic acid, acetic acid and formic acid. Recently the addition of inorganic salts such as NaCl, KCl, CaCl₂ and FeCl₃ to the reaction medium has been reported to enhance furfural production⁸³ at high reaction temperatures (>170 °C).⁸⁴ It has been postulated that halide ion assists the enolization reaction via proton transfer and dehydration reactions by stabilizing the transition states leading to intermediates.⁸⁵

Over the past decade, substantial research has been conducted on the development of a heterogeneous Brønsted acid catalyst for furfural production from xylose.⁸⁶ Many different Brønsted acid catalysts, such as various zeolites,⁸⁷⁻⁹⁰ Amberlyst,^{91, 92} Nafion,⁹³ and MCM-41 based materials,^{92, 94} have been tested.⁹⁵⁻⁹⁸ A key shortcoming in the Brønsted acid catalyzed xylose dehydration process is a high activation barrier of ~30–32 kcal/mol, requiring high operating temperatures (>150 °C) and long residence times in aqueous media.^{99, 100} This resulted in a furfural yield of only ~30% being obtained, mainly as a result of side reactions leading to soluble polymers and humins. However, in a heterogeneously catalysed system where CrCl₃, a Lewis acid, was employed as co-catalyst in combination with a Brønsted acid (HCl), the isomerization of xylose to xylulose showed that the open-chain isomer form is dominant under these conditions, and is subsequently dehydrated to furfural. In this case, as Choudhary *et al.* reported, the furfural yield increased from 29 to 39% in water and to 76% in water/toluene when CrCl₃ was added to HCl.⁷⁹

The furfural yield is typically increased using continuous extraction with an organic solvent in a liquid–liquid biphasic system^{86, 99, 101}, or using a carrier gas to strip out the furfural.^{82, 102} For instance, a biphasic water/toluene system has been widely used in conjunction with different mesoporous acid catalysts and furfural yields as high as 82% have been reported when Arenesulfonic-SBA has been used at 160 °C in a 20 h reaction.¹⁰³

Choudhary and co-workers demonstrated that dehydration of xylulose, an isomer of xylose, results in a much higher furfural yield than xylose dehydration under similar reaction conditions. They also showed that a Lewis acid catalyst such as CrCl_3 can enhance the isomerization of xylose to xylulose and lyxose and thus they proposed two reaction pathways for xylose to furfural transformation. The first of which xylose is directly undergoes Brønsted acid catalysed dehydration to form furfural. In the alternative pathway, xylose is isomerized to xylulose and lyxose over a Lewis acid catalyst, and subsequently xylulose loses 3 water molecules over a Brønsted acid catalyst with furfural being formed.⁷⁹ (**Figure 3.30**)

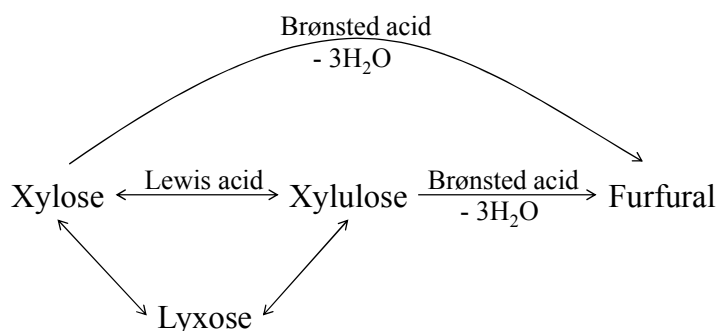


Figure 3.30: Xylose dehydration reaction pathway to form furfural proposed by Choudhary *et al.*⁷⁹

This is in agreement with findings of Weingarten *et al.* regarding the dehydration of xylose over Brønsted acid sites as well as Lewis acids.⁹⁸

In this thesis, bulk sulphated zirconia catalysts have been applied in xylose dehydration reactions in aqueous phase, and analogous behaviour of xylose and glucose in which xylose transforms into its isomer molecule, xylulose, and then the latter converts into furfural, has been reported.

Figure 3.31 demonstrates the conversion of xylose in a 0.5 wt% aqueous solution after 6 h reaction at 100 °C. From this figure, it can be observed that xylose conversion reaches its maximum value of 32.6% where $\theta_{\text{SO}_4} = 0.3$ ML and then drops down to 21% at $\theta_{\text{SO}_4} = 0.6$, remaining unchanged with increasing surface coverage with sulphate species.

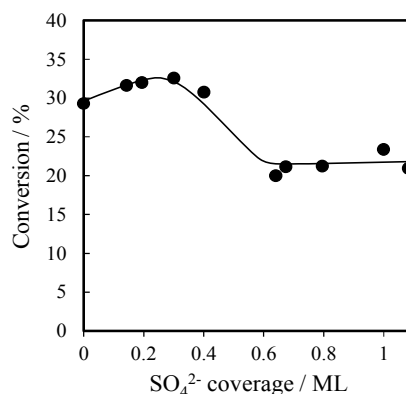


Figure 3.31: Conversion of xylose in a 0.05 wt% aqueous solution after 6 h reaction at 100 °C

The yields of xylulose and lyxose, the two isomers of xylose, have been plotted as a function surface sulphate coverage as shown in **Figure 3.32**. It can be observed that the yield of both compounds decreases modestly as the surface is covered with more sulphate groups due to withdrawal of Lewis acid sites.

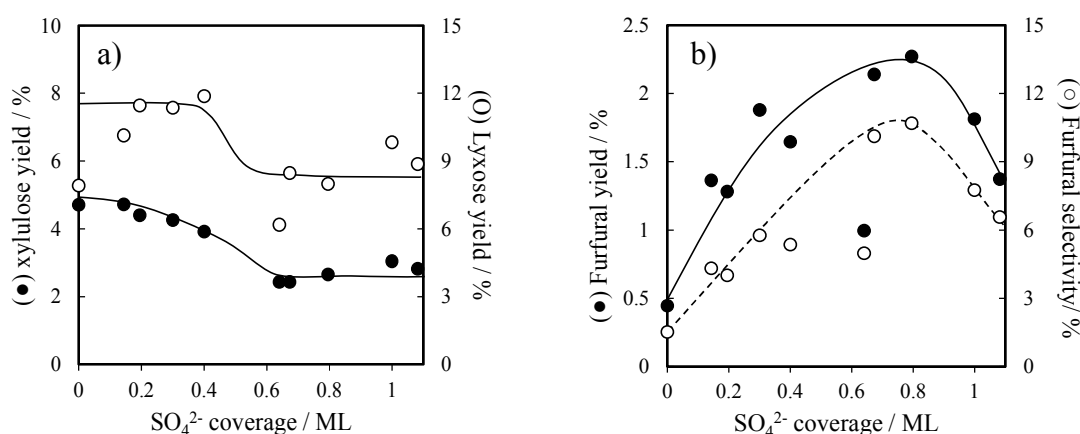


Figure 3.32: a) Xylulose and lyxose and b) Furfural yield and selectivity for SZ catalysed xylose dehydration after 6 h reaction at 100 °C

Moreover, **Figure 3.32** shows that furfural yield moderately increases from 0.5% over pure zirconia to 2.3% at $\theta_{\text{SO}_4} = 0.8$ ML and then drops to 1.4% as the sulphate coverage increases. Also, furfural selectivity rises from 1.5 to 10.7% where sulphate coverage increases from 0 to 0.8 ML and then decreases down to 6.6% when the surface was oversaturated with sulphate species. The increase in yield and selectivity of furfural across the SZ series is in accordance with previous studies regarding the increase of furfural selectivity with Brønsted to Lewis acid sites ratio.⁹⁸ The decrease in furfural yield and selectivity at high surface sulphate coverages can be ascribed to loss of

crystallinity and surface area. Also, as it is demonstrated in **Figure 3.33**, the carbon balance is improved as the ratio between Brønsted and Lewis acid sites increases. Furthermore, the improvement in carbon balance is attributed to the decrease in number of Lewis acid sites, which are known to be responsible for catalysing undesired side reactions to form insoluble polymers and humins.⁹⁸

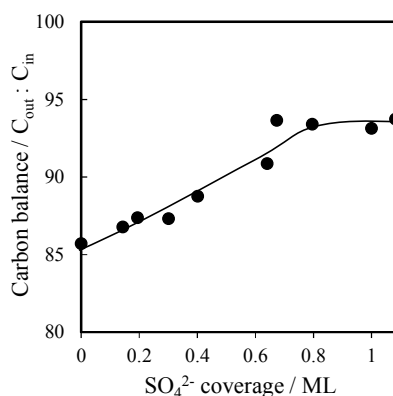


Figure 3.33: Carbon balance for SZ catalysed xylose dehydration after 6 h reaction at 100 °C

Following the conduction of the experiments (**Figure 3.34**), the rates of xylose transformation and furfural formation were measured and subsequently TOFs of xylose and furfural were calculated by normalizing the rates to the number of acid sites. As **Figure 3.35** illustrates, xylose TOF drops dramatically when surface sulphate coverage increases from 0 to 0.6 ML and then plateaus. This is due to the higher number of Lewis acid sites compared to Brønsted acid sites at low surface sulphate coverages. Therefore, when the Lewis acid sites decrease as a result of the sulfation process, fewer xylose molecules are converted (either to furfural, intermediates or humins).

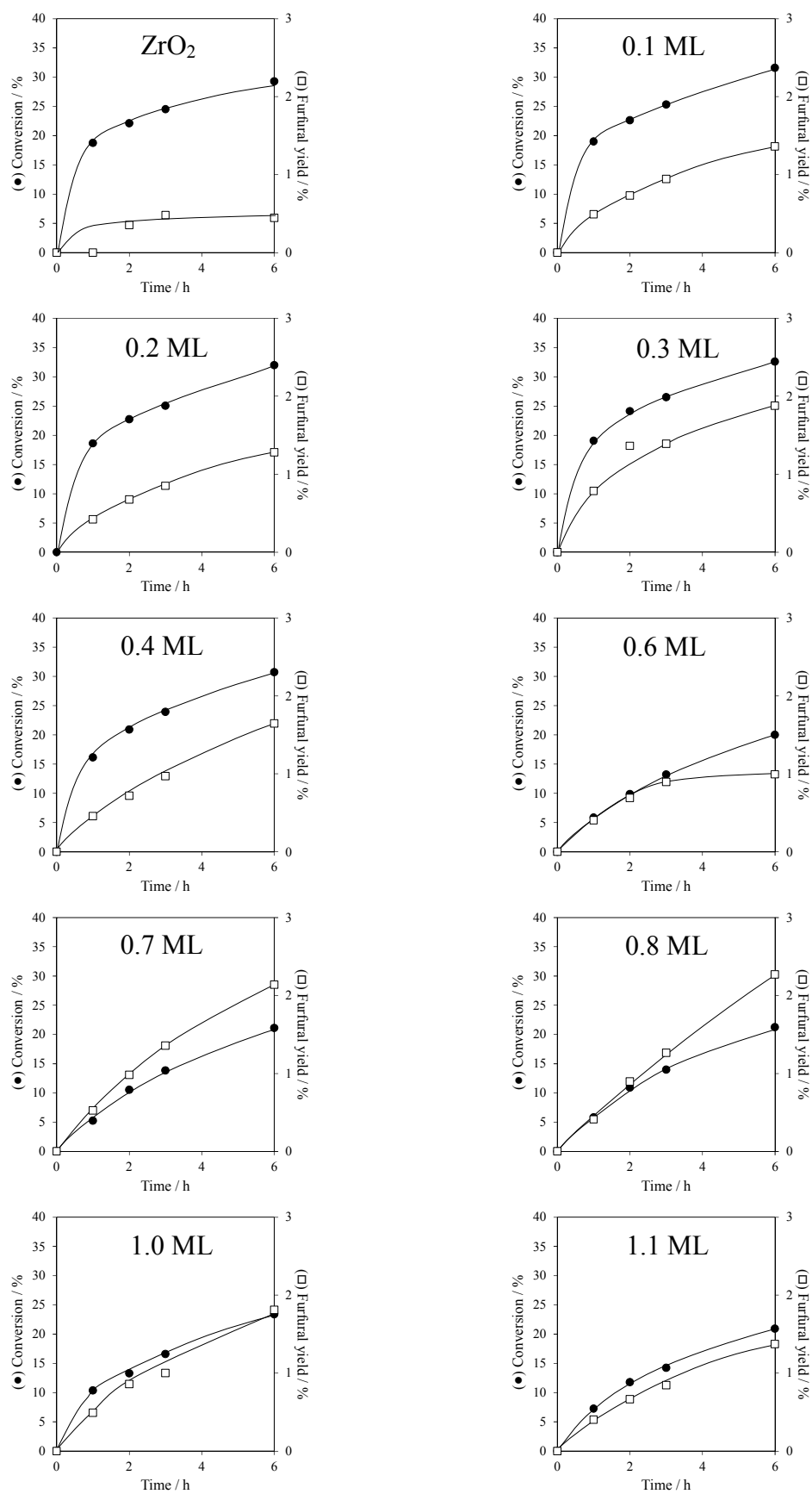


Figure 3.34: Xylose conversion and furfural yield profiles for xylose dehydration reactions over bulk SZ catalysts at 100 °C

Moreover, as it is demonstrated in **Figure 3.35**, furfural TOFs decrease monotonically with θ_{SO_4} . The reason for this also lies in the ratio of Brønsted : Lewis acid sites. So, as the surface sulphate coverage grows, the number of Lewis acid sites decreases, hence the isomerization of xylose to xylulose and lyxose is switched off. Therefore, xylose could only transform to furfural via the direct Brønsted acid catalysed pathway, which is more energy intensive.

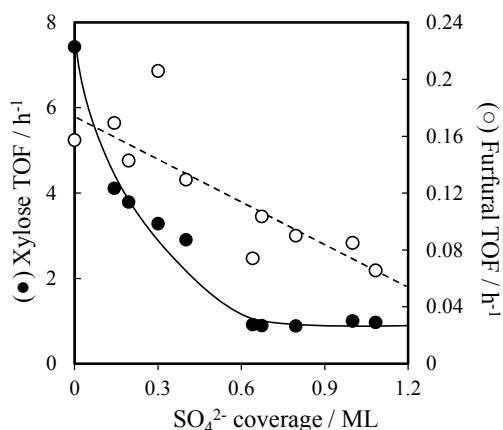


Figure 3.35: (●) Xylose and (○) furfural TOF for xylose conversion at 100 °C over SZ catalysts

In summary, it was proven that in a heterogeneously catalysed xylose transformation to furfural, the ratio between Brønsted and Lewis acid sites is a critical factor in terms of activity of the catalyst and also selectivity towards furfural. Moreover, it was confirmed that the xylose could undergo two different pathways to form furfural; one is via Lewis acid catalysed isomerization to xylulose followed by dehydration of xylulose to produce furfural. And the other pathway is direct dehydration of xylose over Brønsted acid sites.

3.3 Conclusion

The impact of surface sulfation upon the physico-chemical properties of calcined $\text{Zr}(\text{OH})_4$ has been systematically investigated by bulk and surface spectroscopies and chemical probes. The preceding comprehensive characterisation enabled the construction of a model for the SZ system, wherein a coverage-dependent transition occurs from isolated SO_4 species chemisorbed on monoclinic $\text{ZrO}_2 \rightarrow \text{SO}_4$ islands on tetragonal and monoclinic $\text{ZrO}_2 \rightarrow$ a SO_4 monolayer bound to tetragonal ZrO_2 .

The unsulphated precursor forms predominantly monoclinic zirconia possessing mixed Lewis acid and base surface sites which is effective for glucose isomerisation to

fructose but ineffective towards fructose dehydration to 5-HMF. Dilute sulphuric acid pre-treatment of $\text{Zr}(\text{OH})_4$ and subsequent calcination results exclusively in the formation of polydentate surface SO_4^{2-} species, and concomitant stabilisation of tetragonal ZrO_2 . Thus, conferring significant Brønsted acidity and corresponding enhanced HMF production from either glucose or fructose. Higher degrees of surface sulfation ($\theta_{\text{SO}_4} > 0.25 \text{ ML}$), and attendant loss of surface basicity from exposed zirconia, progressively switches off glucose \leftrightarrow fructose isomerisation, while continuing to promote fructose \rightarrow HMF. Saturated sulphate monolayers presented a distribution of mono and polynuclear sulphate species chemisorbed over tetragonal crystalline zirconia and/or amorphous zirconium sulphate, and the resulting materials (which exhibit almost entirely Brønsted acid character) are the least efficient for HMF synthesis from glucose. Sub-monolayer sulphate coverages of approximately 0.3 ML afford the optimal mix of Lewis base sites arising from accessible ZrO_2 , and co-existing Brønsted acid sites arising from mono- or bidentate sulphate, required for the tandem isomerisation of glucose to fructose and the latter's subsequent dehydration to HMF. The design of such bi-functional catalysts capable of effecting one-pot telescopic syntheses in aqueous media will become increasingly critical to achieve atom-economical, selective transformations of bio-derived molecules for sustainable chemicals and fuels.

Moreover, the catalytic activity of sulphated zirconias in xylose transformation to furfural was explored. Furthermore, it was hypothesized that the reaction can take place either via isomerization of xylose to xylulose and lyxose and then dehydration of xylulose to furfural over Lewis acid sites or direct dehydration of xylose to furfural over Brønsted acid sites. Additionally, it was confirmed that by increasing the Brønsted : Lewis acid site ratio the selectivity towards furfural gets improved however the activity of catalyst decreased due to reduced conversion of xylose to undesired insoluble polymers and humins over Lewis acid sites.

3.4 References

1. K. Tanabe, *Materials Chemistry and Physics*, 1985, **13**, 347-364.
2. X. Song and A. Sayari, *Catalysis Reviews*, 1996, **38**, 329-412.
3. G. D. Yadav and J. J. Nair, *Microporous and Mesoporous Materials*, 1999, **33**, 1-48.
4. V. Bolis, G. Magnacca, G. Cerrato and C. Morterra, *Langmuir*, 1997, **13**, 888-894.
5. A. Corma, V. Fornés, M. I. Juan-Rajadell and J. M. L. Nieto, *Applied Catalysis A: General*, 1994, **116**, 151-163.
6. A. Corma, M. I. Juan-Rajadell, J. M. López-Nieto, A. Martinez and C. Martínez, *Applied Catalysis A: General*, 1994, **111**, 175-189.
7. H. Armendariz, B. Coq, D. Tichit, R. Dutartre and F. Figuéras, *Journal of Catalysis*, 1998, **173**, 345-354.
8. F. R. Chen, G. Coudurier, J. F. Joly and J. C. Vedrine, *Journal of Catalysis*, 1993, **143**, 616-626.
9. D. A. Ward and E. I. Ko, *Journal of Catalysis*, 1995, **157**, 321-333.
10. C. M. Volpato, L. G. D. Garbelotto, M. C. Fredel and F. Bondioli, *Advances in Ceramics—Electric and Magnetic Ceramics, Bioceramics, Ceramics and Environment*, edited by C. Sikalidis (InTech, Rijeka, Croatia, 2011), 2011, 397-404.
11. K. Arata, *Applied Catalysis A: General*, 1996, **146**, 3-32.
12. M. Bensitel, O. Saur, J. C. Lavalley and G. Mabilon, *Materials Chemistry and Physics*, 1987, **17**, 249-258.
13. D. A. Ward and E. I. Ko, *Journal of Catalysis*, 1994, **150**, 18-33.
14. D. Farcas, J. Q. Li and S. Cameron, *Applied Catalysis A: General*, 1997, **154**, 173-184.
15. J. Sommer, R. Jost and M. Hachoumy, *Catalysis Today*, 1997, **38**, 309-319.
16. V. Bolis, G. Magnacca, G. Cerrato and C. Morterra, *Topics in Catalysis*, 2002, **19**, 259-269.
17. R. Srinivasan, R. Keogh and B. Davis, *Catalysis Letters*, 1996, **36**, 51-57.
18. R. L. White, E. C. Sikabwe, M. A. Coelho and D. E. Resasco, *Journal of Catalysis*, 1995, **157**, 755-758.

19. F. Pinna, M. Signoretto, G. Strukul, G. Cerrato and C. Morterra, *Catalysis Letters*, 1994, **26**, 339-344.
20. J. Lunsford, H. Sang, S. Campbell, C.-H. Liang and R. Anthony, *Catalysis Letters*, 1994, **27**, 305-314.
21. F. Babou, B. Bigot, G. Coudurier, P. Sautet and J. C. Védrine, in *Studies in Surface Science and Catalysis*, eds. M. M. Hideshi Hattori and O. Yoshio, Elsevier, 1994, vol. Volume 90, pp. 519-529.
22. L. M. Kustov, V. B. Kazansky, F. Figueras and D. Tichit, *Journal of Catalysis*, 1994, **150**, 143-149.
23. V. Adeeva, J. W. Dehaan, J. Janchen, G. D. Lei, V. Schunemann, L. J. M. Vandeven, W. M. H. Sachtler and R. A. Vansanten, *Journal of Catalysis*, 1995, **151**, 364-372.
24. T. Yamaguchi, T. Jin and K. Tanabe, *The Journal of Physical Chemistry*, 1986, **90**, 3148-3152.
25. K. Tanabe, *Catalysis Today*, 1990, **8**, 1-11.
26. K. Arata, in *Advances in Catalysis*, eds. H. P. D.D. Eley and B. W. Paul, Academic Press, 1990, vol. Volume 37, pp. 165-211.
27. K. Arata and M. Hino, *Materials Chemistry and Physics*, 1990, **26**, 213-237.
28. L. Davies, L. Daza and P. Grange, *Journal of Materials Science*, 1995, **30**, 5087-5092.
29. O. Saur, M. Bensitel, A. B. M. Saad, J. C. Lavalley, C. P. Tripp and B. A. Morrow, *Journal of Catalysis*, 1986, **99**, 104-110.
30. M. Bensitel, O. Saur, J. C. Lavalley and B. A. Morrow, *Materials Chemistry and Physics*, 1988, **19**, 147-156.
31. C. Morterra, G. Cerrato, F. Pinna and M. Signoretto, *The Journal of Physical Chemistry*, 1994, **98**, 12373-12381.
32. J. Yang, M. Zhang, F. Deng, Q. Luo, D. Yi and C. Ye, *Chemical Communications*, 2003, 884-885.
33. T. Riemer, D. Spielbauer, M. Hunger, G. A. H. Mekheimer and H. Knozinger, *Journal of the Chemical Society, Chemical Communications*, 1994, 1181-1182.
34. A. Clearfield, G. P. D. Serrette and A. H. Khazi-Syed, *Catalysis Today*, 1994, **20**, 295-312.
35. B. Li and R. D. Gonzalez, *Catalysis Today*, 1998, **46**, 55-67.

36. F. Babou, G. Coudurier and J. C. Vedrine, *Journal of Catalysis*, 1995, **152**, 341-349.
37. J. B. Laizet, A. K. Søiland, J. Leglise and J. C. Duchet, *Topics in Catalysis*, 2000, **10**, 89-97.
38. M. Hino, M. Kurashige, H. Matsushashi and K. Arata, *Thermochimica Acta*, 2006, **441**, 35-41.
39. D. Fraenkel, *Chemistry Letters*, 1999, 917-918.
40. M. A. Aramendía, V. Boráu, C. Jiménez, J. M. Marinas, A. Marinas, A. Porras and F. J. Urbano, *Journal of Catalysis*, 1999, **183**, 240-250.
41. K. Tanabe and T. Yamaguchi, *Catalysis Today*, 1994, **20**, 185-197.
42. X. Qi, M. Watanabe, T. M. Aida and R. L. Smith, Jr., *Catalysis Communications*, 2008, **9**, 2244-2249.
43. X. H. Qi, M. Watanabe, T. M. Aida and R. L. Smith, *Catalysis Communications*, 2009, **10**, 1771-1775.
44. I. J. Dijs, J. W. Geus and L. W. Jenneskens, *The Journal of Physical Chemistry B*, 2003, **107**, 13403-13413.
45. M. A. Ecomier, K. Wilson and A. F. Lee, *Journal of Catalysis*, 2003, **215**, 57-65.
46. C. Morterra, G. Cerrato, C. Emanuel and V. Bolis, *Journal of Catalysis*, 1993, **142**, 349-367.
47. A. E. Hughes and B. A. Sexton, *Journal of Electron Spectroscopy and Related Phenomena*, 1990, **50**, C15-C18.
48. J. F. Moulder and J. Chastain, *Handbook of X-Ray Photoelectron Spectroscopy: A Reference Book of Standard Spectra for Identification and Interpretation of XPS Data*, Perkin-Elmer Corporation, Physical Electronics Division, 1992.
49. J. L. Colón, D. S. Thakur, C.-Y. Yang, A. Clearfield and C. R. Martini, *Journal of Catalysis*, 1990, **124**, 148-159.
50. A. V. Naumkin, A. Kraut-Vass, S. W. Gaarenstroom and C. J. Powell, *NIST Standard Reference Database 20, Version 4.1 (Online version)*, 2014.
51. D. B. C.D. Wagner, M.P. Seah (Eds), *Practical Surface Analysis*, Wiley, Chichester, UK, 1990.
52. S. J. Hug, *Journal of Colloid and Interface Science*, 1997, **188**, 415-422.
53. K. Nakamoto, J. Fujita, S. Tanaka and M. Kobayashi, *Journal of the American Chemical Society*, 1957, **79**, 4904-4908.

54. F. Haase and J. Sauer, *Journal of the American Chemical Society*, 1998, **120**, 13503-13512.
55. C. Morterra, G. Cerrato, F. Pinna, M. Signoretto and G. Strukul, *Journal of Catalysis*, 1994, **149**, 181-188.
56. P. Carniti, A. Gervasini and M. Marzo, *Catalysis Communications*, 2011, **12**, 1122-1126.
57. A. J. Crisci, M. H. Tucker, J. A. Dumesic and S. L. Scott, *Topics in Catalysis*, 2010, **53**, 1185-1192.
58. J. Wang, W. Xu, J. Ren, X. Liu, G. Lu and Y. Wang, *Green Chemistry*, 2011, **13**, 2678-2681.
59. Q. Cao, X. Guo, J. Guan, X. Mu and D. Zhang, *Applied Catalysis A: General*, 2011, **403**, 98-103.
60. S. J. Rak, G. T. Dong and K. S. Bok, *Bulletin of the Korean Chemical Society*, 2001, **22**, 1309-1315.
61. D. I. Torres and J. Llopis, *Superlattices and Microstructures*, 2009, **45**, 482-488.
62. M. Li, Z. Feng, G. Xiong, P. Ying, Q. Xin and C. Li, *The Journal of Physical Chemistry B*, 2001, **105**, 8107-8111.
63. V. Bolis, G. Cerrato, G. Magnacca and C. Morterra, *Thermochimica Acta*, 1998, **312**, 63-77.
64. V. Bolis, C. Morterra, M. Volante, L. Orio and B. Fubini, *Langmuir*, 1990, **6**, 695-701.
65. W. Hertl, *Langmuir*, 1989, **5**, 96-100.
66. R.-J. van Putten, J. C. van der Waal, E. de Jong, C. B. Rasrendra, H. J. Heeres and J. G. de Vries, *Chemical Reviews*, 2013, **113**, 1499-1597.
67. J. F. Saeman, *Industrial & Engineering Chemistry*, 1945, **37**, 43-52.
68. K. R. Heimlich and A. N. Martin, *Journal of the American Pharmaceutical Association*, 1960, **49**, 592-597.
69. S. W. McKibbins, J. F. Harris, J. F. Saeman and W. K. Neill, *Forest Products Journal*, 1962, **12**, 17.
70. P. R. Bienkowski, M. R. Ladisch, R. Narayan, G. T. Tsao and R. Eckert, *Chemical Engineering Communications*, 1987, **51**, 179-192.
71. D. W. Harris and M. S. Feather, *Journal of the American Chemical Society*, 1975, **97**, 178-181.

72. H. S. Isbell, H. L. Frush, C. W. R. Wade and C. E. Hunter, *Carbohydrate Research*, 1969, **9**, 163-175.
73. A. J. Shaw Iii and G. T. Tsao, *Carbohydrate Research*, 1978, **60**, 327-325.
74. M. J. Antal Jr, W. S. L. Mok and G. N. Richards, *Carbohydrate Research*, 1990, **199**, 91-109.
75. Y. Román-Leshkov, M. Moliner, J. A. Labinger and M. E. Davis, *Angewandte Chemie International Edition*, 2010, **49**, 8954-8957.
76. M. Moliner, Y. Román-Leshkov and M. E. Davis, *Proceedings of the National Academy of Sciences*, 2010, **107**, 6164-6168.
77. J. F. Miñambres, M. A. Aramendía, A. Marinas, J. M. Marinas and F. J. Urbano, *Journal of Molecular Catalysis A: Chemical*, 2011, **338**, 121-129.
78. F. J. Urbano, M. A. Aramendía, A. Marinas and J. M. Marinas, *Journal of Catalysis*, 2009, **268**, 79-88.
79. V. Choudhary, S. I. Sandler and D. G. Vlachos, *ACS Catalysis*, 2012, **2**, 2022-2028.
80. M. J. Climent, A. Corma and S. Iborra, *Green Chemistry*, 2014, **16**, 516-547.
81. W. De Jong and G. Marcotullio, *International journal of chemical reactor engineering*, 2010, **8**.
82. H. J. Brownlee and C. S. Miner, *Industrial & Engineering Chemistry*, 1948, **40**, 201-204.
83. B. Danon, G. Marcotullio and W. de Jong, *Green Chemistry*, 2014, **16**, 39-54.
84. G. Marcotullio and W. De Jong, *Green Chemistry*, 2010, **12**, 1739-1746.
85. G. Marcotullio and W. de Jong, *Carbohydrate Research*, 2011, **346**, 1291-1293.
86. M. J. Climent, A. Corma and S. Iborra, *Green Chemistry*, 2011, **13**, 520-540.
87. R. O'Neill, M. N. Ahmad, L. Vanoye and F. Aiouache, *Industrial & Engineering Chemistry Research*, 2009, **48**, 4300-4306.
88. C. Moreau, R. Durand, D. Peyron, J. Duhamet and P. Rivalier, *Industrial Crops and Products*, 1998, **7**, 95-99.
89. S. Lima, M. M. Antunes, A. Fernandes, M. Pillinger, M. F. Ribeiro and A. A. Valente, *Applied Catalysis A: General*, 2010, **388**, 141-148.
90. S. Kim, S. You, Y. Kim, S. Lee, H. Lee, K. Park and E. Park, *Korean J. Chem. Eng.*, 2011, **28**, 710-716.
91. A. Takagaki, M. Ohara, S. Nishimura and K. Ebitani, *Chemistry Letters*, 2010, **39**, 838-840.

92. A. S. Dias, M. Pillinger and A. A. Valente, *Journal of Catalysis*, 2005, **229**, 414-423.
93. E. Lam, E. Majid, A. C. W. Leung, J. H. Chong, K. A. Mahmoud and J. H. T. Luong, *ChemSusChem*, 2011, **4**, 535-541.
94. J. Zhang, J. Zhuang, L. Lin, S. Liu and Z. Zhang, *Biomass and Bioenergy*, 2012, **39**, 73-77.
95. A. Dias, S. Lima, M. Pillinger and A. Valente, *Catal Lett*, 2007, **114**, 151-160.
96. S. Lima, A. Fernandes, M. Antunes, M. Pillinger, F. Ribeiro and A. Valente, *Catal Lett*, 2010, **135**, 41-47.
97. X. Shi, Y. Wu, P. Li, H. Yi, M. Yang and G. Wang, *Carbohydrate Research*, 2011, **346**, 480-487.
98. R. Weingarten, G. A. Tompsett, W. C. Conner Jr and G. W. Huber, *Journal of Catalysis*, 2011, **279**, 174-182.
99. R. Weingarten, J. Cho, J. W. C. Conner and G. W. Huber, *Green Chemistry*, 2010, **12**, 1423-1429.
100. M. J. Climent, A. Corma and S. Iborra, *Chemical Reviews*, 2010, **111**, 1072-1133.
101. J. N. Chheda, Y. Roman-Leshkov and J. A. Dumesic, *Green Chemistry*, 2007, **9**, 342-350.
102. I. Agirrezabal-Telleria, A. Larreategui, J. Requies, M. B. Güemez and P. L. Arias, *Bioresource Technology*, 2011, **102**, 7478-7485.
103. I. Agirrezabal-Telleria, J. Requies, M. B. Güemez and P. L. Arias, *Applied Catalysis B: Environmental*, 2014, **145**, 34-42.

Chapter 4

**Glucose transformation to HMF over SBA-15
supported sulphated zirconia catalysts: the role
of zirconia film and sulphur content**

4.1 Introduction

Chapter 3 has highlighted how tuning acid:base distribution can significantly affect glucose/fructose conversion and how this in turn can be used to optimise HMF production. While such crystalline SZ catalysts are promising, they have inherently low surface areas (typically $< 150 \text{ m}^2 \text{ g}^{-1}$), thus employing techniques to stabilise a highly porous or dispersed ZrO_2 phase would be of great benefit to improving catalyst efficiency.

Direct synthesis of mesoporous $\text{ZrO}_2/\text{SiO}_2$ has been reported using two major techniques. The first one is conventional sol-gel technique using one or both alkoxides^{1, 2}. Generally in the sol-gel method, metallic alkoxides undergo hydrolysis and subsequent condensation in an alcohol solvent, forming a macro-polymeric oxide network which is usually referred to as an alcogel. After drying and calcining, a sol-gel synthesized oxide is obtained. In this technique, preparation conditions such as metallic alkoxide concentration, pH, the type of complexing agent, the amount of hydrolysing water play key roles in determining the textural properties of the catalyst. The second common method of preparing zirconia/silica material is co-precipitation^{3, 4} in which zirconium and silicon precursors are precipitated simultaneously in a neutral environment.

A major drawback associated with most of these syntheses is thermal instability of obtained meso-structured material which results in structural collapse during calcination at high temperatures used to activate the catalyst.⁵ To overcome this problem, robust high surface area supports such as nano-structured silica (e.g. SBA-15, KIT-6, MM-SBA-15) offering process advantages by providing a high surface area and tuneable porosity are suitable scaffolds over which to disperse the ZrO_2 phase. However, to maintain the accessibility of the internal pore network, it is critical that such coatings are applied in a uniform layer-by-layer morphology without the formation of large 3D crystallites or significant pore blockage.

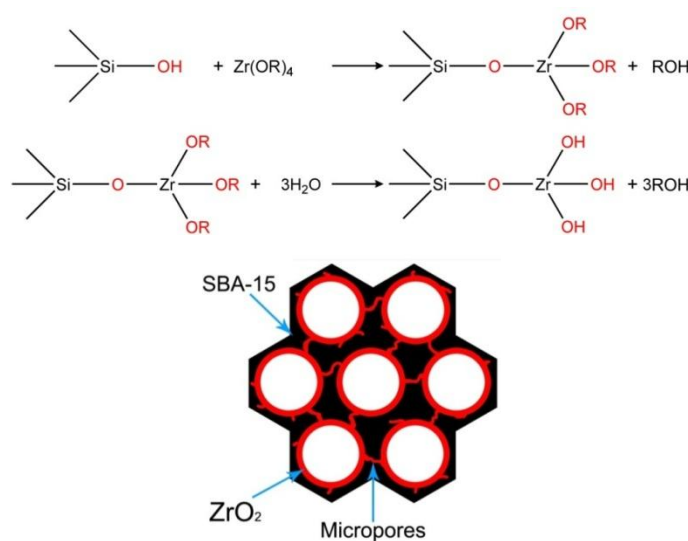
Several groups have explored methods to graft ZrO_2 on SBA-15, using incipient wetness impregnation⁶⁻¹¹, urea hydrolysis¹² or Vapor Induced Hydrolysis (VIH)^{5, 13} methods. Incipient wetness method generally uses zirconium propoxide⁶⁻¹⁰ or acetate¹¹

precursor in an anhydrous organic solvent (e.g. dry hexane or 50:50 vol% anhydrous toluene:ethanol) with the concentration of the precursor varied to obtain materials with different zirconium loadings, which invariably gives large crystallites (3-4 nm). Hydrolysis methods generally involve the precursor zirconium oxychloride ($\text{ZrOCl}_2 \cdot 8\text{H}_2\text{O}$) or zirconyl nitrate⁵ being dispersed over the support and then precipitated via the addition of base (urea or NH_3/Water) to produce zirconium hydroxide inside the pores. Few of these studies explore the sulfation of these materials, although the direct use of $\text{Zr}(\text{SO}_4)_2$ as precursor instead of zirconyl nitrate has also been explored and shows loss of catalyst acidity due to leaching of sulphur species.¹³

Therefore, the main objective of this investigation was to prepare high surface area $\text{SO}_4/\text{ZrO}_2/\text{SBA-15}$ catalysts with good textural and high accessibility of ZrO_2 and SO_4 species. By studying the effect of surface coverage using a layer by layer approach in grafting zirconia on SBA-15 a more uniform coating is expected.

4.2 Results and discussion

Here in this thesis, as it was explained in **Chapter 2**, zirconia was grafted on SBA-15 using anhydrous zirconium propoxide as metal precursor. As represented in **Scheme 4.1**, the zirconium propoxide attacks the hydroxyl groups of SBA-15 and thus the zirconium atoms bond to the surface of support.



Scheme 4.1: Reaction schemes for zirconia grafting on SBA-15 and graphical representation of final $\text{Zr}/\text{SBA-15}$

The concentration of zirconium propoxide used in each cycle was based upon the amount required for a theoretical monolayer assuming a hydroxyl density of SBA-15 of $0.0125 \text{ mole g}^{-1}$. In order to measure the density of OH groups, a sample of the parent SBA-15 was analysed by TGA from room temperature to 1050°C and the mass loss at high temperatures was attributed to liberation of surface OH groups. It is assumed that each OH group that is eliminated from silica will be replaced by a zirconium propoxide molecule. So, it is necessary to calculate the number of OH groups in SBA-15. **Figure 4.1** shows the changes in mass % of the SBA-15 sample as a function of temperature as well as the derivative of mass. The sharp drop in range of room temperature and 200°C attributed to the loss of physisorbed moisture on SBA-15. It is assumed that the mass loss above 200°C is due to elimination of OH groups from silica. The mass change in this range is 1.61 mg that is equal to 0.179 mmole of OH^- . Therefore, there was 0.0125 mole OH per gram of SBA-15 sample. In other words, $0.0125 \text{ mole Zr(OPr)}_4$ can be grafted on each gram of SBA-15. Since the molecular weight of zirconium propoxide is $327.6 \text{ g mole}^{-1}$, hence 4.1 g zirconium propoxide is required. And because the zirconium precursor is provided as a 70 wt\% solution in propanol, 5.85 g of the solution should be theoretically enough to graft a uniform monolayer of zirconium on 1 g SBA-15.

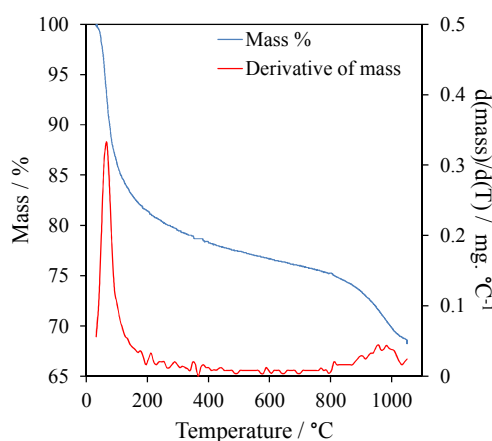


Figure 4.1: Thermal gravimetric analysis on the parent SBA-15

A rehydration step was applied in the preparation protocol in order to make sure all the $-\text{OR}$ groups are replaced by hydroxyls. This is important because under anhydrous conditions the grafted alkoxide is relatively inert toward further reaction with Zr(OPr)_4 .¹⁴ By the end of this process as illustrated in **Scheme 4.1**, it is expected that zirconia fills and or block the micropores of SBA-15 and the mesopores are uniformly coated with zirconia.

For grafting the second layer of zirconia, calcination of 1 monolayer zirconia/SBA-15 material was avoided because calcination will result in change in crystalline form of zirconia layer and could affect the incorporation of the next layers.

4.2.1 Characterization of parent Zr/SBA-15

Initial studies focussed on optimisation of the coating methodology to determine the morphology of deposited ZrO_2 films and how this evolved with film thickness. What follows is a detailed characterisation of these ZrO_2 grafted SBA-15 materials and their sulphated analogues following 1-3 grafting cycles and rehydration.

4.2.1.1 Powder X-ray diffraction

Figure 4.2 presents low-angle diffraction patterns which evidence a major diffraction at $2\theta \sim 1^\circ$, and two less intense signals at $2\theta \sim 1.7^\circ$ and 1.9° for all of the mesostructured samples. These diffractions can be attributed respectively to the 100, 110 and 200 planar symmetries typical of a periodic mesoporous framework with a *p6mm* hexagonal ordering.^{15, 16} The X-ray diffraction patterns of the grafted samples were nearly identical to that of the bare SBA-15, verifying the retention of the pore structure even after grafting process. The decrease in the intensity of the patterns after the grafting cycles, is attributable to the incorporation of zirconia on the support.

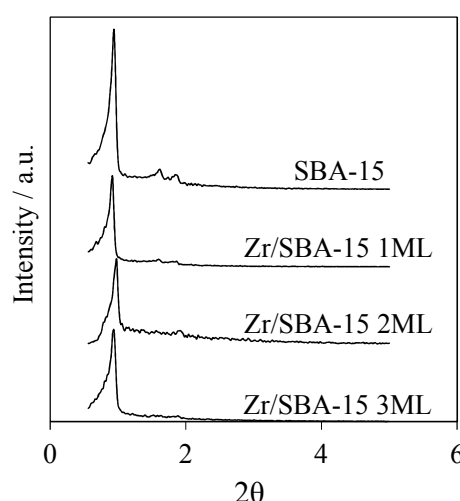


Figure 4.2: Low angle X-Ray powder diffraction patterns of SBA-15 support and Zr/SBA-15 materials as a function of nominal zirconium monolayer

XRD analysis at wider angles, in the range of 10° to 80° , has been performed in order to assess the existence of crystalline zirconium oxide domains on the $\text{ZrO}_2/\text{SBA-15}$

materials. The absence of the monoclinic and tetragonal crystals is verified since their characteristic peaks are not observed in the XRD patterns, indicating that the size of loaded zirconia is in nano-scale and therefore below the detection limit of XRD instrument. (**Figure 4.3**)

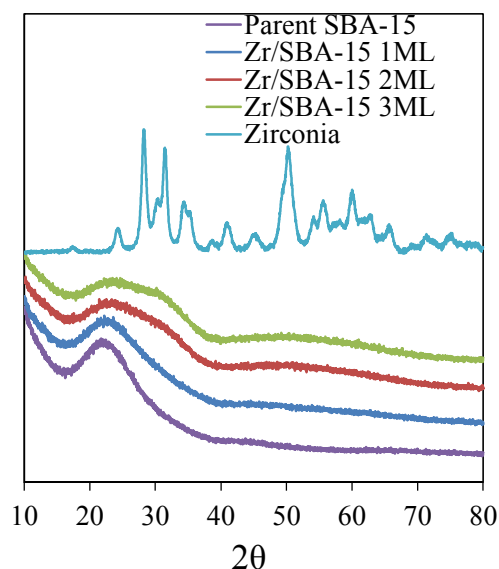


Figure 4.3: Wide angle X-Ray powder diffraction patterns of the parent SBA-15 support, zirconia grafted SBA-15 materials and pure zirconia

4.2.1.2 N₂ porosimetry

One of the deficiencies of zirconia-based catalysts is the low surface area which results in limited interface and therefore most of zirconia species will not be accessible by the reactant molecules.⁶ So designing a zirconia-based catalyst with improved textural properties by use of high surface area supports is of great interest. Among the high surface area supports, SBA-15 silica-type offers additional advantages over other materials, which include a tunable large-sized pore structure together with a high hydrothermal stability.^{17, 18} As it is demonstrated in **Figure 4.4.a**, all of the samples exhibit type IV adsorption isotherms, typical of mesostructure SBA-15. The steep H1 hysteresis loops match with the existence of uniform pores for all of the samples¹⁹, although their sizes decrease as the zirconium loadings increase suggesting that the incorporation of Zr species mainly occurs onto the surface of mesopores, thus leading to the thickening of the mesopores walls as well as reduction of the void volume of the meso-structured porous system. **Table 4.1** summarizes the textural properties of the parent SBA-15 and ZrO₂ grafted samples as a function of nominal monolayers of ZrO₂.

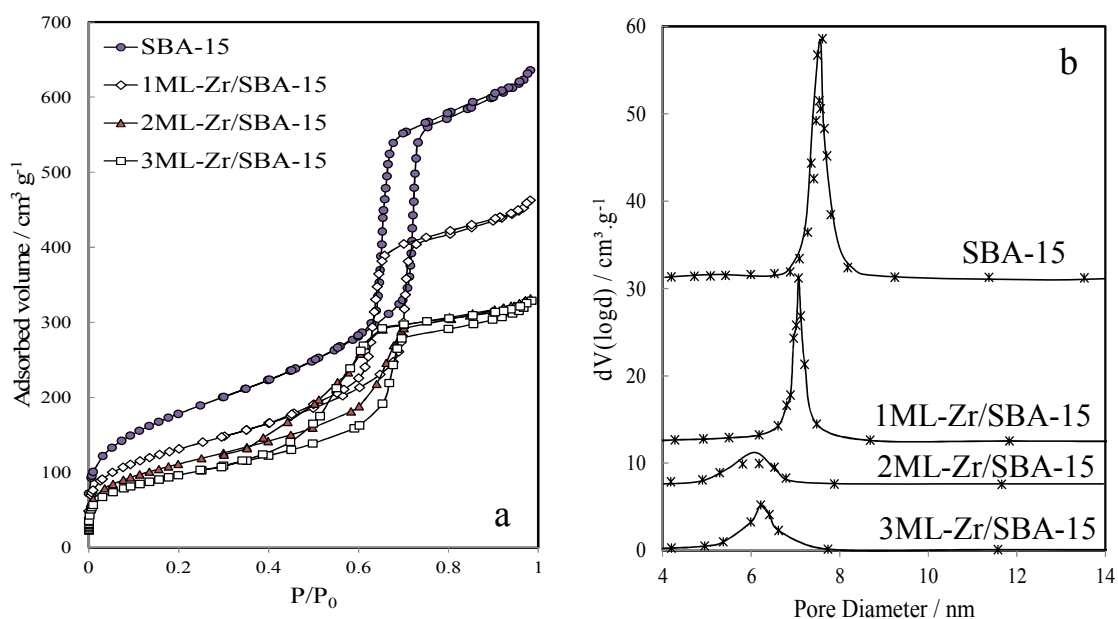


Figure 4.4: a) N₂ adsorption isotherms and b) pore size distribution of parent SBA-15 and Zr/SBA-15 materials

Table 4.1: Surface area, pore diameter, micropore/mesopore and total pore volume of parent SBA-15 and SZ/SBA-15 samples as a function of nominal ZrO₂ monolayer.

Sample	Surface area ^a m ² .g ⁻¹	Pore diameter ^b nm	Micropore vol ^c cm ³ .g ⁻¹	Mesopore vol ^d cm ³ .g ⁻¹	Total pore vol ^e cm ³ .g ⁻¹
SBA-15	647	7.5	0.073	0.574	0.964
1ML-Zr/SBA-15	473	7.1	0.055	0.433	0.700
2ML-Zr/SBA-15	402	6.2	0.041	0.332	0.506
3ML-Zr/SBA-15	348	6.2	0.035	0.302	0.485

^a N₂ BET, ^b BJH desorption branch of isotherm, ^c N₂ t-plot, ^d BJH desorption branch of isotherm, ^e Total pore volume recorded at P/P₀=0.975

4.2.1.3 Calculation of ZrO₂ film thickness and elemental analysis by XPS and SEM/EDX

XPS was employed in order to further confirm the growth mode, using attenuation of the Si 2p signal following each grafting cycle as a measure of film thickness. For this purpose, the following exponential function was plotted (the dashed-line curve in **Figure 4.5**)

$$f(d) = I_d/I_0 = \exp\left(\frac{-d}{\lambda \sin\theta}\right) \quad \text{Equation 4.1}$$

Using $\lambda = 1.26$ nm and $\theta = 42^\circ$ and d is the film thickness. The black circles in **Figure 4.5** shows the variation in Si substrate intensity after each ZrO₂ deposition, which

reveals an exponential decay that fits well to a layer by layer model. The first and second grafting cycles gives rise to a 35.6 and 51.9% attenuation, corresponding to a layer of 0.5 and 0.84 nm thick respectively. This is in remarkable agreement with a (111) oriented layer of monoclinic ZrO_2 which is 0.42 nm as indicated in **Figure 4.5** thus confirming the successful layer-by-layer growth of ZrO_2 in this synthesis.²⁰ **Table 4.2** represents the attenuation of the Si 2p signal as well as calculated and theoretical values for zirconia film thickness.

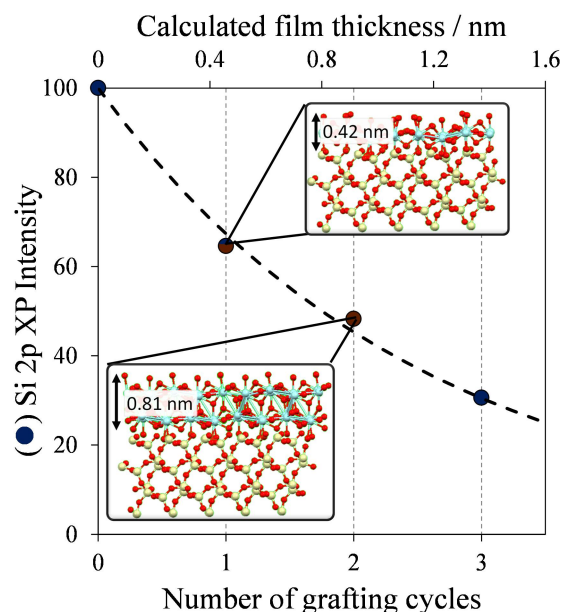


Figure 4.5: Si 2p XP attenuation following 1-3 grafting cycles demonstrating layer-by-layer growth of ~ 0.42 nm thick ZrO_2 sheets. Dashed line shows the theoretical fit and associated film thickness to achieve the observed attenuation;

Table 4.2: attenuation of the Si 2p signal and calculated and theoretical values for zirconia film thickness

	Si 2p intensity	Si 2p relative intensity %	Calculated film thickness nm	Theoretical film thickness ^a nm
SBA-15	7320.5	100.0	0	0
1ML Zr/SBA-15	4727.3	64.6	0.5	0.42
2ML Zr/SBA-15	3534.8	48.3	0.84	0.84
3ML Zr/SBA-15	2240.2	30.6	1.37	1.26

^a Measured thickness of a (111) oriented monolayer of monoclinic ZrO_2 (0.42 nm)²⁰

The XP spectra of the zirconia grafted materials are presented in **Figure 4.6** wherein we can clearly observe that Si 2p signal attenuated as more zirconia is grafted on the SBA-15.

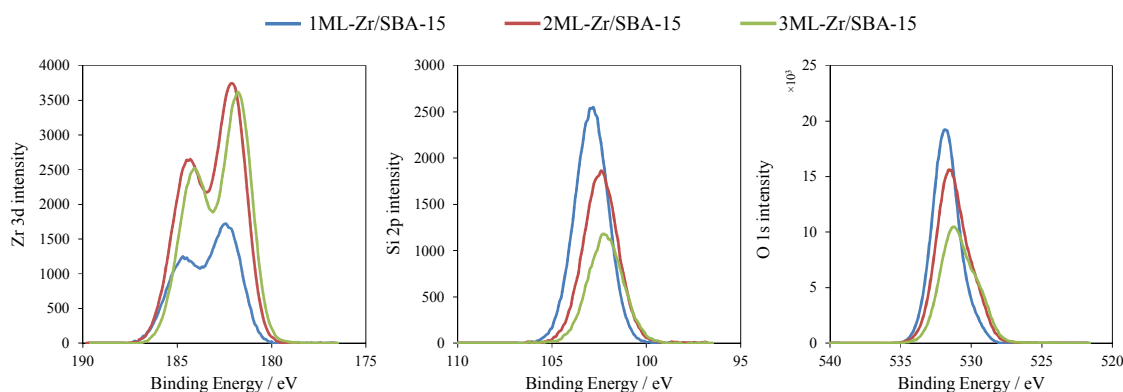


Figure 4.6: High resolution XPS of zirconium, silicon and oxygen for xML-Zr/SBA-15 series as a function of ZrO₂ monolayers.

Furthermore, the surface composition of the zirconia grafted SBA-15 materials was obtained from XPS analysis and results are presented in **Table 4.3**.

Table 4.3: Surface and bulk composition of SBA-15 supported ZrO₂ as a function of nominal zirconia monolayers.

	Surface composition from XPS				Bulk composition from EDX			
	Si	O	Zr	Zr/Si	Si	O	Zr	Zr/Si
	wt%	wt%	wt%	Atomic ratio	wt%	wt%	wt%	Atomic ratio
SBA-15	38.9	61.1	-	-	46.3	53.7	-	-
1ML-Zr/SBA-15	31.1	55.1	13.9	0.1	36.8	53.1	10.1	0.1
2ML-Zr/SBA-15	22.2	50.0	27.8	0.4	33.3	47.4	19.3	0.2
3ML-Zr/SBA-15	18.7	47.8	33.6	0.6	28.5	50.0	21.5	0.2

4.2.1.4 Acid site measurements

NH₃ adsorption calorimetry studies showed that the enthalpy of adsorption for the zirconia grafted SBA-15 samples is below the physisorption threshold, meaning that the number of acid sites on these materials is negligible. This is not particularly surprising as calcined bulk zirconia possesses very few acid sites too. (See **Chapter 3**)

4.2.2 Characterization of xML-SZ/SBA-15 catalysts

The zirconia grafted SBA-15 materials were eventually sulphated using 0.075 M H₂SO₄. Based on the calculations demonstrated in **Chapter 3**, impregnation of bulk zirconia with 0.075 M H₂SO₄ results in formation of a sub-monolayer of sulphate groups. Therefore this concentration was picked in order to stay in SO₄²⁻ sub-monolayer regime.

4.2.2.1 Powder X-ray diffraction

Figure 4.7 shows the low angle XRD patterns for SZ/SBA-15 material after calcination. Similar to non-sulphated samples, XRD patterns exhibit one very intense diffraction peak and two weak peaks, which are characteristic of a 2D hexagonal ($p6mm$) structure.^{15, 16} Therefore, it can be confirmed that the support has retained its well-ordered meso-structure after sulfation and calcination steps.

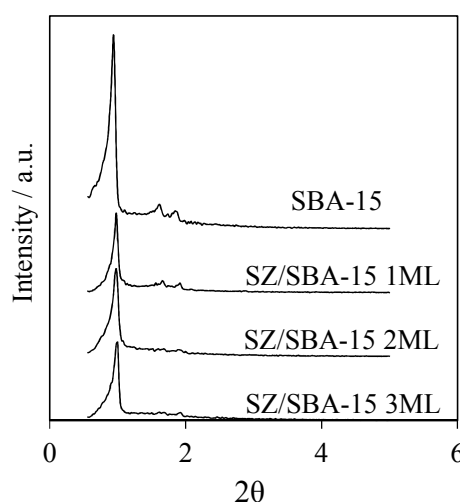


Figure 4.7: Low angle X-Ray powder diffraction patterns of SBA-15 support and SZ/SBA-15 materials as a function of nominal zirconium monolayer

The wide angle XRD patterns can also confirm that sulfation of the Zr/SBA-15 materials did not result in formation of large crystallites. (**Figure 4.8**) The wide angle XRD pattern of a bulk SZ is plotted so that it is possible to see where to expect any potential peak.

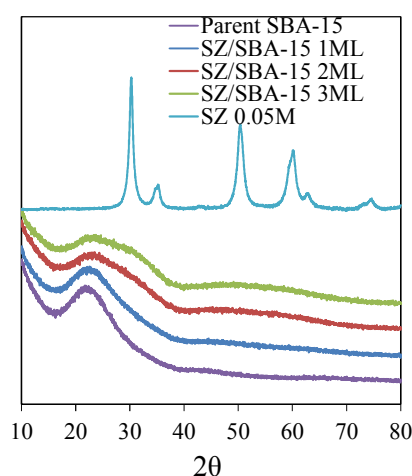


Figure 4.8: Wide angle X-Ray powder diffraction patterns of the parent SBA-15 support, sulphated bulk zirconia and x-ML-SZ/SBA-15 materials

4.2.2.2 N₂ porosimetry

Figure 4.9 demonstrates N₂ isotherms and pore size distribution for parent SBA-15 and the calcined sulphated zirconia grafted SBA-15 catalysts. From there, it can be observed that by incorporating sulphate species on ZrO₂/SBA-15 materials, the structure of SBA-15 support remains intact. Additionally, the N₂ isotherms and pore size distributions are nearly identical to those of non-sulphated samples, however the surface area of the sulphated materials are about 30-40 m² g⁻¹ less than those for non-sulphated ones. The detailed information about textural properties of 1 to 3 ML SZ/SBA-15 samples is given in **Table 4.4**.

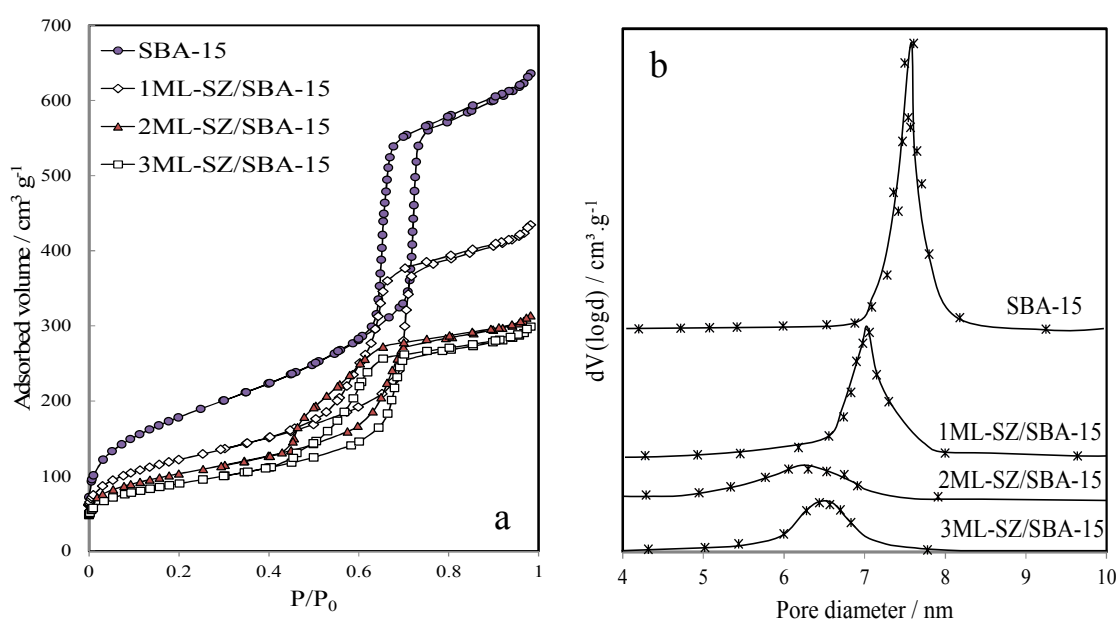


Figure 4.9: a) N₂ adsorption isotherms and b) pore size distribution of parent SBA-15 and xML-SZ/SBA-15 materials

Table 4.4: Textural properties of parent SBA-15 and SZ/SBA-15 samples as a function of nominal ZrO₂ monolayer.

Sample	Surface area ^a m ² .g ⁻¹	Pore diameter ^b nm	Micropore vol ^c cm ³ .g ⁻¹	Mesopore vol ^d cm ³ .g ⁻¹	Total pore vol ^e cm ³ .g ⁻¹
SBA-15	647	7.5	0.073	0.574	0.964
1ML-SZ/SBA-15	437	7.1	0.061	0.382	0.655
2ML-SZ/SBA-15	367	6.3	0.055	0.292	0.474
3ML-SZ/SBA-15	321	6.4	0.045	0.126	0.449

^a N₂ BET, ^b BJH desorption branch of isotherm, ^c N₂ t-plot, ^d BJH desorption branch of isotherm, ^e Total pore volume recorded at P/P₀=0.975

Calculation of the pore wall thickness

Table 4.5 displays the unit cell sizes (a_0) calculated for the different materials assuming a hexagonal array of pores with *pmm6* topology. Pore wall thickness has also been calculated subtracting average pore diameter (calculated from N₂ porosimetry experiments, see **section 4.2.1.2**) from the unit cell size. Incorporating the successive layers of zirconium dioxide leads to a slight reduction in the unit cell size, probably because of the constriction of the mesoporous structure caused by the repeating calcination steps. However, the reduction of the pore size is more intense resulting in the thickening of the pore wall as the amount of Zr incorporated to the mesostructured material increases, confirming the preferential incorporation of the metal species onto the surface of the mesoporous system. Interestingly, the difference between the wall thickness of SBA-15 and 2ML-SZ/SBA-15 is in good agreement with film thickness calculations based on XPS analysis.

Table 4.5: Unit cell sizes and pore wall thickness calculated from XRD and N₂ adsorption-desorption analyses.

Sample	d_{100} ^a nm	Unit cell size (a) ^b nm	Pore size ^c nm	Pore wall thickness (t_w) ^d nm
SBA-15	9.4	10.9	7.5	3.4
1ML-SZ/SBA-15	9.0	10.6	7.1	3.5
2ML-SZ/SBA-15	9.0	10.5	6.3	4.2
3ML-SZ/SBA-15	8.8	10.4	6.4	4.0

^aInterlayer spacing derived from Bragg's Law, ^bPore spacing, ^cBJH average pore diameters from desorption isotherm, ^dWall thickness=($2d_{100}/\sqrt{3}$)-pore diameter.

4.2.2.3 Surface and bulk elemental analysis

The impact of sulfation on ZrO₂/SBA-15 materials was explored by XPS to determine surface composition of the samples. From high resolution XP spectra (**Figure 4.10**), the evolution of Zr and S species in the surface of SBA-15 can be observed, confirming that as the zirconium content of the materials is increased, SO₄²⁻ groups are only incorporated on the zirconia film and not on the surface of silica support. **Table 4.6** presents detailed information about surface composition of SZ/SBA-15 catalysts.

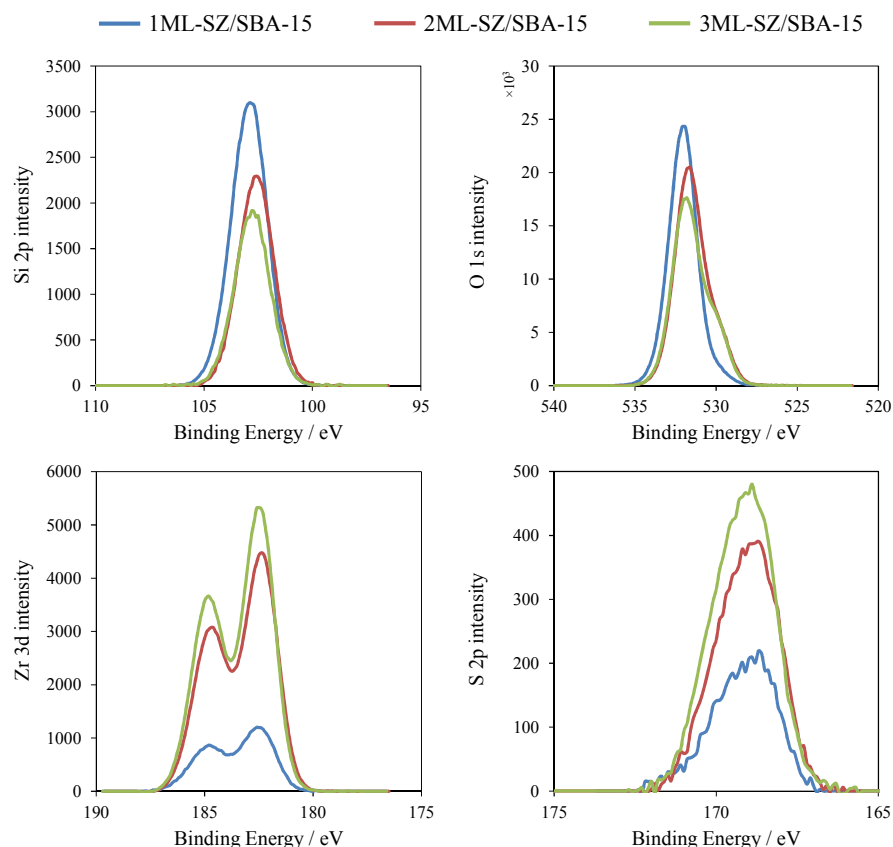


Figure 4.10: High resolution XPS of silicon, oxygen, zirconium and sulphur for xML-SZ/SBA-15 series as a function of nominal ZrO₂ monolayers.

Moreover, plots of the surface Zr:Si against bulk Zr:Si show no change on sulfation (**Figure 4.11.a**), confirming there is no sintering of the ZrO₂ overlayer. The surface S:Zr ratio remains above that of the bulk, again consistent with surface sulfation (**Figure 4.11.b**). Furthermore, comparison of the Zr:Si atomic ratios determined from XPS and EDX (**Figure 4.11.b**) shows these deviate strongly from the 1:1 reference line, as expected for attenuation of the underlying SiO₂ substrate by a uniformly deposited thin SZ film. Note the Zr:Si ratio is unchanged upon sulfation suggesting there is minimal sintering of the ZrO₂ film upon impregnation with H₂SO₄ and calcination under these conditions. In connection to this, **Table 4.6** shows the bulk Zr and S content for each grafting cycle, revealing a steady increase in Zr content from 1-3 ML along with a decrease in the S:Zr ratio, as expected for thicker ZrO₂ coverage in which only the surface layer is sulphated.

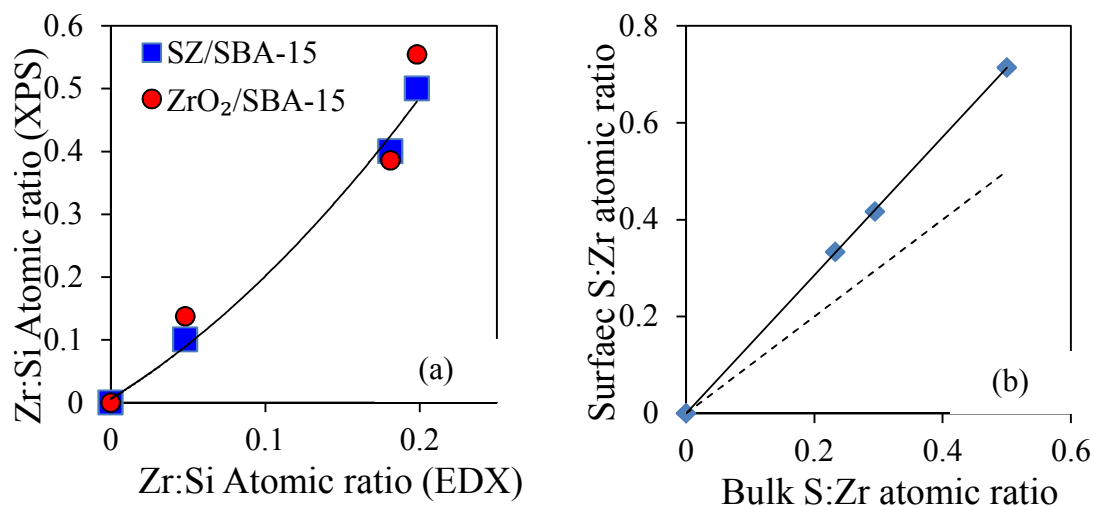


Figure 4.11: Plot of surface and bulk from XPS and EDX measurements for a) Zr:Si atomic ratios for ZrO₂/SBA-15 and SZ/SBA-15 series and b) S:Zr ratios for SZ/SBA-15 materials

Table 4.6: Surface and bulk composition of SBA-15 and SZ functionalized SBA-15 as a function of nominal zirconia monolayers.

	Surface composition from XPS						Bulk composition from EDX					
	Si	O	Zr	S	S/Zr	Zr/Si	Si	O	Zr	S	S/Zr	Zr/Si
	wt%	wt%	wt%	wt%	Atomic ratio	Atomic ratio	wt%	wt%	wt%	wt%	Atomic ratio	Atomic ratio
SBA-15	38.9	61.1	-	-	-	-	46.3	53.7	-	-	-	-
1ML-SZ/SBA-15	32.3	58.0	8.3	1.4	0.7	0.1	38.3	54.7	6.0	1.0	0.5	0.1
2ML-SZ/SBA-15	21.0	50.1	26.6	2.4	0.4	0.4	32.3	47.0	19.0	2.0	0.3	0.2
3ML-SZ/SBA-15	18.2	47.1	31.7	3.0	0.3	0.5	31.7	46.3	20.4	1.7	0.2	0.2

4.2.2.4 Acid and base site measurements

Acid site strength and loading was probed by NH₃ calorimetry (**Figure 4.12** and **Table 4.7**), which shows all samples exhibit a plateau in $-\Delta H_{\text{ads}} \sim 100\text{-}120 \text{ kJ mol}^{-1}$ evidencing strong Brønsted acid sites, the uptake of which is highest for the 2ML-SZ/SBA-15 sample. It is also interesting to note that the 1 and 2 ML samples exhibit a small proportion of sites at low NH₃ coverage with $-\Delta H_{\text{ads}} \sim 180\text{-}200 \text{ kJ mol}^{-1}$ which are attributable to strong Lewis acid sites.²¹ Additionally, the TPD analysis confirms the results obtained by NH₃ adsorption calorimetry (**Figure 4.13**). A decreased proportion of Lewis acid sites with each ZrO₂ grafting cycle is evident from pyridine titration (**Figure 4.14** and **Figure 4.15**) which shows the Brønsted : Lewis acid site ratio increases continually across the series. Such an observation would suggest the initial ZrO₂ layers are more defective or electronically perturbed by the underlying SiO₂ substrate than the multilayer grafted materials. **Figure 4.15** also shows how the corresponding acid site loading from NH₃ TPD varies with ZrO₂ film thickness,

showing a maximum of 0.40 mol g^{-1} for the 2 ML sample. This suggests that a complete surface coverage of acid sites is achieved once the second layer is completed, and the third grafted layer has no benefit to the acidic properties of the catalyst. The requirement for 2ML of ZrO_2 to optimise the acid site loading could be related to the different speciation of Zr species supported onto the SBA-15 support as the amount of ZrO_2 increases. Crystallization of Zr species into the tetragonal structure is necessary to achieve superacidity,²² and might be expected to require a bi-layer to achieve the correct structural properties. Indeed the envelope for the Zr 3d XP spectra (**Figure 4.10**) shows a shift to lower binding energy with increased layer thickness which would be consistent with the first layer being electronically perturbed at the SiO_2 interface.

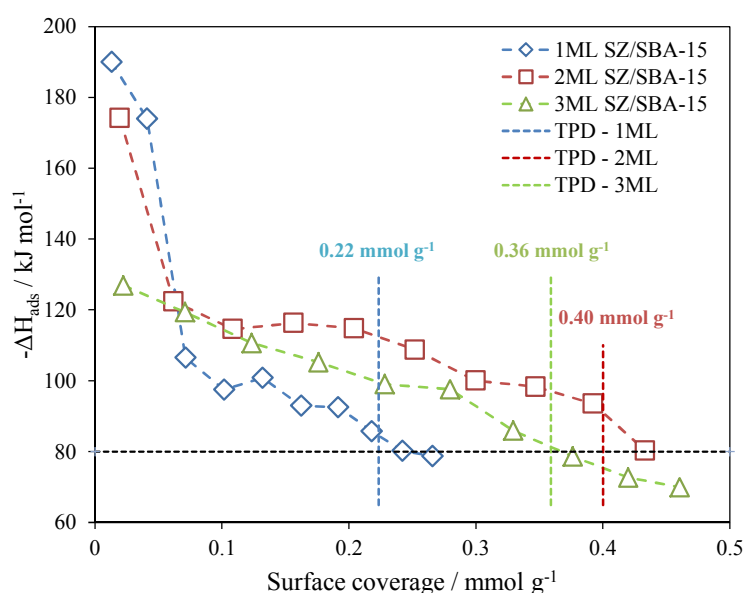


Figure 4.12: Titration of acid sites of xML-SZ/SBA-15 materials with ammonia

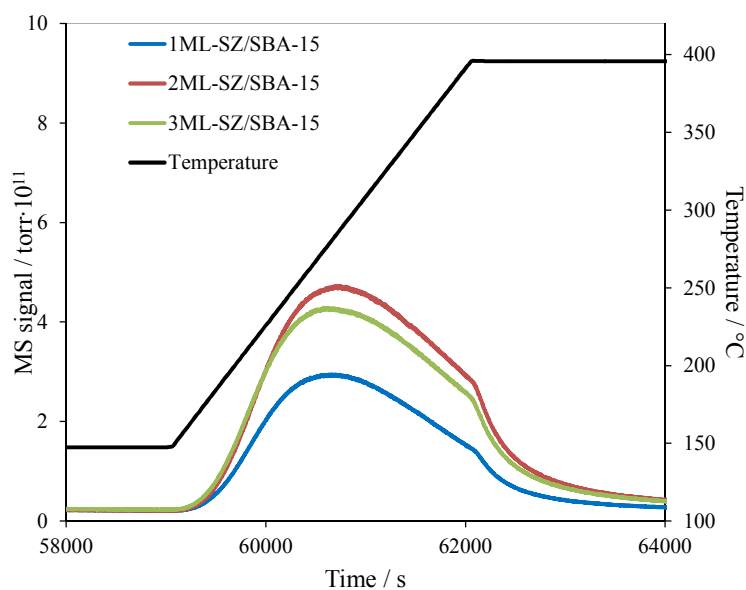


Figure 4.13: Thermal programmed desorption of ammonia for xML-SZ/SBA-15 materials

Table 4.7: Acid site analysis from NH_3 pulse titration/calorimetry and TPD

	1ML-SZ/SBA-15		2ML-SZ/SBA-15		3ML-SZ/SBA-15	
	mmol g ⁻¹	- ΔH_{ads}	mmol g ⁻¹	- ΔH_{ads}	mmol g ⁻¹	- ΔH_{ads}
Pulse 1	0.01	190.0	0.02	174.2	0.02	126.9
Pulse 2	0.04	174.0	0.06	122.4	0.07	119.4
Pulse 3	0.07	106.5	0.11	114.6	0.12	110.6
Pulse 4	0.10	97.5	0.16	116.3	0.18	105.2
Pulse 5	0.13	100.9	0.20	114.8	0.23	99.0
Pulse 6	0.16	92.9	0.25	108.8	0.28	97.6
Pulse 7	0.19	92.5	0.30	100.1	0.33	85.9
Pulse 8	0.22	85.8	0.35	98.3	0.38	78.6
Pulse 9	0.24	80.2	0.39	93.5	0.42	72.7
Pulse 10	0.27	78.7	0.43	80.3	0.46	69.9
Total acid site loading from calorimetry / mmol g ⁻¹	0.24		0.43		0.37	
Total acid site loading from TPD / mmol g ⁻¹	0.22		0.40		0.36	

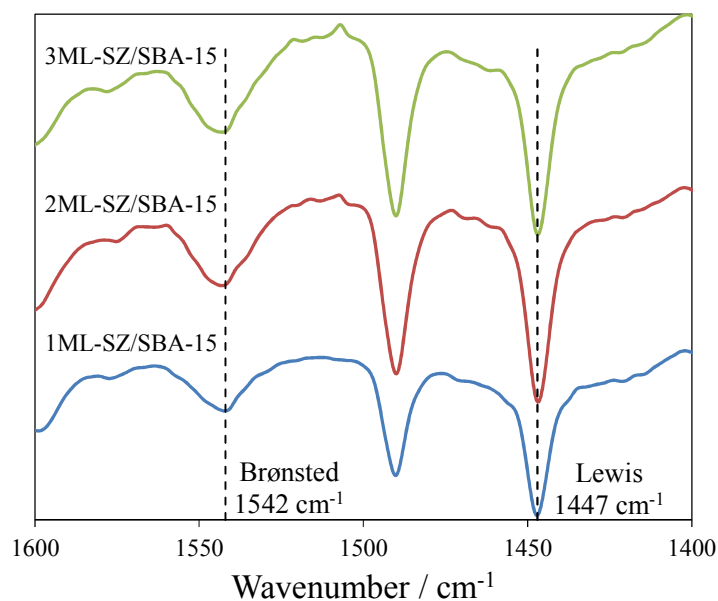


Figure 4.14: DRIFT spectra of xML-SZ/SBA-15 samples after pyridine adsorption

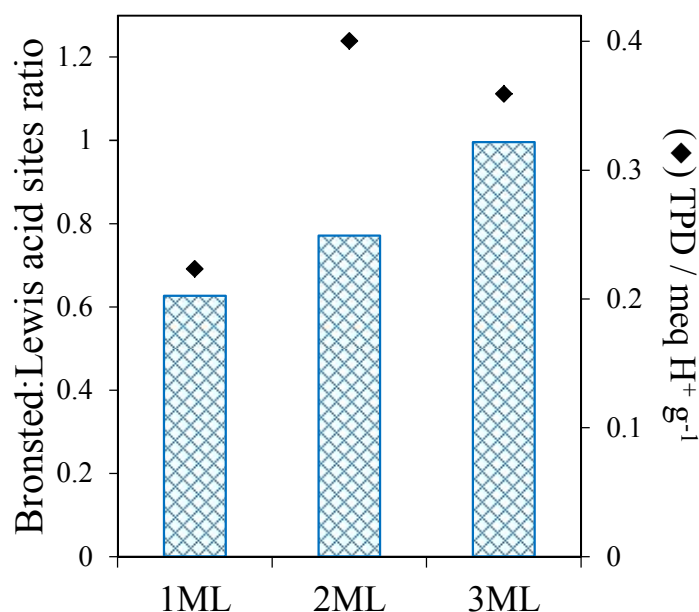


Figure 4.15: Brønsted : Lewis acid sites ratio from pyridine titration and meq of H⁺ per gram of catalyst determined by TPD

Furthermore, SO₂ adsorption calorimetry and TPD was employed to probe the basicity of SZ/SBA-15 catalysts. The enthalpy of SO₂ adsorption falls below the physisorption threshold after the first pulse for all the three SZ/SBA-15 samples (**Figure 4.16**), suggesting the presence of very small number of base sites on these catalysts. SO₂ TPD

reveals that the 1ML-SZ/SBA-15 possesses the smallest number of base sites among the three catalysts. Since the base sites are originated from zirconia, this suggests that the surface of zirconia film is nearly saturated by the SO_4^{2-} groups. Based on SO_2 TPD analysis (**Figure 4.17**), the base site density of 1,2 and 3ML SZ/SBA-15 are 0.002, 0.004 and 0.003 mmole g^{-1} respectively.

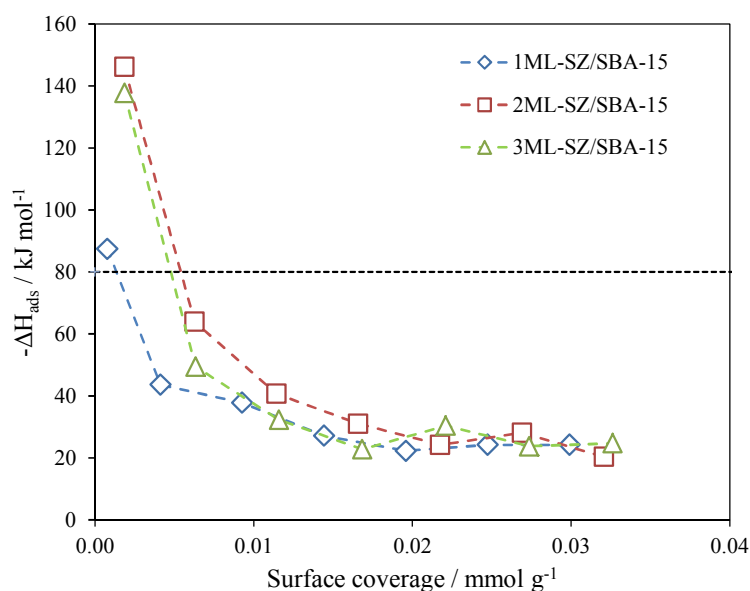


Figure 4.16: SO_2 adsorption and calorimetry on 1, 2 and 3ML SZ/SBA-15

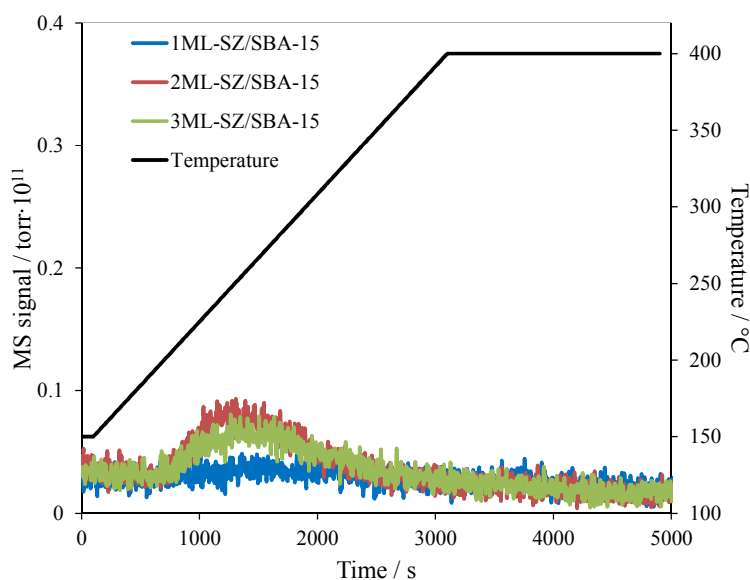


Figure 4.17: SO_2 TPD on 1, 2 and 3ML SZ/SBA-15

4.2.2.5 Transmission electron microscopy

High resolution TEM image (**Figure 4.18**) confirms the long range order of the hexagonal SBA-15 phase is retained, while the pore walls of SBA-15 also remain uniform upon grafting of ZrO_2 and sulfation, with no evidence for large crystallite deposition even after the third cycle.

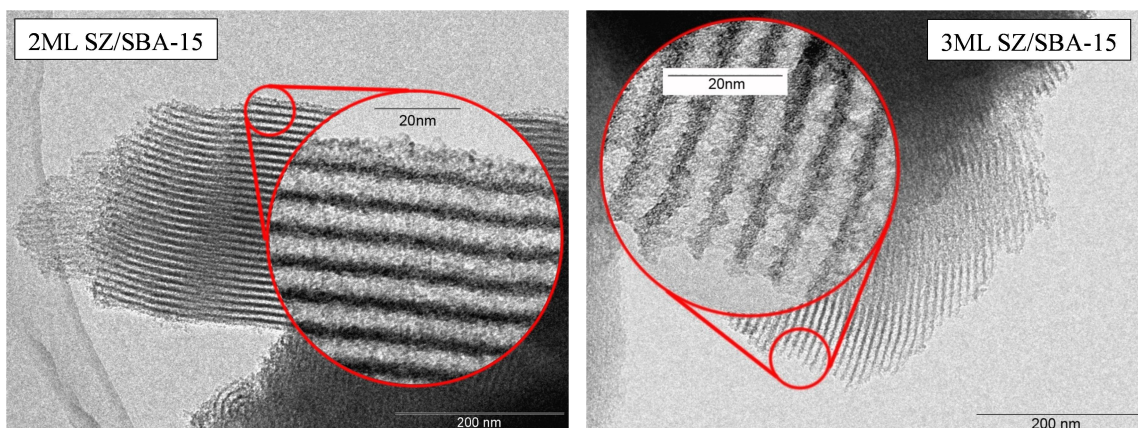


Figure 4.18: HRTEM of left: SBA-15 with 2 grafted ZrO_2 layers and right: SBA-15 with 3 grafted ZrO_2 layers

The TEM image (**Figure 4.19**) shows the width of the SBA-15 channels and confirm a good dispersion of sulphated Zr species on the silica pore surface, and the avoidance of ZrO_2 clusters suggesting the formation of a uniform sulphated zirconia layer on the silica surface after calcination.

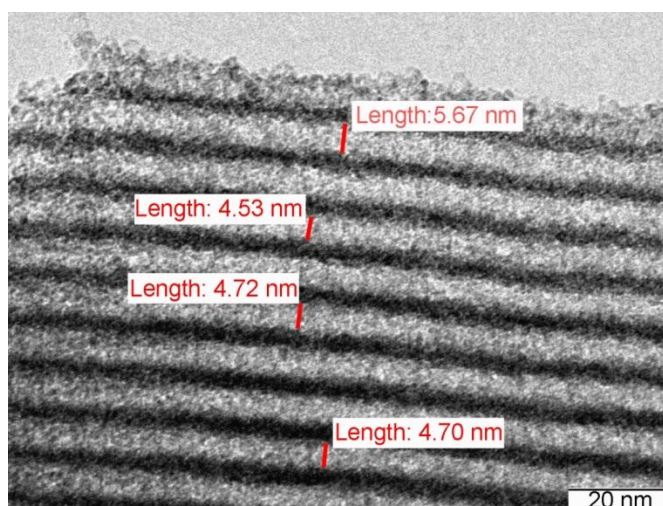


Figure 4.19: TEM image of 2ML-SZ/SBA-15.

4.2.3 Effect of [H₂SO₄] molarity on 2ML Zr/SBA-15

Since the 2 monolayer SZ/SBA-15 exhibited the optimum base:acid site ratio, it was then decided to pick this sample for investigation of S content impact on the physico-chemical properties and catalytic activity of SZ/SBA-15 in glucose and fructose dehydration to HMF. This section highlights the characterizations of 2ML SZ/SBA-15 impregnated with aqueous H₂SO₄ solutions with concentrations ranging from 0 to 0.25 M.

4.2.3.1 Powder X-ray diffraction

Low angle powder XRD was applied to verify successful formation of the *P6mm* space group of the SBA-15, and also to confirm that zirconia grafting did not damage the parent SBA-15. **Figure 4.20** shows the small-angle XRD patterns of the parent SBA-15 and the series of SBA-15 supported sulphated zirconia catalysts. The small-angle XRD pattern of the same calcined SBA-15 material exhibits three well-resolved peaks characteristic of SBA-15^{15, 16}, namely, a very intense peak at about $2\theta = 0.9^\circ$ and two distinct weak peaks at $2\theta = 1.52^\circ$ and 1.76° . The diffraction peaks are indexed as (1 0 0), (1 1 0) and (2 0 0) reflections corresponding to the *p6mm* hexagonal symmetry²³ which can be observed in all patterns, indicating these zirconia grafted mesoporous silica catalysts retained the ordered structure of SBA-15. Similar to xML-SZ/SBA-15 samples, the decrease in intensity is due to incorporation of zirconia. Furthermore, grafting zirconia on SBA-15 resulted in slight shift of the diffraction peaks to high-angle region compared to SBA-15, corresponding to a decrease in cell parameters which suggests shrinkage of mesoporous framework after the grafting process. This may be ascribed to the joint of zirconia layer and pore surface, as the hydrous zirconia loses water at 550°C, the silica framework shrinks in tandem with zirconia to cause a decrease in interlayer spacing.

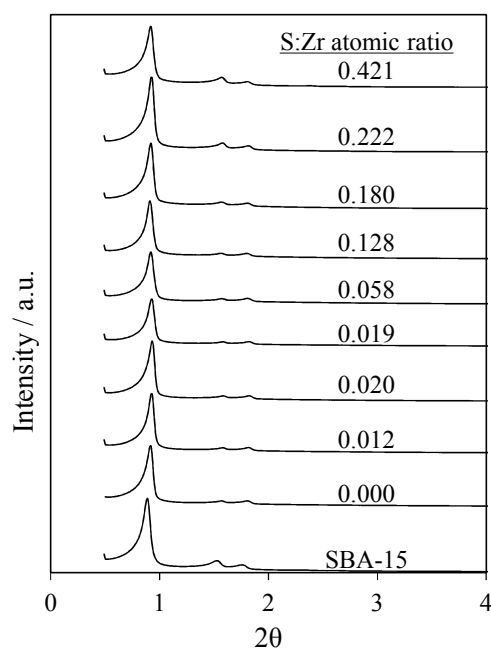


Figure 4.20: Low angle XRD patterns for the parent SBA-15 and SZ/SBA-15 materials

Figure 4.21 exhibits the wide angle XRD patterns of parent SBA-15 and SZ/SBA-15 series. From the high angle XRD, there is no evidence that large zirconia crystallites are formed during the grafting and calcination process.

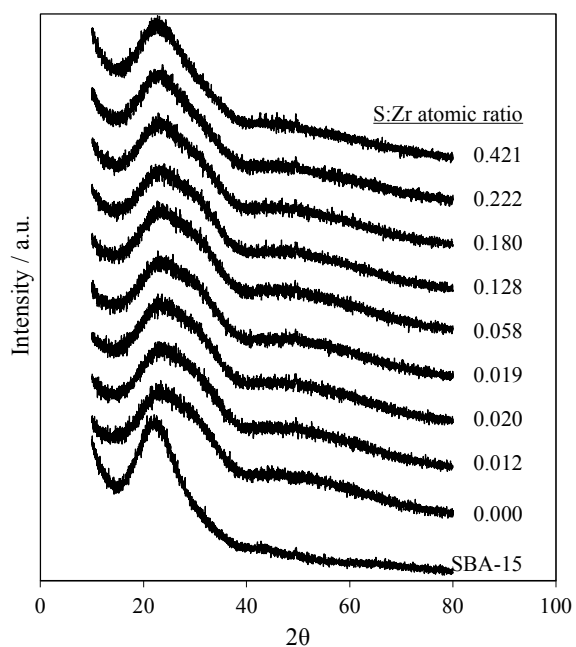


Figure 4.21: High angle XRD patterns SZ/SBA-15 series of catalysts

4.2.3.2 N₂ porosimetry

Porosimetry data (Figure 4.22) shows all materials exhibit type IV adsorption isotherms. The parent SBA-15 with sharp capillary condensation steps at relative pressure (P/P^0) of 0.6–0.8 and an H1 type hysteresis loop.¹⁹ The shape of the N₂ adsorption–desorption isotherm is characteristic of a well-formed SBA-15 material. The hysteresis loop size continuously decreases as the first and second cycle of zirconia grafting is accomplished which may account for decrease in the pore volume due to ZrO₂ grafted on the walls of SBA-15 and also disruption of extended mesoporous network.²⁴ Furthermore, sulfation of the material with aqueous sulphuric acid solutions with concentration range of 0.005–0.1 M has no significant impact on the hysteresis loop size. However for the samples treated with solutions of $0.1 \text{ M} \leq [\text{H}_2\text{SO}_4] \leq 0.25 \text{ M}$ the loop size was slightly increased.

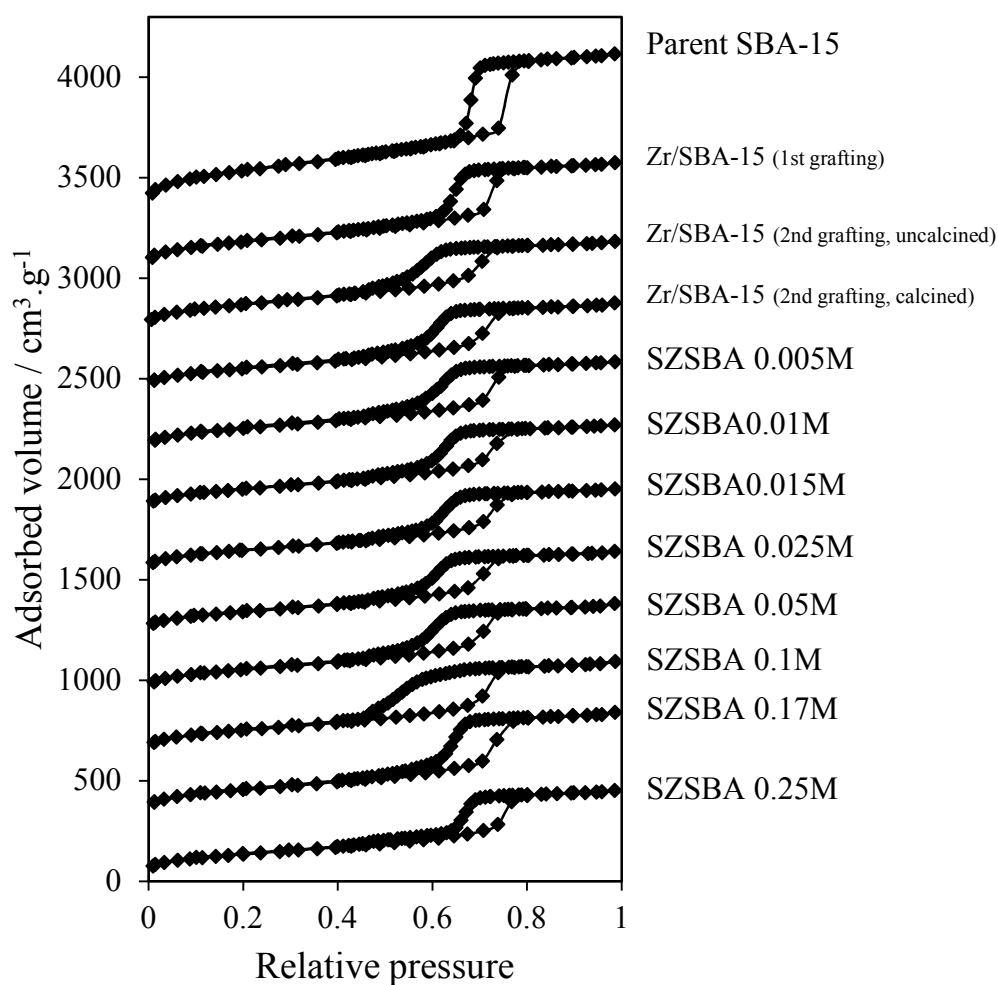


Figure 4.22: N₂ adsorption isotherms of parent SBA-15, ZrO₂ grafted SBA-15 and SZ/SBA-15 materials

Surface areas were calculated using BET²⁵ method and average pore diameters and mesopore volume were measured by employing BJH²⁶ method. Furthermore, The microporosity of the materials were determined using the t-plot²⁷ method.

These textural properties are summarized in **Table 4.8**. Conventional mesoporous SBA-15 has a high specific surface area of 850.1 m²g⁻¹ and pore volume of 1.26 cm³g⁻¹, in good agreement with the literature.^{5, 6, 8} **Table 4.8** shows that by doing the grafting cycles, the specific surface area and total pore volume of the materials decrease dramatically demonstrating the filling of inner surfaces of SBA-15. Also, the reduced pore diameter together with the retention of the uniform pore distribution shows that there is an even dispersion of zirconium 1-propoxide on the pore surface.

But, it can be observed that the sulfation process has minimal impact on the textural properties of SZ/SBA-15 materials for the concentrations below and or equal to 0.05 M. The average pore diameter of the sample treated with 0.1 M sulphuric acid is considerably smaller although its total pore volume remains in the same range as previous samples. The two samples that were treated with the highest sulphuric acid concentrations have got a larger pore diameter compared to the ones that are impregnated with lower concentration of sulphuric acid. The fact that the pore diameter of SZ/SBA-15 0.17 and 0.25 M are almost the same as the 1ML-Zr/SBA-15 and parent SBA-15 respectively (See **Figure 4.23**), suggests that the reason for increased pore diameter could be partial destruction of zirconia film by 0.17 M H₂SO₄ and complete removal of zirconia film by 0.25M acid. Additionally, wall thickness calculations confirm the idea of zirconia film removal at high H₂SO₄ concentrations since after it gets thicker up to [H₂SO₄] = 0.1 M, then the walls become thinner at higher concentrations. (**Table 4.9**) Furthermore, Using Bragg's Law (**Equation 2.12**) the cell parameters for all materials have been calculated, shown in **Table 4.9**.

Table 4.8: Surface area, pore diameter, micropore/mesopore and total pore volume of SZ/SBA-15 materials.

Sample	Surface area $\text{m}^2.\text{g}^{-1}$	Pore diameter nm	Micropore vol $\text{cm}^3.\text{g}^{-1}$	Mesopore vol $\text{cm}^3.\text{g}^{-1}$	Total pore vol $\text{cm}^3.\text{g}^{-1}$
SBA-15	850.1	6.76	0.082	1.158	1.26
1ML-Zr/SBA-15	650.2	5.92	0.059	0.807	0.89
2ML-Zr/SBA-15 (no calcination)	607.6	4.85	0.047	0.69	0.75
2ML-Zr/SBA-15 (calcined)	539.6	5.40	0.04	0.698	0.74
SZ/SBA-15 0.005M	549.8	5.58	0.043	0.708	0.75
SZ/SBA-15 0.01M	538.3	5.58	0.047	0.682	0.73
SZ/SBA-15 0.015M	522.9	5.40	0.045	0.652	0.70
SZ/SBA-15 0.025M	505.5	5.28	0.035	0.648	0.68
SZ/SBA-15 0.05M	546.8	5.25	0.043	0.71	0.74
SZ/SBA-15 0.1M	542.4	4.26	0.044	0.798	0.76
SZ/SBA-15 0.17M	556.8	5.93	0.044	0.803	0.83
SZ/SBA-15 0.25M	483.2	6.33	0.034	0.645	0.70

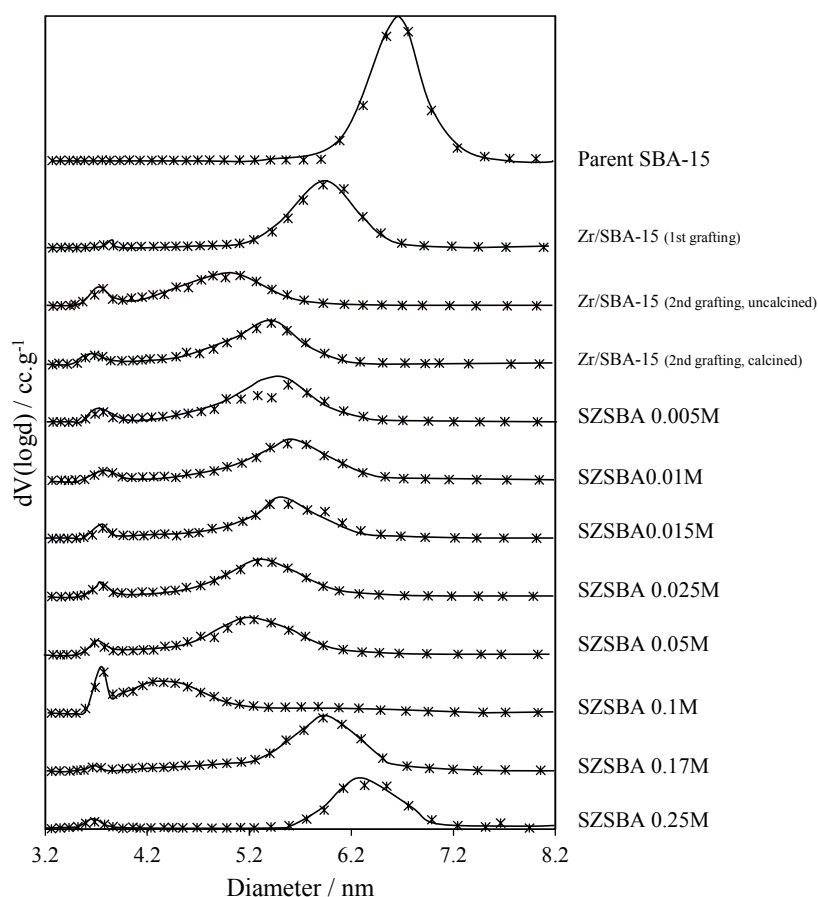


Figure 4.23: Pore size distribution of SZ/SBA-15 materials as a function of $[\text{H}_2\text{SO}_4]$

Table 4.9: Cell parameter, unit cell, pore diameter and wall thickness of SBA-15, Zr/SBA-15 and SZ/SBA-15 series of catalysts

Sample	d_{100} ^a nm	Unit cell size (a) ^b nm	Pore diameter ^c nm	Wall thickness ^d nm
Parent SBA-15	9.91	11.45	6.8	4.7
1ML-Zr/SBA-15	9.91	11.45	5.9	5.5
2ML-Zr/SBA-15 (uncalcined)	9.17	10.59	4.9	5.8
2ML-Zr/SBA-15 (calcined)	9.58	11.06	5.4	5.7
SZ/SBA 0.005	9.48	10.94	5.6	5.4
SZ/SBA 0.01	9.48	10.94	5.6	5.4
SZ/SBA 0.015	9.48	10.94	5.4	5.5
SZ/SBA 0.025	9.58	11.06	5.3	5.8
SZ/SBA 0.05	9.69	11.19	5.2	5.9
SZ/SBA 0.1	9.58	11.06	4.3	6.8
SZ/SBA 0.17	9.58	11.06	5.9	5.1
SZ/SBA 0.25	9.58	11.06	6.3	4.7

^aInterlayer spacing derived from Bragg's Law, ^bPore spacing, ^cBJH average pore diameters from desorption isotherm,^dWall thickness= $(2d_{100}/\sqrt{3})$ -pore diameter.

4.2.3.3 Surface and bulk elemental analysis

The impact of zirconia grafting on SBA-15 and subsequent impregnation by 0.005–0.25 M H₂SO₄ was probed by XPS to determine surface composition of the samples. **Table 4.10** and **Figure 4.24** demonstrate that increasing the concentration of the impregnating acid solution results in a steep initial rise in the surface S content, which subsequently reaches a maximum of ~1.4 wt% at [H₂SO₄] = 0.1 M and drops to 0.7 wt% for the highest acid concentration. **Table 4.10** also shows that the zirconium content of the new batch of 2ML-Zr/SBA-15 is very similar to that of previously made which were discussed in **Section 4.2.1** with only 1.4% difference in Zr weight percent proving the reproducibility of the synthesis method. Moreover the samples treated with [H₂SO₄] ≤ 0.05M retain about the same amount of zirconium as parent Zr/SBA-15. However, further increase in the concentration of impregnating H₂SO₄ results in continuous drop in zirconium loading of SZ/SBA-15 samples in line with **Figure 4.24**. The variations of Zr content in the bulk of the samples measured by SEM/EDX analysis indicating the same fashion as the surface Zr content. Moreover, ICP analysis on the filtrate of impregnation with [H₂SO₄] = 0.05 M and 0.25 M reveals that concentration of Zr ions in those solutions are 385 and 2761 ppm respectively. This is an indication of greater dissolution of zirconia film at higher H₂SO₄ concentrations. This is in good agreement

with previously discussed N₂ adsorption results which showed a shift in pore size distribution towards wider pores for the samples treated with higher concentrations of H₂SO₄. These findings strongly suggest that impregnating ZrO₂/SBA-15 with [H₂SO₄] > 0.1 M will cause some dissolution of zirconia into the solution and hence some loss of the zirconia film on the SBA-15. The fact that surface area and low angle XRD patterns of these samples remain unchanged suggests this observation is not due to any collapse of the pore structure.

Table 4.10: XPS surface composition of parent SBA-15, 2ML Zr/SBA-15 and the resulting SZ/SBA-15 series from impregnation with increasing [H₂SO₄]

Sample	O 1s wt%	Zr 3d wt%	S 2p wt%	Si 2p wt%	O 1s At%	Zr 3d At%	S 2p At%	Si 2p At%
SBA-15	57.5	0.0	0.0	42.5	70.3	0.0	0.0	29.7
1ML-Zr/SBA-15								
2ML-Zr/SBA-15 (No calcination)	43.1	28.2	0.0	28.7	66.9	7.7	0.0	25.4
2ML-Zr/SBA-15 (Calcined)	45.5	26.6	0.0	28.0	68.9	7.1	0.0	24.1
SZ/SBA-15 0.005M	45.4	25.0	0.1	29.4	68.2	6.6	0.1	25.2
SZ/SBA-15 0.01M	45.8	26.3	0.2	27.7	69.1	7.0	0.1	23.8
SZ/SBA-15 0.015M	45.6	26.3	0.2	27.9	68.9	7.0	0.1	24.0
SZ/SBA-15 0.025M	44.8	26.9	0.6	27.8	68.3	7.2	0.4	24.1
SZ/SBA-15 0.05M	42.7	27.0	1.2	29.1	66.1	7.3	0.9	25.6
SZ/SBA-15 0.1M	46.3	22.0	1.4	30.3	68.0	5.7	1.0	25.3
SZ/SBA-15 0.17M	48.6	14.0	1.1	36.4	67.2	3.4	0.8	28.6
SZ/SBA-15 0.25M	52.5	4.7	0.7	42.1	67.6	1.1	0.5	30.9

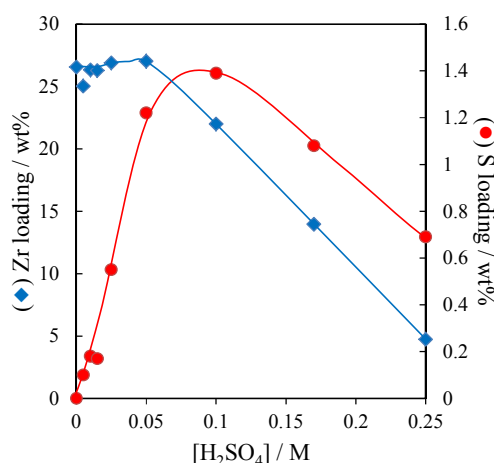


Figure 4.24: Zirconium and sulphur content of the SZ/SBA-15 catalysts from XPS as a function of H₂SO₄ concentration

Figure 4.25, compares the bulk and surface atomic ratios of S:Zr, Zr:Si and S:Si from EDX and XPS analysis wherein S:Zr atomic ratio in bulk and on the surface of the materials steadily increases with concentration of sulphuric acid. Moreover, Zr:Si atomic ratio from EDX and XPS, stay at constant level of 0.2 and 0.3 respectively up to $[H_2SO_4] = 0.05$ M and then the bulk Zr:Si drops to 0.05 while the surface Zr:Si atomic ratio is 0.03. Furthermore, the bulk and surface S:Si atomic ratios, reaches a maximum as the concentration of H_2SO_4 is equal to 0.1 M. The drop in S:Si ratio could be explained by the simultaneous zirconia film removal due to high concentration of H_2SO_4 . **Table 4.11** presents detailed elemental analysis data from SEM/EDX on SZ/SBA-15 materials.

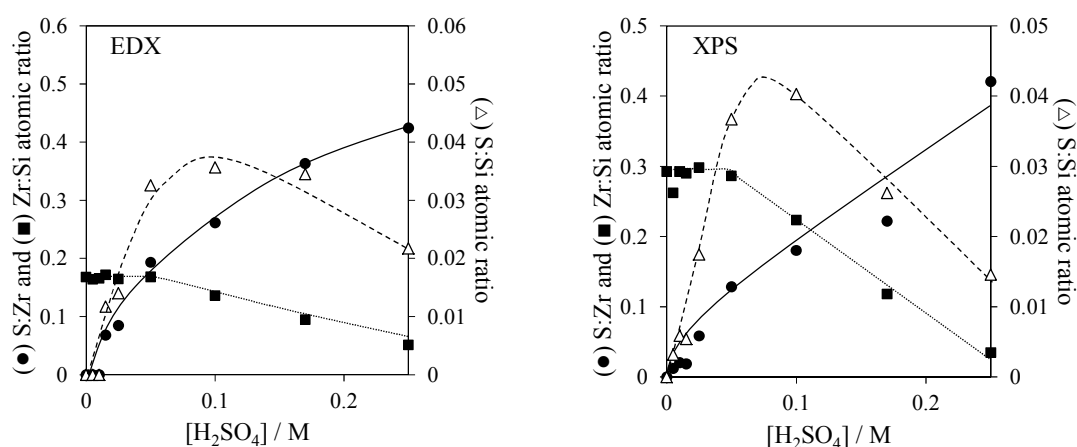


Figure 4.25: (●) S:Zr, (■) Zr:Si and (△) S:Si atomic ratio from left) EDX and right) XPS.

Table 4.11: Elemental analysis on the bulk of SZ/SBA-15 materials with SEM/EDX

Sample	O	Zr	S	Si	O	Zr	S	Si
	wt%	wt%	wt%	wt%	At%	At%	At%	At%
SBA-15	53.7	0.0	0.0	46.3	67.0	0.0	0.0	33.0
1ML-Zr/SBA-15	49.0	11.5	0.0	39.5	66.6	2.8	0.0	30.6
2ML-Zr/SBA-15 (No calcination)	46.3	20.0	0.0	33.7	67.1	5.1	0.0	27.8
2ML-Zr/SBA-15 (calcined)	47.2	18.7	0.0	34.2	67.5	4.7	0.0	27.9
0.005M SZ/SBA-15	40.5	20.7	0.0	38.8	61.1	5.5	0.0	33.4
0.01M SZ/SBA-15	43.1	19.9	0.0	37.0	63.7	5.2	0.0	31.1
0.015M SZ/SBA-15	42.8	20.3	0.5	36.4	63.6	5.3	0.4	30.8
0.025M SZ/SBA-15	42.1	20.0	0.6	37.3	62.7	5.2	0.4	31.7
0.05M SZ/SBA-15	45.5	18.8	1.3	34.4	65.9	4.8	0.9	28.4
0.1M SZ/SBA-15	44.6	16.5	1.5	37.3	64.2	4.2	1.1	30.6
0.17M SZ/SBA-15	49.3	11.8	1.5	37.3	67.2	2.8	1.0	29.0
0.25M SZ/SBA-15	47.0	9.5	1.7	41.8	64.0	2.3	1.2	32.5

4.2.3.4 Diffuse Reflectance Infrared Fourier Transform Spectroscopy

In situ DRIFTS were used to characterize the evolution of sulfate groups with acid concentration (**Figure 4.26**). In SBA-15, the bands centered at 1100 and 815 cm^{-1} are attributed to asymmetric stretching and symmetric stretching of Si–O–Si respectively and the band at 974 cm^{-1} is related to the characteristic stretching vibration of non-bridged Si–OH groups.^{28,29} And the broad transmittance band in the wavenumber range of 3000–3800 cm^{-1} is associated with the surface silanols.³⁰ From the spectra, it is apparent that the transmittance band at 974 cm^{-1} was lost and also the intensity of the sharp peak at 3743 cm^{-1} which is attributed to isolated silanol³¹ decreased significantly after coating zirconia layer on the surface of SBA-15, which indicates the association of Si–OH and Zr–OH groups to Si–O–Zr groups.³² Moreover, the band at 1640 cm^{-1} is related to bending vibration of adsorbed water.³³

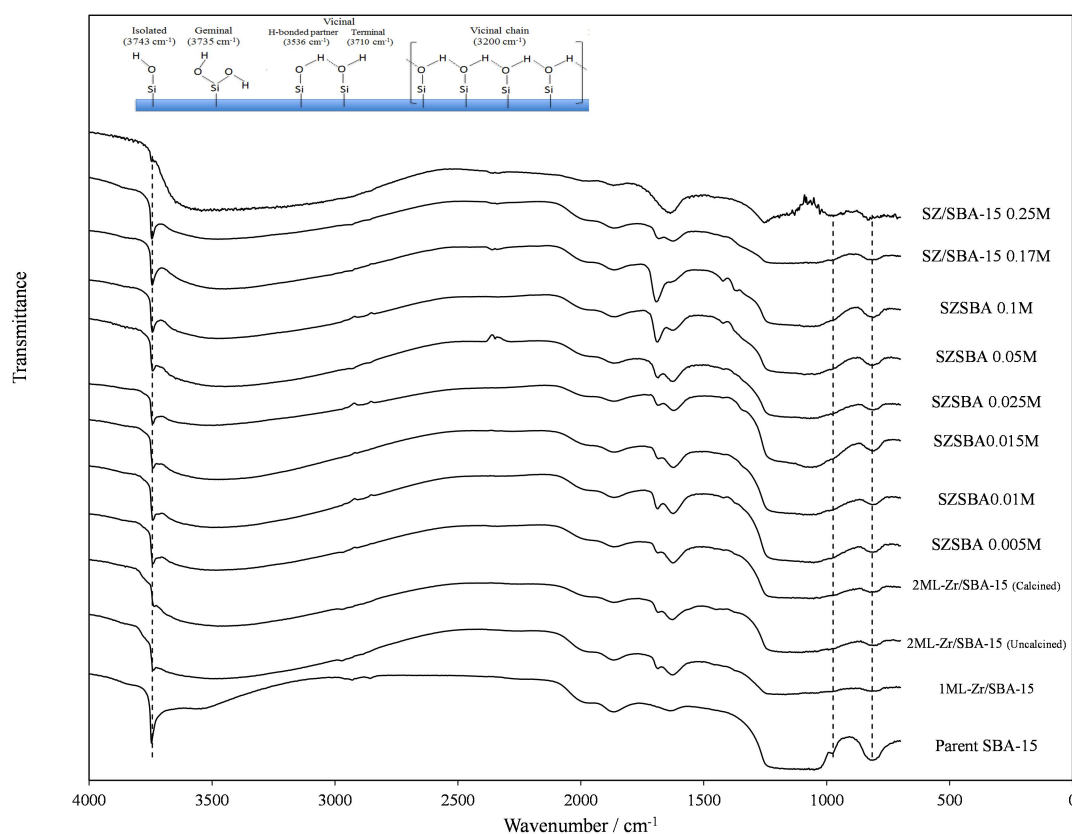


Figure 4.26: DRIFT spectra of Parent SBA-15, Zr/SBA-15 and SZ/SBA-15 series of catalysts recorded in vacuo at 50°C

In order to have a better understanding about the presence of Zr and different sulphur species, the transmittance spectrum of pure SBA-15 was subtracted from the rest of

spectra (**Figure 4.27**). As a function of $[\text{H}_2\text{SO}_4]$, a clear band is seen to evolve at $\sim 1348\text{ cm}^{-1}$, which is a characteristic band of SO_4^{2-} asymmetric stretching mode of (O=S=O) on sulphated metal oxides.³¹ The accompanying modes observed $\sim 950\text{-}1000\text{ cm}^{-1}$ are assigned to the symmetric (O=S=O) SO_4 vibrational mode. The splitting of spectral features as a function of SO_4 coverage is consistent with multiple SO_4 coordination environments (e.g. mono-bi dentate) coverage as discussed in **Chapter 3**. It is interesting to note that the water bending mode at $\sim 1600\text{ cm}^{-1}$ is also split suggesting there is water bound to strong Lewis sites associated with the ZrO_2 film. Loss of resolution of spectral features $> 0.1\text{ M } [\text{H}_2\text{SO}_4]$ may be due to the effect of stronger acid solutions used during impregnation causing dissolution and re-dispersion of the sulphated overlayer.

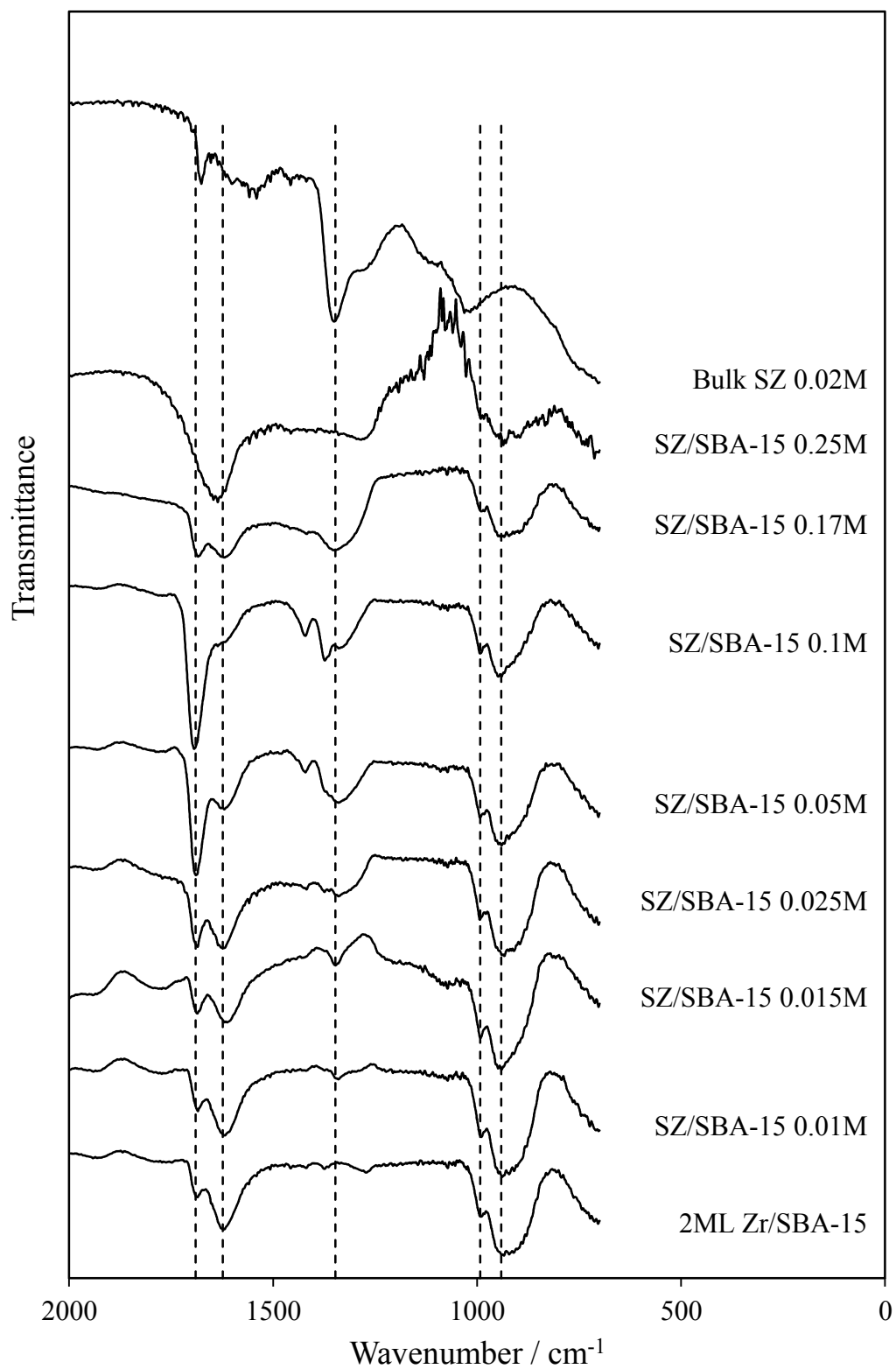


Figure 4.27: SBA-15 subtracted spectra of SZ/SBA-15 materials

4.2.3.5 Acid and base sites measurements

ZrO₂ exhibits both acidic and basic properties³⁴, hence NH₃ and SO₂ titrations were employed to map the acid and base site densities as a function of S:Zr atomic ratio. **Figure 4.28** shows the enthalpy of adsorption of each ammonia pulse as a function of acid site loading. The horizontal dashed line at 80 kJ.mol⁻¹ represents the threshold of significant chemisorption. In other words, pulses with enthalpy of adsorption below 80 kJ.mol⁻¹ are considered as physisorption. So the number of acid sites can be read from wherever each curve meets the chemisorption threshold line. The vertical dotted lines demonstrate the corresponding acid site loading values measured from temperature programmed desorption. **Figure 4.28** demonstrates that the Zr/SBA-15 sample possesses a smaller number of acid sites compare to the sulphated samples. The number of acid sites increases continuously with concentration of impregnating solution except for the sample that was treated with 0.25 M sulphuric acid solution. The drop in number of acid sites for the last sample correlates with increased pore diameter and decrease in Zr content, and as discussed before it could be attributed to dissolution of zirconia film by relatively high concentration of impregnating sulphuric acid solution. Moreover, the enthalpy of adsorptions increases with H₂SO₄ concentration indicating formation of stronger acid sites when treated with more concentrated H₂SO₄ unless impregnation causes zirconia film removal from the SBA-15 surface. The acid strength increases across the series due to a combination of increased SO₄²⁻ density, coordination environment change (bi-mono dentate SO₄²⁻) and potentially more defective ZrO₂ film at 2ML compared to bulk ZrO₂ allowing for generation of more Lewis acid sites. Also for bulk systems monoclinic-tetragonal influences Brønsted : Lewis ratio but since it was not possible to identify the phase of thin films by XRD, therefore this is a speculation, however Raman analysis could be helpful in this matter. Furthermore, the reason for drop in enthalpy of adsorption by injecting more ammonia is because in principle, the stronger active sites are neutralised first and progressively weaker are neutralised in order.

Figure 4.29 shows the ammonia thermal programmed desorption as a function of time for the parent Zr/SBA-15 sample as well as the selected samples from SZ/SBA-15 series of materials. **Table 4.12** shows the enthalpy of adsorption for each injection, as well as measured acid site loading from ammonia pulse titration/calorimetry and also

from TPD. Furthermore, it indicates that the number of acid sites measured by ammonia pulse titration/calorimetry and TPD are in very good agreement with each other.

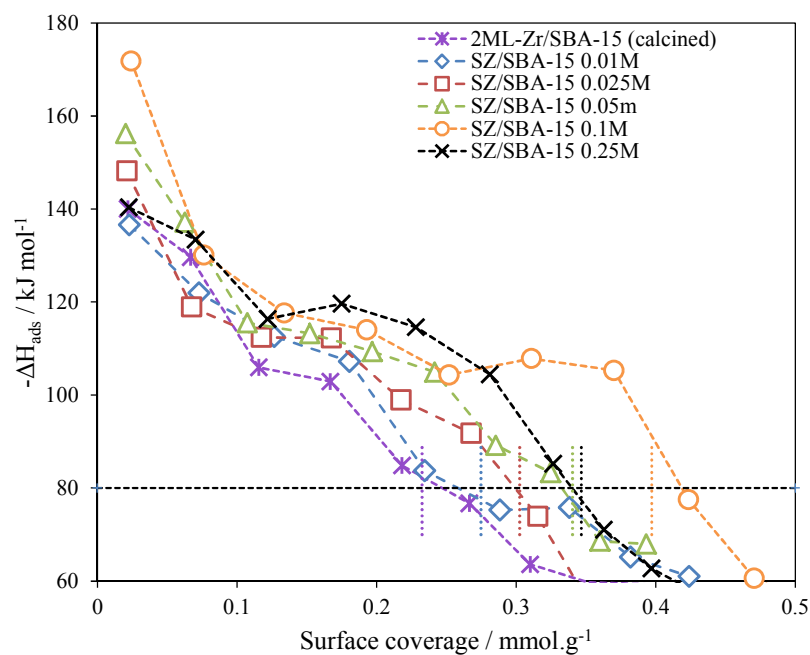


Figure 4.28: Titration of acid sites of Zr/SBA-15 and SZ/SBA-15 materials with ammonia

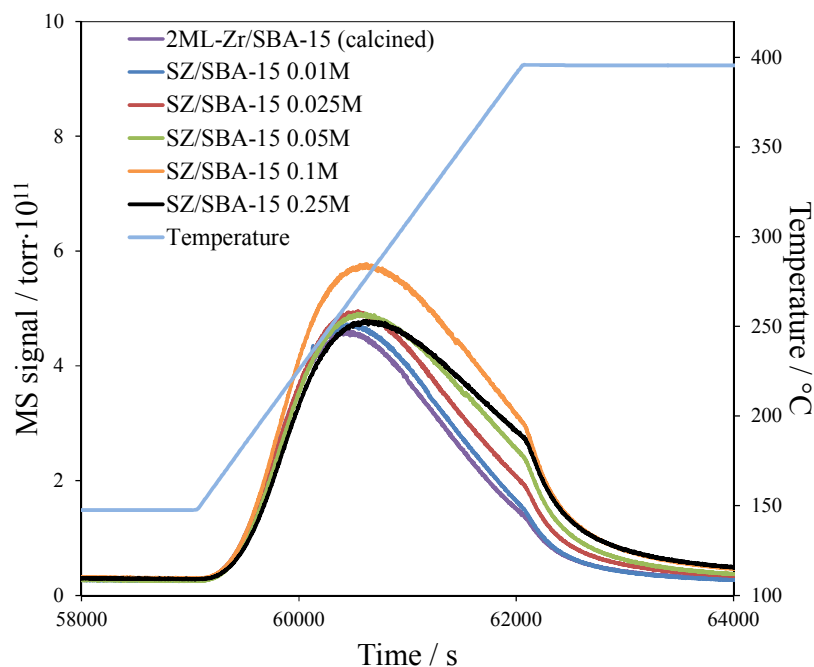


Figure 4.29: Thermal programmed desorption of ammonia for Zr/SBA-15 and SZ/SBA-15 materials

Table 4.12: Acid site analysis from ammonia pulse titration/calorimetry and thermal programmed desorption

	Zr/SBA-15		SZ/SBA-15 0.01M		SZ/SBA-15 0.025M		SZ/SBA-15 0.05M		SZ/SBA-15 0.1M		SZ/SBA-15 0.25M	
	mmol.g ⁻¹	- ΔH _{ads}	mmol.g ⁻¹	- ΔH _{ads}	mmol.g ⁻¹	- ΔH _{ads}	mmol.g ⁻¹	- ΔH _{ads}	mmol.g ⁻¹	- ΔH _{ads}	mmol.g ⁻¹	- ΔH _{ads}
Pulse 1	0.02	140.01	0.02	136.60	0.02	148.19	0.02	156.24	0.02	171.82	0.02	140.35
Pulse 2	0.07	129.64	0.07	121.93	0.07	118.94	0.06	137.17	0.08	130.09	0.07	133.47
Pulse 3	0.12	105.95	0.13	112.60	0.12	112.40	0.11	115.54	0.13	117.65	0.12	116.37
Pulse 4	0.17	102.92	0.18	107.27	0.17	112.27	0.15	113.28	0.19	114.02	0.18	119.65
Pulse 5	0.22	84.86	0.23	83.75	0.22	98.95	0.20	109.35	0.25	104.34	0.23	114.62
Pulse 6	0.27	76.71	0.29	75.27	0.27	91.81	0.24	104.96	0.31	107.85	0.28	104.43
Pulse 7	0.31	63.59	0.34	75.84	0.32	73.93	0.29	89.22	0.37	105.31	0.33	85.27
Pulse 8	0.35	59.72	0.38	65.14	0.36	51.74	0.32	83.36	0.42	77.50	0.36	71.09
Pulse 9	0.39	59.32	0.42	61.01	0.40	54.74	0.36	68.58	0.47	60.64	0.40	62.71
Pulse 10	0.43	52.48	0.46	44.22	0.44	52.13	0.39	68.01	0.52	54.26	0.43	57.47
Total acid site loading from calorimetry mmol.g ⁻¹	0.25		0.26		0.3		0.33		0.42		0.34	
Total acid site loading from TPD mmol.g ⁻¹	0.233		0.275		0.302		0.340		0.397		0.347	

Base site measurements with SO₂ pulse titration/calorimetry reveal that the number of base sites decreases monotonically as the S:Zr atomic ratios increase (**Figure 4.30**). Additionally, TPD confirms the calorimetry data (**Figure 4.31**). **Table 4.13** summarizes SO₂ pulse titration/calorimetry studies as well as the calculated number of base sites for the Zr/SBA-15 and SZ/SBA-15 series and **Figure 4.32** and **Table 4.14** illustrates the absolute number of acid and base sites and the ratio between them and the acid and base site density as a function of [H₂SO₄].

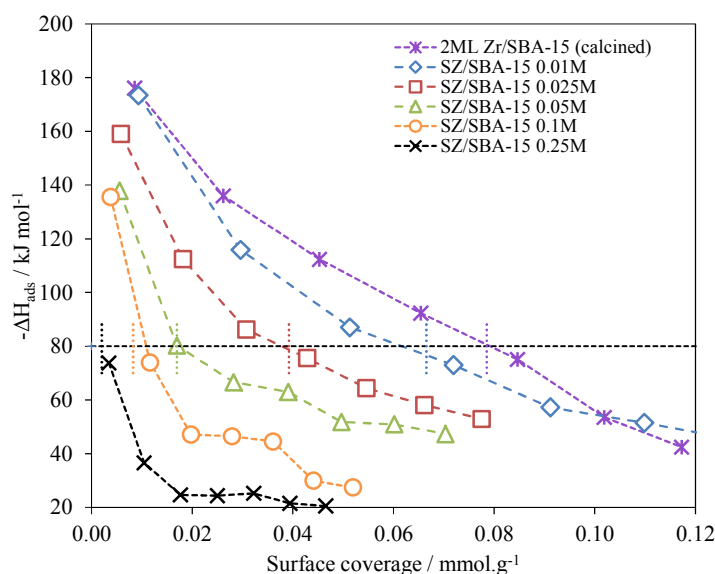


Figure 4.30: Titration of base sites of Zr/SBA-15 and SZ/SBA-15 materials with SO₂

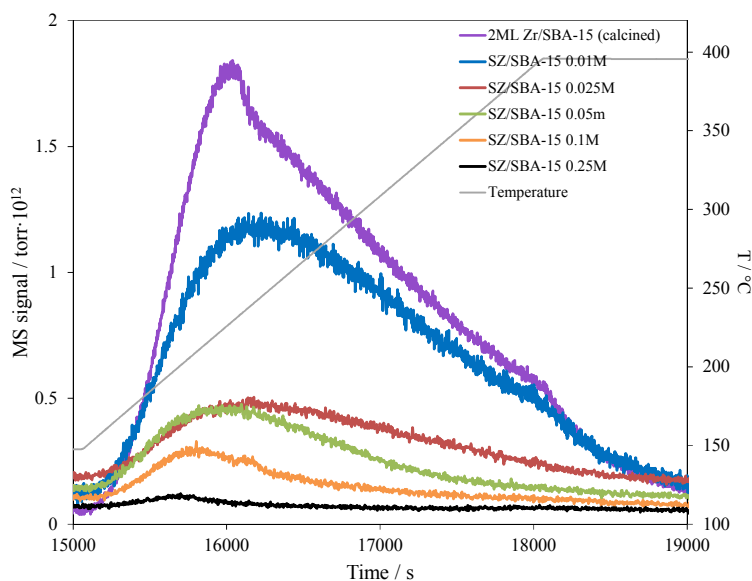


Figure 4.31: Thermal programmed desorption of SO₂ for Zr/SBA-15 and SZ/SBA-15 materials

Table 4.13: Base site analysis from SO₂ pulse titration/calorimetry and thermal programmed desorption

	Zr/SBA-15		SZ/SBA-15 0.01M		SZ/SBA-15 0.025M		SZ/SBA-15 0.05M		SZ/SBA-15 0.1M		SZ/SBA-15 0.25M	
	mmol.g ⁻¹	- ΔH _{ads}	mmol.g ⁻¹	- ΔH _{ads}	mmol.g ⁻¹	- ΔH _{ads}	mmol.g ⁻¹	- ΔH _{ads}	mmol.g ⁻¹	- ΔH _{ads}	mmol.g ⁻¹	- ΔH _{ads}
Pulse 1	0.01	176.07	0.01	173.39	0.01	159.02	0.01	137.88	0.00	135.51	0.00	73.78
Pulse 2	0.03	135.99	0.03	115.87	0.02	112.37	0.02	80.28	0.01	73.96	0.01	36.59
Pulse 3	0.05	112.36	0.05	87.05	0.03	86.17	0.03	66.56	0.02	47.10	0.02	24.65
Pulse 4	0.07	92.32	0.07	72.99	0.04	75.55	0.04	63.00	0.03	46.46	0.02	24.39
Pulse 5	0.08	75.08	0.09	57.25	0.05	64.36	0.05	51.78	0.04	44.52	0.03	25.24
Pulse 6	0.10	53.55	0.11	51.50	0.07	58.12	0.06	50.94	0.04	29.94	0.04	21.52
Pulse 7	0.12	42.46	0.13	45.36	0.08	52.92	0.07	47.31	0.05	27.40	0.05	20.53
Total base site loading from calorimetry mmol.g ⁻¹	0.08		0.06		0.04		0.02		0.01		0.00	
Total base site loading from TPD mmol.g ⁻¹	0.079		0.067		0.039		0.017		0.008		0.002	

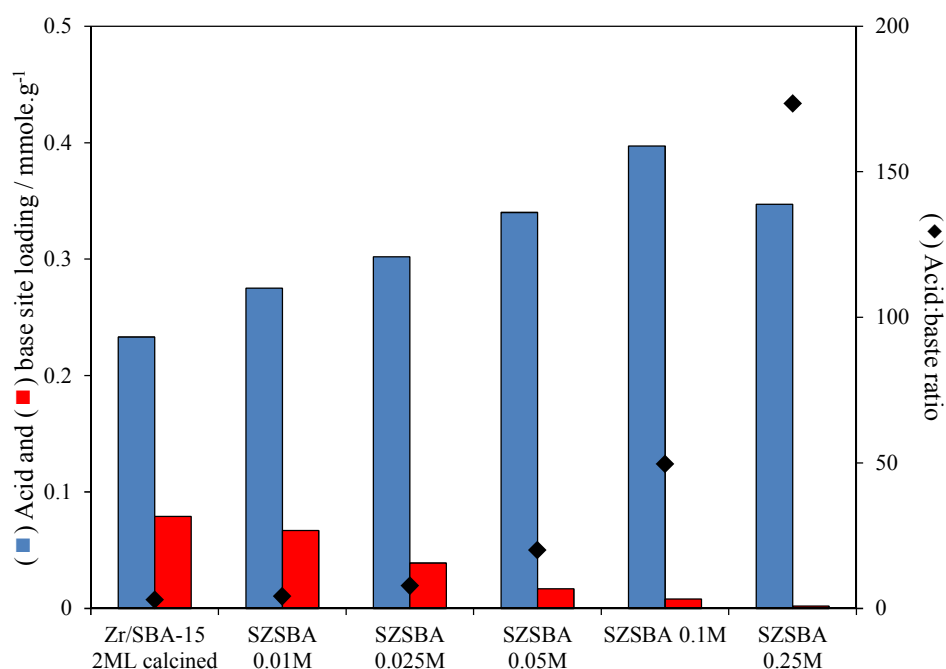


Figure 4.32: Acid and base site loading and the acid to base sites ratio for the series of SZ/SBA-15 materials

Table 4.14: Acid and base site loading and density and acid:base sites ratio for selected samples of SZ/SBA-15 materials

	Acid site loading	Base site loading	Acid density	Base density	Acid:Base ratio
	mmole g ⁻¹	mmole g ⁻¹	mmole m ²	mmole m ²	
Zr/SBA-15 2ML calcined	0.233	0.079	4.3E-04	1.5E-04	2.9
SZSBA 0.01M	0.275	0.067	5.1E-04	1.2E-04	4.1
SZSBA 0.025M	0.302	0.039	6.0E-04	7.7E-05	7.7
SZSBA 0.05M	0.34	0.017	6.2E-04	3.1E-05	20.0
SZSBA 0.1M	0.397	0.008	7.3E-04	1.5E-05	49.6
SZSBA 0.25M	0.347	0.002	7.2E-04	4.1E-06	173.5

The SZ/SBA-15 materials exhibited the presence of both Lewis and Brønsted acid sites as indicated by DRIFT spectra of the samples recorded after pyridine adsorption (**Figure 4.33**). In zirconia-coated SBA-15, the band at 1446 cm^{-1} is attributed to pyridine coordinatively adsorbed on Lewis sites and the peak at 1545 cm^{-1} is related to pyridine adsorbed on Brønsted acid sites. The transmittance band centred at 1491 cm^{-1} arises from interaction of pyridine with both Lewis and Brønsted sites. In pure SBA-15 there were no peak detected at 1545 cm^{-1} and 1491 cm^{-1} indicating that acid sites are generated upon zirconia coating on SBA-15 pore walls.⁵ This generation of Brønsted acidity may be due to changes in the electron density around Si nuclei as result of either differences in the electronegativity or local structure deformation resulting from

introduction of Zr^{4+} ions, which may weaken Si-O-Zr-OH bond³⁵. These results confirmed the presence of Si-O-Zr linkages in zirconia-coated SBA-15 samples.

The unique Brønsted–Lewis features at $1545/1446\text{ cm}^{-1}$ were integrated to quantify the variation in Brønsted : Lewis ratio, which increases with increase in Zr loading as well as sulphur content. **Figure 4.34** shows the ratio of Brønsted to Lewis acid sites for the SBA-15 supported sulphated zirconia samples as a function of S:Zr atomic ratio.

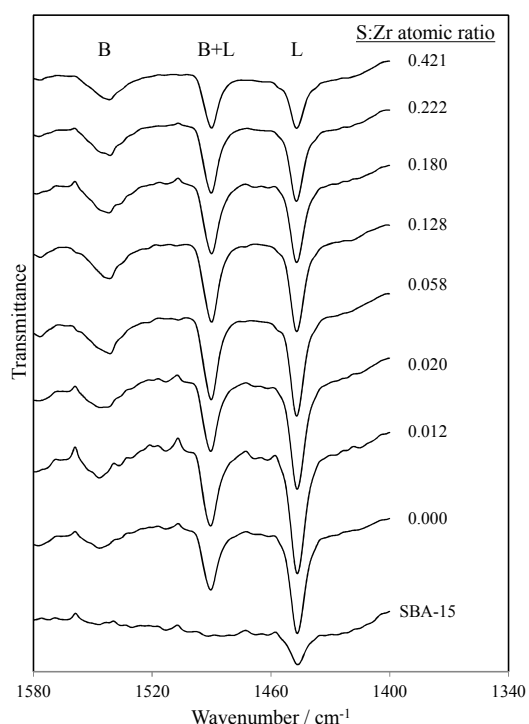


Figure 4.33: DRIFT spectra of the SZ/SBA-15 materials after pyridine adsorption in vacuo at 50 °C

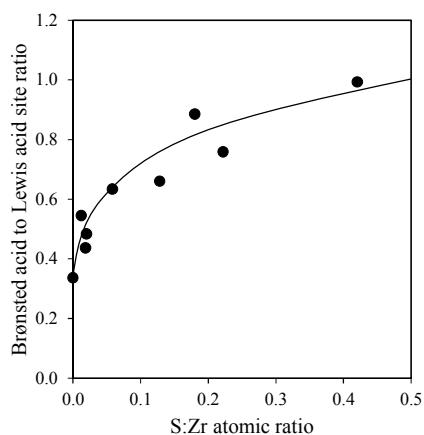


Figure 4.34: Ratio of Brønsted to Lewis acid sites for the SZ/SBA-15-xM series of catalysts.

4.2.4 Glucose and fructose conversion to HMF over SZ/SBA-15 catalysts

Glucose and fructose dehydration reaction was subsequently conducted over SZ/SBA-15 series of catalysts to investigate their performance. Full reaction conditions are described in **Chapter 2**. As it was hypothesized and subsequently verified in **Chapter 2**, the glucose transformation to HMF takes place via isomerization of glucose to fructose followed by dehydration of fructose to form HMF which the former is Lewis acid/base catalysed and the latter is an acid catalysed reaction. Here we investigate the effect of zirconia monolayers followed by studying the effect of sulphur loading.

4.2.4.1 Effect of zirconia monolayers on glucose conversion

Figure 4.35 depicts the profile of glucose conversion over 1-3ML-SZ/SBA-15 catalysts. The first striking observation is that 1ML-SZ/SBA-15 is by far the least active catalysts among three. Moreover, the quantity of glucose converted over 2ML-SZ/SBA-15 was more than two others however the difference in conversion over 2ML and 3ML is not remarkable.

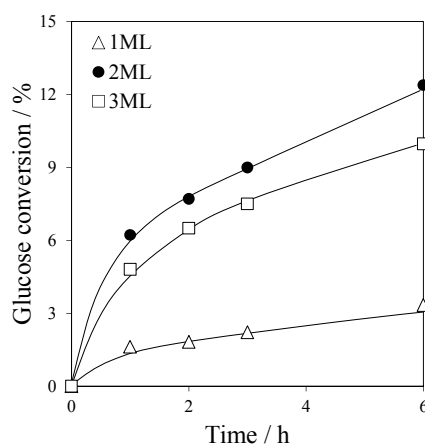


Figure 4.35: Profile of glucose conversion over xML-SZ/SBA-15 catalysts (T=100°C, 0.1 g glucose, 20ml deionized water, substrate : catalyst = 1)

Profiles of glucose conversion as well as yield of fructose and HMF for the 3 catalysts are shown in **Figure 4.36**. In all cases the yield of major products (fructose and HMF) progressively increases over the time. Since all of the catalysts were impregnated with same sulphuric acid solution ($[\text{H}_2\text{SO}_4] = 0.075 \text{ M}$), increasing the amount of zirconia will lead to the formation of more basic/Lewis acidic sites that are responsible for

isomerization of glucose to fructose. This explains the increase in conversion level of glucose (mainly to fructose) from 1ML to 2-3ML. Subsequently because there are more fructose molecules available in the reaction media (over 2-3ML), the yield of HMF gets increased as well.

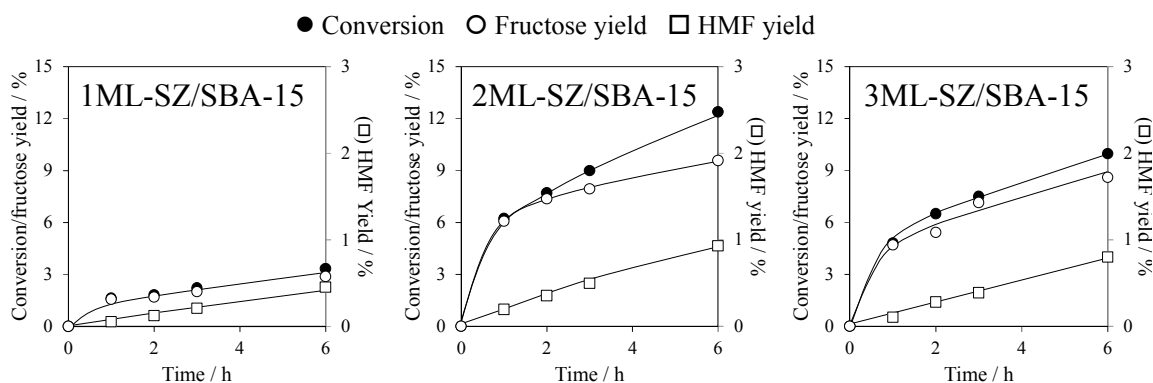


Figure 4.36: Profile of glucose conversion as well as fructose and HMF yield for glucose \rightarrow HMF reaction over xML-SZ/SBA-15 catalysts ($T=100^{\circ}\text{C}$, 0.1 g glucose, 20ml deionized water, substrate : catalyst = 1)

Conversion plots followed similar order and trends when fructose was used as substrate (Figure 4.37) however the levels of conversion were significantly higher.

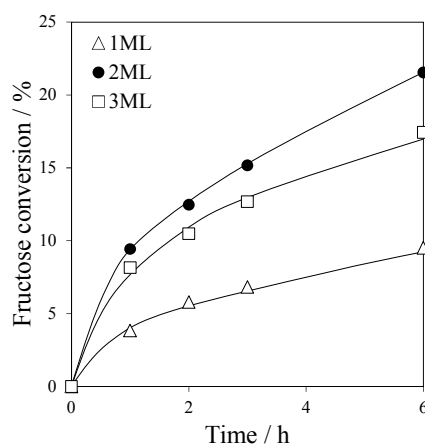


Figure 4.37: Profile of fructose conversion over xML-SZ/SBA-15 catalysts ($T=100^{\circ}\text{C}$, 0.1 g fructose, 20ml deionized water, substrate : catalyst = 1)

The main products of the fructose dehydration reaction at 100°C over SZ grafted SBA-15 were glucose and HMF, the carbon balance is not as good as the reactions started with glucose. This is probably due to easier transformation of fructose to unknown side-

products and humins compared to reaction started with glucose. Profile of fructose reactions are demonstrated in **Figure 4.38**.

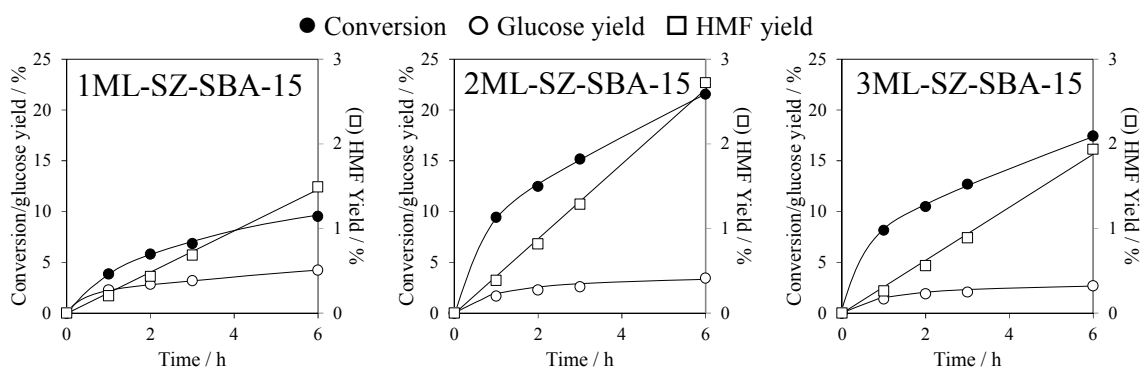


Figure 4.38: Profile of fructose conversion as well as glucose and HMF yield for fructose \rightarrow HMF reaction over xML-SZ/SBA-15 catalysts ($T=100^{\circ}\text{C}$, 0.1 g fructose, 20ml deionized water, substrate : catalyst = 1)

Figure 4.39 compares the yield of major products as well as the TOFs for glucose \rightarrow HMF and fructose \rightarrow HMF reaction over xML-SZ/SBA-15s. While 2ML catalyst gives the highest fructose and HMF yield with a small margin compared to 3ML, the 1ML is the least efficient catalyst among these three. Glucose TOF follows similar trend as it is 0.2 h^{-1} for the 1ML catalyst while the 2 and 3ML samples gives TOFs about 0.5 h^{-1} which implicate a change in the nature of active sites from 1ML to 2-3ML, which is attributed to the presence of more base sites in 2-3ML catalysts compared to 1ML. The HMF turnover frequency remains at constant level of 0.02 h^{-1} for all catalysts which is in accordance with the idea of formation of HMF over Brønsted acid sites which are common for all SZ/SBA-15 catalysts. The right side of **Figure 4.39** shows the yield of glucose and HMF along with fructose TOF for fructose dehydration reaction. The differences between TOFs over 1-3ML catalysts are not remarkable suggesting that fructose is converted over the same type of active sites (that are Brønsted acid sites) in all cases. The details of conversions, yield and selectivity of major products, rate of reactions, TOFs and carbon balance are presented in **Tables 4.15** and **Table 4.16**.

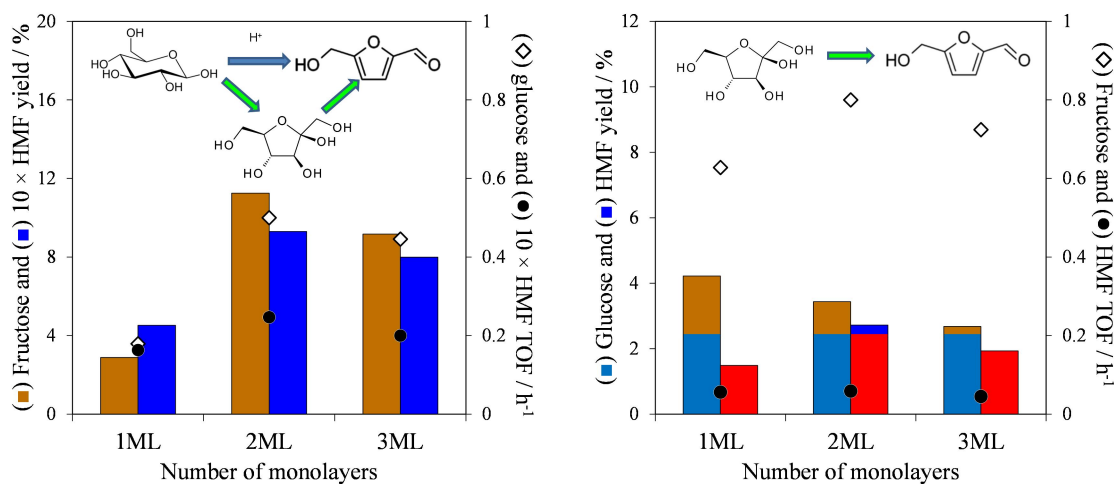


Figure 4.39: Left) fructose and HMF yield and glucose TOF (glucose → HMF), Right) glucose and HMF yield and fructose TOF (fructose → HMF)

Figure 4.40 demonstrates that the yield of HMF in reactions starting from glucose and fructose improves as the acid sites number increases.

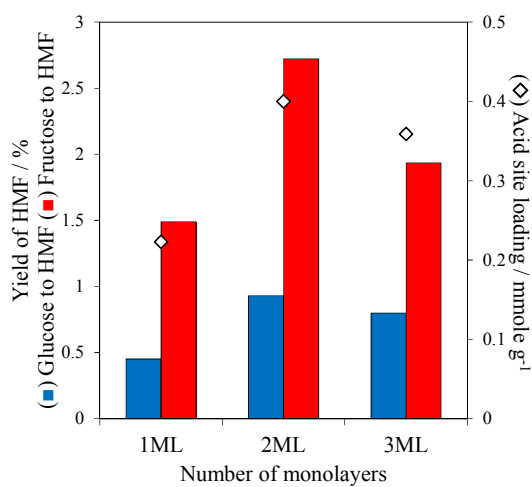


Figure 4.40: Yield of HMF from glucose → HMF and fructose → HMF reactions as well as acid site loading from ammonia TPD

Table 4.15: Conversion, rate of glucose consumption and HMF formation, yield and selectivity of major products following glucose dehydration to HMF over xML-SZ/SBA-15 at 100 °C. (0.1 g glucose, substrate : catalyst = 1, 20 ml deionized water)

Catalyst	Conversion*	Initial rate of glucose consumption	Initial rate of HMF formation	TOF	TOF	Yield		Selectivity		Carbon balance
				Glucose consumption	HMF formation	HMF	Fructose	HMF	Fructose	C _{out} /C _{in}
	%	μmol.h ⁻¹	μmol.h ⁻¹	h ⁻¹	h ⁻¹	%	%	%	%	%
Blank	9.9	13.0	0.06	-	-	0.1	9.3	0.6	93.6	99.4
SBA-15	4.4	-	-	-	-	0.1	4.3	1.2	96.6	102.2
1ML-SZ/SBA-15	3.3	2.0	0.2	0.2	0.02	0.5	2.9	13.6	86.4	103.1
2ML-SZ/SBA-15	12.4	10.0	0.5	0.5	0.02	0.9	9.6	9.1	77.3	98.3
3ML-SZ/SBA-15	10.0	8.0	0.4	0.4	0.02	0.8	8.6	8.0	85.8	99.4

* Conversion after 6h

Table 4.16: Conversion, rate of fructose consumption and HMF formation, yield and selectivity of major products following fructose dehydration to HMF over xML-SZ/SBA-15 at 100 °C. (0.1 g fructose, substrate : catalyst = 1, 20 ml deionized water)

Catalyst	Conversion	Initial rate of fructose consumption	Initial rate of HMF formation	TOF	TOF	Yield		Selectivity		Carbon balance
				Fructose consumption	HMF formation	HMF	Glucose	HMF	Glucose	C _{out} /C _{in}
	%	μmol.h ⁻¹	μmol.h ⁻¹	h ⁻¹	h ⁻¹	%	%	%	%	%
Blank	4.4	4.7	0.3	-	-	0.3	3.1	5.9	70.3	98.9
SBA-15	3.8	-	-	-	-	0.3	3.3	7.9	87.7	101.0
1ML-SZ/SBA-15	9.5	7.0	0.6	0.6	0.06	1.5	4.2	15.7	44.3	96.2
2ML-SZ/SBA-15	21.5	16.0	1.2	0.8	0.06	2.7	3.4	12.6	16.0	85.3
3ML-SZ/SBA-15	17.4	13.0	0.8	0.7	0.05	1.9	2.7	11.1	15.4	87.6

4.2.4.2 Effect of sulphur loading on glucose conversion

Since 2ML-SZ/SBA-15 material possessed the optimum acid:base ratio, it was selected for studying the effect of sulphur content on the activity of catalysts and yield of products. **Figure 4.41** represents the levels of glucose conversion as a function of S:Zr atomic ratio which mirrors the changes in base:acid site ratio very well. The relatively high level of glucose conversion over unsulphated Zr/SBA-15 correlates with high fructose yield over this catalyst which can be attributed to higher number of base sites as well as relatively high Lewis : Brønsted acid ratio compared to the sulphated samples (**Figure 4.42**). However, as the loading of SO_4^{2-} groups increases, glucose conversion monotonically decreases. This could be explained by the fact that the number of base sites decreases gradually across the series and also the ratio of Brønsted : Lewis acid sites increases. Consequently, the isomerization of glucose to fructose, which is known to be limiting step of the telescopic conversion of glucose to HMF, switches off and thus the fructose yield declines as the S:Zr ratio increases. Although, these variations in acid:base ratio and Brønsted : Lewis ratio are in favour of fructose dehydration to HMF. Therefore, HMF yield goes through a maximum (**Figure 4.42**).

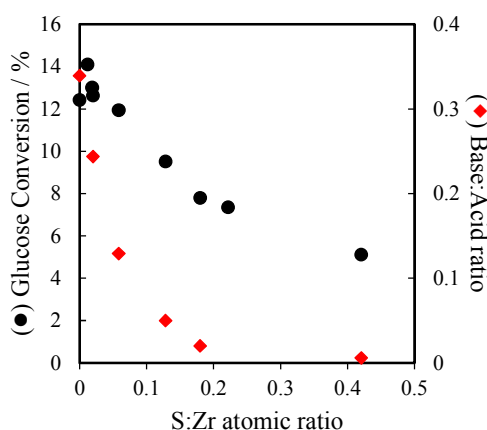


Figure 4.41: (●) Glucose conversion over SZ/SBA-15 series of catalysts and (♦) base:acid site ratio as a function of S:Zr atomic ratio, 100 °C

Moreover, the fructose selectivity drops from 93% over Zr/SBA-15 catalyst to ~87% where S:Zr atomic ratio equals to 0.13 and then levels off. In addition to that, HMF selectivity increases from 7.5% to about 12% over the S:Zr atomic ratio range of 0 to 0.13 and then plateaus.

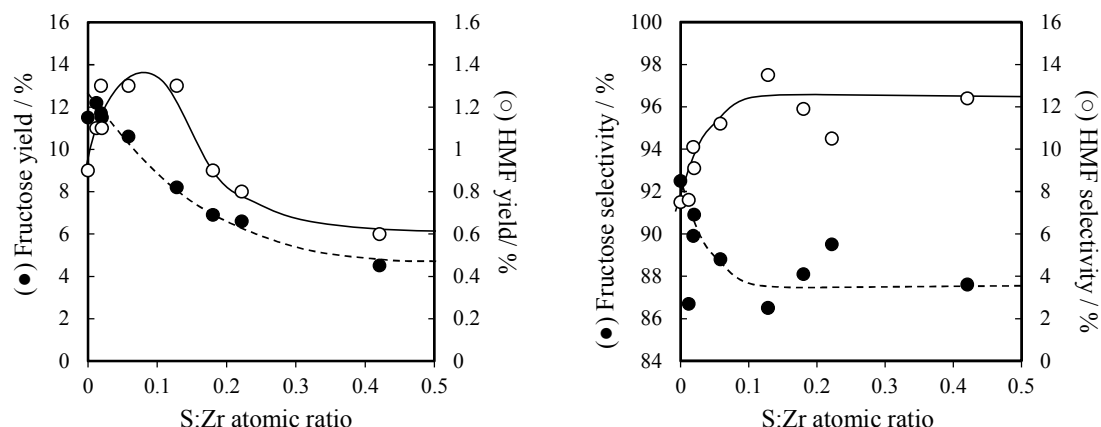


Figure 4.42: Left) Yield and Right) selectivity of fructose and HMF as a function of S:Zr atomic ratio in glucose transformation into HMF after 6 h reaction at 100°C

Furthermore, glucose TOF (normalized to acid sites) drops significantly as the S:Zr atomic ratio increases before reaching a plateau at S:Zr atomic ratio = 0.2 (**Figure 4.43**). The reason for this dramatic drop lies in replacement of surface base sites with acid sites as a result of incorporation of more SO_4^{2-} groups on ZrO_2 layer. Therefore, rate of glucose conversion (glucose \leftrightarrow fructose isomerization) decreases. Thus the numerator of TOF formula (rate of reaction) decreases and simultaneously the denominator (mass of catalysts multiplied by number of acid sites) increases which result in a smaller value for TOF. For the samples with S:Zr ratio above 0.2, the number of base sites are too small and negligible that can be assumed the isomerization over these catalysts only take places non-catalytically, plus that number of acid sites for last two points in **Figure 4.43** are fairly close to each other. (see **Table 4.17**), therefore glucose TOF remains constant. HMF formation is solely dependent on presence of Brønsted acid sites and availability of fructose in the reaction mixture. So in the regime where fructose is formed catalytically over base sites, HMF TOF remains constant at 0.04 h^{-1} and then when there are not much base sites left on the catalyst and isomerization reaction is taking place homogenously, it drops to about 0.015 and levels off. (**Figure 4.43**)

Figure 4.44 illustrates glucose conversion as well as fructose and HMF yield profiles for the glucose to HMF reactions over SZ/SBA-15 catalysts at 100 °C.

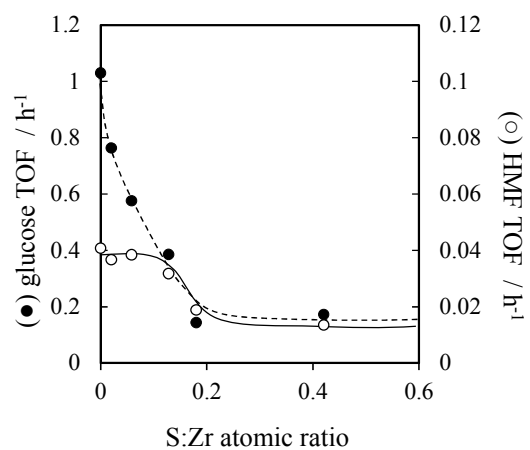


Figure 4.43: Glucose and HMF turnover frequencies as a function of S:Zr atomic ratio for glucose \rightarrow HMF reaction over SZ/SBA-15-xM series of catalysts

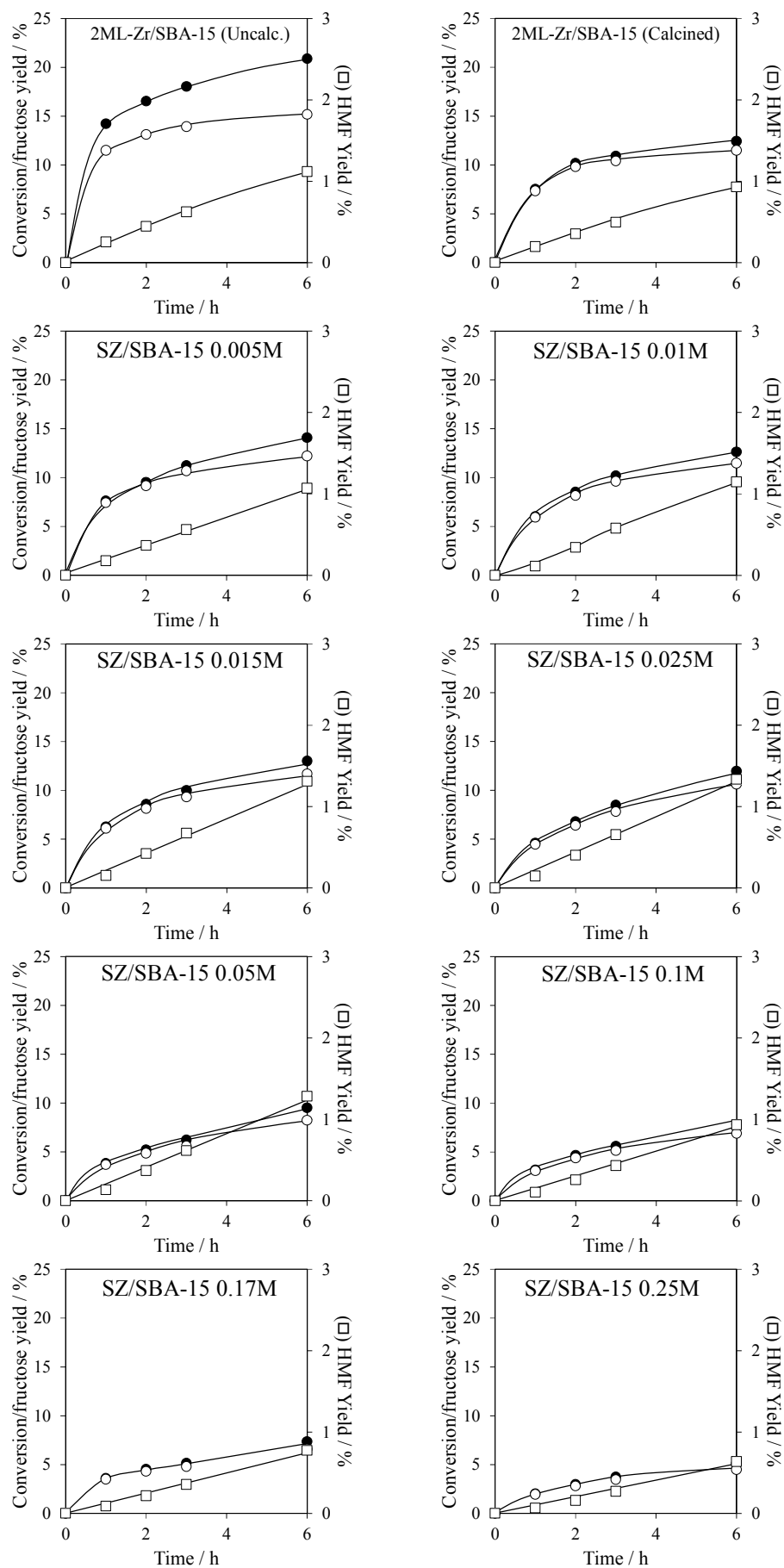


Figure 4.44: Profile of reactions for glucose → HMF over SZ/SBA-15 xM catalysts

Table 4.17: Conversion, rate of glucose consumption and HMF formation, yield and selectivity of major products following glucose dehydration to HMF over SZ/SBA-15 at 100°C

Catalyst	Conversion	Initial rate of glucose consumption	Initial rate of HMF formation	TOF	TOF	Yield		Selectivity		Carbon balance
				Glucose consumption	HMF formation	HMF	Fructose	HMF	Fructose	C _{out} /C _{in}
	%	μmol.h ⁻¹	μmol.h ⁻¹	h ⁻¹	h ⁻¹	%	%	%	%	%
Blank	10.0	13.0	0.0	-	-	0.1	9.2	0.6	91.8	99.2
SBA-15	4.4	-	-	-	-	0.1	4.3	1.2	96.6	102.2
1ML-Zr/SBA-15	15.8	30.0	0.0	-	-	0.9	13.0	5.9	81.9	98.6
2-MLZr/SBA-15 (Uncalcined)	20.9	41.0	1.04	-	-	1.1	15.2	5.4	72.7	95.4
2-MLZr/SBA-15 (Calcined)	12.4	24.0	0.95	1.03	0.04	0.9	11.5	7.5	92.5	102.5
SZ/SBA-15 0.005M	14.1	24.0	1.04	-	-	1.1	12.2	7.6	86.7	99.4
SZ/SBA-15 0.01M	12.6	21.0	1.01	0.76	0.04	1.1	11.5	9.1	90.9	101.4
SZ/SBA-15 0.015M	13.0	21.3	1.20	-	-	1.3	11.7	10.1	89.9	100.6
SZ/SBA-15 0.025M	11.9	17.4	1.16	0.58	0.04	1.3	10.6	11.2	88.8	100.8
SZ/SBA-15 0.05M	9.5	13.1	1.08	0.39	0.03	1.3	8.2	13.5	86.5	101.6
SZ/SBA-15 0.1M	7.8	5.7	0.75	0.14	0.02	0.9	6.9	11.9	88.1	103.0
SZ/SBA-15 0.17M	7.3	8.0	0.63	-	-	0.8	6.6	10.5	89.5	100.4
SZ/SBA-15 0.25M	5.1	6.0	0.47	0.17	0.01	0.6	4.5	12.4	87.6	101.4

4.2.4.3 Effect of sulphur loading on fructose conversion

The performance of SZ/SBA-15 catalysts with different sulphur contents was examined in fructose dehydration to HMF at 100 °C. As it is shown in **Figure 4.45**, however it was expected the activity of catalyst increases with the number of acid sites and increased Brønsted : Lewis acid sites ratio (analogous to fructose conversion over bulk SZ, **Figure 3.21**), fructose conversion does not significantly change. This could be attributed to in-pore adsorption due to high surface area and a combination of side reactions that are insensitive to acidity. While apparently it was not possible to influence the fructose conversion, we could observe a change in the selectivity to HMF which is dependent on Brønsted acidity.

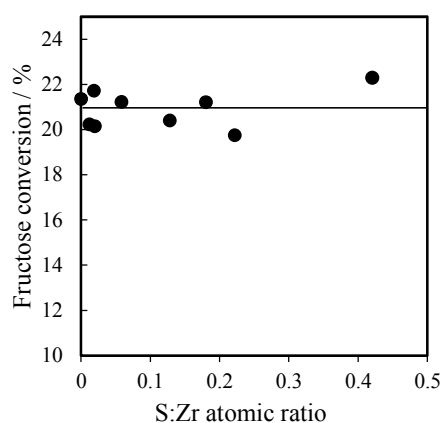


Figure 4.45: Fructose conversion over SZ/SBA-15 series of catalysts as a function of S:Zr atomic ratio after 6 h reaction at 100°C

As it is depicted in **Figure 4.46**, HMF yield monotonically increases with S:Zr atomic ratio from 1.8% over sulphur free SBA-15 supported ZrO_2 sample to 3.9% at S:Zr = 0.42. This is attributable to increased number of acid site and Brønsted acid sites in particular. In addition to that, selectivity toward HMF follows similar fashion as its yield, increasing from 8.8% to 17.4% when S:Zr ratio changes from 0 to 0.42. **Figure 4.46** also demonstrates that variation in physicochemical properties of the SZ/SBA-15 catalyst has minimal effect on glucose yield and selectivity.

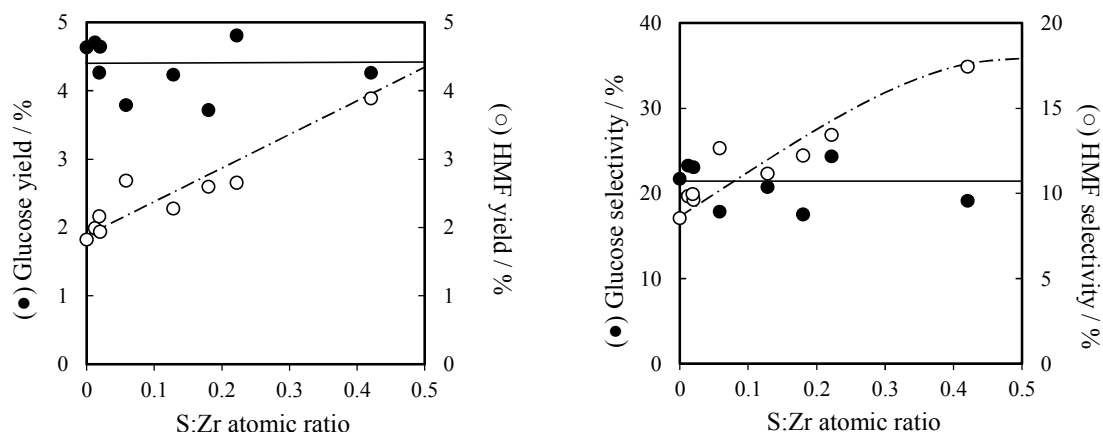


Figure 4.46: Left) Yield and Right) selectivity of glucose and HMF as a function of S:Zr atomic ratio in fructose transformation into HMF after 6 h reaction at 100 °C

The profiles of fructose conversion and yield of the major products for fructose dehydration reaction over SZ/SBA-15 catalysts are given in **Figure 4.48**. Then, the rate of HMF formation was calculated based on the data points which were collected in the first 3 h of the reactions. Following that, TOFs were calculated by normalizing the rates of HMF formation to mass of catalysts and the number of acid sites per unit of catalyst mass. As **Figure 4.47** demonstrates, HMF TOF remains at constant level of $\sim 0.07 \text{ h}^{-1}$ confirming that HMF has been formed over the same type of active sites that are supposed to be Brønsted acid sites. **Table 4.18** summarizes the obtained information about fructose dehydration reaction over the SZ/SBA-15 series of catalysts.

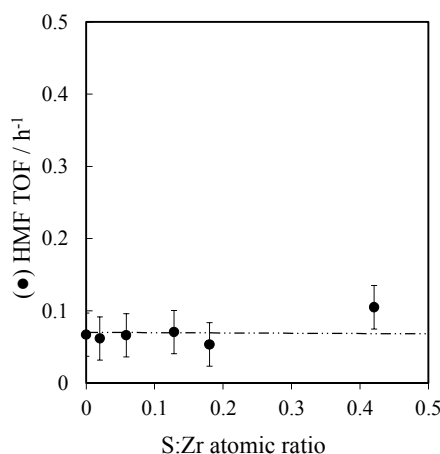


Figure 4.48: HMF turnover frequencies as a function of S:Zr atomic ratio for fructose → HMF reaction over SZ/SBA-15-xM series of catalysts

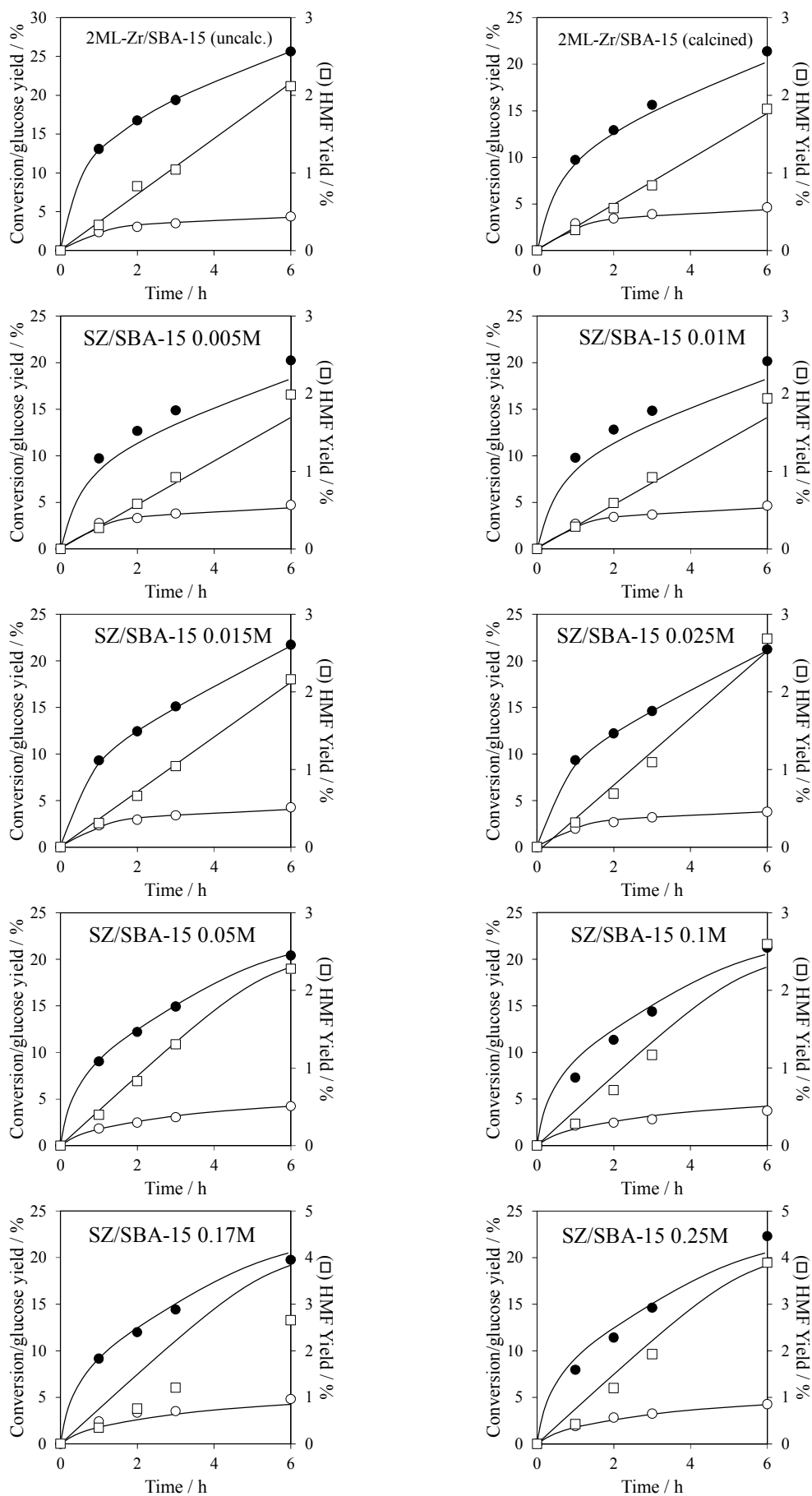


Figure 4.47: Profile of reactions for fructose \rightarrow HMF over SZ/SBA-15 xM catalysts

Table 4.18: Conversion, rate of fructose consumption and HMF formation, yield and selectivity of major products following fructose dehydration to HMF over SZ/SBA-15 at 100°C

	Conversion	Initial rate of fructose consumption	Initial rate of HMF formation	Yield		Selectivity		Carbon balance
				HMF	Glucose	HMF	Glucose	C _{out} /C _{in}
	%	μmol.h ⁻¹	μmol.h ⁻¹	%	%	%	%	%
Blank	4.4	4.7	0.3	0.3	3.1	5.9	70.3	98.9
SBA-15	3.8	-	-	0.3	3.3	7.9	87.7	101.0
1ML-Zr/SBA-15	20.4	33.1	0.8	1.9	4.7	9.2	22.9	87.5
2ML-Zr/SBA-15 (Uncalcined)	25.6	16.1	0.8	2.1	4.4	8.3	17.1	82.4
2ML-Zr/SBA-15 (Calcined)	21.4	16.6	0.8	1.8	4.6	8.5	21.7	86.2
SZ/SBA-15 0.005M	20.2	16.0	0.8	2.0	4.7	9.8	23.3	87.7
SZ/SBA-15 0.01M	20.1	16.1	0.9	1.9	4.6	9.6	23.1	87.8
SZ/SBA-15 0.015M	21.7	16.0	1.0	2.2	4.3	10.0	19.6	86.0
SZ/SBA-15 0.025M	21.2	15.6	1.0	2.7	3.8	12.6	17.9	86.4
SZ/SBA-15 0.05M	20.4	15.7	1.2	2.3	4.2	11.2	20.7	87.3
SZ/SBA-15 0.1M	21.2	11.4	1.1	2.6	3.7	12.2	17.5	86.0
SZ/SBA-15 0.17M	19.8	15.5	1.1	2.7	4.8	13.4	24.3	93.2
SZ/SBA-15 0.25M	22.3	11.9	1.8	3.9	4.3	17.4	19.1	86.5

4.2.5 Comparison between bulk SZ and SBA-15 supported SZ

Chapter 3 highlighted the physical and chemical properties of sulphated zirconia materials and their catalytic performance in glucose and fructose dehydration into HMF. Also, previously in this chapter, the impact of grafting sulphated zirconia layers on a high surface area meso-structure SBA-15 support was studied. This section will provide a comparison between these two sets of catalysts in glucose transformation into HMF.

In order to have a fair comparison between the activities of the two series of catalysts, glucose conversion was normalized to Zr content in the bulk of each catalyst. **Figure 4.49** shows that all the grafted samples have converted larger amount of glucose per gram of Zr. For both sets of catalysts, the normalized glucose conversion drops when $[\text{H}_2\text{SO}_4] = 0.025 \text{ M}$ and then reaches a plateau for concentrations greater than 0.05 M . This is consistent with decreased number of base and Lewis acid sites which are responsible for isomerisation of glucose to fructose. It is worth mentioning that the results for concentrations higher than 0.1 M are not demonstrated since it could be misleading because of dissolution of ZrO_2 film and therefore less well defined zirconia film in the supported materials and also because of loss of crystallinity and structural collapse in bulk SZ materials.

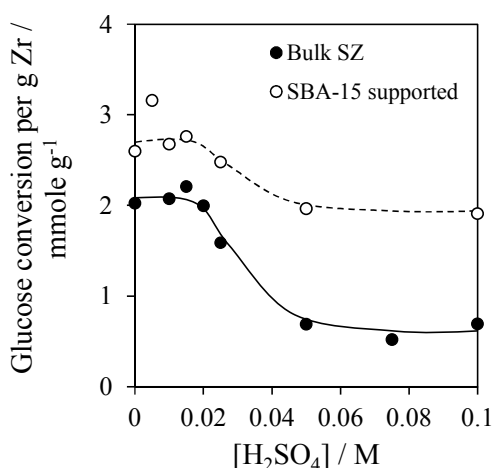


Figure 4.49: Glucose conversion normalized to Zr wt% for (●) Bulk SZ and (○) SBA-15 supported SZ catalysts

Similarly, HMF yield per gram of Zr was calculated and plotted as a function of sulphuric acid concentration for both series of catalysts (**Figure 4.50**). While HMF yield per gram of Zr rises steadily from 194 $\mu\text{mole g}^{-1}$ to 747 $\mu\text{mole g}^{-1}$ when H_2SO_4 concentration increased from 0 to 0.25 M over the grafted catalysts, it increases from 34 over pure zirconia to 117 over bulk SZ 0.05M and then levels off.

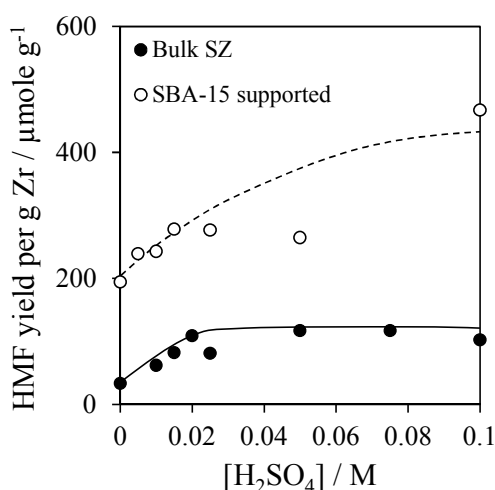


Figure 4.50: HMF yield normalized to Zr wt% for (●) Bulk SZ and (○) SBA-15 supported SZ catalysts

In conclusion, a larger amount of glucose is converted per gram of zirconium content of the supported materials compared to the bulk SZ catalysts. Also more HMF is produced per gram of Zr on the grafted materials than bulk SZs. So we can confirm that for the same amount of zirconium in the catalysts, the SBA-15 supported materials exhibit improved reactivity.

4.2.6 Catalyst stability and recyclability

4.2.6.1 Stability assessment via leaching test

In order to test the solubility of sulphate species, and thus any possible homogeneous contributions to the observed catalysis, a hot filtration test was instigated for the 2ML-SZ/SBA-15 samples impregnated with 0.01, 0.05 and 0.1 M sulphuric acid. Fructose was selected as reactant for this test since the scale of non-catalytic thermal conversion of fructose is smaller than that of glucose (because glucose thermally converts to fructose and could be misleading).

Filtration of the reaction solution at reaction temperature minimises potential re-adsorption of any dissolved SO_4^{2-} back onto the support. If the reaction is truly heterogeneous, i.e. no sulphate species leaching occurs, and subsequently the filtered reaction solution should exhibit almost no activity. **Figure 4.51** shows the results of such a test. Catalyst removal by hot filtration immediately stops further fructose conversion, confirming a purely heterogeneous reaction pathway.

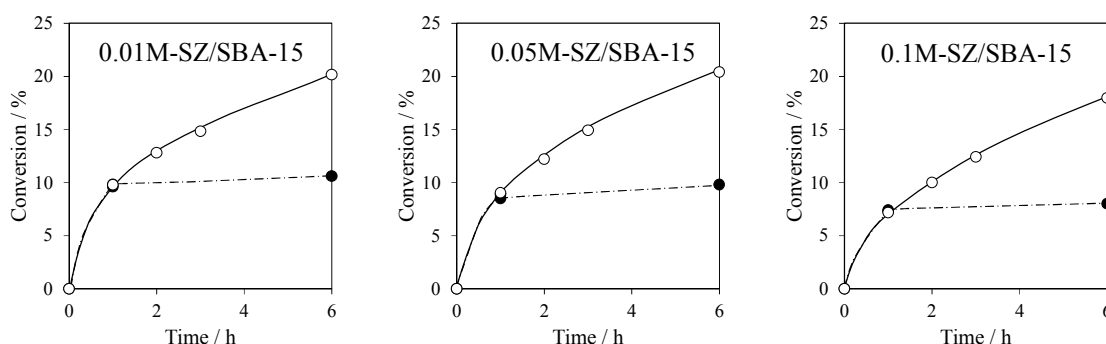


Figure 4.51: Hot filtration tests to assess SO_4^{2-} leaching in fructose dehydration over SZ/SBA-15 catalysts impregnated with 0.01, 0.05, 0.1M sulphuric acid. (catalysts were removed after 1 h)

4.2.6.2 Recyclability

For assessing the recyclability of the SZ/SBA-15 materials, the two most active catalysts in glucose conversion were picked and the catalysts were recovered after 6 h reaction and then dried and re-calcined in order to get rid of any carbonaceous solid materials stuck on the pores of the catalysts. **Figure 4.52** compares the catalytic activity of recovered material and the fresh catalysts in glucose dehydration, confirming that the recovered catalyst has maintained their catalytic properties.

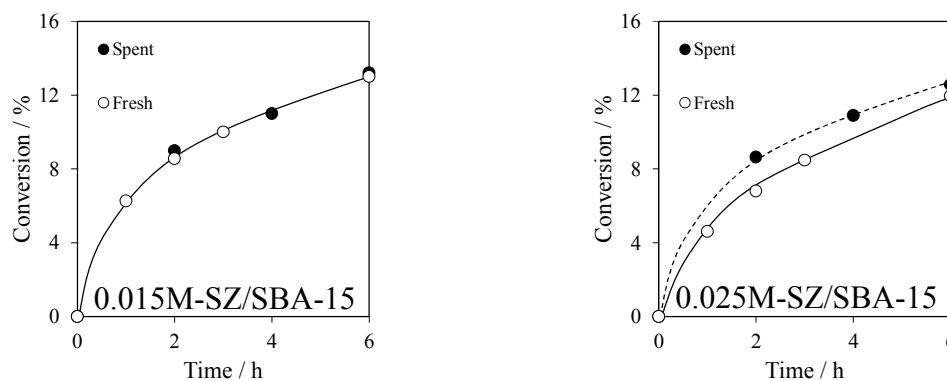
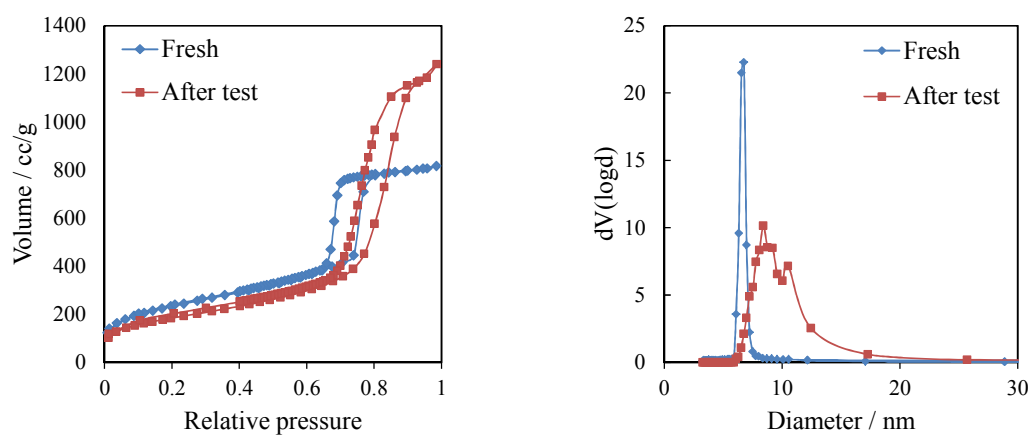


Figure 4.52: Comparison between catalytic activity of Fresh and recovered SZ/SBA-15 catalysts in glucose dehydration reaction

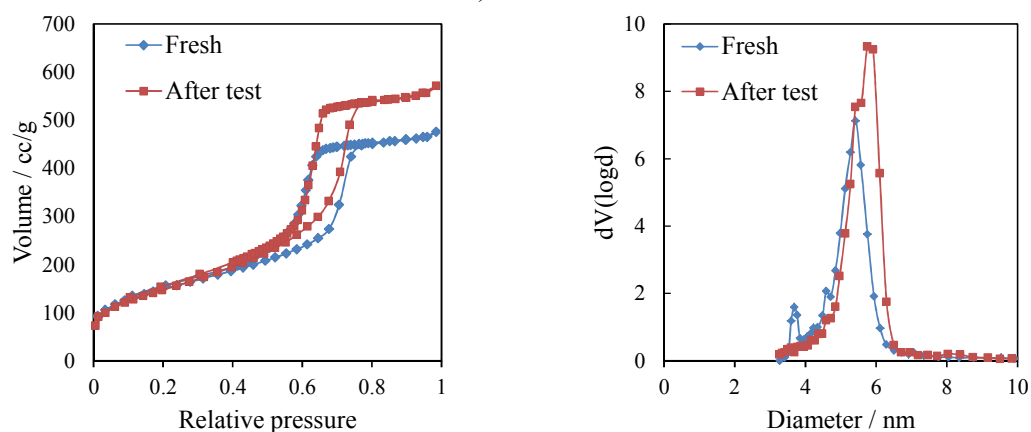
4.2.6.3 Hydrothermal stability test

Ordered mesoporous silicas (OMSs) such as SBA-15 have attractive properties like high specific surface area, large mesopore volume, adjustable pore diameter, narrow pore size distribution, and tailorable surface properties. In spite of their rather satisfactory thermal stability³⁶⁻³⁸, their hydrothermal stability is usually quite poor^{15, 37, 39, 40}, both in steam at high temperatures and in hot water. This deficiency is one of the major factors that hinder prospective applications of OMSs in chemical processing.⁴¹ In this section, it will be shown that grafting ZrO₂ on SBA-15 improves hydrothermal stability of SBA-15. For this purpose, as it was explained in **Chapter 2**, the hydrothermal stability of SBA-15 and 2ML-ZrO₂/SBA-15 was compared with each other.

As it is shown in **Figure 4.53**, the N₂ porosimetry isotherms of fresh SBA-15 and recovered sample after hydrothermal stability test reveal that the structure of the sample has been changed under the test conditions. The narrow pore size distribution of SBA-15 has become considerably broader. Contrary, the zirconia grafted material seems that has not been significantly affected during the course of the test (**Figure 4.53**). Using low angle XRD (**Figure 4.54**) in combination pore diameter measured by N₂ porosimetry, the pore spacing parameter and wall thickness have been calculated. **Table 4.19** shows that after the test, the pore diameter of SBA-15 became wider by 24.3% while its walls got thinner by 39.9%. In similar test conditions, the pore diameter of zirconia grafted SBA-15 only increased by 6.1% and its wall thickness decreased 5.5%. Hence it can be concluded that grafting zirconia is beneficial to hydrothermal stability of the SBA-15 support. The changes in textural properties of SBA-15 could be attributed to dissolution of silicon atoms into water. Dissolution of amorphous silica has been reported by many research groups⁴²⁻⁴⁴, even at room temperature.⁴⁵ While silicon was dissolved unevenly from SBA-15 and hence the pores got expanded, the zirconia film protected the SBA-15 support; therefore, the structure of the support remained intact.



a) SBA-15



b) 2ML-Zr/SBA-15

Figure 4.53: N₂ adsorption/desorption isotherms and BJH pore size distribution before and after hydrothermal stability test on a) SBA-15 and b) 2ML-Zr/SBA-15

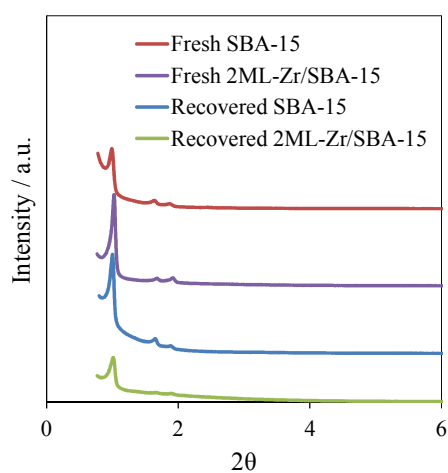


Figure 4.54: Low angle XRD on SBA-15 and zirconia grafted SBA-15 before and after hydrothermal stability test

Table 4.19: Comparison between physical structures of SBA-15 and ZrO₂ grafted SBA-15 before and after a hydrothermal stability test

Sample	Pore diameter	Pore spacing	Wall thickness	Change in pore diameter	Change in wall thickness
	nm	nm	nm	%	%
Fresh SBA-15	6.76	11.72	4.96	-	-
Recycled SBA-15	8.40	11.38	2.98	24.3	-39.9
Fresh Zr/SBA-15	5.42	11.45	6.03	-	-
Recycled Zr/SBA-15	5.75	11.45	5.70	6.1	-5.5

4.2.7 Catalyst deactivation

Humins are known as unwanted products of acid catalysed dehydration of saccharides which arise by the condensation of sugars with HMF and furfural. These dark brown solids are insoluble in water and their structures are often vaguely described. They can polymerize during the reaction and significantly drop the yield and selectivity of HMF. Moreover, humins strongly stick to the surface of the catalyst and block the pores gradually and make the active sites less accessible for the reactants.⁴⁶ However, upon the recovery of catalyst, it could be easily regenerated by burning out the humins.

Other possibility for deactivation of SZ/SBA-15 catalyst could be loss of sulphur species.⁴⁷ In order to investigate the potential decrease in the sulphur content of the materials, XPS analysis has been conducted on fresh catalysts and also on recovered and re-calcined catalysts. The data shows no change in the surface composition of the catalysts after one course of 6 h reaction with glucose in water regardless of the sulphur content. Reduction of oxidation state of sulphur⁴⁸ could be another origin of sulphated zirconia-based catalysts. However after one cycle of reaction with glucose in water, the oxidation state of sulphur in all SZ/SBA-15 remained unchanged confirming the stability of sulphate groups in the catalysts.

4.3 Conclusion

A simple route was developed to creating conformal sulphated zirconia monolayers throughout SBA-15 architecture that confers efficient acid-catalysed one-pot conversion of glucose to HMF. Conformal SZ monolayers with tuneable surface acid strength and site density can be dispersed over a mesoporous SBA-15 framework through a simple wet chemical grafting/hydrolysis protocol. A bilayer SZ/SBA-15 material exhibits the maximum surface acidity and balance of Brønsted : Lewis sites, and exhibits good performance in the one-pot conversion of glucose and fructose to HMF under mild conditions. Additionally, the impact of impregnating sulphuric acid concentration on characteristics and reactivity of the catalyst was probed showing similar behaviour to bulk systems in terms of tunability of acid:base ratio with pre-treatment with 0.05 M H_2SO_4 giving the optimal acid and base mixture for HMF production.

Comparing the catalytic activity of bulk SZ catalysts with supported SZ, it was found that a larger amount of reactant converts over the supported materials per gram of Zr precursor. It was also demonstrated that the hydrothermal stability of such zirconia grafted SBA-15 is remarkably higher than a bare SBA-15.

4.4 References:

1. Z.-G. Wu, Y.-X. Zhao and D.-S. Liu, *Microporous and Mesoporous Materials*, 2004, **68**, 127-132.
2. C. Flego, L. Carluccio, C. Rizzo and C. Perego, *Catalysis Communications*, 2001, **2**, 43-48.
3. A. Infantes-Molina, J. Mérida-Robles, P. Maireles-Torres, E. Finocchio, G. Busca, E. Rodríguez-Castellón, J. L. G. Fierro and A. Jiménez-López, *Microporous and Mesoporous Materials*, 2004, **75**, 23-32.
4. H. J. M. Bosman, E. C. Kruissink, J. Vanderspoel and F. Vandenbrink, *Journal of Catalysis*, 1994, **148**, 660-672.
5. C. K. Krishnan, T. Hayashi and M. Ogura, *Advanced Materials*, 2008, **20**, 2131-2136.
6. Y. Zhu, S. Jaenicke and G. K. Chuah, *Journal of Catalysis*, 2003, **218**, 396-404.
7. B. Katryniok, S. Paul, M. Capron, S. Royer, C. Lancelot, L. Jalowiecki-Duhamel, V. Belliere-Baca, P. Rey and F. Dumeignil, *Journal of Materials Chemistry*, 2011, **21**, 8159-8168.
8. O. Y. Gutiérrez, G. A. Fuentes, C. Salcedo and T. Klimova, *Catalysis Today*, 2006, **116**, 485-497.
9. J. Zhang, Z. Ma, J. Jiao, H. Yin, W. Yan, E. W. Hagaman, J. Yu and S. Dai, *Microporous and Mesoporous Materials*, 2010, **129**, 200-209.
10. W. Thitsartarn and S. Kawi, *Industrial & Engineering Chemistry Research*, 2011, **50**, 7857-7865.
11. Á. Reyes-Carmona, R. Moreno-Tost, J. Mérida-Robles, J. Santamaría-González, P. Maireles-Torres, A. Jiménez-López, E. Moretti, M. Lenarda and E. Rodríguez-Castellón, *Adsorption*, 2011, **17**, 527-538.
12. P. Lanzafame, D. M. Temi, S. Perathoner, A. N. Spadaro and G. Centi, *Catalysis Today*, 2012, **179**, 178-184.
13. B. Chang, J. Fu, Y. Tian and X. Dong, *Applied Catalysis A: General*, 2012, **437–438**, 149-154.
14. M. S. Morey, G. D. Stucky, S. Schwarz and M. Fröba, *The Journal of Physical Chemistry B*, 1999, **103**, 2037-2041.
15. D. Zhao, J. Feng, Q. Huo, N. Melosh, G. H. Fredrickson, B. F. Chmelka and G. D. Stucky, *Science*, 1998, **279**, 548-552.

16. D. Zhao, Q. Huo, J. Feng, B. F. Chmelka and G. D. Stucky, *Journal of the American Chemical Society*, 1998, **120**, 6024-6036.
17. I. Agirrezabal-Telleria, J. Requies, M. B. Güemez and P. L. Arias, *Applied Catalysis B: Environmental*, 2012, **115–116**, 169-178.
18. E. B. Celer, M. Kruk, Y. Zuzek and M. Jaroniec, *Journal of Materials Chemistry*, 2006, **16**, 2824-2833.
19. P. Webb and C. Orr, *Norcross: Micromeritics Instrument Corporation*.
20. U. Martin, H. Boysen and F. Frey, *Acta Crystallographica Section B*, 1993, **49**, 403-413.
21. V. T. Dondur, V. M. Rakić, L. S. Damjanović and A. Auroux, *Journal of the Serbian Chemical Society*, 2005, **70**, 457-474.
22. C. Morterra, G. Cerrato and M. Signoretto, *Catal Lett*, 1996, **41**, 101-109.
23. J. Dhainaut, J.-P. Dacquin, A. F. Lee and K. Wilson, *Green Chemistry*, 2010, **12**, 296-303.
24. I. Nowak, *Colloids and Surfaces A: Physicochemical and Engineering Aspects*, 2004, **241**, 103-111.
25. S. Brunauer, P. H. Emmett and E. Teller, *Journal of the American Chemical Society*, 1938, **60**, 309-319.
26. E. P. Barrett, L. G. Joyner and P. P. Halenda, *Journal of the American Chemical Society*, 1951, **73**, 373-380.
27. B. C. Lippens and J. H. de Boer, *Journal of Catalysis*, 1965, **4**, 319-323.
28. P. Madhusudhan Rao, A. Wolfson, S. Kababya, S. Vega and M. V. Landau, *Journal of Catalysis*, 2005, **232**, 210-225.
29. S. Damyanova, L. Dimitrov, R. Mariscal, J. L. G. Fierro, L. Petrov and I. Sobrados, *Applied Catalysis A: General*, 2003, **256**, 183-197.
30. C. Pirez, K. Wilson and A. F. Lee, *Green Chemistry*, 2014, **16**, 197-202.
31. Q. H. Xia, K. Hidajat and S. Kawi, *Journal of Catalysis*, 2002, **205**, 318-331.
32. B. Rakshe, V. Ramaswamy, S. G. Hegde, R. Vetrivel and A. V. Ramaswamy, *Catalysis Letters*, 1997, **45**, 41-50.
33. Y. Du, Y. Sun, Y. Di, L. Zhao, S. Liu and F.-S. Xiao, *J Porous Mater*, 2006, **13**, 163-171.
34. A. Osatiashtiani, A. F. Lee, D. R. Brown, J. A. Melero, G. Morales and K. Wilson, *Catalysis Science & Technology*, 2014, **4**, 333-342.

35. L. F. Chen, X. L. Zhou, L. E. Noreña, J. A. Wang, J. Navarrete, P. Salas, A. Montoya, P. Del Angel and M. E. Llanos, *Applied Surface Science*, 2006, **253**, 2443-2451.
36. S. Inagaki, Y. Fukushima and K. Kuroda, *Journal of the Chemical Society, Chemical Communications*, 1993, 680-682.
37. C.-Y. Chen, H.-X. Li and M. E. Davis, *Microporous Materials*, 1993, **2**, 17-26.
38. C.-Y. Chen, S.-Q. Xiao and M. E. Davis, *Microporous Materials*, 1995, **4**, 1-20.
39. S. S. Kim, W. Zhang and T. J. Pinnavaia, *Science*, 1998, **282**, 1302-1305.
40. R. Ryoo and J. M. Kim, *Journal of the Chemical Society, Chemical Communications*, 1995, 711-712.
41. Y. Liu and T. J. Pinnavaia, *Journal of Materials Chemistry*, 2002, **12**, 3179-3190.
42. G. Okamoto, T. Okura and K. Goto, *Geochimica et Cosmochimica Acta*, 1957, **12**, 123-132.
43. G. B. Alexander, W. M. Heston and R. K. Iler, *The Journal of Physical Chemistry*, 1954, **58**, 453-455.
44. R. O. Fournier and J. J. Rowe, *Am. Mineral.:(United States)*, 1977, **62**.
45. G. W. Morey, R. O. Fournier and J. J. Rowe, *Journal of Geophysical Research*, 1964, **69**, 1995-2002.
46. R.-J. van Putten, J. C. van der Waal, E. de Jong, C. B. Rasrendra, H. J. Heeres and J. G. de Vries, *Chemical Reviews*, 2013, **113**, 1499-1597.
47. F. T. T. Ng and N. Horvát, *Applied Catalysis A: General*, 1995, **123**, L197-L203.
48. J. C. Yori, J. C. Luy and J. M. Parena, *Applied Catalysis*, 1989, **46**, 103-112.

Chapter 5

**Biodiesel production via esterification of free
fatty acids over sulphated zirconia based
catalysts**

5.1 Introduction

Biodiesel is one of the most promising renewable energy carriers with potential for substituting fossil fuel diesel with no or minor modification to the vehicle engines required.^{1, 2} Moreover, one of the merits of biodiesel is that compared to petroleum based diesel fuel, the combustion of biodiesel produces lower amounts of pollutant materials such as carbon monoxide, sulphur dioxide and unburned hydrocarbons.^{3, 4}

In chemistry, the term biodiesel refers to a fuel composed of mono-alkyl esters of long chain fatty acids derived from renewable sources, either vegetable oils (edible) or non-food plant oils, algal oils and animal fats (non-edible).⁵ A great variety of vegetable oils such as canola, palm, palm kernel, sunflower and coconut oil have been studied as feedstock for biodiesel production. However, there are two major concerns regarding the use of these vegetable oils for biodiesel production; one is the high price of vegetable oils that makes the final product unable to compete with conventional petroleum based diesel. Secondly, to be considered sustainable, biomass sourced from non-edible components of crops, such as stems, leaves and husks or cellulose from agricultural or forestry waste must be used as feedstock.⁶ A newer generation of biodiesel is produced from algae oil which can be solely used for fuel production purposes and also many of the waste-product extracts produced during the processing of algae for biofuel can be used as a sufficient animal feed.^{7, 8}

Bio-oil cannot be directly used in an engine due to its high viscosity, large amount of impurities and high acid content which could damage the engine. Therefore, bio-oil should be converted to biodiesel beforehand. There are a number of ways for production and application of biodiesel. Potentially, it could be produced by microemulsion and or thermal cracking methods; however, biodiesel obtained from microemulsion and thermal cracking suffers from a low cetane number which means incomplete combustion of the product.⁹ The most common method for biodiesel production is via transesterification. Biodiesel production by means of transesterification is rather a simple process and has been widely studied and is already commercially developed.¹⁰ In the transesterification reaction triglyceride (TAG) molecules present in the bio-oil react with an alcohol in presence of a catalyst to form esters and glycerol. (**Figure 5.1**)

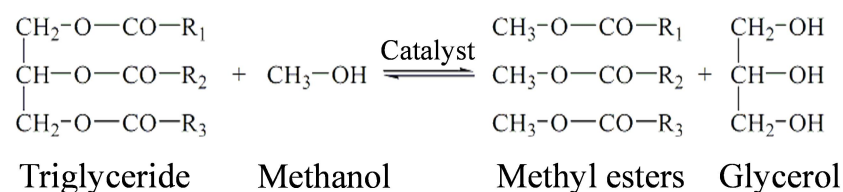


Figure 5.1: Transesterification reaction of triglyceride with methanol

For commercial synthesis of biodiesel, currently C₁₄ to C₂₀ TAGs undergo transesterification in the presence of a liquid base catalyst and either methanol or ethanol.¹¹⁻¹⁴ Transesterification of triglycerides takes place in three consecutive steps. First a triglyceride molecule reacts with one alcohol molecule to form diglyceride and methyl ester. Then, diglyceride reacts with alcohol to produce one more methyl ester and a monoglyceride molecule. Finally monoglyceride will react with alcohol and a glycerol molecule and methyl ester is produced. **Figure 5.2** demonstrates the three steps of transesterification reaction between triglyceride and methanol.^{15, 16}

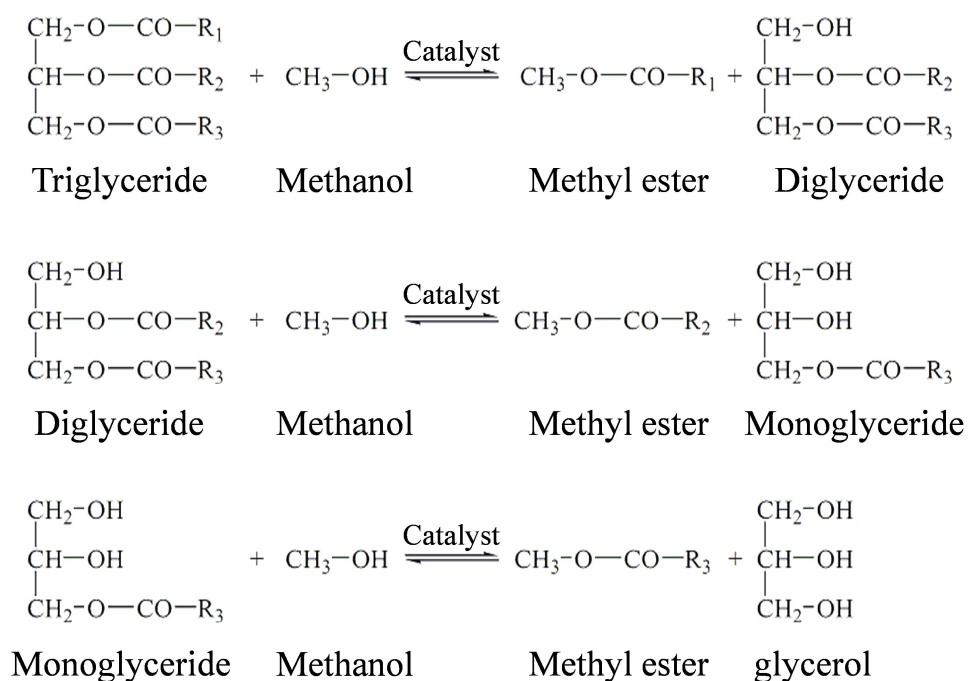


Figure 5.2: Transesterification reaction steps

Generally, base catalysts are more active than acids in transesterification, hence are particularly suitable for high purity oils with low free fatty acid (FFA) content. Use of solid base catalyst in a continuous flow reactor with a packed bed arrangement would be beneficial to catalyst separation and co-production of high purity glycerol, by this

means the production cost will be reduced and enabling catalyst recyclability. Different types of solid base catalysts are known for such a process including alkali or alkaline earth oxides, supported alkali metals, basic zeolites and clays such as hydrotalcites and immobilized organic bases.¹⁷

5.1.1 Esterification

As mentioned previously, biodiesel production from bio-oil sourced from non-edible crops and wastes has attracted much interest. But there is a major problem associated with these types of feedstocks which is the high free fatty acid (FFA) content. FFAs can deactivate base catalysts simply by reacting with them (neutralization reaction). Therefore, when low-quality feedstocks are used, a FFA removal step is necessary prior to transesterification.^{18, 19} This is usually done by means of an esterification reaction to convert FFAs to fatty acid esters.

Traditionally, esterification is carried out in presence of homogeneous acid catalysts such as H₂SO₄, HF, H₃PO₄, HCl and p-toluene sulfonic acid.^{20, 21} However, in the interest of sustainable chemistry, process safety and loss prevention, heterogeneous acid catalysts are considered as an alternative.²² Numerous solid acids have been studied in the FFA esterification reaction including zirconium oxide, titanium oxide, tin oxide, sulfonic ion-exchange resin, sulfonic modified mesostructure silica, sulfonated carbon-based catalyst and heteropolyacids (HPAs). More recently, the use of aluminosilicates (mordenite, halloysite, kaolinite) and cation-exchange resins for esterification of FFAs have also been investigated.²³

SathyaSelvabala *et al.*²⁴ showed that treating H-Mordenite (Al/Si ratio = 19) with phosphoric acid makes an efficient heterogeneous catalyst for esterification of FFA in neem oil. The group demonstrated that the amount of FFA reduced from 24.4 to 1.8 mg KOH/g oil. The optimum reaction parameters were found to be: 6:1 methanol/oil molar ratio; 1% catalyst loading and 60 °C reaction temperature. In another study, the performance of halloysite as heterogeneous catalyst for methylic and ethylic esterification of lauric acid was examined by Zatta *et al.*²⁵ Various alcohol:lauric acid molar ratios and catalyst loadings were studied at 160 °C in 2 h reactions in a pressurised reactor. The optimal reaction conditions were found to be 12:1

alcohol:lauric acid molar ratio and 12% catalyst loading where 95% and 87% of lauric acid was converted in methylic and ethylic esterification reactions respectively.

Cation-exchange resins have shown promise in esterification of FFAs, however their catalytic activity greatly depends on their swelling properties since the accessibility of the reactants could be controlled by swelling capacity of the resin and hence the overall activity could be affected in this way.²⁶ In this respect, Feng *et al.*²⁷ investigated the catalytic activity of three cation-exchange resins in the esterification of acidified oil generated from waste frying oils with methanol. The highest FFA conversion of 90% was obtained over NKC-9 with excellent reusability. This resin was also tested in a continuous flow fixed bed reactor and high FFA conversion and operational stability was observed, while loss of sulfonic acid groups from NKC-9 resin into the production stream during continuous esterification was not detected.²⁸ The use of Amberlysts, acid ion-exchange resins, has also been widely studied on esterification reaction to produce biodiesel.²⁹⁻³²

Zirconia-based catalysts have also been widely studied for the esterification of FFAs. The use of tungsten oxide zirconia has been reported for conversion of FFAs in used vegetable oils with high activity and no leaching.^{19, 33} Among WO_3/ZrO_2 catalysts with WO_3 content ranging from 10 to 30 wt%, 20 wt% is found to be the most active due to the great strength of its acid sites. Kim *et al.*³⁴, have also reported the use of a class of zirconia-supported metal oxide catalysts for biodiesel production from brown grease (acid value: 178 mg KOH/g). High FAME yields through esterification of FFA were achieved. In particular, a ZnO/ZrO_2 catalyst showed a high FAME yield and displayed high durability. The total acid number measured for the product converted over ZnO/ZrO_2 , was 12 mg KOH/g, representing a FAME yield of 78%. In another study, methylic esterification of myristic acid in the presence of TAG and sulphated zirconia catalyst was investigated by Rattanaphra and co-workers.³⁵ The group conducted the reaction at temperatures ranging from 120 to 170 °C, using a catalyst loading of 3 wt% and a FFA:methanol molar ratio of 1:20 and ~97% conversion was reported after 20 h reaction. Despite good catalytic performance of sulphated zirconia catalysts in esterification reactions, there are a number of problems associated with their use. First is the leaching of sulphate species and subsequent deactivation of the catalyst. The second problem is the high cost of zirconia support production, thus its cost is prohibitively

high for use in biodiesel production, as zirconium is a rare and expensive element. Therefore, incorporation of zirconia on a low cost support with acceptable physical properties is highly desirable. A summary of selected papers on solid acid catalysed esterification reactions is presented in **Table 5.1**. Excellent reviews on this research topic can be found elsewhere.³⁶⁻⁴⁰

Table 5.1: Solid acid catalysts for esterification reaction

Catalyst	Feedstock	Alcohol	Oil:Alcohol Molar ratio	Catalyst loading wt%	Temperature °C	Reaction time h	Conversion %	Ref
Kaolins	Oleic acid	MeOH	1:60		160	6	96.8	22
Raw halloysite	Lauric acid	MeOH	1:12	12	160	2	95.0	25
Raw halloysite	Lauric acid	EtOH	1:12	12	160	2	87.1	25
WO ₃ /ZrO ₂	Waste acid oil	MeOH	1:9	20	150	2	96	33
ZnO/ZrO ₂	Brown grease	MeOH	15:10.5 w/w	5.3	200	2	^a	34
SO ₄ ²⁻ /ZrO ₂	Rapeseed oil + myristic acid ^b	MeOH	1:20	3	120	0.33	94.6	35
Ionic exchange resin	Soybean oil + oleic acid ^c	MeOH	-	-	100	2.5	80	29
Amberlyst	Soybean oil + oleic acid ^d	MeOH	1:6	20	80	2	99.8	30
Amberlyst	oleic acid	MeOH	1:1 w/w	5 cm fixed bed	100	Continuous flow	97.5	32

^a 78% FAME yield reported, ^b 10 wt% myristic acid, ^c 50 wt% FFA, ^d 2.5 wt% FFA

In conclusion, the esterification reaction is a key step in the process of biodiesel production and the use of solid acid catalysts for FFA esterification to FAME at mild temperatures is necessary. In this chapter, esterification of FFAs and alcohols in presence of bulk sulphated zirconia catalysts as well as SBA-15 supported sulphated zirconia will be highlighted and the effect of FFA and alcohol chain length will be studied.

5.2 Results and discussion

This section will highlight the performance of the series of sulphated zirconia catalysts as well as SBA-15 supported sulphated zirconias in the esterification of a range of FFAs with a number of primary alcohols. **Chapter 3** and **4** explained the catalytic performance of these catalysts in the dehydration of glucose and fructose into 5-HMF. The detailed characterizations of the catalysts are given in the in **Sections 3.2.1** and **4.2.1**. In the final section of this chapter a comparison between the catalytic performances of the two series of catalysts will be made and the possibility of SO_4 groups leaching to the reaction media will be examined.

5.2.1 Bulk sulphated zirconia for esterification of FFAs

In this section the catalytic performance of bulk sulphated zirconia catalysts with different sulphur contents in the esterification reaction will be presented. Also, the reactivity of four carboxylic acids of different alkyl chain length in esterification with methanol will be discussed. Moreover, the effect of alcohol type on esterification of propionic acid will be covered.

5.2.1.2 Effect of carbon chain length on esterification of fatty acids with methanol

Figure 5.3 shows the reaction profiles for esterification of four free fatty acids of different alkyl chain length with methanol at 60 °C catalysed by the series of bulk sulphated zirconia. As shown in this figure, regardless of the size of FFA molecules, the conversions of the acids increase with $[\text{H}_2\text{SO}_4]$ of the impregnating solution. However, the conversions over SZ 0.5M are slightly lower than that of SZ 0.1M due to a change in crystalline structure when zirconia is treated with H_2SO_4 of high concentration. **Table 5.2** compares the conversion of propionic, hexanoic, lauric and palmitic acid after 24 h esterification reaction with methanol over bulk SZ series at 60 °C.

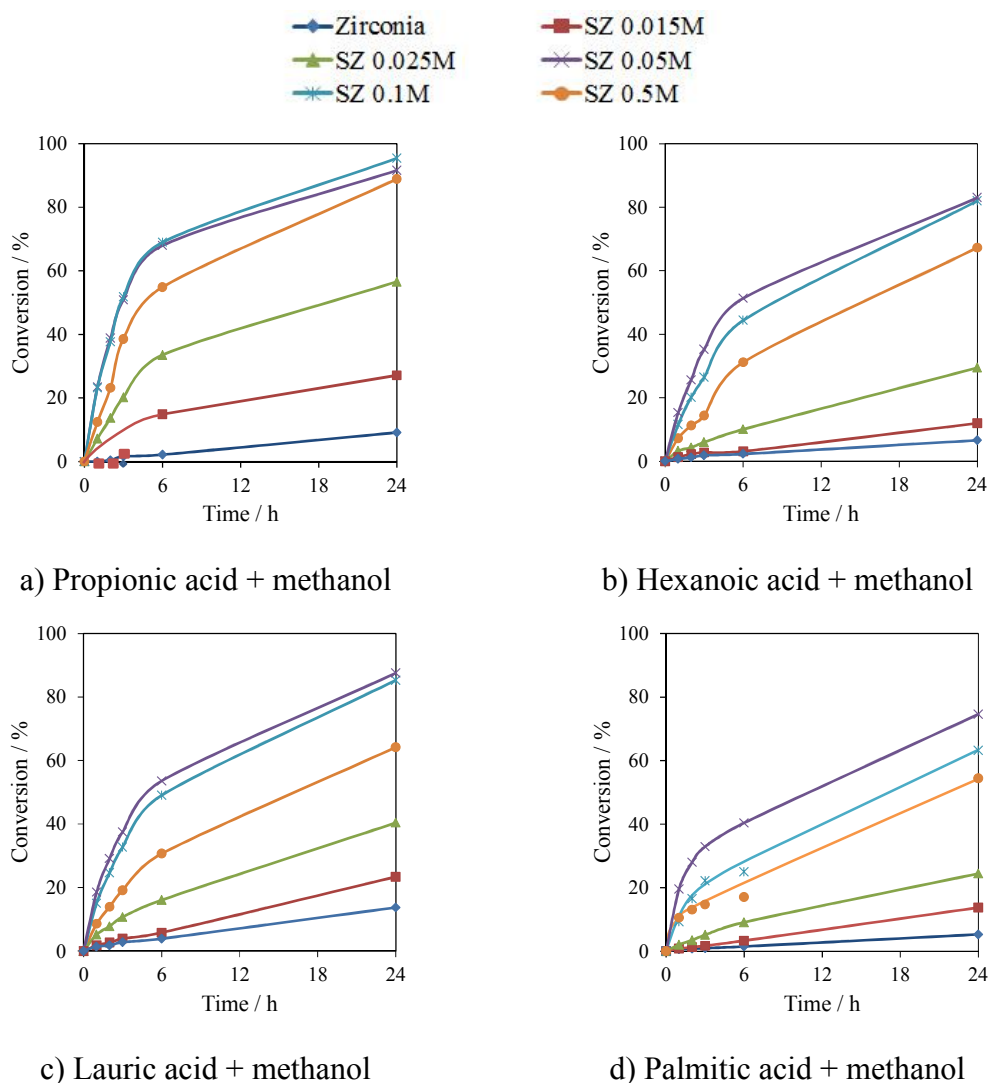


Figure 5.3: Reaction profiles for esterification of C3, C6, C12 and C16 carboxylic acids with methanol over bulk SZ catalysts at 60 °C

Table 5.2: Conversion of C₃, C₆, C₁₂ and C₁₆ carboxylic acids in esterification reaction with methanol at 60 °C after 24 h

Catalyst	Conversion / %			
	Propionic	Hexanoic	Lauric	Palmitic
ZrO ₂	9.1	6.6	5.9	5.3
SZ 0.015M	27.1	12.0	11.9	13.7
SZ 0.025M	56.6	29.5	26.8	24.4
SZ 0.05M	91.6	83.0	77.9	74.6
SZ 0.1M	95.4	82.0	68.8	63.2
SZ 0.5M	88.8	67.3	64.2	54.4

Furthermore, the initial rate of reactions and TOFs as a function of surface SO₄²⁻ coverage for esterification of FFAs over SZ catalysts are shown in **Figure 5.4** and

Table 5.3, showing that rate of esterification reactions and TOFs reach a maximum when the reaction was conducted over SZ 0.05M catalyst. This is the loading where there is a good balance between all physical properties such as surface area, %tetragonal phase and acid site loading and strength and therefore beyond this point extra S loading is not active for the esterification.

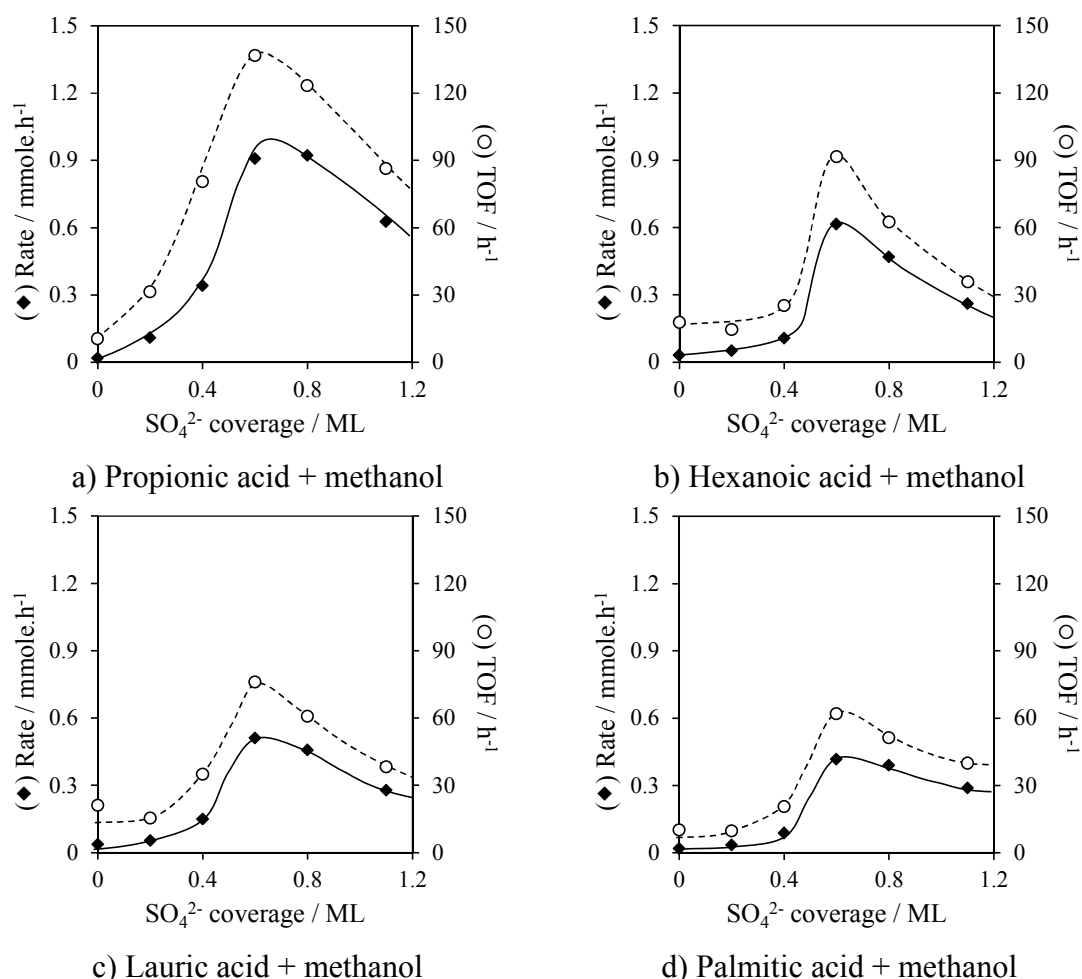


Figure 5.4: Reaction rate and TOF for esterification of methanol with a) propionic acid, b) hexanoic acid, c) lauric acid and d) palmitic acid at 60 °C

Table 5.3: TOFs of C₃, C₆, C₁₂ and C₁₆ carboxylic acids in esterification reaction with methanol at 60 °C

Catalyst	TOF / h ⁻¹			
	Propionic	Hexanoic	Lauric	Palmitic
ZrO ₂	28	13	11	10
SZ 0.015M	31	10	14	10
SZ 0.025M	70	21	26	21
SZ 0.05M	100	71	89	62
SZ 0.1M	91	53	62	51
SZ 0.5M	70	36	46	40

Moreover, **Figure 5.5** depicts that the TOF value over the most active catalyst (SZ 0.05M) decreases as the acid alkyl chain gets longer.

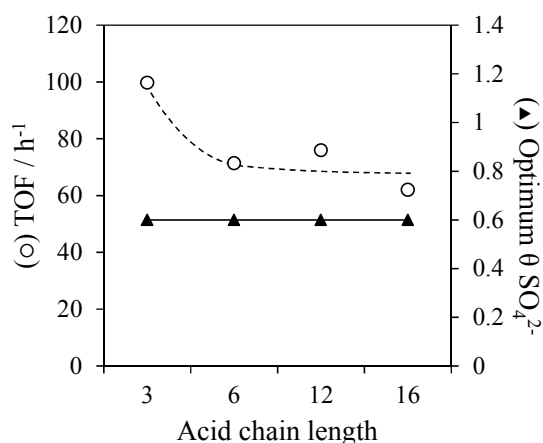


Figure 5.5: (O) Optimum TOFs across the series of SZ catalysts as a function of FFAs carbon chain length and (▲) the corresponding S coverage that gives the optimum TOF

The observed reactivity trend for carboxylic acids can be explained using the mechanistic model for esterification proposed by Rattanaphra, *et al.*⁴¹ They used sulphated zirconia as catalyst for the esterification of myristic acid using methanol. The mechanism of esterification probably follows the Langmuir-Hinshelwood model.^{42, 43} In this mechanism, methanol and myristic acid are preferentially adsorbed on the Brønsted acid sites of sulphated zirconia during esterification. Then the hydroxyl group of methanol is protonated by Brønsted acid on the catalyst surface while the protonation of myristic acid on an adjacent site leads to the carbocation. Deprotonation of the methanol oxygen produces the nucleophile, which attacks the carbocation to generate a tetrahedral intermediate. As shown in **Figure 5.6**, the tetrahedral intermediate eliminates water to form ester.

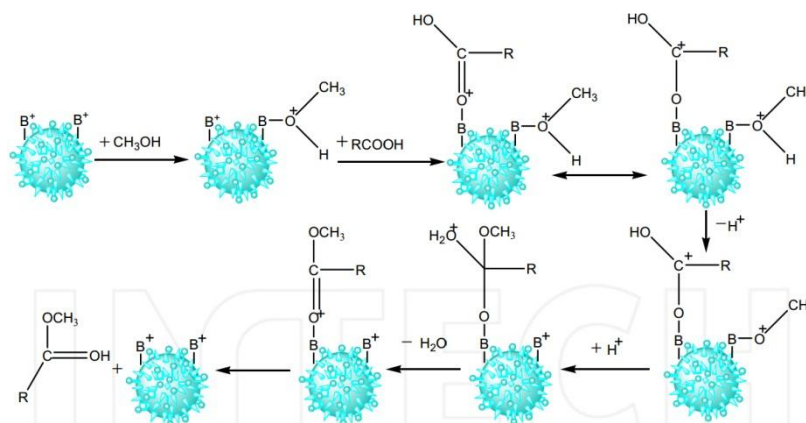


Figure 5.6: Mechanism of esterification reaction over sulphated zirconia⁴⁴

Based on the proposed reaction mechanism, the decreased reactivity with increasing molecular size could be attributed to two factors; an inductive effect and a steric effect.⁴⁵ The inductive effect is a consequence of the increase in electron-donating ability of the acid as its alkyl chain gets longer. The inductive effect accelerates the protonation of the carbonyl oxygen. On the other hand, it also lowers electrophilicity of the carbonyl carbon, resulting in a more energy-hindered rate limiting nucleophilic attack by the alcohol.

The steric effect is assumed to play a more significant role than the inductive effect in carboxylic acid reactivity for acid-catalysed esterification.⁴⁵⁻⁴⁷ Steric hindrance increases with molecular size, inducing electronic repulsion between non-bonded atoms of reacting molecules. This repulsive hindrance decreases electron density in the intermolecular region and disturbs bonding interactions.⁴⁷ Hence, as the alkyl chain in the carboxylic acid become larger, its steric effect intensifies.

However, the size of molecules is not the only factor involved in steric hindrance, but also the preferential conformations.^{48, 49} This enhances the so-called “conformational leveling” effect.⁴⁹ The similar observed reactivity by hexanoic, lauric and palmitic acid (**Table 5.3 Figure 5.5**) can be explained through this model. However, in heterogeneous catalysis any contribution from conformational leveling seems to be minimal. Due to the direct adsorption of alkyl groups upon the catalyst surface, the accessibility of methanol to any protonated (or activated) carboxylic centres is detrimentally affected upon progression to larger alkyl chain substituents, thus leading to an observable drop in catalytic activity. For substrates $> C_6$, we can theorise an apparent rate limitation due not only to restricted methanol-substrate accessibility, but also because the process of substrate-adsorption/product-desorption to/from surface is more laboured.

5.2.1.1 Effect of alcohol type on propionic acid esterification

Propionic acid esterification with four primary alcohols in the presence of bulk sulphated zirconia catalysts was conducted at 60 °C. **Figure 5.6** demonstrates that the activity of SZ catalysts increases with the surface sulphate coverage and reaches its

optimum performance when it was impregnated with sulphuric acid of concentration of 0.05 to 0.1 M.

Furthermore, the effect of alcohol type on esterification of propionic acid was studied using three other alcohols; ethanol, n-propanol and n-butanol. As demonstrated in **Figure 5.6**, substituting methanol with ethanol results in significant drop in propionic acid conversion. Although using ethanol, propanol and butanol, no meaningful variations were observed in the conversions and the rate of reactions. Additionally, the conversion and rate values follow the same trend regardless of alcohol type for C₂ to C₄ alcohols. **Table 5.4** represents a summary of propionic acid conversion in esterification with different types of alcohols in presence of SZ catalysts.

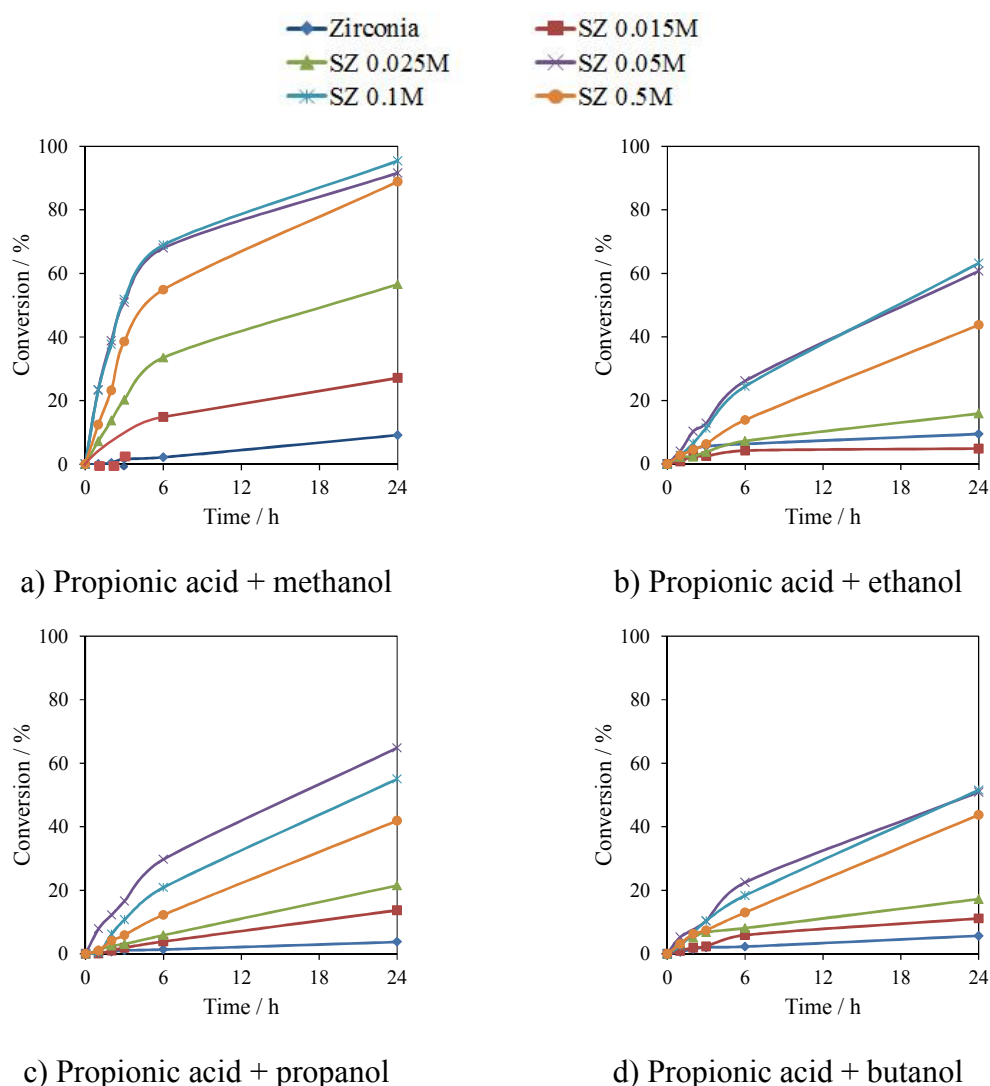
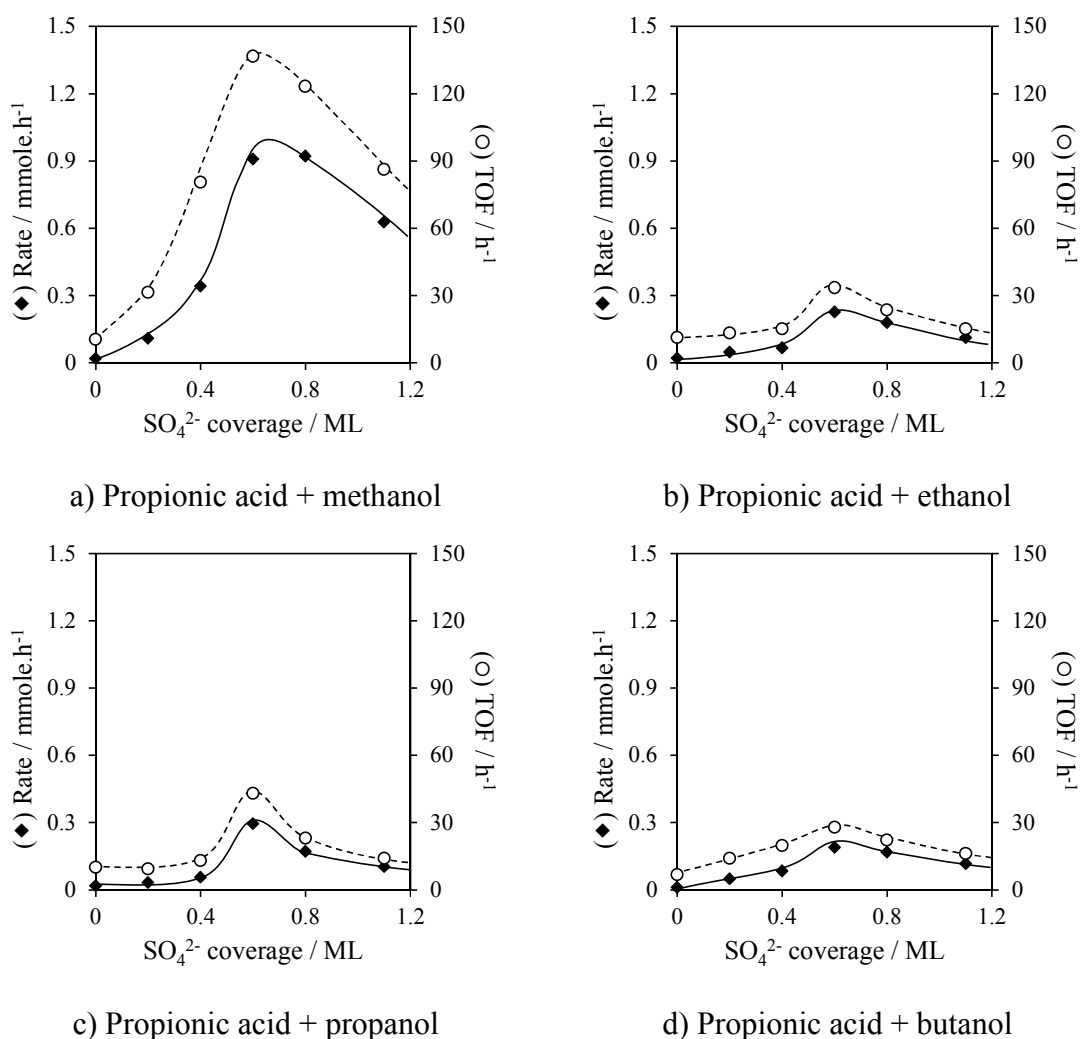


Figure 5.6: Esterification of propionic acid with a) methanol, b) ethanol, c) propanol and d) butanol over bulk SZ catalysts

Table 5.4: Esterification of propionic acid with C₁ to C₄ linear alcohols at 60 °C after 24 h

Catalyst	Conversion / %			
	Methanol	Ethanol	Propanol	Butanol
ZrO ₂	9.1	9.5	3.7	5.7
SZ 0.015M	27.1	4.9	13.7	8.2
SZ 0.025M	56.6	15.9	21.5	17.2
SZ 0.05M	91.6	60.7	64.8	50.9
SZ 0.1M	95.4	63.2	55.0	51.5
SZ 0.5M	88.8	43.8	41.9	43.7

Figure 5.7 presents propionic acid esterification reaction rates and TOFs (normalized to number of acid sites) with different alcohols across the series of bulk SZ catalysts. From this figure, it can be observed that regardless of the alcohol molecular weight, reaction rate and TOF go through a maximum at $\theta_{\text{SO}_4^{2-}} = 0.6$ (SZ 0.05M)

**Figure 5.7:** Reaction rate and TOF for esterification of propionic acid with a) methanol, b) ethanol, c) propanol and d) butanol

As illustrated in **Figure 5.8**, the absolute value of rate and TOF is considerably higher when the esterification reaction is carried out with methanol and the TOFs of reaction with ethanol, propanol and butanol are similar. The lower reactivity of alcohols with longer carbon chains could be explained by their higher boiling temperature⁵⁰, which means for larger alcohols more energy is required to overcome the van der Waals forces and hydrogen bonds between the alcohol molecules. However, the activation energy of alcohols are known to decrease with their molecular size⁵¹. Because the experiments were carried out at constant temperature of 60 °C, the difference between reaction temperature and the boiling temperature of the alcohol increases as we move from methanol to butanol. Hence, it becomes more difficult for larger alcohol molecules to adsorb on the surface of catalyst and react with propionic acid and this results in a decrease in reactivity as the alcohol molecules become larger. **Table 5.5** presents the boiling temperature and activation energy of methanol, ethanol, 1-propanol and 1-butanol in esterification with propionic acid.

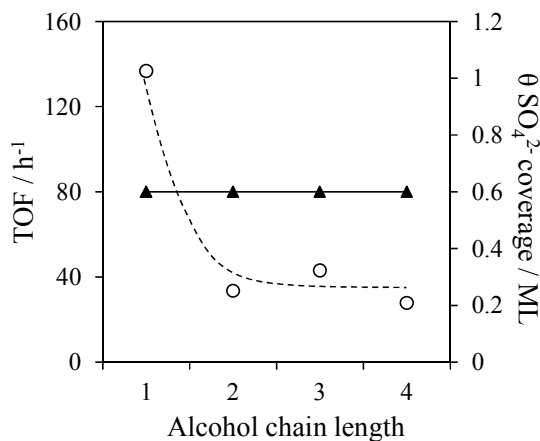


Figure 5.8: (○) Optimum TOFs across the series of SZ catalysts as a function of alcohol carbon chain length and (▲) the corresponding S coverage that gives the optimum TOF

Table 5.5: Boiling temperature and activation energy of C₁ to C₄ alcohols in esterification with propionic acid⁵¹

Alcohol type	Boiling temperature °C	Activation energy kJ mol ⁻¹
Methanol	64.7	-
Ethanol	78.4	52.6
1-Propanol	97	49.9
1-Butanol	117	47.3

As it was explained in **Chapter 2**, in all cases alcohol was used in great excess however the molar ratio between propionic acid and alcohols was not kept constant. In order to ensure that this variation in alcohol:acid ratio did not have a significant effect on the result, particularly when butanol was used as alcohol, a single test with alcohol:acid molar ratio similar to methanol:propionic acid molar ratio was carried out. This test confirms that for esterification of propionic acid with butanol, increasing the alcohol:acid molar ratio from 14 to 30 has only a minor effect. (**Figure 5.9**)

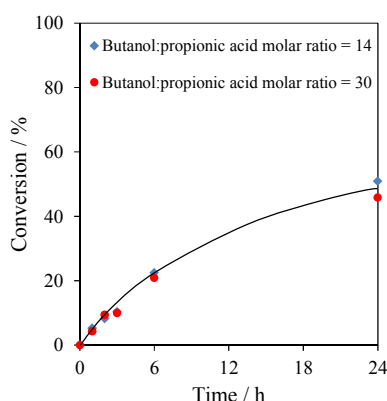


Figure 5.9: Effect of variation in excess amount of butanol in esterification with propionic acid at 60 °C

5.2.2 SBA-15 supported sulphated zirconia catalysts for esterification of FFAs

As it was mentioned in **Chapter 4**, although sulphated zirconia is an interesting catalyst with outstanding acidic properties, it suffers from low surface area. Moreover, it was pointed out earlier in this chapter that zirconium is a rare and expensive element and using it in the form of bulk sulphated zirconia for biodiesel production is not economically viable. Therefore, the application of supported sulphated zirconia catalyst in biodiesel production is of interest. Hence, the catalytic performance of SZ/SBA-15

catalysts in esterification of propionic and palmitic acid will be discussed in this section.

5.2.2.1 Esterification of propionic acid with methanol over the series of SZ/SBA-15 catalysts with different S content

The catalytic performance of the SZ/SBA-15 series with different S content was explored in the esterification of propionic acid with methanol at 60 °C. **Figure 5.10** demonstrates that as the concentration of impregnating H_2SO_4 increases, higher conversions of propionic acid are obtained. The rise in propionic acid conversion across this series of catalysts is associated with the growing number of Brønsted acid sites as the concentration of impregnating H_2SO_4 increases. (See **Figure 4.34**)

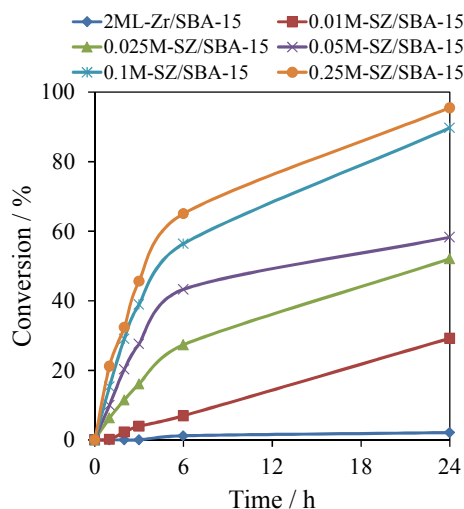


Figure 5.10: Conversion profiles of propionic acid in esterification reaction with methanol over SZ/SBA-15 catalysts at 60 °C

The reaction rates and TOFs follow a similar trend to the conversion levels. It can be observed from **Figure 5.11** that the reaction rates and TOFs increase rapidly when the S:Zr atomic ratio increases from 0 to ~0.2. Increasing above this ratio has a less significant effect on rate and TOF. This exactly mirrors the variations in the number of Brønsted acid sites. Moreover, the increase in TOF is attributable to increased acid strength at higher S:Zr atomic ratios as discussed in **Section 4.2.3.5**.

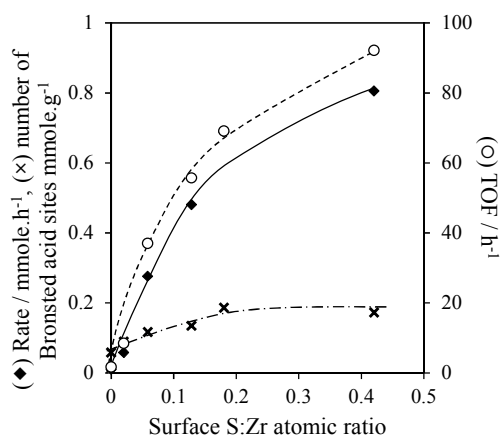


Figure 5.11: (x) Number of Brønsted acid sites of SZ/SBA-15 catalysts, (♦) reaction rates and (○) TOFs for propionic acid esterification with methanol over SZ/SBA-15s at 60 °C

5.2.2.2 Esterification of palmitic acid with methanol over the series of SZ/SBA-15 catalysts with different S content

Catalytic esterification of palmitic acid with methanol was conducted in order to study the effect of fatty acid carbon chain length on its reactivity. Comparable to esterification of propionic acid, palmitic acid conversion increases with the concentration of the impregnating H_2SO_4 up to $[\text{H}_2\text{SO}_4] = 0.1 \text{ M}$ and then levels off. However, compared to propionic acid the conversion levels are considerably lower. (**Figure 5.12**)

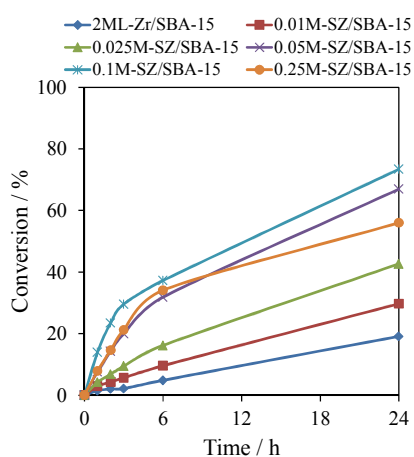


Figure 5.12: Conversion profiles of palmitic acid in esterification reaction with methanol over SZ/SBA-15 catalysts at 60 °C

Figure 5.13 demonstrates that increasing the surface S:Zr atomic ratio from 0 to 0.13 will significantly enhance the rate of palmitic acid esterification. However, further increase in S:Zr ratio has no considerable effect of the reaction rate and TOF.

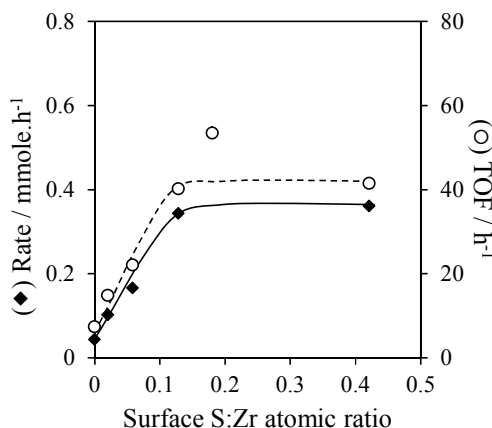


Figure 5.13: (♦) reaction rates and (○) TOFs for propionic acid esterification with methanol over SZ/SBA-15s at 60 °C

5.2.3 Comparison between bulk SZ and SBA-15 supported SZ materials in esterification of FFAs with methanol

In order to compare the catalytic performance of sulphated zirconia catalysts and the grafted materials in esterification of propionic and palmitic acid with methanol, the amount of converted acid is plotted as a function of impregnating H₂SO₄ concentration. To ensure a fair comparison, the conversions were normalized to the Zr content as well as mass of catalysts (**Figure 5.14**), confirming that by supporting sulphated zirconia on SBA-15, a larger amount of reactants (either propionic acid or palmitic acid) per unit mass of zirconium precursor undergo esterification with methanol. Moreover, normalizing the reaction rate to zirconium content per unit mass of catalysts also confirms that for the same amount of zirconium, the reactions over the SZ/SBA-15 catalysts are taking place at a faster rate as shown in **Figure 5.15**. The enhanced catalytic activity of SZ/SBA-15 catalysts compared to bulk SZ materials could be attributed to the textural properties of the supported materials, and their high surface (~500 to 650 m² g⁻¹) area in particular.

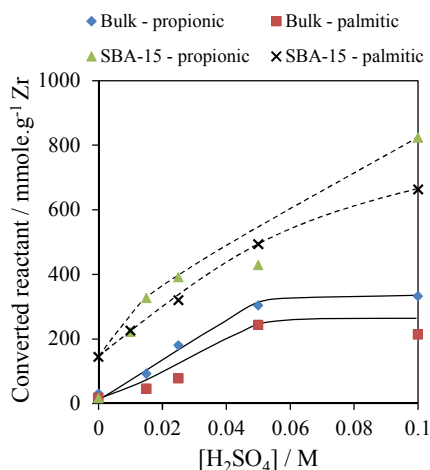


Figure 5.14: The amount of converted of propionic and palmitic acid in esterification reaction with methanol over bulk and SBA-15 supported SZ catalysts as a function of impregnating H₂SO₄ concentration

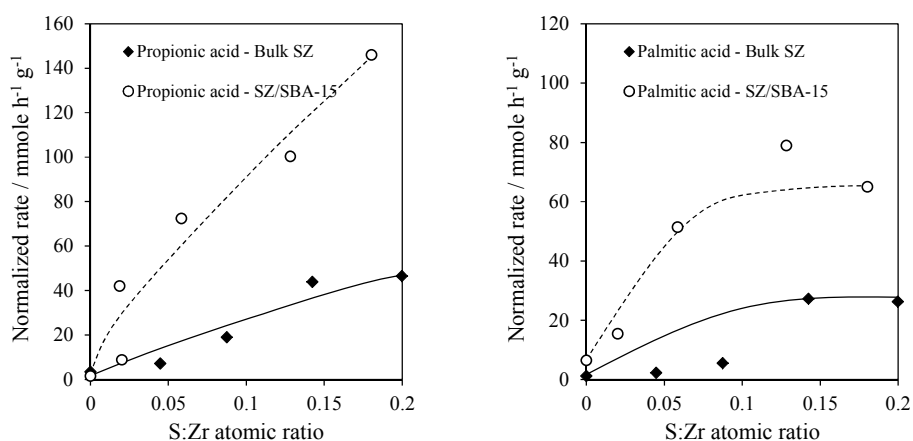


Figure 5.15: Normalized rate (to catalyst Zr content) for esterification reaction of propionic and palmitic acid with methanol over bulk SZ and SBA-15 supported SZs

5.2.4 Leaching test

A leaching test was also carried out on the most active catalysts from bulk and SBA-15 supported sulphated zirconia series as outlined in **Chapter 2**. Esterification of propionic acid was performed with methanol at 60 °C over SZ 0.1M and SZ/SBA-15 0.25M. The catalysts were removed after an hour by means of hot filtration technique and the reactions were continued for another 23 h in absence of catalysts. A significant drop in conversion of propionic acid was observed after catalyst removal compared to normal catalytic reactions confirming that the contribution of homogeneous catalysis from leaching of active sites is not significant. (**Figure 5.16**)

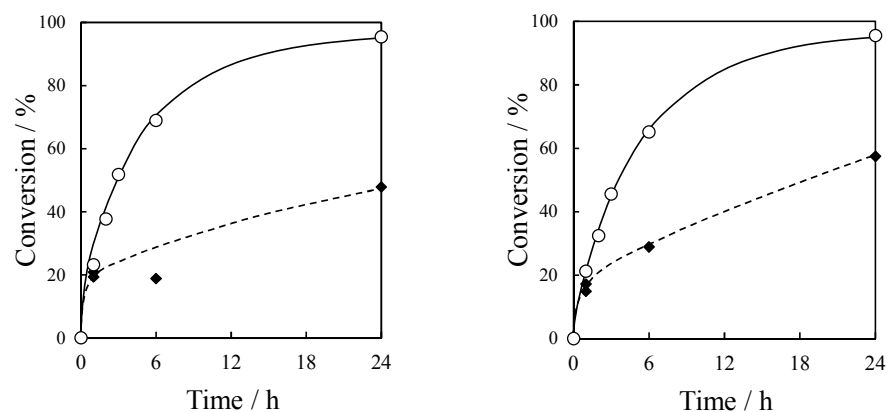


Figure 5.16: Leaching test during esterification of propionic acid with methanol over (Left) SZ 0.1M and (right) SZ/SBA-15 0.25M (catalyst was removed after 1 h)

5.3 Conclusion

To summarize, the impact of surface sulfation of zirconia on its catalytic activity in esterification of free fatty acids with alcohols was explored. It was shown that sulfation of zirconia results in significant enhancement in its activity for esterification reactions. Particularly, the SZ 0.05M showed the highest activity among the bulk SZ catalysts due to its optimum number of acid sites and acid strength. Furthermore, the effect of FFA alkyl chain length on its reactivity in esterification reaction was assessed and it was demonstrated that the reactivity of carboxylic acids decreases with their alkyl chain length. Propionic acid exhibited the highest reactivity compared to hexanoic, lauric and palmitic acids. Moreover, the impact of alcohol type on the esterification of propionic acid was studied and it was determined that at a constant temperature of 60 °C, the use of alcohols of smaller molecular size is beneficial to esterification of propionic acid.

Additionally, the application of SBA-15 supported sulphated zirconia catalysts in the esterification of propionic acid and palmitic acid was explored. The impact of sulphur loading was determined, confirming that by increasing the sulphur loading, and consequently the number of Brønsted acid sites, the activity of the catalysts improves. However, impregnation of zirconia grafted SBA-15 with H_2SO_4 concentration greater than 0.1 M results in zirconia film dissolution and therefore decreased number of active sites and a lower catalytic activity. Moreover it was demonstrated that by means of grafting zirconia onto SBA-15 superior catalytic activity per unit mass of zirconium could be achieved.

5.4 References

1. C. C. Enweremadu and M. M. Mbarawa, *Renewable and Sustainable Energy Reviews*, 2009, **13**, 2205-2224.
2. D. Y. C. Leung, X. Wu and M. K. H. Leung, *Applied Energy*, 2010, **87**, 1083-1095.
3. Y. Chen, B. Xiao, J. Chang, Y. Fu, P. Lv and X. Wang, *Energy Conversion and Management*, 2009, **50**, 668-673.
4. L. Guerreiro, P. M. Pereira, I. M. Fonseca, R. M. Martin-Aranda, A. M. Ramos, J. M. L. Dias, R. Oliveira and J. Vital, *Catalysis Today*, 2010, **156**, 191-197.
5. M. C. Math, S. P. Kumar and S. V. Chetty, *Energy for Sustainable Development*, 2010, **14**, 339-345.
6. M. Zabeti, W. M. A. Wan Daud and M. K. Aroua, *Fuel Processing Technology*, 2009, **90**, 770-777.
7. A. Demirbaş, *Energy Sources, Part A: Recovery, Utilization, and Environmental Effects*, 2008, **31**, 163-168.
8. Y. C. Sharma, B. Singh and J. Korstad, *Fuel*, 2011, **90**, 1309-1324.
9. Z. Helwani, M. R. Othman, N. Aziz, W. J. N. Fernando and J. Kim, *Fuel Processing Technology*, 2009, **90**, 1502-1514.
10. J. C. Juan, D. A. Kartika, T. Y. Wu and T. Y. Y. Hin, *Bioresource Technology*, 2011, **102**, 452-460.
11. M. J. Climent, A. Corma, S. Iborra and A. Velty, *Journal of Catalysis*, 2004, **221**, 474-482.
12. U. Costantino, F. Marmottini, M. Nocchetti and R. Vivani, *European Journal of Inorganic Chemistry*, 1998, **1998**, 1439-1446.
13. K. Narasimharao, A. Lee and K. Wilson, *Journal of Biobased Materials and Bioenergy*, 2007, **1**, 19-30.
14. M. R. Othman, Z. Helwani, Martunus and W. J. N. Fernando, *Applied Organometallic Chemistry*, 2009, **23**, 335-346.
15. A. Banerjee and R. Chakraborty, *Resources, Conservation and Recycling*, 2009, **53**, 490-497.
16. A. P. Vyas, J. L. Verma and N. Subrahmanyam, *Fuel*, 2010, **89**, 1-9.
17. Y. Ono and T. Baba, *Catalysis Today*, 1997, **38**, 321-337.

18. I. Jiménez-Morales, J. Santamaría-González, P. Maireles-Torres and A. Jiménez-López, *Applied Catalysis A: General*, 2010, **379**, 61-68.
19. Y. M. Park, J. Y. Lee, S. H. Chung, I. S. Park, S. Y. Lee, D. K. Kim, J. S. Lee and K. Y. Lee, *Bioresource Technology*, 2010, **101**, S59-S61.
20. A. C. Carmo Jr, L. K. C. de Souza, C. E. F. da Costa, E. Longo, J. R. Zamian and G. N. da Rocha Filho, *Fuel*, 2009, **88**, 461-468.
21. K. Srilatha, N. Lingaiah, B. L. A. P. Devi, R. B. N. Prasad, S. Venkateswar and P. S. S. Prasad, *Applied Catalysis A: General*, 2009, **365**, 28-33.
22. L. A. S. do Nascimento, R. S. Angélica, C. E. F. da Costa, J. R. Zamian and G. N. da Rocha Filho, *Applied Clay Science*, 2011, **51**, 267-273.
23. M. K. Lam, K. T. Lee and A. R. Mohamed, *Biotechnology Advances*, 2010, **28**, 500-518.
24. V. SathyaSelvabala, T. K. Varathachary, D. K. Selvaraj, V. Ponnusamy and S. Subramanian, *Bioresource Technology*, 2010, **101**, 5897-5902.
25. L. Zatta, J. E. F. D. C. Gardolinski and F. Wypych, *Applied Clay Science*, 2011, **51**, 165-169.
26. E. Lotero, Y. Liu, D. E. Lopez, K. Suwannakarn, D. A. Bruce and J. G. Goodwin, *Industrial & Engineering Chemistry Research*, 2005, **44**, 5353-5363.
27. Y. Feng, B. He, Y. Cao, J. Li, M. Liu, F. Yan and X. Liang, *Bioresource Technology*, 2010, **101**, 1518-1521.
28. Y. Feng, A. Zhang, J. Li and B. He, *Bioresource Technology*, 2011, **102**, 3607-3609.
29. R. Tesser, M. Di Serio, L. Casale, L. Sannino, M. Ledda and E. Santacesaria, *Chemical Engineering Journal*, 2010, **161**, 212-222.
30. J. Y. Park, D. K. Kim and J. S. Lee, *Bioresource Technology*, 2010, **101**, S62-S65.
31. J. Y. Park, Z. M. Wang, D. K. Kim and J. S. Lee, *Renewable Energy*, 2010, **35**, 614-618.
32. S. M. Son, H. Kimura and K. Kusakabe, *Bioresource Technology*, 2011, **102**, 2130-2132.
33. Y. M. Park, S. H. Chung, H. J. Eom, J. S. Lee and K. Y. Lee, *Bioresource Technology*, 2010, **101**, 6589-6593.
34. M. Kim, C. DiMaggio, S. Yan, H. Wang, S. O. Salley and K. Y. Simon Ng, *Bioresource Technology*, 2011, **102**, 2380-2386.

35. D. Rattanaphra, A. P. Harvey, A. Thanapimmetha and P. Srinophakun, *Renewable Energy*, 2011, **36**, 2679-2686.
36. S. A. Basha and K. Raja Gopal, *Renewable and Sustainable Energy Reviews*, 2012, **16**, 711-717.
37. B. L. Salvi and N. L. Panwar, *Renewable and Sustainable Energy Reviews*, 2012, **16**, 3680-3689.
38. A. F. Lee, J. A. Bennett, J. C. Manayil and K. Wilson, *Chemical Society Reviews*, 2014.
39. M. J. Climent, A. Corma and S. Iborra, *Chemical Reviews*, 2010, **111**, 1072-1133.
40. A. Corma, S. Iborra and A. Velty, *Chemical Reviews*, 2007, **107**, 2411-2502.
41. D. Rattanaphra, A. Harvey and P. Srinophakun, *Top Catal*, 2010, **53**, 773-782.
42. K. Arata, *Green Chemistry*, 2009, **11**, 1719-1728.
43. B. M. Reddy and M. K. Patil, *Chemical Reviews*, 2009, **109**, 2185-2208.
44. Z. Zeng, L. Cui, W. Xue, J. Chen and Y. Che, *Chemical Kinetics*, 2012, 255-282.
45. R. W. Taft and M. S. Newman, *Steric effects in organic chemistry*, Wiley, New York, 1956.
46. M. Charton, *Journal of the American Chemical Society*, 1975, **97**, 1552-1556.
47. H. Fujimoto, Y. Mizutani, J. Endo and Y. Jinbu, *The Journal of Organic Chemistry*, 1989, **54**, 2568-2573.
48. T. Fujita, C. Takayama and M. Nakajima, *The Journal of Organic Chemistry*, 1973, **38**, 1623-1630.
49. D. Datta and D. Majumdar, *Journal of Physical Organic Chemistry*, 1991, **4**, 611-617.
50. M. Canakci and J. Van Gerpen, *Transactions of the ASAE-American Society of Agricultural Engineers*, 1999, **42**, 1203-1210.
51. J. Lilja, J. Wärnå, T. Salmi, L. J. Pettersson, J. Ahlqvist, H. Grénman, M. Rönnholm and D. Y. Murzin, *Chemical Engineering Journal*, 2005, **115**, 1-12.

Chapter 6

Conclusion

6.1 Conclusion

This thesis set out to explore the structure reactivity correlations in sulfated zirconia catalysts for the conversion of sugars to 5-HMF which is an important platform chemical. Two approaches were taken utilising a commercial mesoporous zirconium hydroxide in which the sulfate coverage was tuned, and a coating method in which preformed mesoporous SBA-15 was used as a scaffold to assemble ultra-thin zirconia films. The versatility of these materials was also explored through their application in esterification reactions which is an important reaction for biodiesel synthesis and also the synthesis of fine and speciality chemicals.

In the first approach a series of bifunctional sulphated zirconia catalysts were shown to possess acid and basic properties which varied systematically with concentration of impregnating sulphuric acid solution. This enabled the relationship between the surface functionalities of these materials and their catalytic activity in dehydration of biomass derived sugars in aqueous solution to be explored. In this respect, characterization of the catalysts by chemisorption methods (CO_2 , NH_3 and Pyridine) using adsorption calorimetry, TPD and IR spectroscopy confirmed that monoclinic parent zirconia exhibits mixed Lewis acid and basicity, making it an effective catalyst for glucose isomerisation to fructose but poor towards fructose dehydration to HMF. XRD and Raman spectroscopy were particularly useful in probing the crystalline phase of these materials and how the contributions of monoclinic and tetragonal phase vary when pre-treated with dilute sulphuric acid and calcined. The formation of polydentate surface SO_4^{2-} species leads to stabilisation of tetragonal ZrO_2 , conferring significant Brønsted acidity and enhancing the ability of sulfated zirconia to form HMF from either glucose or fructose. There is an critical ratio of acid:base sites of 17:4 required to achieve optimum production of HMF from glucose. Above this ratio, further sulfation of zirconia surface ($\theta_{\text{SO}_4} > 0.25 \text{ ML}$) resulted in disappearance of base sites, making the catalysts exhibit exclusively Brønsted acidity, switching off the isomerization of glucose to fructose and therefore diminishing HMF yield from glucose. Furthermore, XRD, Raman and nitrogen porosimetry revealed that an uncontrolled sulphation of zirconia with high concentrations of sulphuric acid ($[\text{H}_2\text{SO}_4] > 0.25 \text{ M}$) will result in structural collapse of the material and loss of crystallinity and therefore significant reduction in reactivity of the catalyst. So, it was found out that the catalyst with surface

sulphate coverage of 0.3 ML possesses an optimal mix of base, Lewis acid and Brønsted acid sites, enabling it to maximize HMF yield from glucose.

The conversion of xylose over such series of sulphated zirconia catalyst was also explored and the reaction pathway proposed by Choudhary et al.¹ was investigated. Analogous to glucose conversion to HMF, xylose transformation to furfural could take place via isomerization of xylose to lyxose and xylulose over Lewis acid sites and then Brønsted acid catalysed conversion of xylulose to furfural. Alternatively, xylose could directly convert to furfural over Brønsted acid sites however this requires higher activation energy.² While, increasing the sulphur content of the catalysts results in reduction in xylose conversion due to loss of Lewis acid sites as a consequence of more intense sulfation (analogous to decreased glucose conversion when the Lewis and base sites were disappeared), furfural yield and selectivity monotonically increased with [H₂SO₄] confirming that the telescopic conversion of xylose to furfural is not the only pathway and xylose could also transform directly to furfural over Brønsted acid sites. However, calculations show that the number of furfural molecules produced over each acid site decreases with sulphur content of the catalysts in agreement with higher activation energy for the direct conversion route. It also found that the mass balance worsens with increased Lewis acidity suggesting these are responsible for promoting undesired side-reactions.

Enhancement of textural properties of these materials was attempted and achieved through conformal zirconia monolayers deposition on SBA-15 support. Zirconia monolayers were first grown in a consecutive fashion over SBA-15, via sequential grafting and hydrolysis cycles employing a zirconium propoxide precursor. The uniformity of the grafted layers was confirmed by N₂ porosimetry which reveals a progressive decrease in pore volume, mean pore size and BET surface area with each grafting cycle, consistent with a layer-wise growth. Furthermore, a layer-by-layer growth mode of zirconia film was confirmed based on attenuation of the Si 2p signal from XPS and also the zirconia film thickness was calculated equating to 0.5, 0.84 and 1.38 nm for the first, second and third grafting cycles respectively which is in excellent agreement with the thickness of a (111) oriented monolayer of monoclinic ZrO₂ (0.42 nm), confirming the successful growth of conformal ZrO₂ monolayers over SBA-15. Afterwards, the impact of number of zirconia monolayers on reactivity of SZ/SBA-15

catalysts in glucose and fructose dehydration was explored suggesting that a 2 ML-SZ/SBA-15 exhibits much more activity than a 1 ML-SZ/SBA-15 catalyst while having 3 layers of zirconia has no significant advantages. Therefore, 2 ML SBA-15 supported zirconia was selected to study the impact of sulphur loading on its reactivity in glucose and fructose conversion to HMF. Similar to bulk sulphated zirconia, the highest catalytic activity across the series was shown by samples treated with dilute H_2SO_4 (< 0.025 M), however the optimal mix of base, Lewis and Brønsted acidity was obtained when the catalyst was treated with 0.05 M sulphuric acid solution. Bulk and surface elemental analysis in conjunction with nitrogen porosimetry suggested that aqueous solutions of sulphuric acid with concentrations > 0.1 M dissolve the grafted zirconia film and has no benefit to the catalysis. Comparing the supported materials with the bulk sulphated zirconia, it was demonstrated that for the same amount of zirconium precursor, the supported materials exhibits higher activity which is attributed to high surface area and therefore enhanced accessibility of active sites. The hydrothermal stability of pure SBA-15 was compared with zirconia-grafted SBA-15 confirming that incorporation of zirconia significantly improves the hydrothermal stability of the support, making it a good candidate for application in harsher reaction environments such as high pressures and high temperatures.

Finally, the catalytic performance of both series of materials (bulk SZ and SZ/SBA-15) were examined in biodiesel production via esterification of free fatty acids. The effect of FFA alkyl chain length on its reactivity in esterification with methanol was studied confirming that the reactivity of short alkyl chain FFAs ($\geq \text{C}_3$) is considerably higher than larger carboxylic acids due to steric and inductive effect. Moreover, the impact of alcohol type was investigated showing that their reactivity decreases with increase in the boiling temperature, meaning that methanol is the most reactive alcohol if the reaction is conducted at a constant temperature. Again the superiority of supported material over bulk SZ is proved since higher FFA conversions were obtained per gram of zirconium for the SZ/SBA-15 materials.

6.2 Future work

In this thesis, the application of bifunctional sulphated zirconia based catalyst in production of platform chemicals and biodiesel at constant temperatures and atmospheric pressure were studied. Therefore, the optimization of temperature and pressure are yet to be carried out. Moreover, since the SBA-15 supported zirconia showed promise for high hydrothermal stability, wider applications of such catalysts in aqueous phase biomass reforming under harsher reaction conditions will be an advantage.

Exploring other materials for production of HMF from glucose, such as weaker acidic materials like phosphated metal oxides or NbPO_4 as well as other classes of materials with acid:base properties³ could be interesting.

Also the application of hierarchical macro-mesoporous supports in such reactions could be of great interest since they offer improved mass transport arising via the interconnected pore network. This could be particularly advantageous in esterification of large molecule free fatty acids.

Furthermore, the use of sulphated zirconia based catalysts could be explored in continuous systems such as Oscillatory Baffled Reactors (OBR) since they are known to offer possibilities for alternative clean chemical processes employing heterogeneous catalysts.⁴

6.3 References

1. V. Choudhary, S. I. Sandler and D. G. Vlachos, *ACS Catalysis*, 2012, **2**, 2022-2028.
2. J. Lilja, J. Wärnå, T. Salmi, L. J. Pettersson, J. Ahlqvist, H. Grénman, M. Rönholm and D. Y. Murzin, *Chemical Engineering Journal*, 2005, **115**, 1-12.
3. A. A. Elmekawy, N. R. Shiju, G. Rothenberg and D. R. Brown, *Industrial & Engineering Chemistry Research*, 2014.
4. V. C. Eze, A. N. Phan, C. Pirez, A. P. Harvey, A. F. Lee and K. Wilson, *Catalysis Science & Technology*, 2013, **3**, 2373-2379.